2009

Characterization of a Novel 53BP1-Dependent Mechanism that Promotes Non-Homologous End Joining of Deprotected Telomeres by Increasing Chromatin Mobility

Nadya Dimitrova

CHARACTERIZATION OF A NOVEL 53BP1-DEPENDENT MECHANISM THAT PROMOTES NON-HOMOLOGOUS END JOINING OF DEPROTECTED TELOMERES BY INCREASING CHROMATIN MOBILITY

A Thesis Presented to the Faculty of

The Rockefeller University

In Partial Fulfillment of the Requirements for

the Degree of Doctor of Philosophy

by

Nadya Dimitrova

June 2009

CHARACTERIZATION OF A NOVEL 53BP1-DEPENDENT MECHANISM THAT PROMOTES NON-HOMOLOGOUS END JOINING OF DEPROTECTED TELOMERES BY INCREASING CHROMATIN MOBILITY

Nadya Dimitrova, Ph.D.
The Rockefeller University 2009

When a double-stranded break (DSB) occurs in mammalian genomes, the local chromatin is altered through the modification of histones (notably the phosphorylation of H2AX) and the binding of DNA damage response factors (e.g. MDC1, 53BP1). Although several lines of evidence have pointed to a role for some of these factors in DSB repair through non-homologous end-joining (NHEJ), the mechanism of their contribution has not been established.

To study the regulation of NHEJ, we have used as a model system dysfunctional telomeres, which are uncapped by the removal of the shelterin component, TRF2. As a consequence of TRF2 loss, deprotected chromosome ends trigger a sequence of events normally activated by the presence of DSBs. These include the instigation of ATM-mediated activation of cell cycle checkpoints and the accumulation of DNA damage response factors at the telomeric chromatin. In addition, the NHEJ pathway repairs deprotected telomeres to generate chromosome end-to-end fusions.

We have examined the roles of the Mre11/Rad50/NBS1 (MRN) complex, H2AX, MDC1, and 53BP1 in the NHEJ of dysfunctional telomeres. We have demonstrated that among these factors, 53BP1 is required for the fusion of telomeres, whereas the MRN complex, H2AX, and MDC1 only stimulate the efficiency of the repair process, most likely by mediating the recruitment of 53BP1 to uncapped chromosome ends.

Furthermore, we have revealed the mechanism by which 53BP1 acts. We have shown that upon deprotection, telomeres become more dynamic and explore larger territories in a 53BP1-dependent manner. Faster mobility of DNA ends increases the chance that dysfunctional telomeres, which are uniformly scattered throughout the nucleus, will find one another and fuse. We have proposed that the dynamic behavior of DNA ends may be required to promote long-distance repair in general, and that it may play a role in other instances of NHEJ, such as during recombination in the immunoglobulin genes, where the DNA ends are initially at a distance.

Furthermore, we have shown that the mechanism that promotes the mobility of uncapped chromosome ends requires microtubules. This finding suggests an unprecedented role for microtubules in the process of DNA repair in mammalian interphase cells. Moreover, it points to the existence of a trans-nuclear envelope bridge between damaged chromatin and cytoplasmic microtubules. Accordingly, our data indicate that mobility depends on the acetylation status of chromatin, signifying that specific chromatin modifications are involved in establishing that connection.

Finally, we have preliminary evidence that the dynamic process that we have uncovered might play a role in the repair of all DNA lesions. We speculate that a microtubule-dependent chromatin mobility provides a proofreading mechanism preventing HDR between non-sister chromatids, possibly by physically pulling apart inappropriate connections. Overall, this thesis presents a novel view on how the dynamic behavior of DNA ends might be required for efficient and accurate repair of DNA lesions.

ACKNOWLEDGEMENTS

Most of all, I would like to thank my thesis advisor Titia de Lange for her unfaltering support over the past five years. I have learned from her how to approach a scientific problem, how to design my experiments, how to analyze the data, and how to interpret the results. She has taught me clarity and accuracy not only at the bench but also in scientific thinking and writing. Most importantly, I have learned from her how to dream about science, and how the smallest results matter and add up to our understanding of biology.

I would also like to thank my committee members, David Allis and Bob Roeder, for their advice and encouragement over the years. I would like to express my appreciation to Steve Elledge for traveling from Boston to serve as the external examiner on my thesis committee. Additionally, the Rockefeller University Dean's Office has been helpful at all stages of my thesis work.

I am grateful to Junjie Chen from Yale University for sharing his 53BP1$^{-/-}$ and MDC1$^{-/-}$ mice with us and to Andre Nussenzweig from the NIH for providing us with the NBS1$^{F/-}$ mouse. I am also indebted to Tarun Kapoor for his expertise advice on microtubules.

I am especially grateful to Maria Chen from the lab of David Spector at Cold Spring Harbor Laboratories for welcoming me into their lab and for instructing me on live-cell imaging.

To all the past and present members of the de Lange lab, I would like to thank for their friendship and for their help. I would like to express my deepest gratitude to my classmate Dirk Hockemeyer for the countless hours he spent teaching me how to do

experiments with German precision. I would like to thank Agnel Sfeir, Eros Lazzerini-Denchi, Giulia Celli, Hiro Takai, Megan van Overbeek, Sean Rooney, and Peng Wu for generously sharing their scientific knowledge and reagents. Francisca Lottesberger, Jan-Peter Daniels, Jill Donigian, Kaori Takai, Kristina Hoke, Sara Buonomo, Teresa Davoli, Wilhelm Palm, and Yi Gong are thanked for making the lab a very enjoyable place to work.

I would like to thank Devon White for watching over me and my mouse colonies. Stephanie Blackwood is thanked for sharing her lunches with me and for organizing the lab. Stew Barnes is thanked for his timely help with all computer-related issues. I thank Rita Rodney, Rosy Mejia, Lola MacRae, Steven Reisenweber, and Diana Argibay for taking care of the lab. I owe gratitude to Peng Wu for proofreading parts of my thesis and to Lola MacRae for proofreading and helping with the formatting.

I would like to dedicate this thesis to my mother, Mariyana and to my father, Miroslav, who is going to read every word of it. Thank you for supporting every step of my journey far away from my hometown Sofia, Bulgaria, and for always encouraging me to rest and take care of myself. I would like to thank my brother Mladen for being the best older brother at all times and for his help with the analysis of probabilities. And I thank Justin for helping me go through difficult times.

TABLE OF CONTENTS

LIST OF FIGURES

LIST OF VIDEOS

LIST OF ABBREVIATIONS

53BP1	-	p53-binding protein 1
Ab	-	Antibody
AID	-	Activation-induced cytidine deaminase
A-T	-	Ataxia-telangiectasia
ATLD	-	Ataxia-telangiectasia-like disorder
ATM	-	Ataxia-telangiectasia mutated
ATR	-	ATM- and Rad3-related
BRCA1	-	Breast cancer 1
BRCT	-	BRCA1-related C-terminal
BrdU	-	Bromo-deoxyuridine
Cdc2	-	Cell division cycle 2
CDK	-	Cyclin-dependent kinase
ChIP	-	Chromatin immunoprecipitation
CK2	-	Casein kinase 2
CSR	-	Class-switch recombination
DAPI	-	4, 6-diamidino-2-phenylindole
DMSO	-	Dimethyl sulphoxide
DNA-PKcs	-	DNA-dependent protein kinase, catalytic subunit
DSB	-	Double-stranded break
dsDNA	-	Double-stranded DNA
eGFP	-	Enhanced green fluorescent protein
FISH	-	Fluorescence *in situ* hybridization
FHA	-	Fork-head associated
H4-K20diMe	-	Histone H4, Lysine 20, dimethylated
HDAC	-	Histone deacetylase
HDR	-	Homology-directed repair
IF	-	Immunofluorescence
IF-FISH	-	Immunofluorescence - Fluorescence *in situ* hybridization
IP	-	Immunoprecipitation
IR	-	Ionizing radiation
IRIF	-	Ionizing radiation-induced focus
FAR assay	-	Fraction of activity released assay
KO	-	Knock-out
MEF	-	Mouse embryonic fibroblasts

MDC1	-	Mediator of DNA damage checkpoint 1
MNase	-	Micrococcal nuclease
Mre11	-	Meotic recombination 11
MRN complex	-	Mre11/Rad50/NBS1 complex
NBS	-	Nijmegen breakage syndrome
NBS1	-	Nijmegen breakage syndrome 1
NHEJ	-	Non-homologous end-joining
OB	-	Oligonucleotide/oligosaccharide-binding
PCR	-	Polymerase chain reaction
PIKK	-	Phospho-inositol 3-kinase related kinase
PD	-	Population doublinga
RNAi	-	RNA interference
RNF8	-	RING-finger ubiquitin ligase 8
RDS	-	Radioresistant DNA synthesis
RT-PCR	-	Reverse transcriptase – polymerase chain reaction
SAHA	-	Suberoylanilide hydroxamic acid
SCD	-	S/TQ cluster domain
s.d.	-	Standard deviation
shRNA	-	Short hairpin RNA
SMC1	-	Structural maintenance of chromosomes 1
ssDNA	-	single-stranded DNA
SV40-LT	-	Simian virus 40; Large T antigen
TIF	-	Telomere dysfunction-induced focus
TIN2	-	TRF1-interacting nuclear factor 2
T-SCE	-	Telomeric sister-chromatid exchange
TRF1	-	Telomere repeat binding factor 1
TRF2	-	Telomere repeat binding factor 2
TRF2-DN	-	Dominant negative allele of TRF2
TRFH	-	TRF homology
TSA	-	Trichostatin A
UNG	-	Uracil-N-glycosylase

CHAPTER 1: INTRODUCTION

PART I: CELLULAR RESPONSE TO DNA DAMAGE

Double-strand breaks are a threat to genome integrity

A single unrepaired double-strand break (DSB) can lead to significant loss of genetic information, as acentric fragments cannot be properly segregated during mitosis. Furthermore, incorrect repair of a single DSB can be mutagenic and result in chromosome rearrangements, potentially giving rise to alterations of gene expression or unstable dicentric chromosomes.

DSBs can arise spontaneously or result from programmed events during immune-receptor rearrangements in lymphocytes and recombination in germ cells. In addition, exposure to ionizing radiation (IR) or radiomimetic agents, accidentally in the environment as well as intentionally as part of a cancer treatment, also generate extensive DNA damage. Finally, the linear nature of eukaryotic chromosomes presents the problem of DNA ends that have to be actively shielded by the telomeric nucleo-protein complex in order to prevent recognition as DSBs. When the protective function of telomeres is disrupted, chromosomes can enter bridge-breakage-fusion cycles that can lead to disastrous alterations of genome organization. To neutralize the potential dangers posed by exogenous and endogenous sources of DNA damage, an extensive network of DNA damage response factors has evolved to ensure the integrity of the genome.

The DNA damage response machinery detects disruptions in DNA and executes checkpoint response and DNA repair. These events are elegantly coordinated so that even a single DSB is sensed immediately, within seconds, and a signaling cascade efficiently

promotes delay in cell cycle progression while repair takes place. Normal cell cycle progression resumes only when DNA repair has been successfully completed. In the event when the DNA lesion cannot be repaired, persistent checkpoint signaling promotes permanent cell cycle arrest or induces apoptosis, which eliminates the damaged cell thereby minimizing potential transformation events.

ATM kinase

ATM kinase is a central component of the response to DSBs

At the core of the DSB response machinery is the ATM (ataxia-telangiectasia mutated) kinase, mutated in the rare autosomal recessive human disorder A-T [1]. The hallmarks of cells derived from A-T patients are chromosome breakage and sensitivity to γ-irradiation and other genotoxic agents [2,3]. As a consequence of the impaired response to DSBs, A-T patients are predisposed to cancer, highlighting the essential role of ATM in maintaining genome stability. It is not clear whether the other characteristic manifestations of A-T, cerebellar degeneration and immunodeficiency, are also a result of defective DNA damage response [4].

ATM is a serine-threonine kinase and a member of the phospho-inositol 3-kinase related kinase (PIKK) family [1,5], which also includes ATR (ATM and Rad3-related), the major kinase responding to DNA lesions with single-stranded DNA, and DNA-PKcs (DNA-dependent protein kinase, catalytic subunit), a kinase involved in the non-homologous end-joining (NHEJ) repair pathway [6]. ATM kinase is activated under physiological and pathological conditions that induce DSBs and phosphorylates proteins involved in cell cycle control, apoptotis, and DNA repair.

The consensus target sequences for PIKKs are S/TQ sites [7,8]. Since many ATM targets have multiple S/TQ sites, it has been difficult to determine which sites are functionally important. In some cases, it has been established that phosphorylation at a particular site is essential for a specific functional aspect (e.g. p53 S15 [9]), whereas in other cases, phoshorylation of multiple sites in S/TQ cluster domains (SCDs) might be necessary to overcome an activation threshold (e.g. Chk2 SCD [10]).

The mechanism of ATM activation

The mechanism of ATM activation has been a controversial subject over the past several years. Initially, Kastan and colleagues observed that ATM is sequestered as an inactive dimer or higher order multimer in unperturbed cells [11]. They identified a site within ATM, S1981, which is autophosphorylated upon the induction of DSBs [11]. They proposed that this autophosphorylation event releases inhibitory contacts between the catalytic domain in one ATM molecule and the region surrounding S1981 in another, resulting in the dissociation of ATM dimers into active monomers. Autophosphorylation of ATM at S1981 has since been commonly accepted as an indicator for ATM activity. In addition, because they observed a relatively large number of ATM molecules being rapidly phosphorylated in response to a small number of DSBs, Bakkenist and Kastan argued against a model where ATM activation requires a direct contact with DSBs. Instead, they proposed that the introduction of DNA breaks must somehow signal to ATM molecules at a distance, for example, by causing a rapid change in some aspect of the higher-order chromatin structure [11]. Global chromatin relaxation has indeed been detected as a consequence of DSBs [12]. Furthermore, DSBs generated at I-PpoI

endonuclease-specific endogenous sites have been suggested to lead to local disruption of the nucleosome structure [13]. However, both of these changes in chromatin structure were found to require ATM function, suggesting that they are a consequence rather than the cause of ATM activition.

Recent data have implicated that autophosphorylation at S1981 is neither sufficient nor required for ATM activation. In the first place, Kozlov et al. identified two additional ATM autophosphorylation sites, S367 and S1893 [14]. In their study, introduction of S367A, S1981A, or S1893A ATM mutants into A-T cells failed to rescue the defects of ATM deficiency. These data argued that there are at least three functionally important radiation-induced autophosphorylation events required for ATM activation.

Another set of data demonstrated that autophosphorylation at S1987 (mouse residue corresponding to S1981 in human ATM) is dispensable for murine ATM activation *in vivo* [15]. B-cells isolated from $ATM^{-/-}$ mice, expressing ATM S1987A mutant from a BAC transgene were proficient in the phosphorylation of well-established ATM targets, SMC1 (Structural maintenance of chromosomes 1) and Chk2, in response to DSB-inducing agents [15]. In addition, lymphocyte development and genomic stability were restored in B- and T-cells isolated from $ATM^{-/-}$ mice expressing the S1987A mutant allele. Although it is possible that the mechanism for ATM activation may operate differently in murine and in human cells, this set of evidence demonstrated that phosphorylation at S1987 is not causative to activation of ATM, and also, importantly, it is not required for ATM activity.

The role of the MRN complex in ATM activation

As discussed below, mounting evidence argues that the MRN complex is an activator of ATM kinase [16-21]. The model speculates that ATM is recruited to chromatin via the MRN complex, which senses the presence of DSBs. After this initial recruitment event, ATM is locally converted to a catalytically active conformation. Subsequently, high local concentration of ATM proximal to DNA lesions might facilitate rapid autophosphorylation of the nucleoplasmic pool of ATM molecules.

The role of ATM kinase in regulating cell cycle progression

Once activated, ATM phosphorylates a series of substrates to alter cell cycle progression at G_1/S, in S phase, and at the G_2/M transition (Figure 1.1).

In the presence of DSBs in G1, phosphorylation and stabilization of the p53 protein induces p21, which is a negative regulator of CDKs (cyclin-dependent kinases), thereby preventing entry into S-phase. ATM is a central player in this pathway. In the first place, ATM directly phosphorylates p53 on serine 20 leading to its activation and stabilization [22]. In addition, ATM phosphorylates and deactivates the negative regulator of p53, Mdm2, thus promoting p53 accumulation through an independent pathway [23]. Indeed, in A-T cells, p53 phosphorylation as well as the accumulation of p53 protein are diminished following treatment with IR, resulting in defective G_1/S checkpoint [24]. Finally, ATM phosphorylates the checkpoint factor, Chk2, which in turn contributes to the G_1/S checkpoint both by phosphorylating p53 and by inhibiting Cdc25A activity [25].

An additional checkpoint defect in A-T cells is manifested as a radioresistant DNA synthesis (RDS) phenotype. In normal cells, exposure to IR provokes a rapid

decrease in DNA synthesis through the activation of the intra-S-phase checkpoint (Figure 1.1). ATM contributes to the intra-S-phase checkpoint by phosphorylating and activating Chk2 kinase, which, in turn, phosphorylates Cdc25A and marks it for proteasomal degradation. Absence of Cdc25A results in persistence of phosphorylated CDK2, which remains bound to cyclin E and A in inactive complexes, preventing the initiation of DNA synthesis [26]. In the absence of ATM, this pathway is impaired due to reduced Chk2 phosphorylation. Regulation of the intra-S-phase checkpoint further appears to be dependent on several ATM phosphorylation targets, including NBS1 (Nijmegen breakage syndrome 1), SMC1, and BRCA1 (Breast cancer 1) [27,28].

Failure to arrest before mitosis represents a third checkpoint defect in A-T cells (Figure 1.1). In response to DSBs, the G2/M transition is inhibited by ATM-mediated phosphorylation of Chk2, which in turns leads to phosphorylation of Cdc25C phosphatase, resulting in its inactivation and translocation to the cytoplasm [10,29-32]. In absence of Cdc25C, the cyclin B/Cdc2 complex remains in its inactivated phosphorylated state, thus preventing entry into mitosis.

In addition to its role in checkpoint signaling, ATM-dependent phosphorylation also promotes the accumulation of multiple DNA damage response factors at the chromatin surrounding DNA lesions in structures referred to as DNA damage foci or irradiation-induced foci (IRIFs). The constitution of these ATM-dependent DNA damage foci is discussed at length below, whereas their function is the primary focus of this thesis work.

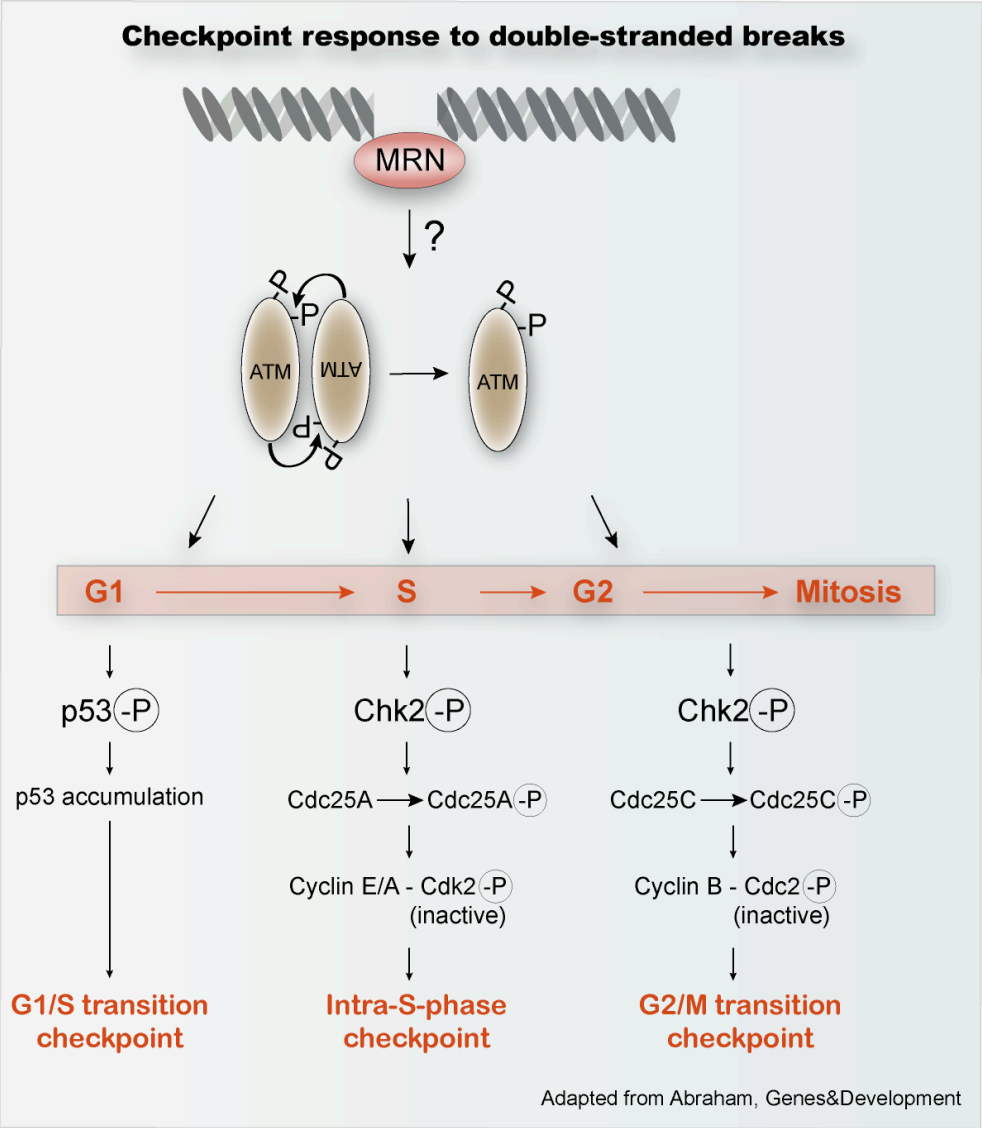

Figure 1.1. ATM-mediated checkpoint response to DSBs

In response to IR, it has been proposed that the MRN complex signals the presence of DNA lesions and promotes the activation and autophosphorylation of the ATM kinase. Depending on the cell cycle stage when DNA damage is induced, ATM phosphorylates downstream checkpoint factors to trigger cell cycle arrest at the G1/S transition, in S-phase, or at the G2/M checkpoint.

The Mre11/Rad50/NBS1 complex

Structure of the MRN complex

The MRN complex is a highly conserved protein complex involved in multiple aspects of the response to DSBs, including ATM activation, cell cycle control, and DNA repair. Here we discuss the arsenal of recently characterized structural and biochemical features that allow the MRN complex to accomplish these various tasks.

The MRN complex is composed of two Mre11, two Rad50, and an unknown number of NBS1 molecules [33]. Initial analysis by scanning force microscopy revealed that the overall architecture of the MRN complex appears as two highly flexible intramolecular coiled-coils emanating from a central globular DNA binding domain [34]. The globular domain consists of an Mre11/Rad50 dimer, in which each Mre11 molecule interacts with the Walker A and B ATPase domain of the corresponding Rad50 molecule [33]. The polypeptide that separates the two Walker motifs in Rad50 folds back on itself to form a protruding coiled-coil structure, whose apex contains a pair of cysteine residues capable of coordinating a Zn ion if paired with two analogous cysteines from another Rad50 molecule [35,36]. NBS1 is also a component of the globular domain and a binding partner of Mre11 but its stoichiometry within the complex is uncertain.

These striking architectural features allow the MRN complex to facilitate DNA repair by tethering two DNA ends [34]. On the one hand, upon binding to DNA, the Mre11 dimer adopts a conformation that promotes the parallel alignment of DNA ends and stimulates their short-range synapsis [37]. On the other hand, long-range tethering of DNA strands is supported by the ability of Rad50 to oligomerize via intramolecular Zn coordination [36,38-40].

Nuclease activities of the MRN complex and its associated factor, Sae2/CtIP

In addition to its ability to interact with and tether DNA ends, *in vitro* analysis has established that the Mre11/Rad50 complex possesses several DNA processing activites including: DNA annealing, Mn2+ -dependent 3' -5' ds exonuclease, ssDNA endonuclease, and DNA unwinding [35,41-47]. The nuclease activity of Mre11 has been of special interest because the MRN complex promotes the initial steps of HDR in all organisms [48] and contributes to NHEJ in budding yeast [49]. Recent studies in mammalian cells have dissected the role of the nuclease activity in various aspects of the DNA damage response and have determined that it is required for cell viability as well as for DNA replication, especially in stress conditions, but it does not play a promonent role in ATM dependent checkpoint signaling or NHEJ [44,50-53]. These data suggest a specialized role for the Mre11nuclease activity in the processing of a subset of complex DNA replication intermediates [54].

In *S. cerevisiae*, deletion of Mre11 causes a general defect in DNA resection at DSBs processed by homology-directed repair (HDR) [55-57]. This phenotype cannot be explained by loss of the nuclease activity alone, as it does not have the correct polarity to perform 5'-3' resection, which is required during HDR [42]. This apparent discrepancy has been resolved with the identification of Sae2 (referred to as CtIP in mammalian cells and Cpt1 in *S. pombe*). Sae2 is a novel factor with potential intrinsic nuclease activity that associates and functions closely with the MRN complex [58-64]. MRN/Sae2 promotes a 5'-3' resection step, which generates an essential intermediate in the HDR pathway.

The role of NBS1 in the MRN complex

NBS1 is required for the nuclear transportation of the MRN complex and is an important regulator of MRN function. The NBS1 protein contains an amino-terminal FHA (fork-head associated) domain adjacent to putative BRCT (BRCA1-related C-terminal) repeats and several S/TQ motifs at a central region, suggesting its potential role in multiple phospho-dependent interactions [65]. In particular, the serine residues at 278 and 343 are phosphorylated by ATM in response to radiation both *in vitro* and *in vivo*, and these phosphorylations are associated with the role that NBS1 plays in the intra-S-phase checkpoint [66,67].

The MRN complex localizes to DSBs in response to radiation exposure [68]. This is accomplished, however, through an interaction that is not DNA damage-dependent. The BRCT repeats of NBS1 recognize and bind to the constitutively phosphorylated S-T-D-rich region of MDC1 [69-73]. Therefore, as described later in this chapter, the current model argues that NBS1 is passively recruited to the chromatin at DSBs when MDC1 binds to γ-H2AX. In turn, NBS1, which contains an Mre11-interacting domain at its carboxy-terminus, is required for the association of Mre11/Rad50 with DSBs.

In addition, NBS1 binds directly to ATM through a short motif located at its carboxy-terminus [21,74,75]. This interaction contributes to the signal amplification loop that promotes foci formation at the chromatin near DSBs and it may also be required for the initial recruitment and activation of ATM.

The role of the MRN complex in the ATM pathway

Over the years, the MRN complex has emerged as an essential component of the ATM signaling pathway. Most of the initial studies were performed using cells derived from patients with Nijmegen Breakage Syndrome (NBS) or Ataxia-Telangiectasia-like disorder (A-TLD), which are caused by hypomorphic alleles of NBS1 [76,77] or Mre11 (Meiotic recombination 11) [78] genes, respectively. Since NBS and A-TLD patients exhibited features similar to A-T, including ionizing radiation sensitivity, chromosomal instability, and defects in cell cycle checkpoints, the MRN complex appeared functionally connected to ATM [78,79]. Indeed, NBS1 is phosphorylated in an ATM-dependent manner after DNA damage on multiple serines at positions 278, 343, and 615 [27,80]. In particular, serine 343 has been shown to be functionally important in the ATM pathway since expression of the S343A mutant in NBS cells fails to rescue the checkpoint defects of NBS1 deficiency [16,26,27,79,81].

These studies indicate that MRN is an important component of the ATM pathway but one outstanding question is whether the MRN complex fulfills the criteria to be characterized as the sole sensor for DSBs and thus the activator of the ATM pathway. The capacity of the MRN complex to interact with DNA ends and bind to ATM make it a plausible candidate for a DNA damage sensor. This model is further corroborated by the observation that ATM-mediated phosphorylation is not required for the localization of NBS1 at DSBs, as shown by the proficient radiation-induced foci formation in NBS1 S343 cells [82]. In addition, Mre11 foci are detected at DSBs and dysfunctional telomeres in caffeine-treated cells and hence can form through a PIKK-independent mechanism [68,83].

Arguing against this model is the observation that the extent of RDS is greater in A-T cells than either in NBS or in A-TLD cells [26]. To explain the difference, it has been proposed that parallel pathways contribute to the intra-S-phase checkpoint: the NBS1-dependent ATM/NBS1/SMC1 [84,85] and ATM/FANCD2 pathways [86], and the NBS1-independent ATM/Chk2/Cdc25A/CDK2 pathway [26]. In the first two pathways, ATM-mediated phosphorylation of the effectors SMC1 and FANCD2 requires the phosphorylation of NBS1, suggesting that NBS1 might serve as an adaptor between ATM and its targets. Data have been controversion with regard to the third pathway. Whereas in some studies the phosphorylation of Chk2 and Cdc25A has been reported as normal both in NBS and in A-TLD cells, several independent studies have indicated a requirement for NBS1 at low damage levels, suggesting a partial involvement.

Irradiation-induced delays at the G1/S and G2/M transitions are also partial in NBS cells. In the absence of a functional MRN complex, the cellular levels of p53 and the phosphorylation of Mdm2 and Chk2 is sub-optimal but not abolished [17,78,87,88]. These findings argue that defects in the MRN complex reduce but do not abolish the activation of checkpoint factors, raising the possibility that MRN might not be absolutely required for ATM activation but may only contribute to the recruitment of specific substrates by ATM [74].

A drawback in the interpretation of these studies is the potential ability of another PIKK, in particular ATR kinase, to complement the absence of active ATM. This has been a significant concern, especially in the case of experiments analyzing the consequences of IR- or laser-induced DNA damage. Both methods generate large amounts of single-stranded DNA in addition to multiple DSBs. In these instances, the

ATR kinase, which is activated via an MRN-independent pathway, can promote the phosphorylation and activation of ATM and downstream checkpoint factors [89].

Another complication arises from the fact that the MRN complex is essential for cellular viability, and therefore the *in vivo* experiments have been performed in cell lines bearing hypomorphic alleles, likely to underestimate the contribution of MRN.

Multiple studies have attempted to circumvent these difficulties. For example, using adenoviral infections as a model system that elicits an ATM-specific response, it has been found that the MRN complex is required for activation of ATM and for execution of the G2/M checkpoint [16]. In a different setting, using I-Ppol endonuclease to generate site-specific DSBs, it has been demonstrated that NBS1 is required for ATM autophosphorylation as well as for the association of active ATM with damaged chromatin [13]. Another study determined *in vitro* that ATM activity is robustly stimulated by linear DNA only when the MRN complex is present, consistent with the view that MRN is both an activator of ATM and a sensor for DNA damage [20]. These findings strongly argue that a functional MRN complex is required for the activation of ATM at DSBs.

This conclusion is further corroborated through the characterization of the $Rad50^{S}$ allele, which is hypermorphic for DNA damage signaling [90]. $Rad50^{S/S}$ cells have constitutive low-level activation of the DNA damage response even in the absence of exogenous DNA damage that leads to ATM/Chk2-mediated apoptosis. The ability of the gain-of-function Rad50 mutant to promote the ATM pathway in the absence of DNA damage is strongly indicative of a sensor function for the MRN complex. Curiously, however, the $Rad50^{S}$ allele partially rescues the phenotypes of ATM-deficiency in

$Rad50^{S/S}ATM^{-/-}$ mice, implicating a role for the MRN complex in an ATM-independent pathway [90].

Recent analysis of cells isolated from mice, carrying a conditional allele for NBS1 ($NBS1^{F/-}$ [18]) or Mre11 ($Mre11^{F/-}$ [54]) as well as from mouse models expressing transgenic mutant alleles [18,54,88,90,91] have provided further support for the model that the MRN complex is the sensor for ATM. Since deficiency in MRN leads to embryonic lethality, initial analysis focused on transgenic mice that bore the hypomorphic $NBS1^{\Delta B/\Delta B}$ and $Mre11^{ATLD/ATLD}$ alleles, initially characterized in NBS and A-TLD patients, respectively. Whereas MEFs derived from these mouse models recapitulated closely the phenotypes observed in NBS and A-TLD cells, their analysis yielded conflicting results as to whether or not the MRN complex is the sensor in the ATM pathway. On the one hand, these cells are characterized by severe RDS phenotype, a G2/M checkpoint defect, and irradiation-induced chromosome instability. On the other hand, following IR treatment the phosphorylation of the ATM targets Chk2 and SMC1, the induction of p53/p21, and the recruitment of γ-H2AX to DSB are not affected significantly. Interestingly, in $NBS1^{\Delta B/\Delta B}$ cells, ATM can be detected in its activated, autophosphorylated form, suggesting that the ATM pathway is active [18]. In contrast, when NBS1 is deleted in $NBS1^{F/-}$ MEFs through the expression of Cre recombinase, ATM, Chk2, and SMC1 phosphorylation in response to IR is abrogated [18]. These findings confirm that hypomorphic alleles retain some of the MRN function and that analysis of cells lacking MRN is required to dissect its contribution to the ATM pathway. However, even in the absence of NBS1, γ-H2AX still associates extensively with laser-induced DSBs, raising the possibility that ATM can be activated without the aid of MRN complex [18]. In sum, it seems that the MRN complex

contributes to some but not to all aspect of the ATM pathway. On the background of this controversial set of data, the findings presented in this thesis and in a recent paper [54] provide uncontestable evidence that at sites of DNA damage, which exclusively activate the ATM pathway, absence of MRN function precludes the activation of the DNA damage response (Discussed in more detail in Chapter 2).

ATM-dependent accumulation of DNA damage response factors at sites of DNA damage: IRIFs

Following ATM activation, the response to DSBs is characterized by a dramatic relocalization of a number of DNA damage response factors to sites of damage (Figure 1.2) [92,93]. In the absence of DNA damage, most DNA damage response factors are distributed homogeneously in the nucleoplasm. Upon induction of DSBs by γ-irradiation, these factors accumulate in large foci, referred to as IRIFs. IRIFs are cytologically visible under the fluorescent microscope as bright speckles and can be used as an indicator for the presence of DNA damage. It is thought that each IRIF represents one or several DSBs and that the factors accumulated in each focus are involved in promoting cell cycle arrest and active repair processing. This initial concept originated from observations that IRIFs appear within seconds after the induction of DNA damage, concomitant with the activation of ATM kinase [94]. The disappearance of IRIFs, on the other hand, has often been used as a marker for successful completion of DNA repair although this connection has not been experimentally proven.

IRIFs are very large structures. Chromatin immunoprecipitation (ChIP) experiments have shown that IRIF formation is not limited to the immediate vicinity of

DSBs but stretches for several megabases on either side of DNA lesions. Phospho-specific interactions between ATM targets and proteins containing phospho-recognition modules such as FHA and BRCT domains contribute to the formation of IRIFs. In addition, recent work has established that the recruitment, spreading and retention of IRIF factors is intimately linked to chromatin modifications induced or exposed in the presence of DNA damage. Another feature of IRIFs is their dynamic nature as visualized by real-time photobleaching microscopy imaging. Although IRIFs can persist for many hours, factors become only transiently immobilized around the DSB-flanking chromatin and are constantly exchanged [94].

In the past few years, enormous progress has been made towards understanding the structural organization of IRIFs in mammalian cells. In particular, the factors involved in IRIF assembly and the steps required for IRIF amplification and maintenance have been dissected (Figure 1.2). However, the functional contribution of IRIFs to the DNA damage response and their roles in checkpoint signaling and DNA repair have remained unclear.

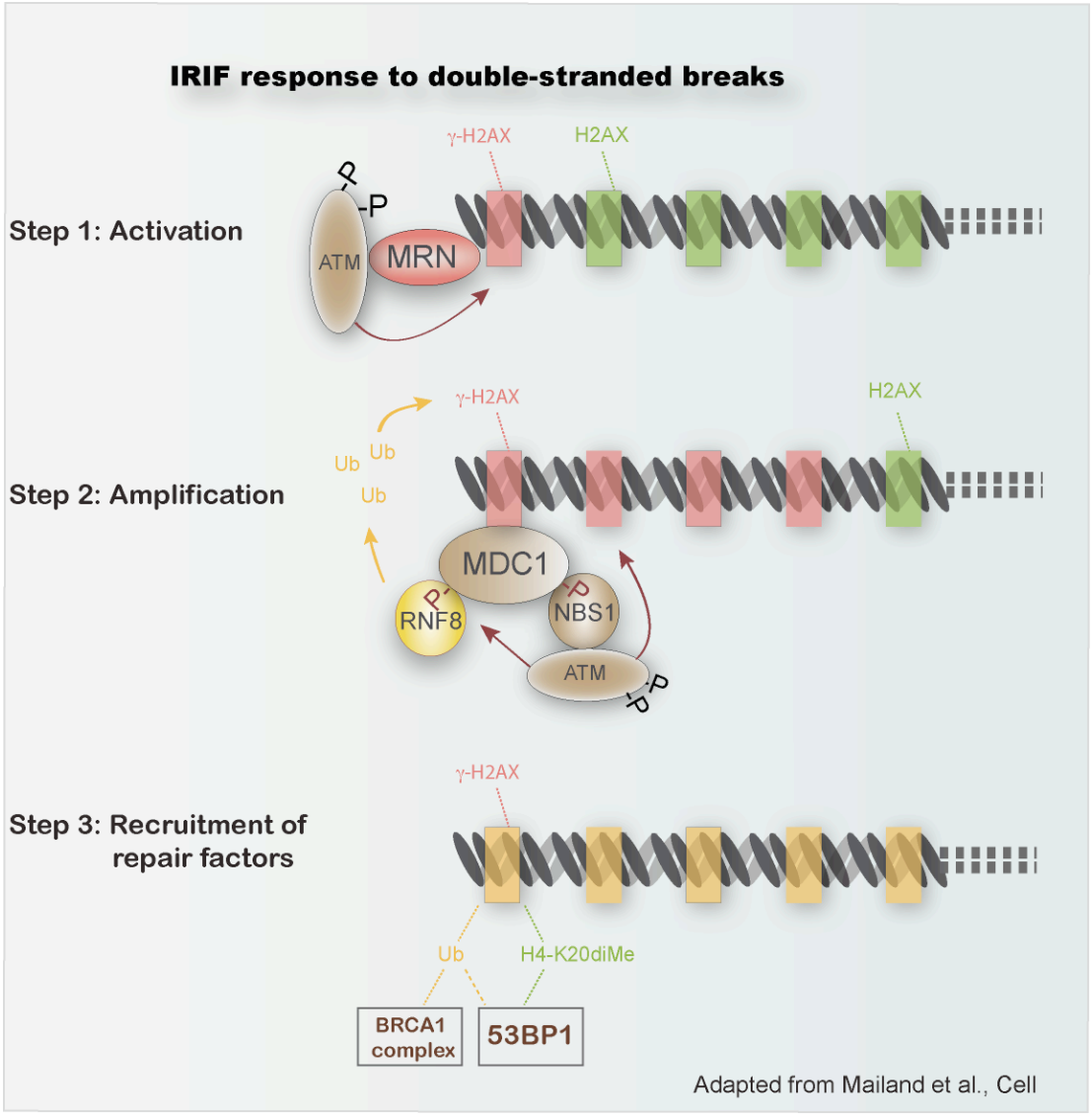

Figure 1.2. Mechanism of IRIF formation in response to DSBs

IRIF formation is initiated when activated ATM kinase phosphorylates H2AX adjacent to the DNA lesion to trigger the recruitment of numerous other DNA damage response factors to the site of damage. γ-H2AX is specifically recognized by MDC1. MDC1 is constitutively phosphorylated by CK2, a mark recognized by NBS1, which in turn functions to recruit more active ATM molecules. The ATM kinase, associated with IRIFs, phosphorylates adjacent H2AX, establishing a signal amplification step, and also phosphorylates MDC1 on its SCD, which is important for the recruitment of RNF8 to DSBs. At DSBs, RNF8 deposits ubiquitilation marks on the chromatin flanking the DNA lesion, establishing a platform for the recruitment for DNA damage repair factors, including the BRCA1 complex and 53BP1. 53BP1 is also recruited via an independent association with H4-K20diMe.

IRIF factor: γ-H2AX

PIKK-mediated phosphorylation of an H2A histone variant, H2AX, is at the heart of IRIF formation (Figure 1.2) [95,96]. H2AX makes up 10-15% of total cellular histone H2A and exists as a component of the nucleosome core structure. In response to DNA lesions, H2AX is phosphorylated on a conserved serine residue at its carboxy terminal, S139, located within a S-Q-E-Y motif [97]. The phosphorylated form of H2AX (referred to as γ-H2AX) occupies an extensive region of chromatin flanking the DNA lesion [98], and it is believed that this event establishes the scaffold for IRIFs [99]. In the absense of H2AX or when the phosphorylation site is mutated, IRIF formation by other DNA damage response factors is impaired [100,101]. For some IRIF factors, such as MDC1 (Mediator of DNA damage checkpoint 1), the recruitment to DSBs is abolished in H2AX-null cells. In other cases, including 53BP1 (p53 binding protein 1), NBS1, and BRCA1, the long-term residence at IRIFs is severely compromised [102].

Mice lacking the H2AX gene show male infertility, in part due to defective repair of SPO11-induced DSBs in meiosis, and have reduced levels of secondary immunoglobulin isotypes, indicative of impaired class-switch recombination (CSR), a process that also involves a DSB repair reaction [100]. In addition, cells derived from H2AX-deficient mice exhibit elevated levels of IR-induced chromosome abnormalities, indicating that H2AX is involved in the signaling and/or repair of DSBs [100]. As H2AX is dispensable for the activation of irradiation-induced checkpoints at the G_1/S transition, in S phase, and at the G_2/M transition [102], it has been suggested that H2AX must play a role in promoting DNA repair. In support of this model, H2AX phosphorylation appears tightly correlated with the persistence of un-repaired DSBs [103] and H2AX de-

phosphorylation coincides with successful completion of DNA repair. However, further studies have indicated that H2AX is not required for NHEJ, but may play a role in HDR [104,105]. In sum, these experiments led to the conclusion that H2AX is not absolutely required for DNA repair, and although it might contribute to its efficiency [106], the exact mechanism is not well understood.

IRIF factor: MDC1

The ATM target MDC1 (mediator of DNA damage checkpoint 1) is a large protein that contains multiple protein-protein interaction domains, including an N-terminal FHA domain, a unique Ser-Asp-Thr (S-T-D) repetitive motif, and C-terminal tandem BRCT repeats [107-110]. MDC1 is recruited to IRIFs through a direct interaction with γ-H2AX [110-112] where it acts as a scaffold for the recruitment of other IRIF factors, including ATM, the MRN complex, and 53BP1 (Figure 1.2) [107,109,112-114].

The tandem BRCT repeats of MDC1 form a pocket that selectively recognizes phosphorylated S-Q-E-Y motif of γ-H2AX. The structural basis for this interaction has been determined from crystallography of the MDC1 BRCT region with a phosphorylated H2AX C-terminal peptide [111,112]. BRCT repeats, first described in BRCA1 but also found in other DNA damage response factors such as 53BP1 and BARD1, generally recognize phosphopeptides. In the case of MDC1, however, the BRCT repeats establish a binding cleft that is exclusively tailored to recognize the free carboxyl terminal of γ-H2AX with high selectivity and stability. The structural data also identify specific residues in MDC1 that are required for the contact with the H2AX phosphopeptide. Consequently, mutations in any of these residues within the MDC1 BRCT region, as well as mutations

in the C-terminal serine or tyrosine residues of H2AX, severely compromise the accumulation of MDC1 at IRIFs and impair the DNA damage response [112,115].

Consistent with the association between MDC1 and H2AX, MDC1$^{-/-}$ mice have phenotypes similar to the defects observed in H2AX-deficient mice, including radiosensitivity, male infertility, and impaired CSR [114]. Similarly, analysis of IRIF formation in MDC1-deficient MEFs has shown that MDC1 is required for the extended association of factors such as the MRN complex and 53BP1 with DSBs [114]. Even though NBS1 and 53BP1 can transiently be recruited to laser-induced DSB-containing tracks, they fail to accumulate and prematurely dissociate from DSB sites in absence of MDC1 [116]. The phenotypes of MDC1 deficiency are thus reminiscent of the data obtained in H2AX-deficient cells where the stabilization of MRN and 53BP1 at IRIFs, but not their initial recruitment, is severely affected by the absence of γ-H2AX [102]. MDC1 loss also leads to impaired phosphorylation of ATM targets Chk2 and SMC1 and the intra-S-phase checkpoint is compromised in cells treated with low levels (0.5-2 Gy) of γ-irradiation [72,107]. These findings have suggested a potential role for MDC1 as a signal amplifier in the ATM pathway.

IRIF factor: The MRN complex

Chromatin bound MDC1 recruits other DNA damage response factors to IRIFs, including the MRN complex. As described in the model above, the MRN complex acts as a sensor for DSBs and is required for ATM activation and consequently, for γ-H2AX and MDC1 IRIF formation. This initial recognition of DSBs by the MRN complex is an intrinsic feature of MRN and it may only involve a few molecules (Figure 1.2). In contrast, the

cytologically discernible prolonged accumulation of MRN complex at IRIFs depends on ATM and requires γ-H2AX and MDC1 (Figure 1.2).

The interaction between MDC1 and the MRN complex involves a phospho-dependent contact between the phosphorylated S-T-D-rich region of MDC1 and the FHA domain of NBS1 [69-73]. Interestingly, the conserved S-T-D repeat motif in MDC1 is constitutively phosphorylated by CK2 (casein kinase 2), which explains why the interaction between MDC1 and MRN is detectable even in the absence of DNA damage. One possibility is that some MRN always binds to MDC1 and accumulates at DNA lesions when MDC1 binds to γ-H2AX.

Since the MRN complex also interacts with ATM through the C-terminal domain of NBS1 [21,117], it can recruit to IRIFs more active ATM kinase, which in turn can phosphorylate adjacent H2AX, establishing a signal amplification step. One current model proposes that the spreading of γ-H2AX for several megabases along the chromatin flanking a DSB is a consequence of the accumulation of chromatin-bound ATM kinase on the γ-H2AX-MDC1-MRN scaffold [114,118].

IRIF factor: RNF8

An additional level of regulation is exercised by the RING-finger ubiquitin ligase, RNF8, which localizes to IRIFs through a specific interaction between its FHA domain and the phosphorylated S/TQ cluster of MDC1 [119-122]. At sites of damage, RNF8 ubiquitilates γ-H2AX to promote the retention of 53BP1 and the BRCA1 complex (Figure 1.2). It has been proposed that MDC1-mediated RNF8-executed histone ubiquitilation licenses the DSB-flanking chromatin to concentrate repair factors near the DNA lesion [121].

IRIF factor: 53BP1

Although 53BP1 was first identified in an yeast-two hybrid screen for p53 interacting factors [123], it is now clear that this protein is an important regulator of genome stability that protects cells against DSBs [124-128]. Recent data has further indicated that 53BP1 is downregulated during the transition of precancerous stage to carcinoma [129], and loss of a single 53BP1 allele in mice causes genome instability and lymphoma [130].

The presence of C-terminal BRCT repeats adjacent to a Tudor domain has led to the speculation that 53BP1 is the human ortholog of yeast Rad9, a central component of the DNA damage signaling network in *S. cerevisiae* [131]. In contrast to Rad9, however, downregulation of 53BP1 in human cells by RNAi and 53BP1-deficiency in MEFs only lead to a partial defect in the intra-S phase checkpoint, and show mild defects in irradiation-induced G_2/M checkpoint after low doses of radiation [126,132]. 53BP1 is also phosphorylated by ATM kinase on multiple sites but little is known about their functional role in the DNA damage response [133].

The most apparent phenotypes of 53BP1 deficiency are radiosensitivity and defects in CSR, similar to the phenotypes of H2AX or MDC1 loss [132,134-136]. Despite the similarities, the penetration and severity of the phenotypes can be different. For example, CSR is more severely compromised in cells lacking 53BP1 than in H2AX- or NBS1-deficient B cells. Ward et al. observed that despite equivalent proliferation rates the percentage of IgG1-positive 53BP1-deficient B cells is reduced 15-fold compared to wild-type control cells [136]. In contrast, CSR is impaired only 6-7 fold in $H2AX^{-/-}$ B cells [100], and, in NBS1-deficient cells, the reduction of class switching is only about 2-3 fold compared to control [137].

53BP1 requires two independent interactions with modified chromatin in order to stably associate with sites of DNA damage (Figure 1.2). On one hand, the Tudor domain of 53BP1 forms a pocket that specifically recognizes dimethylated lysine 20 on histone H4 (H4-K20diMe) at DSBs [138]. Structural studies have identified residues essential for this interaction and mutation in one of these, D1521, abrogates the interaction in vivo [139]. Furthermore, the interaction of 53BP1 with chromatin is stabilized by the S/TQ cluster of MDC1, which recruits the RNF8 ubiquitin ligase [107,108,110,115,116]. It seems that both H4-K20diMe and γ-H2AX/MDC1 contribute to the recruitment of 53BP1 to sites of damage. In MEFs deficient for SUV4-20-h1, -h2 methyltransferases, where dimethylation of H4-K20 is abrogated, the accumulation of 53BP1 at DSBs is delayed and diminished [140]. Conversely, as described above, in H2AX- and MDC1-null MEFs, 53BP1 is initially recruited to laser-induced DSBs but its accumulation is strongly diminished over time compared to wild-type cells. This suggests that, in the context of intact nucleosomes, the Tudor domain may support only a transient interaction of 53BP1 with chromatin. Interestingly, H4-K20diMe is a constitutive chromatin mark, so it has been argued that the specificity for the recruitment of 53BP1 to IRIFs is likely to come from γ-H2AX/MDC1. In this regard, it is conceivable that phosphorylation and/or ubiquitilation of H2AX might expose the H4-K20diMe mark or facilitate its interaction with 53BP1.

The role of IRIFs in amplifying the DNA damage signal

γ-H2AX, MDC1, and 53BP1 seem to play a minor role in DNA damage signaling. H2AX- and MDC1-deficient cells exhibit mild defects in the phosphorylation of ATM targets and in the induction of the intra-S-phase checkpoint arrest [102,114], while the

absence of 53BP1 weakly affects ATM autophosphorylation and Chk2 activation [132]. The decrease in ATM activity is only pronounced at low levels of γ-irradiation, suggesting that these factors might be involved in amplification of the damage signal [118]. In this regard, it is possible that the stimulating effects on the ATM pathway may be mediated through stabilization of the MRN complex at IRIFs and its ability to locally activate ATM [69,70]. At the same time, these studies convincingly show that γ-H2AX, MDC1, and 53BP1 are not absolutely required for activation and maintenance of the checkpoint-signaling cascade.

The extensive contribution of the MRN complex to checkpoint signaling is due to its role as a sensor in the ATM pathway. Indeed, MRN participates both in ATM-dependent intra-S-phase checkpoint [16,26,27,79], as well as in ATM-mediated arrest at the G2/M transition [16,81].

Two major pathways for DSB repair: HDR and NHEJ

There are two primary pathways for the repair of DSBs in eukaryotic cells, homology-directe repair (HDR) and NHEJ. HDR occurs during late S or G2 phases of the cell cycle when the sister chromatids are in close proximity [141-143]. HDR ensures error-free repair because the break in one chromatid is repaired using the identical information in the sister chromatid. The HDR pathway has been studied extensively and the functional contributions of numerous DNA damage repair factors have been implicated. As an introduction to this thesis work, it is important to point out that in the first step of HDR, the MRN complex, together with the nuclease Sae2/CtIP, resects DSB ends to generate short single-stranded overhangs, which are an essential prerequisite for subsequent steps

of HDR. Interestingly, this resection step appears to be tightly controlled by CDKs, which can activate Sae2/CtIP through phosphorylation on a conserved C-terminal residue [62,144]. This regulatory step ensures that HDR is only activated in S/G2, in the presence of sister chromatids. Additionally, CDK-dependent phosphorylation of NBS1 on S432 has also been identified as a potential regulator of this resection step (pers.comm. S. Jackson and pers. comm. J. Petrini and R. Fisher).

The alternative mechanism for repair of DSBs is the NHEJ pathway, which does not require a homologous chromosome (Figure 1.3) [143,145]. NHEJ can therefore function throughout the cell cycle, although it has been suggested that it is most active in G1, when resection at DSBs is limited [60,62]. NHEJ involves direct ligation of the two DNA ends in a manner that might lead to nucleotide loss (typically, 1-10 nt) or untemplated nucleotide addition (typically, 0-3 nt) at the rejoining site. Because of its imprecision, NHEJ is potentially mutagenic.

The first step of NHEJ is the binding of the Ku70/Ku80 heterodimer to the two DNA ends (Figure 1.3) [146,147], where it promotes the synapsis of DNA ends and facilitates the recruitment of other NHEJ factors. The Ku complex can bind to DNA due to its toroidal structure, which has a 20 Å hole through the center that permits it to thread like a ring onto DNA ends [148]. In addition, Ku interacts with and can recruit to DSBs multiple NHEJ factors, including the nuclease Artemis [149,150]; the kinase DNA-PKcs [151]; the polymerases μ and λ [152-154]; and the ligase complex Cernunnos(XLF)-XRCC4-DNA ligase IV [155,156]. The second step of NHEJ occurs at a subset of DSBs, at which the two broken ends are incompatible and require further processing. End-processing of overhangs can be mediated by the nuclease activity of Artemis complexed with DNA-

PKcs. DNA-PKcs is a PIKK that acquires serine/threonine protein kinase activity when bound to a DNA end, and phosphorylates itself and Artemis. *In vitro* Artemis has a weak 5'-3' exonuclease activity on its own but as part of the Artemis-DNA-PKcs activated complex, it acquires an endonuclease activity towards both 3' and 5' overhangs of variable length. In addition to resection, end-processing may also involve the activities of the X-pol family polymerases to promote template-dependent fill-in synthesis at gaps. The final step of NHEJ is the direct ligation of the two ends by the Cernunnos(XLF)-XRCC4-DNA ligase IV complex (reviewed in [157]).

The ligase complex Cernunnos(XLF)-XRCC4-DNA ligase IV plays a critical role in the NHEJ pathway. Studies of human patients who harbor hypomorphic mutations, as well as analysis of mice that carry conditional alleles, have indicated that Cernunnos(XLF), XRCC4, and DNA ligase IV are core components of the NHEJ pathway. When the function of these factors is impaired in human patients, or when the genes are conditionally deleted in a specific cellular compartment in genetically modified mice, the consequences are striking. The marked failure to repair DSBs leads to genetic instability, developmental delay, and immunodeficiency [155,156,158,159]. On the other hand, analyses of several other factors involved in NHEJ have revealed that they do not play an essential role. Ku70, Artemis, and DNA-PK-deficient mice exhibit reduced but not abolished proficiency to perform V(D)J recombination, an established read-out for ability to execute NHEJ repair (see below)[149,150,160,161].

It has been speculated that rather than being essential components, Ku, Artemis, and DNA-PKcs might contribute to the efficiency of the NHEJ process. For instance, as described above, the Artemis-DNA-PKcs complex may only be required for the repair of

a subset of DSBs that contain incompatible DNA ends [150]. Ku, on the other hand, has been implicated to contribute to NHEJ by maintaining close proximity between the two DNA ends. The synapsis role of Ku has been demonstrated in an experiment where a unique I-SceI endonuclease site, flanked by a TetO array on one side and a LacO array on the other side, was introduced into mouse cells [162]. Upon I-SceI-mediated introduction of a single DSB, the dynamic behavior of the two DNA ends was monitored over time in living cells by imaging the movement of fluorescently-labeled TetR and LacR. Whereas in wild-type cells, the two DNA ends exhibited positional stability and remained in close proximity for extended periods of time, in cells with reduced Ku protein levels, the two ends often moved apart. Thus, the local mobility of broken ends is prevented in the presence of Ku, extending into living cells the hypothesis, based on structural observations, that Ku forms an asymmetric ring around the two broken ends and functions to align broken chromosome termini at the site of repair [148].

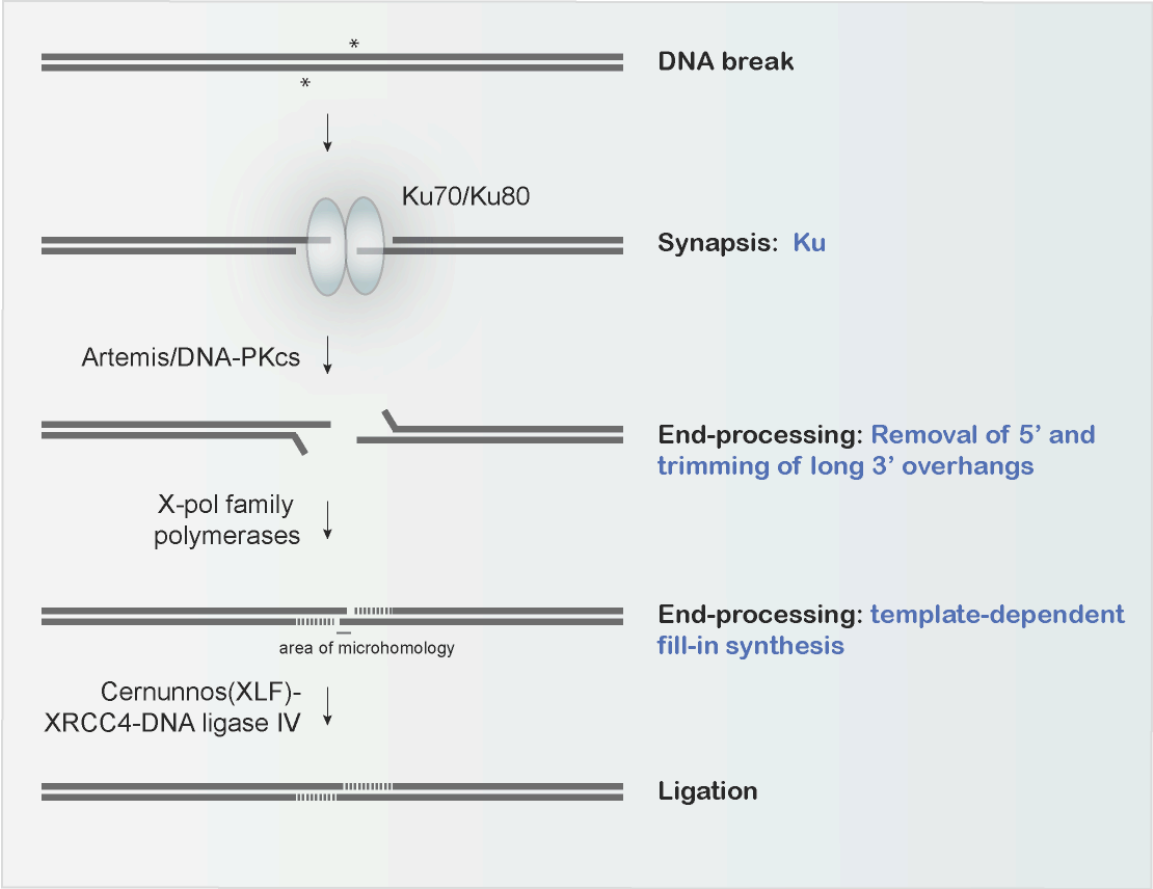

Figure 1.3. Schematic representation of the NHEJ pathway

Ku70/Ku80 complex has been implicated in promoting the positional stability of the two DNA ends of a DSB, induced by various factors. Incompatible DNA ends further are processed by the Artemis-DNA-PKcs complex, which removes 5' and trims long 3' overhangs. Based on the presence of microhomologies, the two ends are brought together and polymerases from the X-pol family perform template-dependent synthesis to fill in remaining gaps. In the last step of NHEJ, the ligation reaction is executed by the Cernunnos(XLF)-XRCC4-DNA ligase IV complex.

Different NHEJ model systems reveal conflicting roles of IRIF factors

Irradiation-induced DSBs

The contribution of IRIF factors to the regulation of NHEJ has been addressed in several model systems. As mentioned above, the persistence of IRIFs is tightly correlated with the presence of un-repaired DSBs following exposure to γ-irradiation. In addition, H2AX-, MDC1-, and 53BP1-deficient cells are radiosensitive. Given the minor contribution of these factors to DNA damage signaling, the accumulation of chromosomal abnormalities following exposure to DSB-inducing agents strongly suggests a role in DNA repair. However, standard experimental techniques such as Comet assay and FAR pulse-field gel analysis have failed to assign a role to H2AX, MDC1, or 53BP1 in the repair of γ-irradiation-induced DSBs [100,136,163]. The shortcoming of these techniques is that they examine gross chromosomal repair and therefore require very high doses of γ-irradiation (20-80 Gy). This disadvantage would preclude identification of factors involved in subtle, regulatory aspects of the NHEJ pathway.

I-SceI cut

Rare-cutting endonucleases, such as I-SceI, allow the introduction of one or a few DSBs into complex genomes. Similar to γ-irradiation-induced DSBs, the accumulation of IRIF factors at an I-SceI cut can be monitored by immunofluorescence, but chromatin immunoprecipitation studies can also take advantage of the site specificity. Importantly, depending on the sequences surrounding an I-SceI cut, successful repair through NHEJ or HDR pathways can be measured by the expression of a fluorescent marker whose reading frame is re-established only if a correct NHEJ or HDR repair reaction has taken place.

NHEJ repair requires little or no homology but frequently results in small deletions or insertions. HDR, on the other hand, re-establishes the correct reading frame through recombination-dependent repair involving a homologous gene.

This technique has been instrumental in establishing a role for Ku in maintaining positional stability of the two ends of a DSB (described above). In contrast, detailed analysis of the roles of MDC1 and 53BP1 in promoting repair using HDR- and NHEJ-specific I-SceI assays has revealed conflicting results [115,164]. On one hand, Xie et al. observed that MDC1 contributed primarily to HDR and sister chromatid recombination, in a manner strictly dependent upon its ability to bind γ-H2AX, whereas 53BP1 appeared to be involved exclusively in NHEJ [115]. 53BP1's function, in these assays, depended on its interaction with H4-K20diMe, and was largely independent of γ-H2AX [115]. Based on these data, it has been proposed that MDC1 and 53BP1 function to promote different repair pathways, HDR and NHEJ, respectively [115]. On the other hand, a previous study had demonstrated a role for MDC1 in NHEJ [163], whereas a different study had identified no role for 53BP1 in NHEJ [136]. This controversial set of data suggests that under certain circumstances IRIF factors may contribute to repair. Curiously, a direct interaction between MDC1 and DNA-PKcs has been reported, which appears to promote the autophosphorylation and therefore activation of DNA-PKcs [163]. Similarly, the HDR factor RAD51 was found to interact with MDC1 [164]. It is not clear whether these interactions have any functional significance.

V(D)J recombination

The contribution of IRIF factors to NHEJ has also been examined in the context of V(D)J recombination, which rearranges the immune locus in B- and T-cells in the process of antigenic receptor diversification. The V(D)J recombination process assembles the Variable (V), Diversity (D), and Joining (J) encoding gene segments through a specialized somatic DNA rearrangement mechanism. The locus is rearranged in two steps; first one D and one J gene segments are joined, followed by the addition of one V gene segment to the (D)J product to form the final rearranged V(D)J locus. The reaction is initiated by the lymphoid-specific factors RAG1 and RAG2, which recognize recombination signal sequences in the immunoglobulin locus of a B- or a T-cell and introduce two DSBs at specific locations. The DNA ends to be joined, called the coding and the signal ends, are maintained in close proximity by the RAG complex while repair takes place. The two coding ends, whose joining gives rise to the rearranged locus, are characterized by terminal hairpins that require removal by the Artemis-DNA-PKcs complex prior to the ligation event. The two ends of the intervening sequence, called signal ends, are blunt, and they are also ligated to release an extrachromosomal circle. The joining is accomplished by the classical NHEJ repair machinery. As mentioned above, the ligase complex components Cernunnos(XLF), XRCC4, and DNA ligase IV are essential for V(D)J recombination, whereas the factors Ku, Artemis, and DNA-PKcs have been implicated in promoting the V(D)J process.

Analysis of V(D)J recombination in MRN- [165,166], H2AX- [100], MDC1- [114], and 53BP1- [136] deficient mice has not revealed any obvious defects.

Class switch recombination

On the other hand, NBS1-, H2AX-, MDC1-, and 53BP1-null mice have prominent defects in CSR [100,106,134-137,167]. Similarly to V(D)J recombination, CSR is a programmed pathway in the immune system that requires NHEJ-mediated repair of DSBs [168]. During the terminal maturation of B-lymphocytes, which occurs upon antigen recognition, immunoglobulin genes undergo an additional molecular processing step called CSR, whose purpose is to increase the efficiency of the humoral response. During class switching, the constant region of the immunoglobulin heavy chain is exchanged while the variable region stays the same. This allows daughter cells from the same activated B cell to produce antibodies with the same antigen specificity but of different isotypes or subtypes.

CSR is initiated by the B-cell specific enzyme AID (activation-induced cytidine deaminase), which, in a transcription dependent manner, deaminates cytidine residues in the constant regions to generate uridines. The U/G mismatches are recognized by the enzyme UNG (uracil-N-glycosylase) and removed to create abasic sites. In turn, the abasic sites are most likely cleaved by a specific endonuclease, such as Ape1, thus creating DNA nicks. DNA nicks generated on the two DNA strands lead to staggered DNA DSBs that can be modified by nucleases and/or polymerases in the process of repair. The free DNA ends are rejoined by NHEJ in a manner that specifies a new constant region of the heavy chain of the antibody. The intervening DNA is concomitantly deleted from the chromosome, removing the unwanted heavy chain constant region exons. The distance between the old and the new constant regions can be

as much as 100 Kb. A specific factor that would promote the synapsis of these distant regions, similarly to the RAG complex in V(D)J, has not been identified.

The role of NHEJ factors in CSR cannot be easily analyzed in knockout mice as they lack a mature immune system. Several independent approaches have been used to circumvent this problem. In one experiment, a monoclonal mature B-cell compartment was reconstituted in mice deficient for NHEJ factors. In this setting, Ku70- and Ku80-deficiency impaired CSR, but this defect could result from a reduced proliferation or increased apoptosis of B cells rather than a CSR defect *per se* [169,170]. In another experimental approach, to overcome the embryonic lethality associated with DNA ligase IV-deficiency, a conditional allele that can be specifically removed in mature B-cells was introduced [171]. Surprisingly, although reduced by more than 50%, CSR still occurred in absence of XRCC4 and DNA ligase IV, suggesting the existence of an 'alternative' NHEJ repair pathway. Indeed, two recent reports have demonstrated that in the absence of essential NHEJ factors, both CSR and V(D)J recombination may rely on an alternative end-joining pathway [172,173]. However, the 'classical' NHEJ pathway is most likely dominant in the case of CSR, as it is for V(D)J recombination. Consistent with this conclusion, two studies reported that both CSR and V(D)J recombination occur in G1 stage of the cell cycle, when NHEJ is thought to be active [174,175].

CSR is promoted by a number of upstream DNA damage response factors, ATM, γ-H2AX, MDC1, the MRN complex, and 53BP1, all of which are known to localize at AID-induced DSBs [175]. Among these factors, 53BP1 deficiency gives the strongest CSR defect [134,136]. For instance, comparison of experimental data from several reports reveals that 53BP1 loss reduces the frequency of the IgG1 isotype by about 15-fold, whereas

absence of ATM, NBS1, or H2AX causes a 2-6-fold decrease [100,136,137]. Furthermore, in the absence of 53BP1, DSBs in different switch regions fail to join successfully, resulting in a predominance of intra-switch recombination events [135]. As a consequence of the impaired repair of AID-induced DBSs, activated B-cells isolated from H2AX-, MDC1-, and 53BP1-null mice accumulate chromosome breaks and translocations [106]. To explain the extensive contribution of IRIF factors to CSR, it has been proposed that IRIF factors, in particular 53BP1, might either facilitate the synapsis of DNA ends or 'shepherd' NHEJ factors to the break [135].

Dysfunctional telomeres as a model system to study the regulation of NHEJ

In sum, previous analysis of the contribution of IRIF factors to NHEJ has implicated a potential involvement but also yielded conflicting results and failed to provide a unifying mechanism that would explain the phenotypical variability under different circumstances.

We have developed dysfunctional telomeres as an alternative model system to study novel aspects of the regulation of NHEJ. In part II of this chapter, the components of the telomeric nucleo-protein complex are introduced and insight is provided into how telomeres protect chromosome ends from recognition as DSBs. In this context, it is described how we can disrupt telomere function in order to generate DSBs at specific locations – at the ends of chromosomes. This background is the basis for the techniques used in this thesis work to genetically dissect the contribution of IRIF factors to the regulation of the NHEJ repair pathway.

PART II: TELOMERE STRUCTURE AND FUNCTION

In the 1940s the special qualities of 'natural' ends of linear chromosomes were first recognized [176]. Barbara McClintock observed that in contrast to 'broken' ends, which tended to fuse and create dicentric chromosomes, 'natural' chromosome ends were stably maintained [177]. We now know that chromosome ends are stable because they are capped by telomeres, dynamic and complex nucleoprotein machineries that protect the integrity of chromosomes and are essential for cellular survival.

The telomeric DNA is comprised of a long array of double-stranded TTAGGG repeats that extend into a single-stranded overhang on the G-rich strand [178,179]. The shelterin complex, composed of six telomere-specific factors, TRF1 (Telomere repeat binding factor 1), TRF2 (Telomere repeat binding factor 2), POT1 (Protection of telomeres 1), RAP1, TIN2 (TRF1-interacting nuclear factor 2) and TPP1, specifically coats the telomeric DNA and is essential for the prevention of detrimental genome instability.

In this chapter we discuss the abilities of shelterin to remodel the telomeric DNA into a protected structure and to locally inhibit the activation of the DNA damage response machinery (Figure 1.4a). Although not a focus of this thesis work, gradual telomere loss limits the replicative potential of human somatic cells. Hence it has been proposed that telomeres play an important role as a tumor suppressor mechanism. In this regard, shelterin plays a critical role in determining telomere length by suppressing excessive nuclease activity at the chromosome terminus and by regulating telomerase, the enzyme that elongates telomeres by adding TTAGGG repeats to the 3'end (Figure 1.4b).

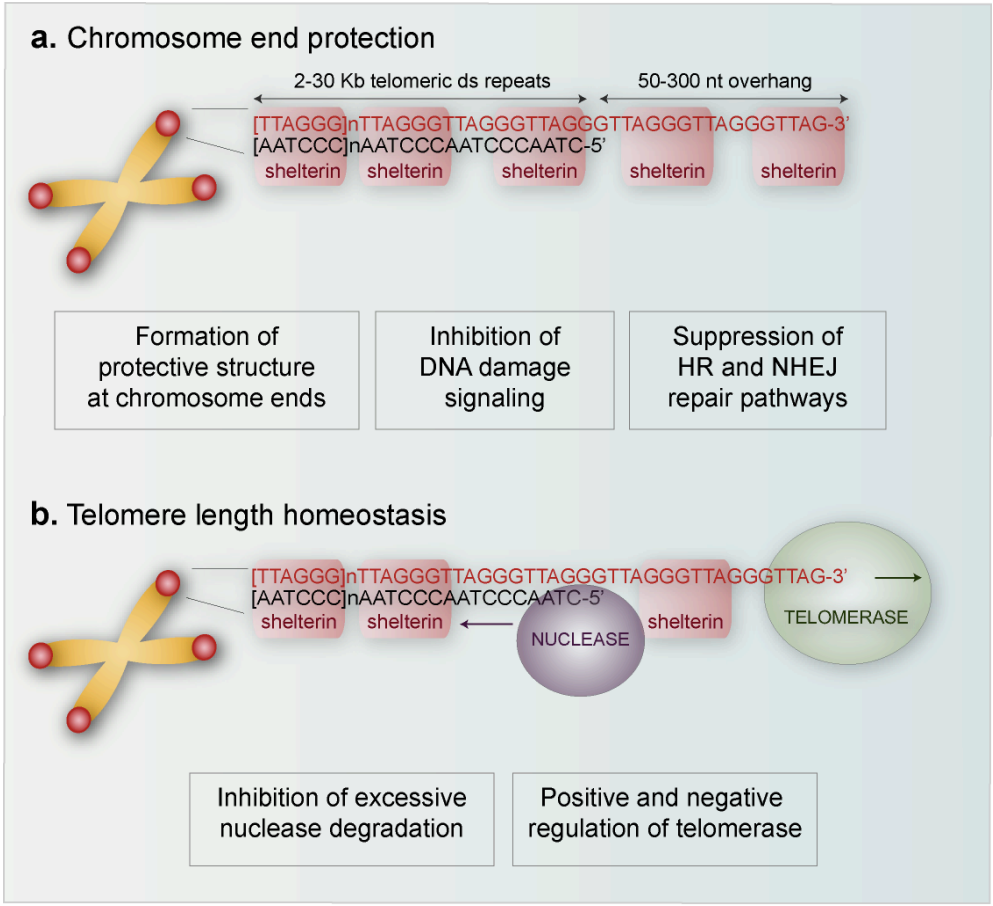

Figure 1.4. Overview of the multiple roles of shelterin at telomeres.

a, Shelterin protects chromosome ends. Telomeric DNA consists of 2-30 Kb dsTTAGGG repeats in human cells and 20-150 Kb in mouse cells with a 50-300 nt ssTTAGGG overhang on the 3' strand. Shelterin complex specifically coats both the ds portion of the telomere and the ss extension. The presence of shelterin at telomeres promotes the formation of a protective structure at chromosome ends and also suppresses the activation of DNA damage signaling and repair pathways.

b, Shelterin regulates telomere length. Telomere ends are subject to degradation by unknown 5'-3' nuclease(s) that resects the 5'-strand in order to generate the telomere overhang. Shelterin regulates the activity and/or recruitment of this nuclease and thereby prevents excessive nuclease degradation and telomere shortening. At the same time, telomerase can elongate telomeres by adding TTAGGG repeats to the 3' end, an activity that is positively and negatively regulated by shelterin.

Telomere-binding proteins in mammalian cells

The shelterin complex

The first two shelterin factors, TRF1 and TRF2, bind to the double-stranded portion of the telomere and are essential for the recruitment and stabilization of the other shelterin members (Figure 1.5) [180-182]. The high specificity of TRF1 and TRF2 for telomeric DNA is achieved by two complementary mechanisms. In the first place, both proteins contain homologous carboxy-terminal DNA-binding (SANT/Myb-type) domains that recognize 5'-YTAGGGTTR-3' sequence in double-standed DNA with high specificity [183-185]. In addition, both TRF1 and TRF2 contain structurally similar dimerization (TRFH) domains and exist as homodimers in solution, with TRF2 having a propensity to form higher-order oligomers [182,186,187]. Both TRF1 and TRF2 are essential for cell viability, since deletion of either genes leads to early lethality in mouse embryonic development [188-190].

TRF1 and TRF2 are bridged by another shelterin factor, TIN2, which plays a core role in the shelterin complex (Figure 1.5). TIN2 can interact simultaneously with TRF1 and TRF2, and, in turn, can recruit to the telomere two other shelterin components, TPP1 and its binding partner POT1 [191-195]. The main function of TPP1 is to link TIN2 and POT1 [193,195,196]. Interestingly, although POT1 contains two oligonucleotide/oligosaccharide-binding (OB) folds that are highly specific for the single-stranded telomeric sequence 5'-(T)TAGGGTTAG-3', its recruitment to chromosome ends is not dependent on its ability to bind to the 3'telomeric overhang. Instead, the association of POT1 with telomeres is mediated through its interaction with TPP1 (Figure 1.5). Indeed, it has been shown that in the absence of TPP1, POT1 is not recruited to chromosome ends and the phenotypes mirror POT1 loss.

Whereas human cells contain one POT1 gene, mouse cells have two POT1 genes – POT1a and POT1b [197,198]. Both proteins associate with telomeres and share similar sequences and domain structures. However, they are not functionally redundant. While POT1a is an essential gene, as its deletion leads to early embryonic lethality, POT1b-deficient mice are viable [197].

The sixth shelterin component, RAP1, is a binding partner of TRF2 (Figure 1.5) [199]. The interaction between the two factors is required for the recruitment of RAP1 to telomeric DNA and is essential for the stability of RAP1 protein levels [190,199].

Taken as a whole, the intricate interconnections between the different members of shelterin ensure that the complex has high affinity and specificity for telomeric DNA. Indeed, shelterin is highly abundant exclusively at telomeres and its known functions are restricted to telomere maintenance.

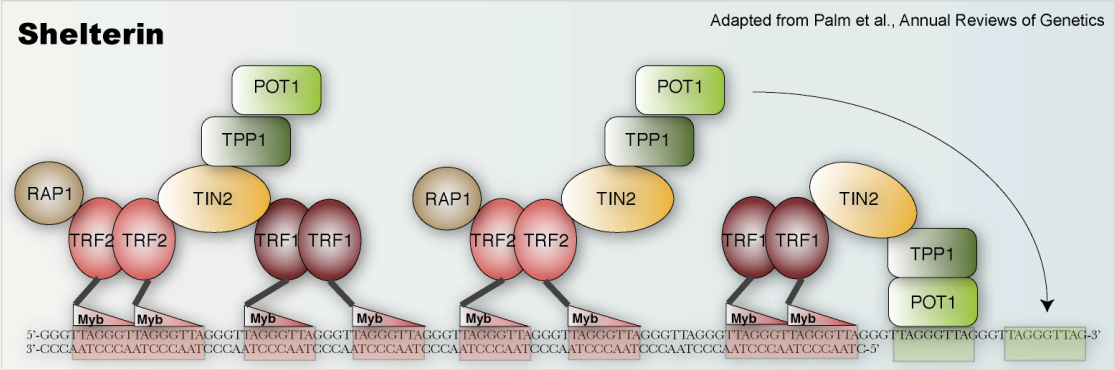

Figure 1.5. Shelterin.

The shelterin complex consists of six subunits. TRF1 and TRF2 are dimers that specifically recognize and bind to ds telomeric DNA with their Myb domains. The binding site for each TRF1 or TRF2 dimer can be overlapping or separate sequences as indicated. RAP1 is a TRF2 binding partner. TIN2 can interact with both TRF1 and TRF2 and recruits TPP1 and POT1 to the ds portion of the telomere. The ability of TIN2 to bind to both TRF1 and TRF2, independently or simultaneously, creates the possibility for different shelterin subcomplexes as shown. The TRF1/TIN2, TRF2/TIN2 and TRF1/TRF2/TIN2 shelterin subcomplexes could all potentially play roles in the enrichment of TPP1/POT1 at ssDNA. The POT1 binding sequence at ssDNA can be located at an internal site or at the 3' end as indicated.

Telomere-associated proteins

In addition to shelterin, a number of other proteins have been detected at human telomeres. Most of these factors are DNA damage signaling and repair molecules that have been implicated to associate transiently with telomeres and to perform essential accessory functions in telomere maintenance. However, all of these proteins have primary functions that are independent from telomere biology. Examples of such factors include the MRN complex [200]; XPF/ERCC1 [201], a component of the nucleotide-excision repair pathway; Apollo [202,203], a putative 5' exonuclease; DNA-PKcs [204,205]; Ku70/80 [204,206,207]; BLM and WRN RecQ helicases [208-211], implicated in branch migration of

recombination structures; Rad51D [212], a factor with a potential role in homologous recombination; and others. Deficiencies in some of these factors lead to abnormalities in telomere structure and function and have been implicated in human diseases.

As described below, the main protective functions of shelterin are to mask telomeres from recognition by the ATM and ATR signaling pathways and to prevent the processing of chromosome ends by the HDR and NHEJ machineries. Therefore, it seems paradoxical that factors involved in these pathways are specifically recruited to telomeres. It is possible that their function is tailored in the context of shelterin to service telomeres without activating their respective signaling and repair pathways.

Shelterin shapes telomeric DNA into a protected structure

3' telomeric overhang

An important requirement for telomere protection is the generation of a 3' overhang, which POT1 binds to and which is an essential element of t-loop formation. Telomeric overhangs arise from degradation of the terminal RNA primer laid down during lagging strand synthesis as well as from additional resection of the C-rich strand [179,213]. In most human cells, the average length of the telomeric overhang is 50-300 nucleotides [214,215]. The nuclease responsible for telomere end resection has so far eluded identification.

Studies of POT1 genes in mouse and human cells suggested that POT1 function might be required to regulate the resection activities of this nuclease(s). Strikingly, deletion of mouse POT1b, but not POT1a, leads to extreme overhang elongation, observed both in MEFs isolated from POT1b-deficient embryos and in liver samples taken from adult POT1b-deficient mice [197]. The increase in single-stranded TTAGGG

repeats is attributed to excessive 5'-3' nucleolytic activity and the resulting degradation of the C-rich 5' strand. Although POT1b-deficient mice are viable, the excessive loss at the 5' strand leads to progressive telomere shortening [216]. Therefore, mouse POT1b, by an unknown mechanism, functions to prevent de-regulated resection at the chromosome terminus.

It has been speculated that human POT1 is also involved in regulating end-processing events, since the precise 5' end on the resected strand of human telomeres (CCAATC-5') is randomized upon downregulation of POT1 protein levels by RNAi [217,218]. These studies documented that human POT1 sets the 5' end sequence, and, similarly to mouse POT1b, implicated human POT1 in the regulation of nuclease(s) activity at chromosome ends. The mechanism of overhang generation and maintenance would be further clarified if the identity of the nuclease(s) responsible for the generation of the 3' telomeric overhang were known.

T-loop formation

Once the overhang is generated, the next step in telomere protection is thought to be the formation of a lariat structure at the chromosome terminus, referred to as telomeric loop (t-loop). In the t-loop configuration, the single-stranded telomeric DNA invades the double-stranded portion of the telomere, displaces the G-rich strand, and base pairs with the complementary strand. The predicted role of t-loops is to effectively shield the chromosome end from nucleolytic attack and from recognition by DNA damage factors.

T-loops can be visualized directly by electron microscopy if the telomeric DNA has been cross-linked to maintain the strand invasion [219]. Analysis of the structural

features confirms a strand invasion event, including the presence of the displaced single-stranded G-rich strand, which forms a displacement loop (D loop). The size range of t-loops is heterogeneous and roughly correlates with the total telomere length, suggesting that the strand invasion takes place at a random site along the telomere duplex array [219]. Recently, electron microscopy analysis of whole telomere chromatin isolated from chicken erythrocytes and mouse splenocytes further revealed the presence of intact nucleosome arrays along the t-loop structures [220]. The current model argues that t-loops are probably present at all chromosome ends, throughout the cell cycle, except perhaps temporarily during S-phase when the passage of the replication machinery would release the invading strand, thereby revealing a naked or POT1-bound single-stranded DNA end.

Both TRF1 and TRF2 have been implicated in t-loop formation. *In vitro* data suggest that TRF2 has the ability to remodel DNA [219,221] and biochemical analysis further suggests that TRF2 has the ability to modify DNA topology and more specifically, to induce untwisting of neighboring DNA, thereby promoting strand invasion [222]. TRF1 also has *in vitro* DNA remodeling capacity including ability to bend, loop and pair distant regions containing telomeric repeats [183,186,187]. It is also likely that some of the telomere-associated factors described above may also participate in t-loop assembly. In particular, the MRN complex and BLM helicase have the functional requirements to promote t-loop formation and/or resolution but experimental evidence in support of this hypothesis is lacking.

Suppression of the ATR-dependent DNA damage response at telomeres

Stretches of single-stranded DNA are recognized as sites of damage by the ATR pathway. The ATRIP/ATR complex is recruited to RPA-coated single-stranded DNA with the help of TOPBP1, the 9-1-1 complex, Rad17, and RFC [223-226]. The ATR kinase induces cell cycle arrest through the phosphorylation and activation of the downstream checkpoint kinase Chk1 [227].

Telomeres also contain stretches of single-stranded DNA even when the 3' overhang is base-paired as in the t-loop configuration because the D-loop is exposed and can potentially recruit RPA and activate the ATR pathway [219]. Recent data in mouse and human cells have established that telomeres can indeed activate ATR signaling and that POT1 is the shelterin component that prevents the activation of the ATR pathway at telomeres (Figure 1.6) [228]. Conditional deletion of POT1a in MEFs, knockdown of its recruiter, TPP1, or downregulation of human POT1 by RNAi lead to acute activation of the DNA damage response at chromosome termini [197,198,229]. This response is characterized by activation of the ATR-dependent signaling pathway, as evidenced by Chk1 phosphorylation, which is not observed in absence of ATR. In addition, ATR mediates the accumulation of DNA damage response factors, including γ-H2AX, MDC1, MRN, and 53BP1, in telomeric foci, called telomere dysfunction-induced foci (TIFs) [197,198,228]. These findings suggest that POT1 protects chromosome ends from recognition by the ATR-dependent DNA damage response pathway. One possibility is that POT1, which binds to single-stranded telomeric DNA with high specificity and affinity, can prevent the activation of DNA damage by displacing the single-stranded DNA sensor in the ATR pathway, RPA, from telomeric sequences.

Suppression of the ATM-dependent DNA damage response at telomeres

TRF2, on the other hand, is responsible for the suppression of the ATM pathway (Figure 1.6) [228]. ATM kinase, as discussed in part I of this chapter, responds primarily to the presence of DSBs and its principal downstream effector is the Chk2 kinase [30]. When TRF2 is deleted from MEFs bearing one null and one conditional allele of TRF2 ($TRF2^{F/-}$), the protective function of telomeres is lost and chromosome ends are recognized as DSBs. Mounting evidence indicates that the consequences of TRF2 loss are identical to the events activated in response to DSBs. They involve the dramatic accumulation of a number of DNA damage response factors, including γ-H2AX, MDC1, 53BP1, and the MRN complex, at chromosome ends to form TIFs [190]. In addition, loss of TRF2 leads to activation of ATM-dependent checkpoint signaling as evidenced by the detection of ATM, autophosphorylated at S1981, and by the phosphorylation and activation of Chk2 kinase. The response to telomere dysfunction in cells lacking TRF2 is entirely dependent on ATM function. Dysfunctional telomeres in TRF2- and ATM-null cells are not associated with TIFs and do not trigger a checkpoint response [228]. These data establish that the ATM pathway is uniquely positioned to recognize and respond to loss of TRF2 function.

Telomere dysfunction can also be induced in human cells when the function of human TRF2 is suppressed as a result of the overexpression of a dominant negative allele of TRF2, which lacks the amino-terminal basic and the carboxy-terminal Myb domains (TRF2-DN) [230]. TRF2-DN dimerizes with the endogenous protein but since it lacks the DNA binding domain, the resulting heterodimer does not localize to telomeres. In addition to activating the DNA damage response [83] as described above, overexpression of

TRF2-DN results in p53-dependent cell cycle arrest or apoptosis, depending on the cell type [231,232]. In human cells, however, the response to TRF2-DN-induced telomere dysfunction is not entirely dependent on ATM kinase, as a reduced number of TIFs can still form in A-T cells. One possible explanation for the inconsistency between mouse and human cells is that complete loss of TRF2 and inhibition of TRF2 function through a dominant negative allele may have different impacts on telomere structure.

There are several models for how TRF2 prevents the activation of ATM kinase at functional telomeres. One possibility is that TRF2 is required to maintain the terminal t-loop structure, which the ATM sensor, MRN, may not be able to recognize as a DSB. A complementary model suggests that TRF2 directly inhibits the activation of ATM by binding to ATM in a region that contains S1981 [233]. Presumably, since TRF2 is exclusively enriched at chromosome termini and not elsewhere in the cell, ATM activation would be specifically dampened in the vicinity of telomeres. Therefore, even if telomeres present DNA structures that would normally signal to the ATM pathway, TRF2 might locally suppress any downstream propagation.

Prevention of inappropriate NHEJ and HDR repair at chromosome ends

In addition to suppressing the activation of ATR and ATM signaling, shelterin efficiently prevents inappropriate repair reactions at chromosome ends (Figure 1.6). The consequences of aberrant repair processing of telomeres in human cells can be deleterious. In particular, fused chromosomes, which have been joined end-to-end, are dicentric and cannot properly segregate in mitosis. Instead, they propagate the bridge-

breakage-fusion cycle [234], which can lead to extensive genomic instability as chromosomes are broken and re-joined at random places during each cell division.

The role of shelterin in suppressing inappropriate repair at telomeres can be best appreciated in the setting when loss of TRF2 function leads to uncapping of chromosome ends. Upon inhibition of TRF2 – both in the TRF2 conditional knockout MEFs and upon overexpression of the TRF2-DN allele in human cell – telomere-mediated protection is lost and chromosome ends undergo extensive repair processing [190,230]. The consequences are striking. Metaphase spreads collected five days after deletion of TRF2 reveal that many chromosomes have fused to one another, creating long trains, with the telomeric DNA retained at the sites of fusion [190]. Evidence for the involvement of the NHEJ pathway came from genetic experiments, which showed that DNA ligase IV is required for this process [190,235]. In DNA ligase IV-deficient MEFs, the rate of NHEJ of TRF2-depleted dysfunctional telomeres is reduced 100-fold compared to the rate of fusion of dysfunctional telomeres observed in control cells. On the other hand, the requirement for another NHEJ factor, Ku70, appears less stringent, since in the absence of Ku70 the rate of NHEJ is reduced only 12-fold [236]. Recently, it has been shown that the ATM kinase also promotes the efficienty of NHEJ of dysfunctional telomeres [228].

NHEJ of dysfunctional telomeres in absence of TRF2 takes place preferentially during the G1 stage of the cell cycle [237]. Prior to or simultaneously with the fusion step, the 3' telomere overhangs are removed in a reaction stimulated by the XPF/ERCC1 endonuclease complex [201]. Interestingly, in mouse cells overhang cleavage and end-joining are coupled [190], whereas in human cells, the two processes can occur independently [230].

Two models reason how TRF2 might prevent NHEJ-mediated processing of telomeres. Overhang loss is a prerequisite for the execution of the NHEJ reaction and therefore, one possibility is that TRF2 prevents inappropriate repair by hiding the overhang into the t-loop structure. The circular configuration of t-loops would be expected to prevent the first step of NHEJ – loading of the Ku70/80 complex – by masking the free DNA end. Alternatively, it is possible that TRF2 prevents NHEJ repair by suppressing ATM-mediated DNA damage signaling. Although DNA damage signaling and repair have been viewed as largely separate processes, loss of TRF2 in ATM-deficient MEFs does not lead to NHEJ [228]. Therefore, TRF2 might repress NHEJ by preventing the activation of ATM, which in turn is required for efficient NHEJ of dysfunctional telomeres.

Interestingly, TRF2 plays a role in the repression of the HDR pathway as well. As described above, dysfunctional telomeres resulting from TRF2 loss are repaired primarily through the NHEJ pathway. However, in the absence of Ku70, deletion of TRF2 leads to reduced overhang loss and diminished frequency of telomere fusion events. Instead, extensive HDR between sister telomeres takes place, leading to numerous telomeric sister-chromatid exchanges (T-SCEs) [236]. It is important to note that increased HDR at chromosome ends in this setting is not due to lack of NHEJ-processing, since T-SCEs are not observed as a phenotype of TRF2 deletion from DNA-ligase IV-deficient cells. One interpretation of these data is that, at functional telomeres, TRF2 together with Ku actively suppresses T-SCEs in order to prevent drastic telomere length changes that would be an inevitable consequence of unequal exchanges.

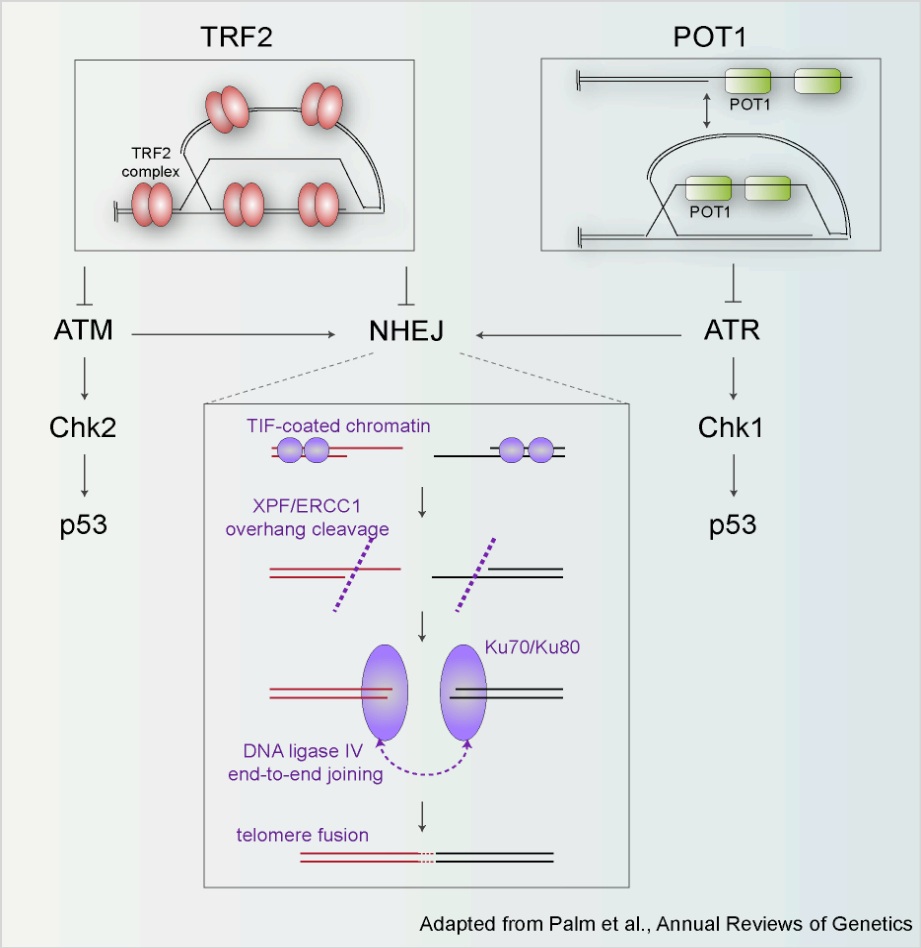

Figure 1.6. Shelterin protects chromosome ends from recognition by the DNA damage signaling and repair machineries.

TRF2 complex inhibits the activation of the ATM pathway and prevents NHEJ of telomeres *(left)*. In the absence of TRF2, ATM is activated and phosphorylates Chk2 kinase, which in turn promotes the p53/p21 pathway, leading to senescence or apoptosis, depending on the cell type. Active ATM kinase also leads to the accumulation of multiple TIF factors at chromosome ends. The overhang is cleaved in a reaction dependent on the XPF/ERCC1 endonuclease, the Ku70/80 complex is loaded on the DNA ends to promote DNA ligase IV-executed fusion reaction. Chromosome end-to-end fusions can be deleterious as they lead to the formation of dicentric chromosomes that cannot be segregated properly during mitosis. On the other hand, POT1 (bound along the overhang or on the D loop) suppresses the ATR signaling pathway *(right)*. Upon loss of POT1, ATR is activated and in turn phosphorylates and activates the downstream Chk1 kinase. In the absence of TRF2, ATM and POT1 in mouse cells, ATR activation also promotes the NHEJ pathway.

Advantages of dysfunctional telomeres as a model for NHEJ

In the studies described in this thesis work, we use telomere dysfunction, experimentally induced by the deletion of the telomere protective factor TRF2, as a model system to study the regulation of the NHEJ pathway by DNA damage response factors. We focus on the roles of the MRN complex (*Chapter 2*), γ-H2AX/MDC1 (*Chapter 3*), and 53BP1 (*Chapters 4 and 5*).

Dysfunctional telomeres exhibit multiple features that make them an advantageous model for the study of DNA repair. In the first place, damage signaling and repair occur in a largely synchronized fashion following Cre-mediated deletion of TRF2 from $TRF2^{F/-}p53^{-/-}$ MEFs [190]. TIF formation and activation of checkpoint factors can be detected 48-72 hours after Cre expression, whereas progressive repair of dysfunctional telomeres can be monitored 72-120 hours after Cre-mediated TRF2 deletion. The absence of p53 or SV40-LT-mediated inhibition of p53 function prevent the activation of the G1/S checkpoint [232], allowing analysis of the consequences of telomere dysfunction over several cell divisions.

In the second place, loss of TRF2 induces DNA damage response at all chromosome ends [190]. These sites feature known molecular markers both in the presence and in the absence of TRF2 function, namely the repetitive TTAGGG DNA and other shelterin components, such as TRF1. This allows immunofluorescence (IF), live-cell imaging, FISH (fluorescent *in situ* hybridization), and ChIP (chromatin immunoprecipitation) analysis of the molecular events at the same sites before and after the induction of damage.

In the third place, TRF2 deletion activates specifically the ATM pathway, allowing investigation into the identity of the sensor in this pathway [228].

In the fourth place, NHEJ of dysfunctional telomeres takes place gradually, over several days, so that its rate can be reproducibly measured. In addition, NHEJ-mediated repair of dysfunctional telomeres occurs primarily during the G1 stage of the cell cycle [237]. Therefore, the determinants for this cell cycle specificity can be addressed.

Finally, the response to dysfunctional telomeres is indistinguishable from the response to chromosome-internal DSBs, arguing that a novel mechanism found to contribute to NHEJ repair of dysfunctional telomeres may also play a part in the repair of chromosome-internal DSBs [83,190,230,231,235,236].

In this thesis, I define the relative involvement of the MRN complex, γ-H2AX, MDC1, and 53BP1 in the NHEJ pathway at dysfunctional telomeres and propose a unifying mechanism for their role in repair.

CHAPTER 2: DISSECTING THE ROLE OF MRE11/RAD50/NBS1 COMPLEX AT FUNCTIONAL AND DYSFUNCTIONAL TELOMERES

Introduction

The MRN complex has been implicated in multiple aspects of telomere function and in the first part of this chapter we explore the role of MRN at functional telomeres. An association between MRN and the TRF2 complex has been well-documented [200], although the mechanism and the functional importance of this interaction have remained unclear. Recent studies have implicated NBS1 as an accessory component for telomerase-mediated telomere extension [238] and suggested a role for the MRN complex in overhang maintenance in telomerase-positive cells [239]. Given the role of MRN complex in HDR, it has further been proposed that MRN might play a role in the generation of the telomeric overhang and/or promote t-loop formation [240]. On the other hand, as described in the introduction, MRN most likely functions as the DSB sensor in the ATM pathway. An association, therefore, between MRN and functional telomeres seems counterintuitive, since the primary goal of telomeres is to prevent the DNA damage response at natural chromosome ends.

In order to address these functional questions, we aimed at understanding the mechanism of MRN recruitment to functional telomeres. We tested a potential model for the interaction between NBS1 and TRF2, and in the beginning of this chapter we describe some of the experimental limitations we encountered. We also report evidence that the MRN complex might play a regulatory role in overhang generation/maintenance but is not otherwise required for the function and structure of mouse telomeres.

The MRN complex also localizes to telomeres rendered dysfunctional through depletion of TRF2 from chromosome ends [83,190,190]. In the second part of this chapter, we asked whether MRN is required for the activation of the ATM-dependent DNA damage response at deprotected telomeres. Previous data on the response to telomere dysfunction in human cells have already hinted that the MRN complex might be the sensor. Treatment with the PIKK inhibitor caffeine, which effectively disrupts the recruitment of 53BP1 to TIFs, does not prevent the accumulation of Mre11 at TRF2-depleted telomeres [83], arguing that the recruitment of MRN is kinase-independent. However, in human cells, the response to telomere dysfunction induced by a dominant negative allele of TRF2, TRF2-DN, is not entirely dependent on ATM since in A-T cells the TIF response is only mildly reduced [83]. The redundancy of the kinase, which signals telomere dysfunction in human cells, complicates the analysis of MRN's contribution. Here, we focus on mouse cells, in which the requirement for ATM kinase in the response to telomere dysfunction elicited by loss of TRF2 has been genetically established [228]. We undertook several independent approaches in order to dissect the role of the MRN complex, including chemical inhibition, RNAi to MRN and to factors closely associated with MRN, as well as genetic knockout of the MRN component, NBS1. Ultimately, the main conclusions came from the genetic analysis, which exposed key roles for MRN in signaling as well as in repair of dysfunctional telomeres.

The interaction between MRN and TRF2 is enhanced in the absence of a phosphorylation event

The interaction between endogenous MRN and TRF2 complexes can be weakly but reproducibly detected by immunoprecipitation of nuclear extracts isolated from human cells [200]. With this technique, roughly 1-5% of total TRF2 can be recovered with an Mre11-specific antibody. We asked whether phosphorylation plays a role in promoting this association by adding phosphatase inhibitors to the nuclear extract. We saw the opposite result by immunoblot – TRF2 was absent from the Mre11 immunoprecipitate in the presence of the phosphatase inhibitors NaF and β-glycerophosphate (Figure 2.1a), suggesting that a phosphorylation event strongly inhibits the association.

Recently, the structural basis for the interaction between TRF2 and a telomere-associated nuclease Apollo has been determined [241]. The crystal structure reveals a close contact between a loop located in the TRFH domain of TRF2 and a Y-x-L-x-P motif in Apollo (Figure 2.1b). Indeed, a mutant of Apollo in which this motif is changed to Y-x-E-x-A no longer associates with TRF2, and vice versa, mutation of the critical residue in TRF2 (F120) abolishes the Apollo-TRF2 interaction. As NBS1 contains a Y-x-L-x-P motif at amino acid position 429 [242], we asked whether it might be a point of contact between the MRN complex and TRF2. In NBS1, this motif contains a serine residue, Y-x-L-S-P, creating a potential CDK phosphorylation site. Structural modeling predicts that phosphorylation at this site (S432 in human; S433 in mouse NBS1) would lead to a steric clash with the TRFH domain, consistent with our findings above that phosphorylation inhibits the MRN-TRF2 interaction.

Unpublished data from two groups (S. Jackson, pers. comm. and J. Petrini and R. Fisher, pers. comm.) have identified S432 of human NBS1 (S433 in mouse NBS1) as a CDK2 target that is preferentially phophorylated during the S and G2 stages of the cell cycle. Moreover, phosphorylation at that particular residue has been implicated in promoting resection during HDR-mediated repair of DSBs. Interestingly, while Mre11 and Rad50 remain associated at human telomeres throughout the cell cycle, NBS1 is preferentially recruited to telomeres only in S phase. If NBS1 indeed binds to TRF2 through the Y-x-L-S-P motif, such an interaction can only occur in absence of S432 phosphorylation, suggesting a potential model for how TRF2 might be regulating the DNA damage response function of MRN. In this model, NBS1 bound to TRF2 would be kept in an inactive, de-phosphorylated form, preventing ATM activation as well as unwanted resection at chromosome termini. At the same time, MRN might be employed in promoting a different aspect of telomere function.

In order to test this model, we wished to study the interaction of TRF2 with various versions of human and mouse NBS1, bearing relevant mutation at S432/S433. However, we were unable to perform any functional analysis because the expression levels of tagged NBS1 transiently transfected into 293T cells were very low (at least 100-fold below endogenous levels). We could not overexpress human or mouse NBS1 in 293T cells even when the other members of the complex, Mre11 and Rad50, were co-transfected. Since the presence of an N-terminal tag might affect expression levels, we tried a C-terminal tag or no tag at all, but did not observe a higher level of expression. We also cloned NBS1 into a vector that contained a chimeric intron, pCi, in case transcription was splice-dependent, without any success in bolstering protein levels. Finally,

expression levels of exogenously introduced NBS1 remained low even in Cre-treated $NBS1^{F/-}$ cells that lacked endogenous NBS1 (Figure 2.1c), arguing against a model in which the total levels of NBS1 within a cell are strictly regulated. Because of low protein levels, even in the case of exogenously introduced wild-type NBS1, we could neither detect an association with telomeric proteins by co-IP nor recover telomeric DNA by ChIP (Figure 2.1d), precluding further analysis of mutants.

Successful expression of exogenous human NBS1 in cells derived from NBS patients has been previously shown on immunoblots [243]. However, it is not excluded that the reported expression of NBS1 in human NBS cells failed to reach wild type expression since these experiments lacked the internal control for normal NBS1 levels. As shown here (Figure 2.1c), the expression of NBS1 protein was also detectable in immunoblots of Cre-treated $NBS1^{F/-}$ mouse cells but the NBS1 levels were substantially reduced compared to the endogenous protein. Importantly, although we could detect protein expression, it was not enough for functional analysis by ChIP. In addition, expression of exogenous NBS1 was lost over time and thus we could not stably rescue Cre-treated $NBS1^{F/-}$ cells. Recently, several groups have used fluorescently tagged NBS1 in live-cell imaging experiments [109]. These constructs seem expressed at normal levels, and importantly, appear to be functional at least in terms of localization to DSBs. It is therefore prudent to test whether the presence of a fluorescent protein tag stabilizes NBS1 protein and enhances its expression levels so that the planned experiments can be done.

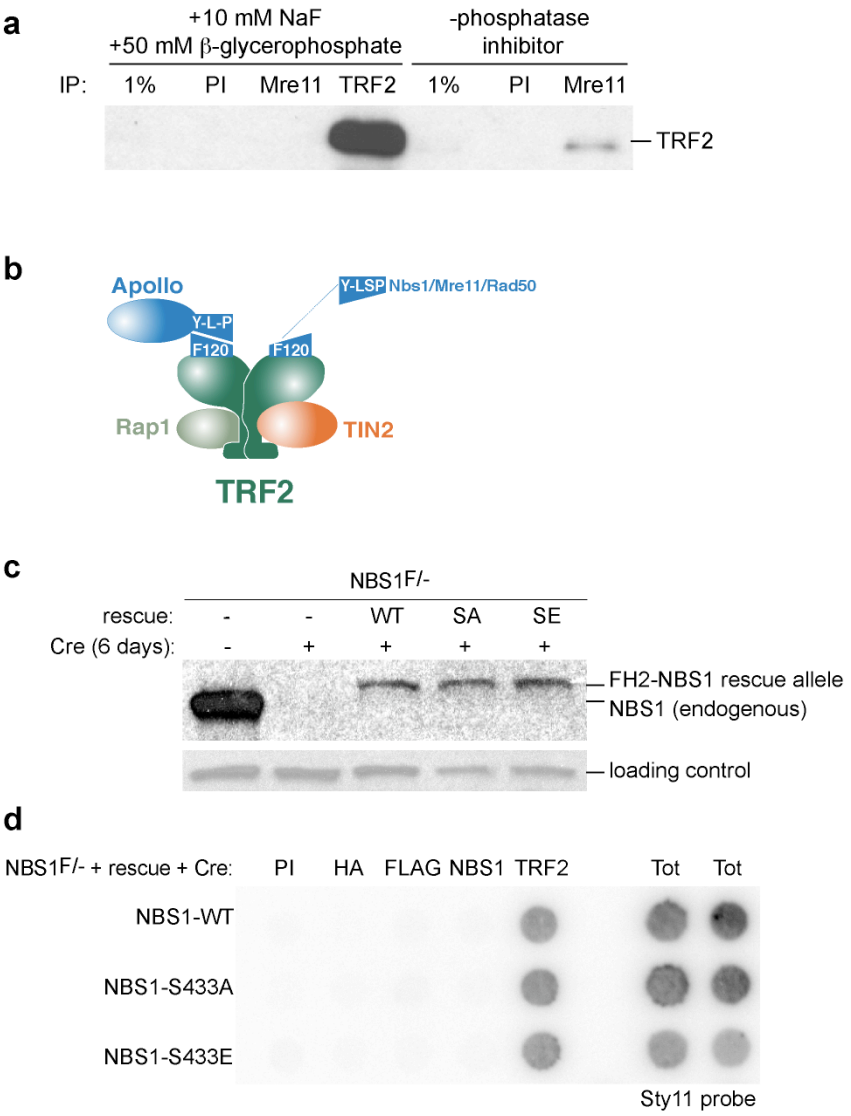

Figure 2.1. Mechanistic insight into the interaction between MRN and TRF2 complexes

a, Immunoblot of IPs from HeLa1.2.11 nuclear extracts, incubated with pre-immune serum, human Mre11- (874), or human TRF2 (647)-specific rabbit Abs, in the presence or absence of the phosphatase inhibitors 10 mM NaF and 50 mM β-glycerophosphate. 1% cell extract was loaded as control for input. TRF2 IP was used as a positive control for the efficiency of the IP. The blot was probed with a mouse monoclonal Ab raised against human TRF2.

b, Schematic representation of the TRF2 complex, highlighting the critical F120 residue in the TRFH domain of TRF2, which mediates the interaction with the Y-x-L-x-P motif in Apollo and, potentially, with the same motif in NBS1 from the MRN complex.

c, Immunoblot of whole cell lysates prepared from NBS1$^{F/-}$ MEFs or NBS1$^{F/-}$ MEFs, stably expressing the following N-terminally FH2-tagged constructs from pLPC-puro expression vector:

NBS1-WT (wild type), NBS1-S433A, or NBS1-S433E, retrovirally infected with pWzl-hygro vector or pWzl-hygro-Cre, and harvested after 6 days of hygromycin selection. The blot was probed with a mouse NBS1-specific Ab (93'6). A non-specific band from the same blot was used a loading control.

d, Dot blot of telomeric DNA ChIP of nuclei prepared from $NBS1^{F/-}$ cells rescued with WT, S433A, or S433E NBS1 and treated with pWzl-hygro-Cre to delete the endogenous protein, as shown in **(c)**. The following Abs were used for ChIP: pre-immune, HA (11), FLAG (M2), NBS1 (93'6), and TRF2 crude serum (647). Telomeric DNA was detected by hybridization to a TTAGGG repeat-specific, radioactively labeled probe. 25% input labeled as Total.

MRN complex plays a regulatory role in overhang processing

Next we asked whether MRN plays a structural and functional role at mouse telomeres. We analyzed SV40-LT transformed, NBS1 conditional knockout MEFs ($NBS1^{F/-}$) [137,244]. Although NBS1 is an essential gene, SV40 transformed cells can survive up to 10 days after deletion of NBS1 with Cre, allowing the long-term analysis of NBS1 loss. At early (3-4 days post Cre) as well as at late (8-10 days post Cre) time points, we did not find any evidence for telomere dysfunction in absence of NBS1. We did not detect TIFs at chromosome ends in more than 200 cells examined by immunofluorescence and we did not observe enrichment for end-to-end fusions or T-SCEs on metaphase spreads.

Previously published data examining the effect of MRN RNAi in human cells reported transient shortening of G-overhang upon knockdown of MRN components [239]. This effect, however, was only observed in telomerase expressing cells, arguing for a role of MRN in telomerase-mediated overhang regulation rather than in overhang maintenance *per se*. We examined the effect of NBS1 loss on overhang structure in $NBS1^{F/-}$ MEFs harvested at consecutive time-points after Cre-mediated deletion of the conditional allele and analyzed by overhang assay. In this assay, the 3' telomeric

overhang is detected in-gel, under native conditions, with a telomere-specific probe. The single-stranded signal is then normalized to the total telomeric DNA signal quantified on the same gel after denaturation. The relative value represents the change in overhang signal compared to control. While in one overhang assay, we saw a progressive increase in relative overhang signal in the absence of NBS1 (Figure 2.2a), in an independent experiment, we saw no significant change in the relative overhang signal up to 10 days after deletion of NBS1 from $NBS1^{F/-}$ MEFs (Figure 2.2b). The latter result was confirmed in a subsequent experiment (Figure 2.2c), indicating that the MRN complex is not essential for overhang maintenance.

Loss of NBS1, on the other hand, appeared to diminish the overhang increase associated with inhibition of POT1b function. As described in the introduction, POT1b protects chromosome termini from nuclease-dependent degradation [197,216]. To test whether NBS1 plays a role in the pathway triggered in absence of POT1b, we used a dominant-negative allele of POT1b function as a tool to induce aberrant overhang elongation [245]. POT1-HA is a chimeric protein that is composed of the N-terminal half of human POT1 and the C-terminal half of mouse POT1a. The resulting fusion protein acts as a dominant-negative allele because it localizes at mouse telomeres but lacks a segment from POT1b that is required to prevent excessive nuclease activity [245]. We introduced POT1-HA into $NBS1^{F/-}$ MEFs and assayed for overhang signal with or without Cre-mediated NBS1 deletion (Figure 2.2c). NBS1 loss by itself did not affect overhang length in this experiment. As an additional control, overexpression of POT1-HA led to a 3-fold increase in overhang signal in NBS1-proficient cells, confirming its role as a dominant-negative allele. In NBS1-deficient cells, on the other hand, we observed only a 2-fold

increase in the intensity of the relative overhang signal upon POT1-HA overexpression. The 30% reduction in overhang signal in the absence of NBS1 establishes a potential regulatory role for NBS1 in overhang processing. On the other hand, the incomplete reversal of the dominant negative effect implies the presence of redundant pathway(s).

The identity of the nuclease(s) that resect telomeric DNA upon POT1b inhibition is not known, and it might or might not be the nuclease that is also responsible for overhang generation under normal circumstances. The data presented here suggested that NBS1, as part of the MRN complex, might be involved in regulating this nuclease activity. An obvious potential candidate for such nuclease is CtIP, which has been demonstrated to function in conjunction with the MRN complex.

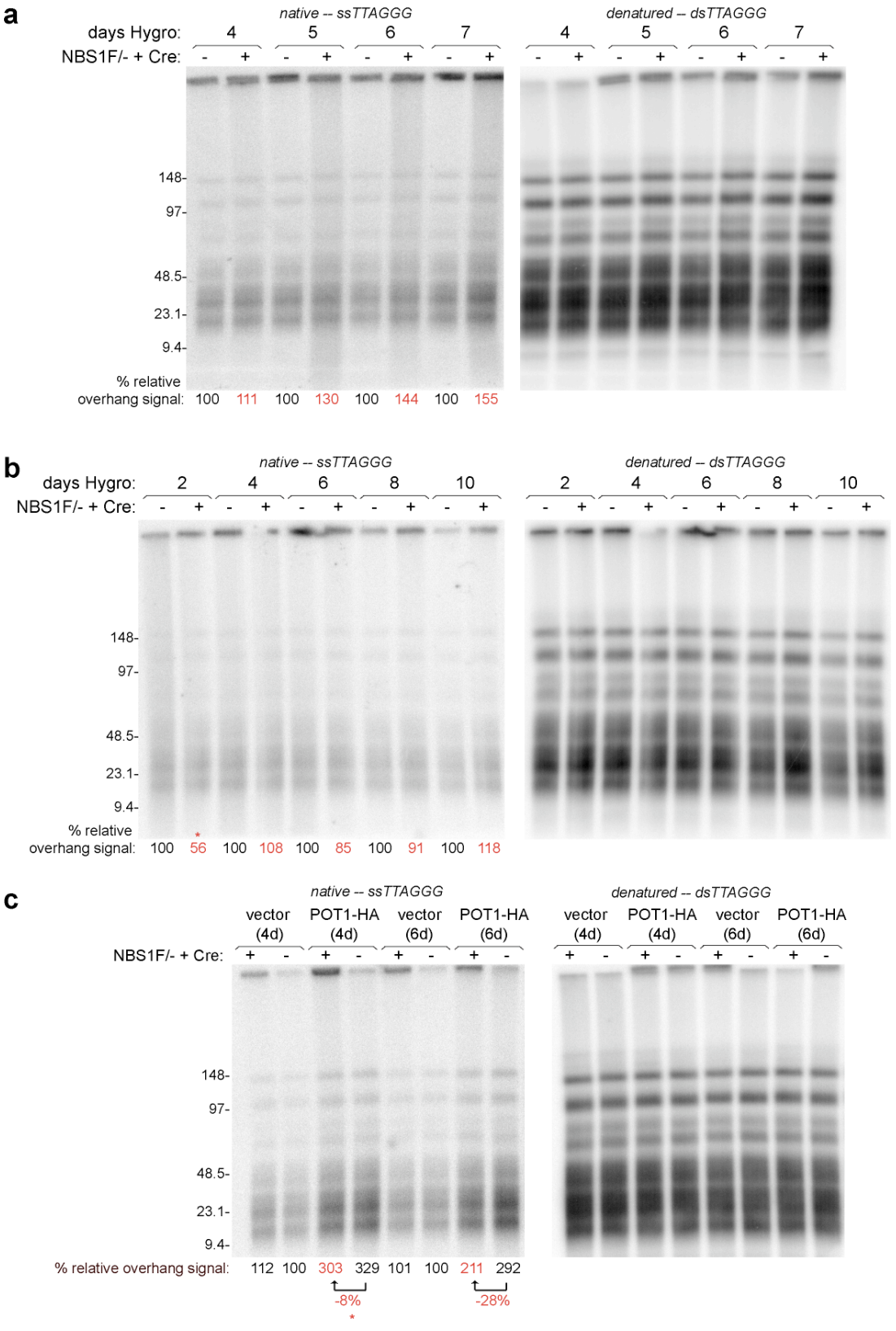

Figure 2.2. Role of NBS1 in the maintenance of the telomeric 3' overhang

Figure 2.2. Role of NBS1 in the maintenance of the telomeric 3' overhang

a-c, In-gel detection of telomeric DNA from cells, described below. DNA in agarose plugs was separated on agarose gel by pulse-field gel electophoresis and hybridized in-gel to a radioactively labeled $(CCCTAA)_4$ probe (*native*). The DNA was denatured *in situ* and rehybridized to the same probe (*denatured*). In each lane, the ssTTAGGG signal quantified under native condition was normalized to the total TTAGGG signal, detected after denaturation.

a, $NBS1^{F/-}$ cells were harvested 4, 5, 6, and 7 days after introduction of pWzl-hygro vector or pWzl-hygro-Cre introduced by 4 retroviral infections, delivered at 12 hour intervals and followed by hygromycin selection. The relative overhang signal represents the normalized ssTTAGGG signal in Cre-treated cells (in red), compared to control, vector-treated cells (set at 100%, in black) at each time point.

b, same as in **(a)** but cells were collected 2, 4, 6, 8, and 10 days after Cre infection.

c, $NBS1^{F/-}$ cells were infected with pWzl-hygro vector or pWzl-hygro-Cre introduced via 3 retroviral infections at 12 hour intervals, followed by retroviral infections with vector or POT1-HA dominant negative allele, composed from N-terminal half of human POT1 and the C-terminal half of mouse POT1a [245], expressed from pWzl-hygro, introduced via 3 consecutive retroviral infections. At that point cell were placed under hygromycin selection. Cells were harvested 4 or 6 days after the second round of infections. The overhang signals are normalized to vector-treated, NBS1-proficient controls at each time point. The numbers in red below the arrows indicate the effect of NBS1 deficiency on POT1-HA-induced overhang signal increase.

* NBS1 deletion was not complete at the indicated time points in **(b)** and **(c)**.

No evidence for a role of CtIP in overhang processing and in the repair of dysfunctional telomeres

As described in the introduction, CtIP, the human homolog of Sae2, is a putative nuclease that, as a part of the MRN complex, promotes the initial resection step in HDR of DSBs [63,144,246]. This resection step is regulated by CDK activity and displays cell cycle specificity for the S and G2 stages of the cell cycle [58]. We were interested in the potential roles CtIP nuclease might play in overhang generation at functional telomeres and in the repair of dysfunctional telomeres.

We tested whether CtIP is the nuclease responsible for overhang generation at functional telomeres. We assayed the telomeric overhang signals at 6 and 8 days after the introduction of two CtIP-specific shRNAs[144]. Both shRNAs reduced CtIP protein levels efficiently, as evidenced by diminished CtIP signals in immunoblots (Figure 2.3a). Downregulation of CtIP, however, did not affect the relative overhang signal at functional telomeres (Figure 2.3b), arguing against CtIP as the only nuclease required for overhang generation. A genetic knockout would be required to further substantiate this conclusion.

We next asked whether CtIP played a role in the processing of dysfunctional telomeres. We based our analysis on experimental evidence obtained from analysis of chromosome internal DSBs, where it has been proposed that CtIP, together with the MRN complex, promotes resection in the S and G2 stages of the cell cycle and stimulates HDR. Interestingly, in experiments designed to address the proficiency of fission yeast cells lacking Ctp1 (*S. pombe* homolog of Sae2/CtIP) to execute HDR and NHEJ, the former repair pathway was found to be impaired, while the efficiency of the latter

appeared enhanced [60]. These results led Takeda and colleagues to propose a model where HDR is stimulated in S/G2 by increased resection at DSBs [60]. NHEJ, on the other hand, is limited to G1, because in G2 high levels of CDK activity promote end-processing. A prediction of this model is that if resection were artificially inhibited through CtIP or MRN downregulation, NHEJ could be potentially activated in G2.

We were interested in testing this model at TRF2-depleted mouse dysfunctional telomeres, which are known to be subject to NHEJ repair preferentially in G1 [237]. Interestingly, G2 fusion events of dysfunctional telomeres can be promoted by CDK inhibition with roscovitine [237]. This experimental evidence supported a model where NHEJ could in principle occur in G2, but is suppressed by CDK activity. Analysis of the interplay between HDR and NHEJ pathways at dysfunctional telomeres is, however, complicated by the initial presence of 3' telomeric G-overhangs, which are removed by an endonuclease cut prior to or concomitant with the NHEJ-mediated fusion. The removal of the telomeric overhang is thought to occur in G1, since overhang loss and end-joining reactions are coupled in mouse cells Therefore, the 3' overhang is most likely present in S/G2, when NHEJ is normally suppressed. Mechanistically, it is not clear what prevents HDR from engaging dysfunctional telomeres containing 3' overhangs during S/G2, but it has been previously established that this is not the case. To avoid these complications, in our analysis we only focused on whether the cell cycle specificity of NHEJ of dysfunctional telomeres is determined by CtIP without addressing the role of CtIP in HDR and resection.

To address whether CtIP function regulated the cell cycle specificity of NHEJ of TRF2-depleted mouse dysfunctional telomeres, we introduced two independent CtIP-

specific shRNAs into TRF2$^{F/-}$p53$^{-/-}$ MEFs and analyzed metaphase spreads 84 hours post adenoviral Cre infection (Figure 2.3c). We scored for G1 and G2 fusions of dysfunctional telomeres. G1 fusions appear as chromosome-type fusions on metaphase spreads (see schematic in Figure 2.3d). Because they occurred prior to replication, both of the arms from one chromosome are fused to the sister telomeres on another. In contrast, chromatid fusions, where one of the sister chromatids fuses to the arm of a different chromosome, and sister fusions, where both sisters fuse intrachromosomally, (see schematic in Figure 2.3d) are indicative of post-replicative, G2 NHEJ events. As mentioned above, G1 fusions are predominant upon TRF2 deletion, whereas G2 fusions are less frequent. Both in control and in CtIP shRNA-treated cells, there were 35-39% chromosome type-fusion events per chromosome end and a significantly smaller fraction of the chromosome ends, 3-5%, were engaged in chromatid- and sister-type fusions (Figure 2.3d). These results argued against a role for CtIP in determining the cell cycle specificity of NHEJ-mediated repair of dysfunctional telomeres. In addition, CtIP downregulation did not affect the loss of the telomeric G-overhang (Figure 2.3b), which is another major consequence of TRF2 deletion that precedes or coincides with the fusion reaction, further establishing that CtIP does not play a role in NHEJ of dysfunctional telomeres. It is possible that analysis of CtIP knockout cells may be required to detect a functional phenotype.

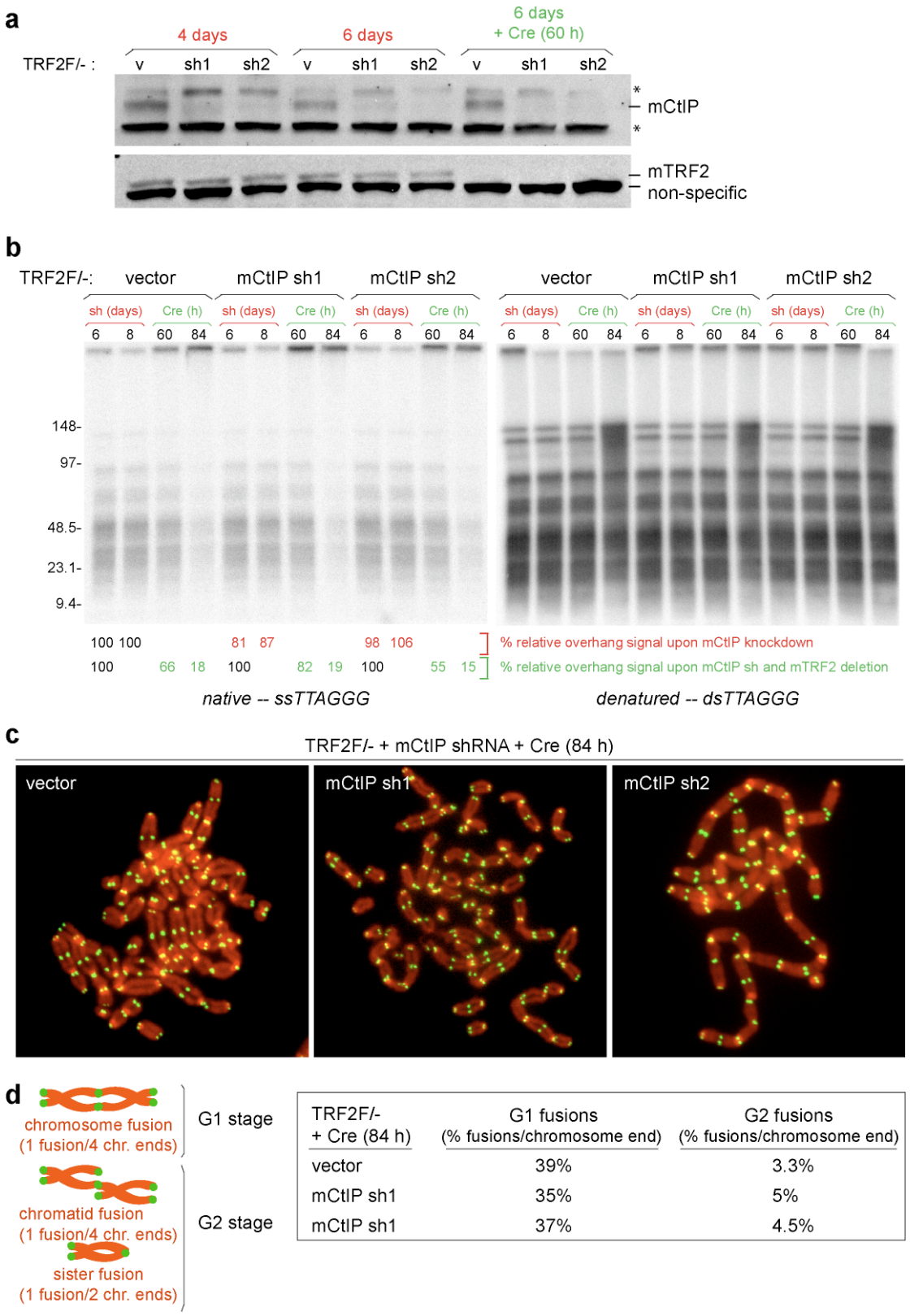

TRF2F/- + Cre (84 h)	G1 fusions (% fusions/chromosome end)	G2 fusions (% fusions/chromosome end)
vector	39%	3.3%
mCtIP sh1	35%	5%
mCtIP sh1	37%	4.5%

Figure 2.3 Effect of CtIP downregulation on functional and dysfunctional telomeres

Figure 2.3 Effect of CtIP downregulation on functional and dysfunctional telomeres

a, Immunoblots of whole cell lysates, prepared from $TRF2^{F/-}p53^{-/-}$ MEFs expressing vector or mouse CtIP-specific shRNA, sh1 or sh2, from pSuperior retroviral expression vector. Cells were harvested 4 or 6 days after shRNA infections (*Left*) or 60 hours post mock or adenoviral Cre infections delivered 4 days after the shRNA infections (*Right*). The blots were probed with Abs raised against human CtIP (H-300) and human TRF2 (647). Astericks indicate non-specific bands in the CtIP immunoblot. A non-specific band from the TRF2 blot was used as a loading control.

b, In-gel detection of telomeric DNA from cells, treated as in **(a)**. DNA in agarose plugs was separated on agarose gel by pulse-field gel electophoresis and hybridized in-gel to a radioactively labeled $(CCCTAA)_4$ probe (*native*). The DNA was denatured *in situ* and rehybridized to the same probe (*denatured*). In each lane, the ssTTAGGG signal quantified under native condition was normalized to the total TTAGGG signal, detected after denaturation. The relative overhang signal in red represents the overhang signal in shRNA-treated cells, compared to control, vector-treated cells (set at 100%, in black) at each time point, indicating the effect of CtIP knockdown on 3' overhang at functional telomeres. The relative overhang signal in green represents the overhang signal in Cre-treated cells, compared to mock-treated cells (set at 100%, in black) at each time point. These values demonstrate the effect of CtIP knockdown on overhang loss following TRF2-deletion.

c, Metaphase spreads of $TRF2^{F/-}p53^{-/-}$ cells expressing vector or CtIP-specific shRNA, sh1 or sh2, harvested 84 hours after adenoviral Cre infection and processed for FISH with telomere-specific FITC-OO-$(AATCCC)_3$ oligonucleotide (green); DNA is counterstained with DAPI (red).

d, Table summarizing the percentage of chromosome- and chromatid-type fusions scored per chromosome end ($n \geq 1000$) in metaphases in **(c)**. Schematic diagrams provide visual descriptions for each type of fusion and desribes the scoring method.

Testing MRN function at telomeres with a small molecule inhibitor, mirin

Since inhibition of individual components of the MRN pathway did not reveal a possible role for this complex in telomere function, we sought a more general way of inhibiting the MRN complex. Mirin is a small molecule that was isolated from a chemical screen for inhibitors of the ATM pathway [247]. Instead of affecting ATM kinase activity, mirin was found to inhibit the MRN-dependent activation of ATM. As a consequence, mammalian cells treated with mirin exhibit impaired G2/M checkpoint response and homology-dependent repair defects. *In vitro*, mirin was found to inhibit the nuclease activity of the MRN complex but the relevance of this inhibition to the ATM pathway has not been established [247].

In our experiments, treatment with mirin led to a profound defect in cell growth (after 6 days in culture mirin-treated cells had undergone 5.2 population doublings versus 9.9 population doublings for the control cells). Impaired growth, however, was not due to telomere dysfunction. Treatment with mirin did not induce TIFs, and did not lead to detectable abnormalities in telomere structure on metaphase spreads or in overhang assays. The integrity of telomeres in the presence of mirin indicated that the function of the MRN complex that is affected by mirin does not play a major role at telomeres.

We also tested whether mirin affected the response to telomere dysfunction by introducing mirin into Cre-treated $TRF2^{F/-}p53^{-/-}$ MEFs. As the response to TRF2 loss is entirely ATM-dependent, we expected a significant effect. Mirin, however, did not affect the accumulation of γ-H2AX and 53BP1 at dysfunctional telomeres (Figure 2.4a). In contrast, the association of NBS1 with dysfunctional telomeres seemed to be stabilized in the presence of mirin (Figure 2.4a), which is consistent with previous data showing that

mirin stimulates MRN-dependent DNA tethering *in vitro* [247]. The functional basis for this increased association is not clear, but it has been suggested that in the presence of mirin, the MRN complex cannot dissociate from DNA [247].

We also noted a slight effect of mirin on NHEJ of dysfunctional telomeres (Figure 2.4b). While control cells lost 40% of their telomeric G-overhang at 72 hours post Cre-mediated TRF2 deletion, mirin-treated cells lost a comparable amount of overhang signal (33%) with a delay of 24 hours, at 96 hours post Cre infection. Furthermore, there appeared to be fewer fusions on metaphase spreads prepared from mirin-treated cells compared to control cells (Figure 2.4c). However, due to the growth defect associated with mirin treatment, there were not enough metaphases to score the number of fusions reliably.

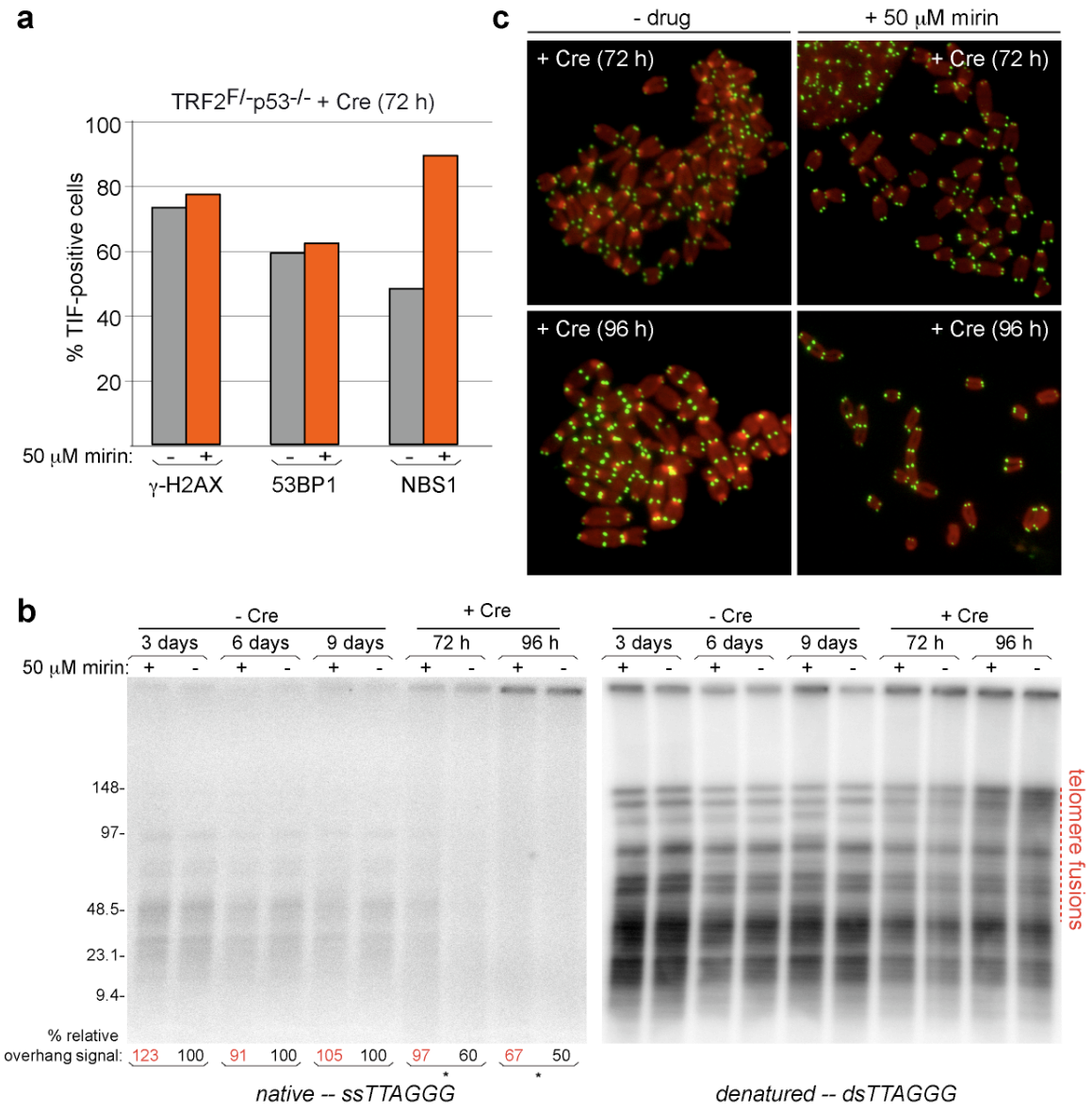

Figure 2.4. Effect of MRN inhibitor, mirin, on the response to telomere dysfunction

a, Bar graph presenting percentage of cells (n≥100), which contained 10 or more IF signals that co-localized with the TTAGGG-repeat specific FISH probe. $TRF2^{F/-}p53^{-/-}$ MEFs, infected with Hit&Run Cre retrovirus and grown in the absence or in the presence of 50 μM mirin, added to the medium 12 hours after the last infection, were fixed 72 hours post Cre and processed for IF-FISH. IF was performed with Abs raised against γ-H2AX, 53BP1 (100-304), or NBS1 (93'6). Telomeric DNA was detected in FISH with a telomere-specific FITC-OO-$(AATCCC)_3$ probe.

b, In-gel detection of telomeric DNA from cells, described below. DNA in agarose plugs was separated on agarose gel by pulse-field gel electophoresis and hybridized in-gel to a radioactively labeled $(CCCTAA)_4$ probe (*native*). The DNA was denatured *in situ* and rehybridized to the same

probe (*denatured*). In each lane, the ssTTAGGG signal quantified under native condition was normalized to the total TTAGGG signal, detected after denaturation. Lane 1-6 (-Cre): $TRF2^{F/-}$ $p53^{-/-}$ MEFs were mock treated or incubated with 50 μM mirin for 3, 6 or 9 days to analyze the effect of mirin on overhang signal at functional telomeres. The relative overhang signal (in red) represents the overhang signal in mirin-treated cells, compared to control, mock-treated cells (in black) at each time point. Lane 7-10 (+Cre): To assay for the role of MRN in the processing of dysfunctional telomeres, $TRF2^{F/-}p53^{-/-}$ MEFs were treated with Cre for 72 or 96 hours in the presence or absence of 50 μM mirin. The overhang signal at 72 and 96 hours post Cre is normalized to the signal in –Cre cells collected at day 3 post mock or mirin treatment.
c, Examples of metaphase spreads of $TRF2^{F/-}p53^{-/-}$ cells, treated or untreated with 50 μM mirin, harvested 72 or 96 hours after Hit&Run Cre infections and processed for FISH with telomere-specific FITC-OO-$(AATCCC)_3$ oligonucleotide (green); DNA was stained with DAPI (red).

NBS1 is required for ATM-dependent response to telomere dysfunction

Since the experiments with mirin-mediated MRN inhibition led to inconclusive results, we decided to address genetically the role of the MRN complex in the response to telomere dysfunction. We crossed $TRF2^{F/F}$ mice [190] with $NBS1^{F/-}$ mice [137,244] to generate $TRF2^{F/+}NBS1^{F/+}$ and $TRF2^{F/+}NBS1^{+/-}$ progeny. These were crossed again to obtain $TRF2^{F/F}NBS1^{F/-}$ and $TRF2^{F/F}NBS1^{F/+}$ litters. Crosses of these mice generated E13.5 mouse embryos, from which we isolated MEFs with $TRF2^{F/F}NBS1^{F/-}$ and $TRF2^{F/F}NBS1^{F/+}$ genotypes. MEFs were immortalized at passage 2 with SV40-LT to abrogate the ability of these MEFs to arrest in G1/S after telomere deprotection [232]. Western blotting confirmed that treatment with Cre recombinase in $TRF2^{F/F}NBS1^{F/-}$ led to deletion of the NBS1 gene and, at the same time, resulted in TRF2 loss (Figure 2.5e). In the control, $TRF2^{F/F}NBS1^{F/+}$ MEFs, Cre infection induced TRF2 deletion in the presence of functional MRN complex (Figure 2.5e).

As described in the introduction, the major consequence of TRF2 deletion is the recognition of all chromosome ends as sites of DSBs by the ATM signaling machinery [228]. Using this system, we could, therefore, directly address whether or not NBS1 is required for the activation of ATM kinase. First, we determined whether NBS1 behaves as a sensor for DNA damage by scoring TIFs in $TRF2^{F/F}NBS1^{F/-}$ and $TRF2^{F/F}NBS1^{F/+}$ cells 72 hours post Cre treatment (Figure 2.5a-c). We found that NBS1 is indeed required for the activation of the DNA damage response machinery. In the presence of NBS1, ~90% of the cells scored positive for γ-H2AX, MDC1 and 53BP1 TIFs, whereas in cells lacking NBS1, less than 1% contained damage foci at telomeres (Figure 2.5d). The phenotype of NBS1 loss is more severe compared to observations made in MDC1-deficient cells (see Chapter 3), in which γ-H2AX TIF formation was not significantly affected. The difference demonstrates that unlike MDC1, which is involved in amplification of the damage signal, NBS1 is required for its activation.

In addition to the effect on TIF formation, absence of NBS1 also resulted in complete abrogation of checkpoint signaling. While in NBS1-proficient cells, we detected robust Chk2 phosphorylation following Cre-mediated induction of telomere deprotection; in NBS1-deficient cells, we failed to observe Chk2 activation even upon efficient TRF2 deletion (Figure 2.5e). This phenotype is identical to observations made in ATM-deficient cells [228] and establishes a critical role for NBS1 in the ATM signaling pathway. On the other hand, there was no difference in cell proliferation between Cre-treated $TRF2^{F/F}NBS1^{F/-}$ and $TRF2^{F/F}NBS1^{F+}$ (Figure 2.5f), demonstrating that the absence of DNA damage response and lack of checkpoint activation in NBS1-deficient MEFs was not due to defects in cell cycle progression. In sum, the complete lack of Chk2

activation and TIF formation in NBS1-deficient cells support the conclusion that the MRN complex is the only sensor in the ATM pathway.

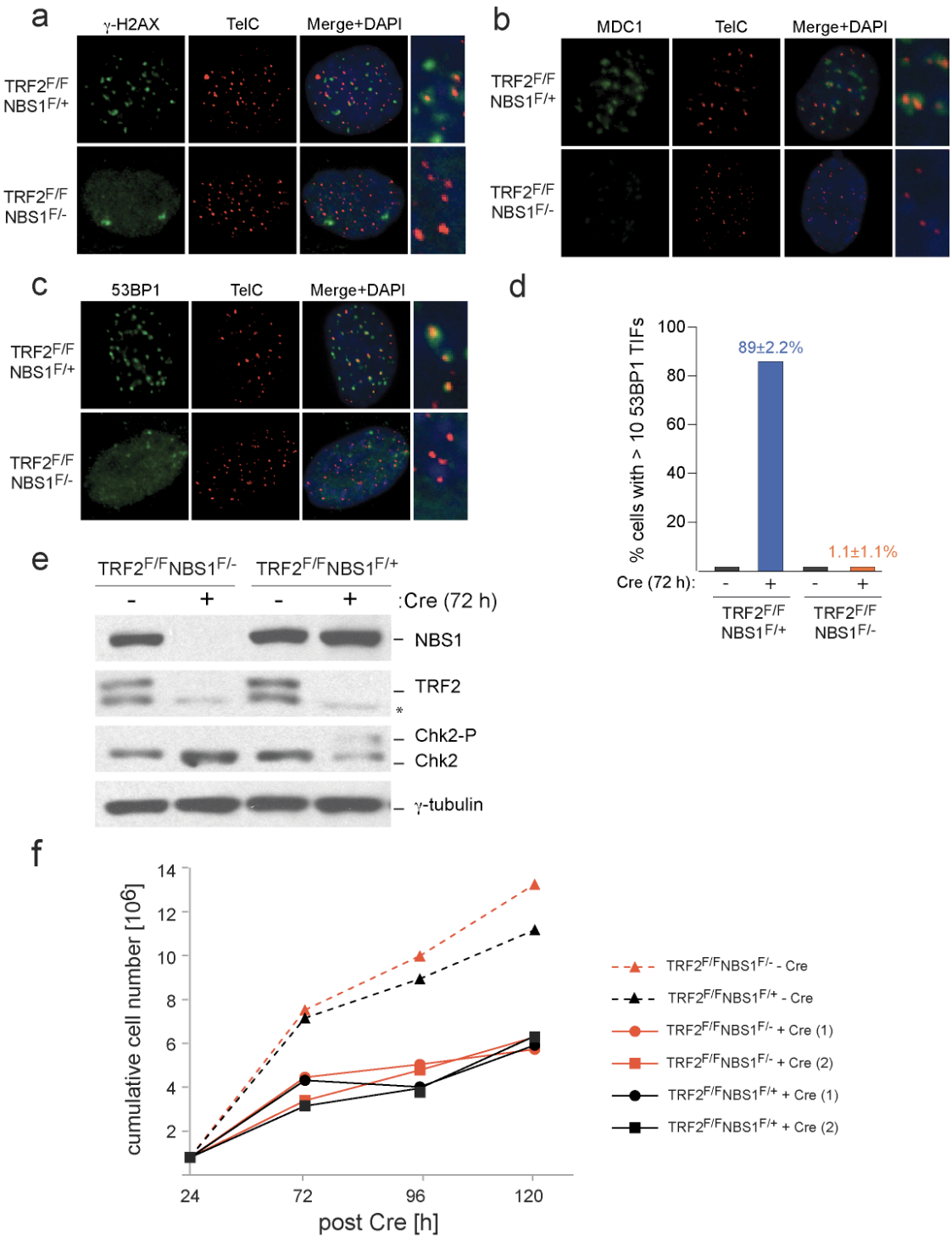

Figure 2.5. Analysis of the contribution of NBS1 to the ATM pathway activated in response to telomere dysfunction

Figure 2.5. Analysis of the contribution of NBS1 to the ATM pathway activated in response to telomere dysfunction

a-d, Representative examples of $TRF2^{F/F}NBS1^{F/-}$ and $TRF2^{F/F}NBS1^{F/+}$, fixed 72 hours post Hit&Run Cre retroviral infections and processed for IF-FISH. IF (in green) was performed with Abs specific to γ-H2AX, mouse MDC1, and 53BP1 (100-304). Telomeric DNA was detected by FISH (in red) with a TTAGGG-repeat specific FISH probe. DNA (in blue) was counterstained with DAPI. Images were merged and enlarged.

d, Bar graph summarizing the average percentage of cells (n≥100), which contained 10 or more 53BP1 IF signals co-localizing with TTAGGG-specific FISH probe. IF-FISH was performed as in **(c)** in $TRF2^{F/F}NBS1^{F/-}$ and $TRF2^{F/F}NBS1^{F/+}$ MEFs, fixed 72 hours post mock or Hit&Run Cre infections. Meand and s.d. from three independent experiments is indicated.

e, Immunoblots of whole cell lysates prepared from $TRF2^{F/F}NBS1^{F/-}$ and $TRF2^{F/F}NBS1^{F/+}$ MEFs harvested 72 hours post mock or Hit&Run Cre infections. Blots were probed with Abs raised against mouse NBS1 (93'6), mouse TRF2 (1254), Chk2, and γ- tubulin (clone GTU; as loading control).

f, Total cell numbers of $TRF2^{F/F}NBS1^{F/-}$ and $TRF2^{F/F}NBS1^{F/+}$ MEFs, plated at 24 hours post mock or 2 independent Hit&Run Cre retroviral infections and counted at 72, 96, and 120 hours post Cre.

NBS1 promotes NHEJ of dysfunctional telomeres

Previous data have indicated that ATM is required for NHEJ of TRF2-depleted dysfunctional telomeres [228]. Since our results demonstrate that NBS1 is in turn necessary for ATM activation, we asked whether NBS1 is also an essential component of the NHEJ process at dysfunctional telomeres. For these experiments, we scored and compared the number of fusions per chromosome end detected in metaphase spreads from $TRF2^{F/F}$ $NBS1^{F/-}$ and $TRF2^{F/F}$ $NBS1^{F+}$ MEFs in the presence or absence of Cre (Figure 2.6a, b). Indeed, whereas control MEFs displayed the expected frequency of fusion events after Cre treatment, in $TRF2^{F/F}NBS1^{F/-}$ cells, there were hardly any fusions at 96 hours post Cre, and at the late, 120-hour time-point we observed a 5-fold reduction in the frequency of fused chromosome ends (Figure 2.6a-c). At the same time growth rates were comparable when TRF2 was deleted in the presence or absence of NBS1 (Figure 2.5f). Therefore, in NBS1-deficient cells, telomere fusions occurred inefficiently and with delayed kinetics compared to control cells and this was not due to an obvious change in cell cycle progression.

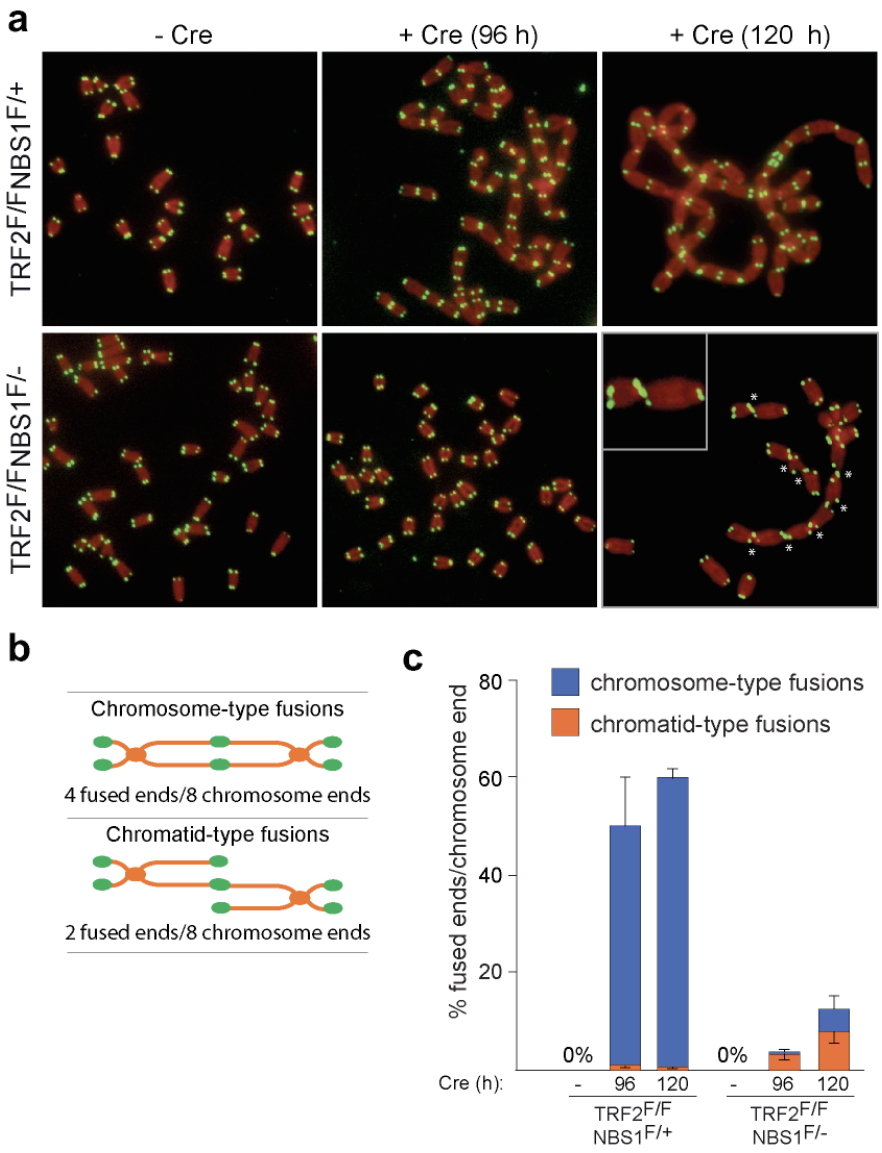

Figure 2.6. Effect of NBS1 deficiency on NHEJ of dysfunctional telomeres

a, Examples of metaphase spreads of TRF2$^{F/F}$NBS1$^{F/-}$and TRF2$^{F/F}$NBS1$^{F/+}$MEFs collected 96 or 120 hours after mock or Hit&Run Cre infections, and processed for telomere-specific FISH with FITC-OO-(AATCCC)$_3$ probe (green). DNA was stained with DAPI (red).

b, Schematic description of the method used to determine the frequency of fused ends in metaphase spreads containing chromosome-type, chromatid-type, and sister telomere fusion events.

c, Bar graph informing on the percentage of chromosome- and chromatid-type fusions detected per chromosome end in metaphases prepared as in **(a)** in the indicated cell lines and scored as in **(b).** Error bars represent s.d. from three independent experiments.

Occurrence of chromatid-type fusions in the absence of TRF2 and NBS1

We noted, however, that in Cre-treated TRF2$^{F/F}$NBS1$^{F/-}$ cells, the type of fusions differed from the type of fusions normally observed as a consequence of TRF2 loss. The repair of TRF2-depleted telomeres takes place mostly in G1, leading to chromosome-type fusions in metaphase spreads that had occurred prior to replication. In accordance, we found that more than 90% of the NHEJ events detected in metaphase spreads of control cells were chromosome-type fusions (Figure 2.6a, c). In contrast, 60-80% of the fusion events scored in TRF2$^{F/F}$NBS1$^{F/-}$ cells at 96 and 120 hours post Cre were chromatid-type, indicative of post-replicative repair that had occurred in S/G2 (Figure 2.6a, c). Although we detected a low frequency of chromosome-type fusions in this setting (Figure 2.6c), we argue that these fusions most likely did not arise as a consequence of G1 telomere fusion events but represent chromatid-type fusions that have undergone an additional round of replication prior to harvesting. In particular, short arm fusions of mouse chromosomes are known to segregate stably during mitosis.

These data argue that NBS1 is in fact an essential component of the NHEJ pathway in G1. In addition, the increased incidence of chromatid-type fusions only when both TRF2 and NBS1 were absent suggests a novel redundant function for TRF2 and NBS1 in the protection of telomeres after replication.

MRN deficiency does not affect overhang loss upon TRF2 deletion

We next asked whether NBS1 deficiency affected the removal of the telomeric 3' overhang, a step that, as mentioned previously, occurs simultaneously with the joining of dysfunctional telomeres. Over time, we observed a decrease of the overhang signal in

NBS1-deficient cells upon TRF2 deletion, but it occurred with a delay compared to NBS1-proficient cells (Figure 2.7a, b). This is consistent with previous data in Ku70- and DNA ligase IV-deficient cells, where a strict coupling between overhang removal and fusion of dysfunctional telomeres has been documented [190,236]. In addition, the appearance of high molecular weight signals on the denatured gel, which are indicative of end-to-end telomere fusions following TRF2 deletion, was reduced but not abolished in the absence of NBS1 (Figure 2.7a). Most likely, these are consequent to the post-replicative fusion events that occur in TRF2- and NBS1-deficient cells.

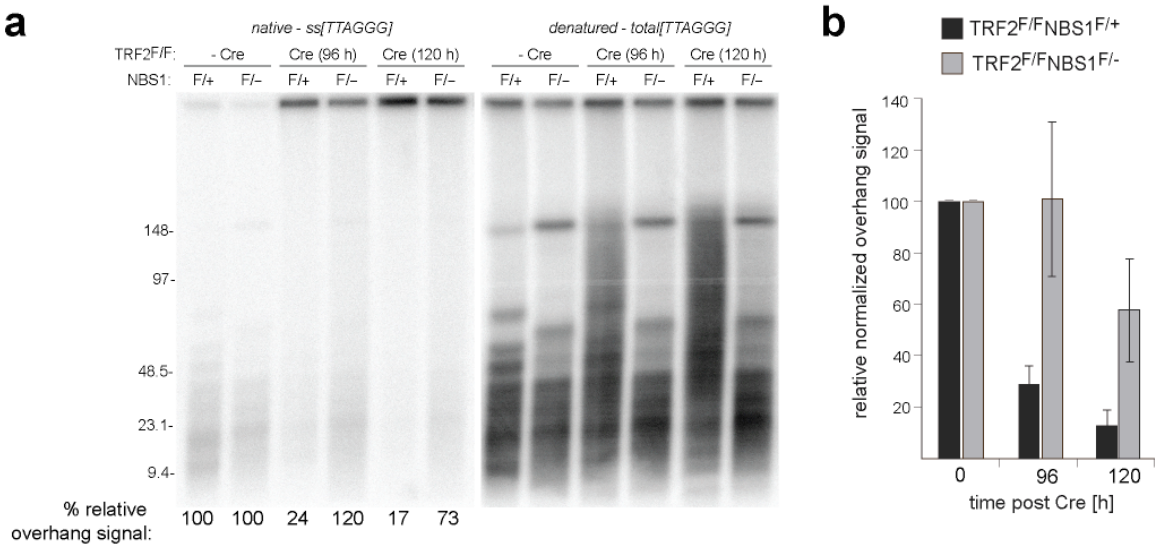

Figure 2.7. Effect of NBS1 deficiency on the rate of overhang loss induced by TRF2 deletion
a, In-gel detection of telomeric DNA from $TRF2^{F/F}NBS1^{F/-}$ and $TRF2^{F/F}NBS1^{F/+}$MEFs collected at 96 or 120 hours after mock or Hit&Run Cre infections. DNA in agarose plugs was separated on agarose gel by pulse-field gel electophoresis and hybridized in-gel to a radioactively labeled $(CCCTAA)_4$ probe (*native*). The DNA was denatured *in situ* and rehybridized to the same probe (*denatured*). In each lane, the ssTTAGGG signal quantified under native condition was normalized to the total TTAGGG signal, detected after denaturation. The relative overhang signal

represents the overhang signal in Cre-treated cells (in red), compared to control, mock-treated cells (set at 100%, in black) for each cell line.
b, Quantification of the results in 5 indepenent experiments. Error bars indicate s.d. from the average.

TRF2-DN allele revisited

Chromatid-type telomere fusions have previously been described in human cells as a prominent outcome of telomere dysfunction, induced by the overexpression of TRF2-DN. As described in the introduction, this allele, which lacks the DNA binding domain, acts by binding to endogenous TRF2 and sequestering it away from chromosome ends. However, since TRF2-DN retains the interaction with the MRN complex, overexpression of this dominant-negative allele also prevents the association of MRN with chromosome ends[200]. Therefore, the chromatid-type fusions, incurred by TRF2-DN overexpression, are likely due to the combined absence of both TRF2 and MRN from telomeres, similarly to the situation described in this study.

Consistently, in a previous experiment, downregulation of Mre11 and NBS1 by shRNA in human cells (Figure 2.8a), treated with control β-gal or TRF2-DN adenovirus to induce telomere dysfunction, did not affect the frequency of fusions (Figure 2.8b, c). This negative result stands in contrast to the data obtained from Cre-expressing NBS1- and TRF2-conditional knockout MEFs, but can be explained through a double-dominant effect of TRF2-DN on TRF2 and the MRN complex.

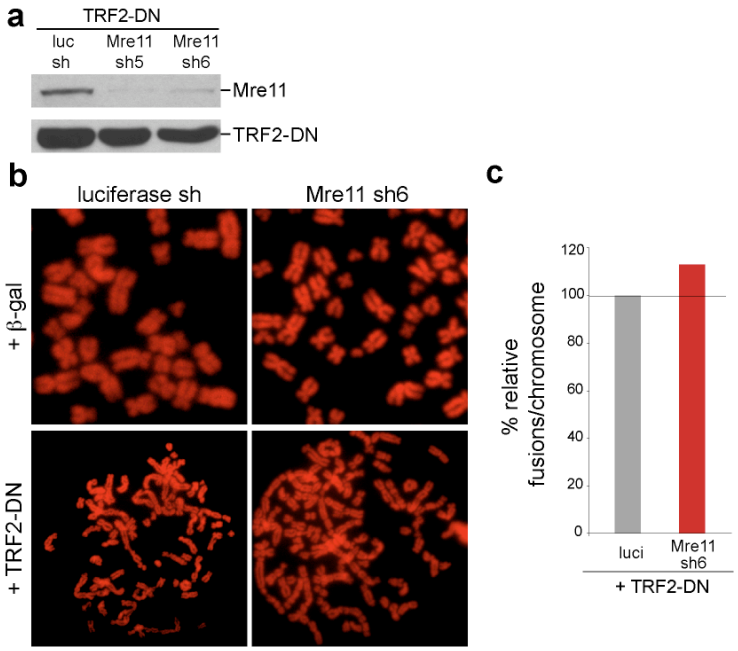

Figure 2.8. Effect of Mre11/NBS1 downregulation by shRNA on NHEJ of dysfunctional telomeres

a, Immunoblots performed with Abs raised against human Mre11 (874) and anti-myc (9E10) with whole cell lysates prepared from HeLa1.3 cells, expressing control luciferase or Mre11-specific shRNAs, sh5 or sh6, from pSuperior retroviral expression vector, harvested 48 hours post-infection with adenovirus expressing myc-tagged TRF2 dominant negative allele (TRF2-DN).

b, Representative metaphase spreads stained with DAPI (red) of HeLa1.3 cells expressing luciferase or Mre11-specific shRNA, sh6, fixed 48 hours post β-gal or TRF2-DN adenoviral infection.

c, Bar graph presenting the relative number of fusions per chromosome end scored in metaphase spreads prepared as in **(b)**.

Summary of findings in Chapter 2

In this chapter we dissected the function of the MRN complex at natural as well as at deprotected chromosome ends. We were unable to prove our hypothesis that a direct contact exists between the TRFH domain of TRF2 and the Y-x-L-S-P motif in NBS1. However, we found some evidence that NBS1 might be redundantly involved in the regulation of the nuclease(s) that aberrantly resects telomeric DNA in the absence of POT1b function.

Whether or not the MRN complex is the only sensor in the ATM pathway has been an open question, despite mounting evidence in support of this model [248]. To test this hypothesis, we examined the contribution of NBS1 in the response to TRF2 loss which activates exclusively the ATM kinase [228]. When we examined the response to telomere dysfunction in TRF2-deficient cells that also lacked NBS1, we observed that chromosome ends were no longer recognized as sites of DNA damage. H2AX at telomeric chromatin was not phosphorylated and TIFs did not form. Additionally, Chk2 phosphorylation, as read-out for the activation of checkpoint signaling, did not occur. These findings indicate that NBS1, and hence a functional MRN complex, is required to activate the ATM pathway. Our conclusions have been confirmed in a recent report [54], which examined the role of Mre11 in the response to telomere dysfunction induced by the overexpression of a dominant negative allele of TPP1. TPP1 ΔRD causes activation of the ATM pathway by an unknown mechanism. The report revealed that in cells lacking Mre11, expression of TPP1 ΔRD does not lead to ATM autophosphorylation and does not induce TIF formation, establishing that the MRN complex is required to activate ATM in this setting. Together, our data and the report by Buis et al. provide

uncontestable evidence in support of the long-standing hypothesis that the MRN complex is the only sensor of DSBs that can activate ATM kinase.

In addition, we showed that in the absence of NBS1, dysfunctional telomeres are not repaired in G1, indicating an essential requirement for the MRN complex in G1 NHEJ. We also found compelling evidence that TRF2 and the MRN/ATM pathway act in concert to protect telomeres from NHEJ after replication. We observed that combined deficiency in TRF2 and MRN gives rise to a novel type of post-replicative telomere fusions at approximately 10% of chromosome ends that were not detected as a consequence of TRF2 or NBS1 deletion alone. Based on these findings, we speculated that simultaneous loss of TRF2 and the MRN/ATM pathway causes the specific deprotection of telomeres after replication.

To reconcile the data that only combined loss of TRF2 and MRN uncovers a defect at post-replicative chromosome ends, we argue that telomere protection after replication is enacted through two redundant pathways, one directly dependent on TRF2 and one mediated through the MRN/ATM pathway. We envision that the function of MRN/ATM can be carried out at functional telomeres, possibly under the control of TRF2, which can recruit both MRN and ATM to chromosome ends. The MRN/ATM pathway, however, can also execute this role at dysfunctional telomeres in TRF2-depleted cells. In this case, the MRN complex senses the presence of telomere damage and locally activates the ATM kinase. Further studies are necessary to dissect the mechanism of how TRF2 and the MRN complex protect telomeres after replication.

CHAPTER 3: THE CONTRIBUTION OF γ-H2AX/MDC1 TO NHEJ OF DYSFUNCTIONAL TELOMERES

Introduction

In the previous chapter we uncovered important roles for the MRN complex in activating the response to telomere dysfunction and in regulating the cell-cycle specificity of NHEJ. Here, we investigate the role of another DNA damage response factor, MDC1, at functional and dysfunctional telomeres. We show that MDC1 localizes to telomeres only in response to telomere dysfunction. Using RNAi to knock down MDC1 protein levels, we dissect the role of MDC1 in the DNA damage response pathway at deprotected telomeres and explore its contribution to NHEJ. At the end of the chapter, we confirm our findings in a genetic setting.

MDC1 is not detectable at functional telomeres

MDC1 interacts with NBS1 and is required for the stable accumulation of the MRN complex at DSBs [69-73]. In view of that model and given that the molecular basis of the TRF2-MRN interaction is not known, we asked whether MDC1 is involved in the association of MRN with functional telomeres.

Previous reports have demonstrated a weak but reproducible association of the MRN complex with functional telomeres, which can be detected by IP [200] and ChIP [249] analysis. Although we could reproduce those data in our study, we found no evidence for MDC1 at chromosome ends. For instance, we analyzed the recovery of telomeric DNA in ChIP of nuclei prepared from immortalized human fibroblasts (BJ-hTERT) expressing

vector or FLAG-tagged MDC1 (Figure 3.1a). Although we could detect the expected fractions of shelterin components and Mre11 associated with telomeric DNA, ChIP with anti-FLAG antibody did not lead to significant recovery of telomeric DNA (Figure 3.1b). Furthermore, endogenous MDC1 was not recovered in TRF2 immunoprecipitate in transformed human cells (HeLa1.2.11), whereas the TRF2 interacting partner, Rap1, was immunoprecipitated efficiently. Similar results were obtained in co-IP experiments with 293T cells where transiently overexpressed FLAG-MDC1 was not recovered in anti-myc immunoprecipitates of transiently transfected myc-tagged TRF1, TRF2 or Rap1 (Figure 3.1d). In addition, we did not observe co-localization of MDC1 with the shelterin components TRF1 or TRF2 by IF analysis of either in primary (IMR90 and BJ) and transformed (HeLa1.2.11) human cells (Figure 3.2a) or in MEFs (Figure 3.2b). For each cell line, we examined more than 100 cells to exclude the possibility that MDC1, analogous to its interacting partner NBS1, transiently associates with telomeres in S phase. Importantly, downregulation of MDC1 with RNAi (Figure 3.1e) did not affect the interaction of MRN with TRF2 as evidenced by equal levels of endogenous TRF2 present in Mre11 immunoprecipitates in HeLa1.2.11 cells expressing control luciferase- or MDC1-specific siRNA.

These data strongly argue that MDC1 is not localized at functional telomeres, does not interact with telomeric proteins, and is not required for the recruitment of the MRN complex to functional telomeres. Although our initial hypothesis that MDC1 facilitates the recruitment of MRN complex to functional telomeres was not substantiated, our data are consistent with the established role of shelterin to actively

suppress the DNA damage response at natural chromosome ends and to prevent the accumulation of DNA damage factors, such as γ-H2AX and MDC1, at telomeres.

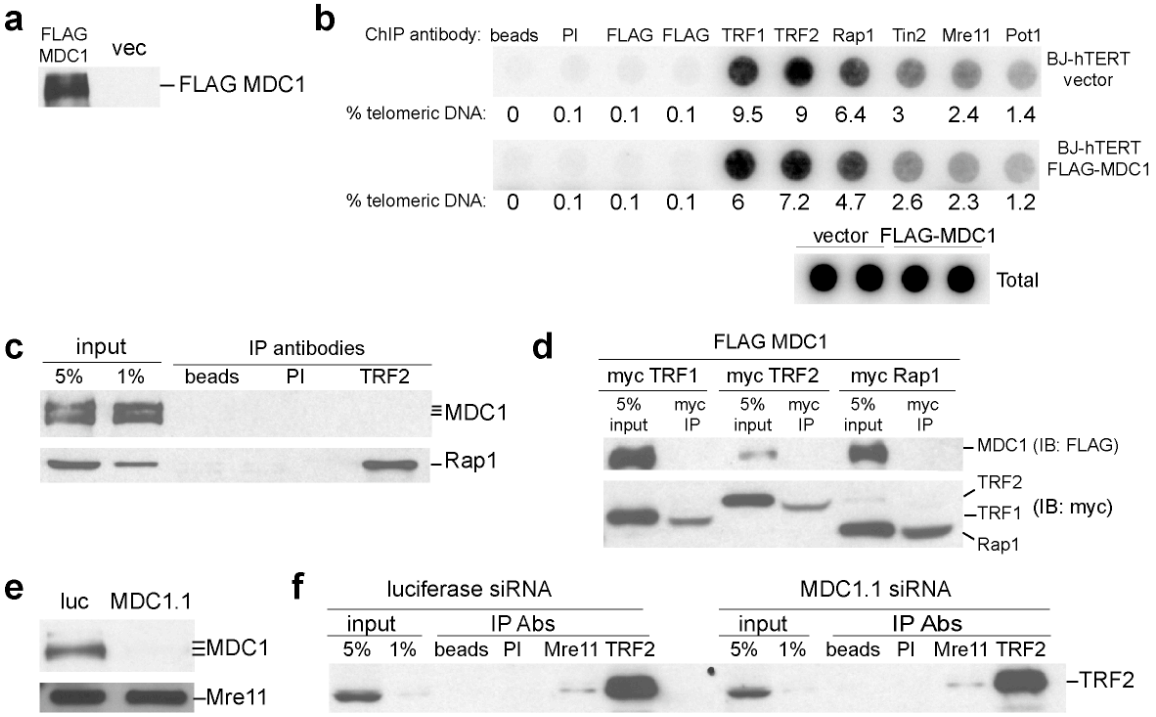

Figure 3.1. MDC1 is not at functional telomeres and is not required for the recruitment of Mre11 to TRF2 complex at telomeres

a, Immunoblot of whole cell lysates from BJ-hTERT cells with or without pLPC-puro-FLAG-MDC1 introduced by retroviral infections. Blot was probed with anti-FLAG (M2) Ab.

b, Dot blot of telomeric DNA ChIP of nuclei prepared from cells described in **(a)**. The following crude sera were used for ChIP: pre-immune, FLAG (M2), TRF1 (371), TRF2 (647), Rap1 (765), Tin2 (864), Mre11 (874), and Pot1 (1048). Telomeric DNA was detected by hybridization to a TTAGGG repeat-specific, radioactively labeled probe. 25% input labeled as Total. % telomeric DNA for each IP was calculated based on the signal relative to the corresponding total DNA

c, Immunoblots of IPs from HeLa1.2.11 nuclear extracts incubated with beads, pre-immune serum, or human TRF2-specific mouse Ab. Blots were probed with Abs specific to human MDC1 and human Rap1 (765). 1 and 5% input of cell extract loaded as indicated.

d, Immunoblots of myc co-IPs from 293T cells transiently transfected with FLAG-MDC1 and myc-tagged TRF1, TRF2, or Rap1. Blots were probed with FLAG (M2) and myc (9E10) Abs. 5% input loaded in indicated lanes.

e, Immunoblots of whole cell lysates from HeLa1.2.11 cells transfected with luciferase- or MDC1-specific siRNA and probed with Abs specific to human MDC1 and human Mre11 (as loading control).
f, Immunoblot detected with human TRF2-specific mouse Ab of IPs from cells described in **(e)**. IPs were performed in the presence of beads only, pre-immune serum, or rabbit Abs specific to human Mre11 (874) or human TRF2 (647). 1 and 5% input loaded in indicated lanes.

MDC1 localizes to dysfunctional telomeres

Whereas MDC1 was not observed at functional telomeres, it accumulated at chromosome ends when telomere function was compromised by the adenoviral introduction of TRF2-DN, a dominant negative allele of TRF2 that inhibits the endogenous protein in human cells. Upon TRF2-DN overexpression, MDC1 formed large foci that co-localized with telomeres detected with the telomere marker TRF1, which remains associated at telomeres upon TRF2-DN overexpression [230] (Figure 3.2a). Similarly, MDC1 formed TIFs in $TRF2^{F/-}lig4^{-/-}p53^{-/-}$ MEFs upon Cre-mediated deletion of TRF2. We used lig4-deficient cells for this analysis, because in the absence of DNA ligase IV-mediated repair of deprotected telomeres, TIFs persist longer [190,250]. Furthermore, the cells lacked a functional p53 pathway, abrogating their ability to arrest at G1/S after telomere deprotection [232]. Upon deletion of TRF2 from such $TRF2^{F/-}lig4^{-/-}p53^{-/-}$ cells, MDC1 formed TIFs that co-localized with telomeres detected with a FISH probe and coincided with 53BP1 foci detected by IF (Figure 3.2b). Thus, MDC1 localizes to telomeres that are dysfunctional as a consequence of TRF2 loss.

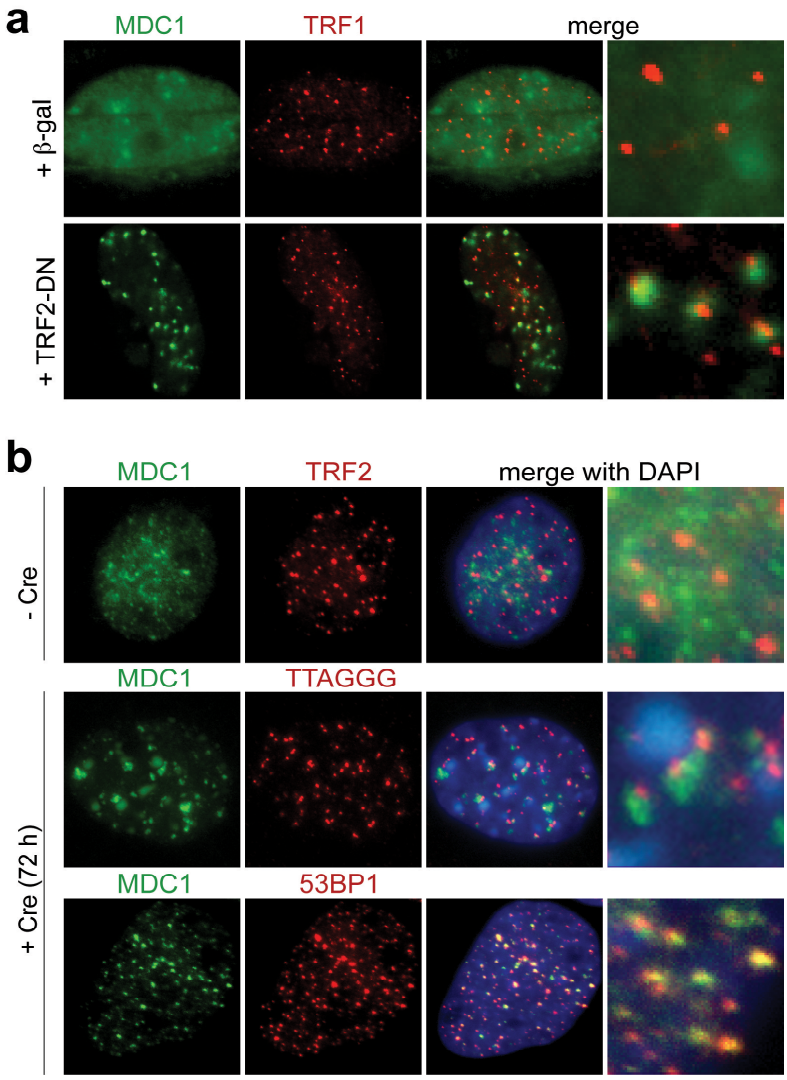

Figure 3.2. Nuclear localization of MDC1 in cells with functional and dysfunctional telomeres

a, Examples of HeLa1.2.11 cells, infected with control β-gal or TRF2-DN adenovirus for 48 hours, and processed for IF with a rabbit Ab specific to human MDC1 (ab11169) (green) and a mouse Ab specific to human TRF1 (red). Images were merged and enlarged.

b, Representative images of $TRF2^{F/-}lig4^{-/-}p53^{-/-}$ MEFs, untreated or treated for 72 hours with retroviral Hit&Run Cre recombinase and processed for IF or IF-FISH. IF was performed with a mouse Ab raised against mouse MDC1 (green) co-stained with mouse TRF2-specific rabbit Ab (1254) (red) or with 53BP1-specific rabbit Ab (100-304) (red). IF-FISH was performed with mouse Ab raised against mouse MDC1 (green). Telomeric DNA was detected by FISH (red) with a TTAGGG-specific FISH probe. DNA (blue) was counterstained with DAPI. Images were merged and enlarged.

Efficient downregulation of MDC1 by RNAi

To examine the role of MDC1 in the telomere damage response, we targeted mouse MDC1 with shRNAs expressed from pSuperior retroviral expression vector. IF indicated a significant reduction in mouse MDC1 protein levels after treatment with two independent shRNAs, sh4 and sh5 (Figure 3.3a) and RT-PCR indicated a 75-90% decrease in MDC1 mRNA levels (Figure 3.3b). We also designed 3 independent shRNAs specific to human MDC1, sh1, sh2 and sh3, which efficiently downregulated human MDC1 protein levels in primary and transformed human cells (Figures 3.5a, 3.10b, and 3.11a).

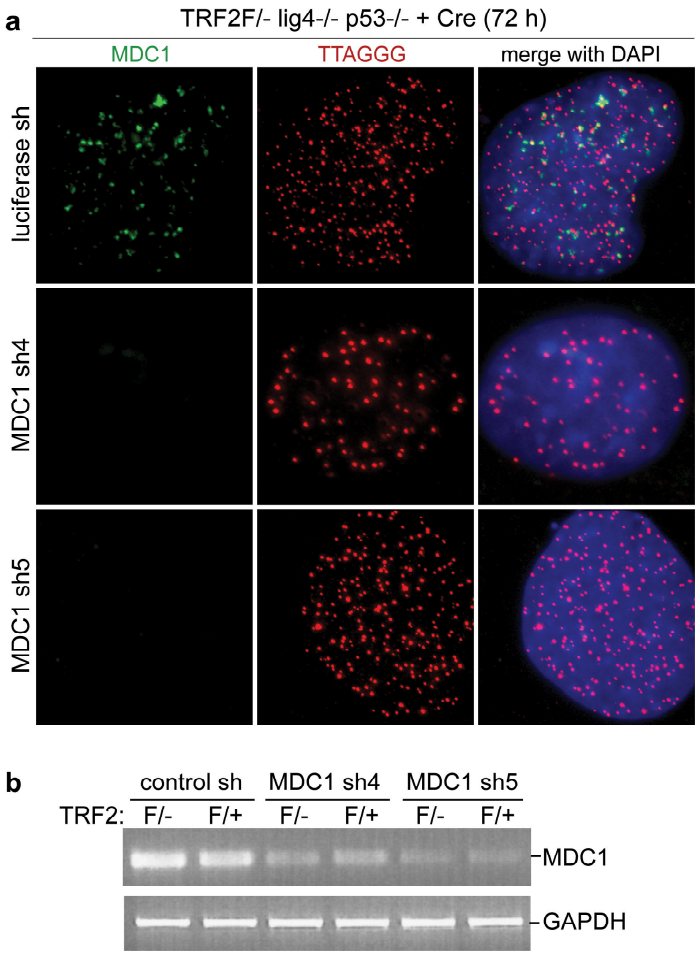

Figure 3.3. RNAi mediated inhibition of mouse MDC1

a, IF for MDC1 in TRF2$^{F/-}$lig4$^{-/-}$p53$^{-/-}$ MEFs, infected with pSuperior retroviral construct expressing luciferase- or two mouse MDC1-specific shRNAs, sh4 or sh5, and treated with Hit&Run Cre for 72 hours to induce telomere dysfunction. IF was performed with anti-mouse MDC1 Ab (green) co-stained with a TTAGGG-specific FISH probe (red). DNA was counterstained with DAPI (blue). Images were merged.

b, RT-PCR monitoring mouse MDC1 mRNA levels in TRF2$^{F/-}$p53$^{-/-}$ and TRF2$^{F/+}$p53$^{-/-}$ MEFs treated with luciferease- or two mouse MDC1-specific shRNAs, sh4 or sh5. GAPDH-specific RT-PCR was used as control. RT-PCR products were detected by ethidium bromide staining after agarose gel-electropheresis.

MDC1 downregulation affects TIF formation

We used these shRNAs to address the role of MDC1 in the response to telomere dysfunction. As expected from its role in promoting the persistence of DNA damage factors in IRIFs, [118], MDC1 also played a central role in TIF formation. Knockdown of mouse MDC1 abrogated the recruitment of 53BP1 and ATM-S1981-P to dysfunctional mouse telomeres in Cre-treated $TRF2^{F/-}lig4^{-/-}p53^{-/-}$ MEFs. While in 40% of cells, expressing luciferase shRNA and Cre recombinase, 53BP1 and ATM-S1981-P localized to deprotected telomeres and formed bright foci, in MDC1 shRNA-treated Cre-expressing cells, the staining of both factors remained diffuse and homogenous (Figure 3.4a, b). Quantification of the frequency of cells with more than five 53BP1 or ATM-S1981-P foci at dysfunctional telomeres indicated that MDC1 knockdown reduced the TIF response to background levels (Figure 3.4d).

TIF formation by γ-H2AX, on the other hand, was affected to a lesser extent by MDC1 knockdown (Figure 3.4c). Reliable scoring of γ-H2AX TIFs is complicated by the presence of multiple γ-H2AX foci in S-phase. Fortuitous overlap of these foci with telomeres gives rise to a high background in control samples (~10% of –Cre cells contain more than 5 telomeric γ-H2AX foci (Figure 3.4d)). In luciferase-treated $TRF2^{F/-}lig4^{-/-}p53^{-/-}$ MEFs, fixed 72 hours after Cre infections, we observed 5 or more γ-H2AX TIFs in 60% of the cells. Cells treated with MDC1 sh4 showed a partial reduction (from ~60% to ~40%) in the fraction of cells that were γ-H2AX TIF positive, whereas downregulation of MDC1 with sh5 led to a less significant reduction in the fraction of γ-H2AX TIF positive cells (Figure 3.4d). The relative reduction in γ-H2AX TIF positive cells we observe upon MDC1 downregulation is consistent with a role for MDC1 in signal amplification as

proposed by Jackson and colleagues [118]. On the other hand, the minor reduction is in conflict with evidence obtained from MDC1$^{-/-}$ MEFs, where γ-H2AX IRIF formation is not affected by MDC1 absence [114]. This issue was clarified later in this chapter in a genetic setting.

Therefore, it is parsimonious to assume that the role of MDC1 at dysfunctional telomeres is similar (if not identical) to its function at DSBs.

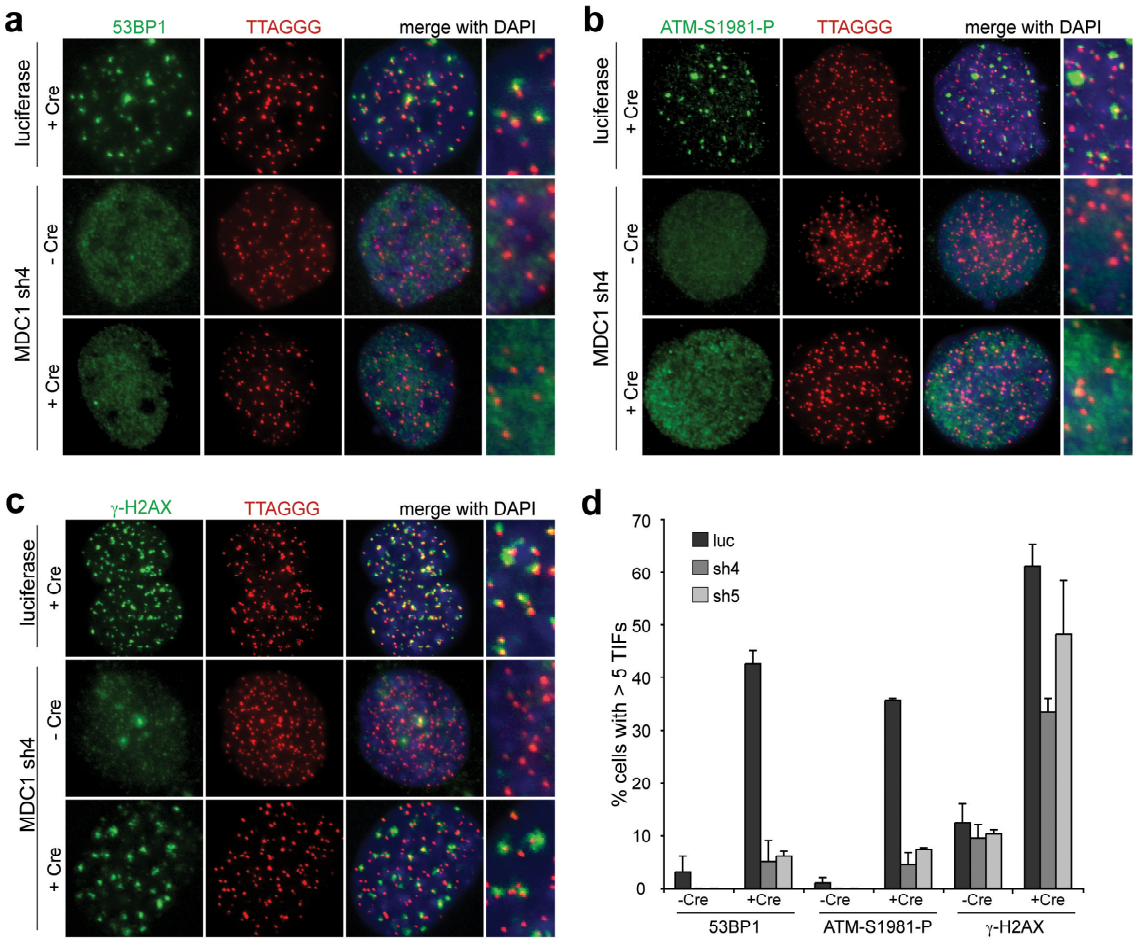

Figure 3.4. Effect of MDC1 RNAi on TIF formation in mouse cells

a-c, Representative fluorescent microscopic images of TRF2$^{F/-}$lig4$^{-/-}$p53$^{-/-}$ MEFs, expressing luciferase- or mouse MDC1-specific shRNA, sh4, fixed 72 hours post mock or Hit&Run Cre retroviral infections and processed for IF-FISH to monitor the effect of MDC1 knockdown on TIF formation in response to deletion of TRF2. FISH (red) with a probe specific to TTAGGG repeats was performed in combination with IF (green) with Abs specific to (**a**) 53BP1(100-304), (**b**) ATM-S1981-P, and (**c**) γ-H2AX. DNA was counterstained with DAPI (blue). Images were merged and enlarged.

d, Quantification of the data shown in **(a-c)**. Bars show the fraction of cells containing 5 or more IF signals for the indicated factors that co-localize with TTAGGG-specific FISH. At least 100 cells were scored in each experiment. Error bars display s.d. derived from three independent experiments.

A similar result was obtained in human cells, in which overexpression of the TRF2-DN allele described above was used to induce telomere deprotection. MDC1 knockdown in these cells (Figure 3.5a) completely abrogated TIF formation by several DNA damage factors we examined. We analyzed by IF-FISH more than 100 cells treated with MDC1 sh1 and observed that upon introduction of TRF2-DN the nuclear staining of 53BP1, ATM-S1981-P, and Nbs1-S343-P remained homogenous, whereas these factors localized to TIFs in luciferase-treated cells (Figure 3.5b, c). In this setting MDC1 knock down by sh1 did not result in a quantitative difference in the fraction of cells containing γ-H2AX TIFs (Figure 3.5b, c). These results reporting on the contribution of human MDC1 to TIF formation are consistent with our analysis on the role of mouse MDC1 described above.

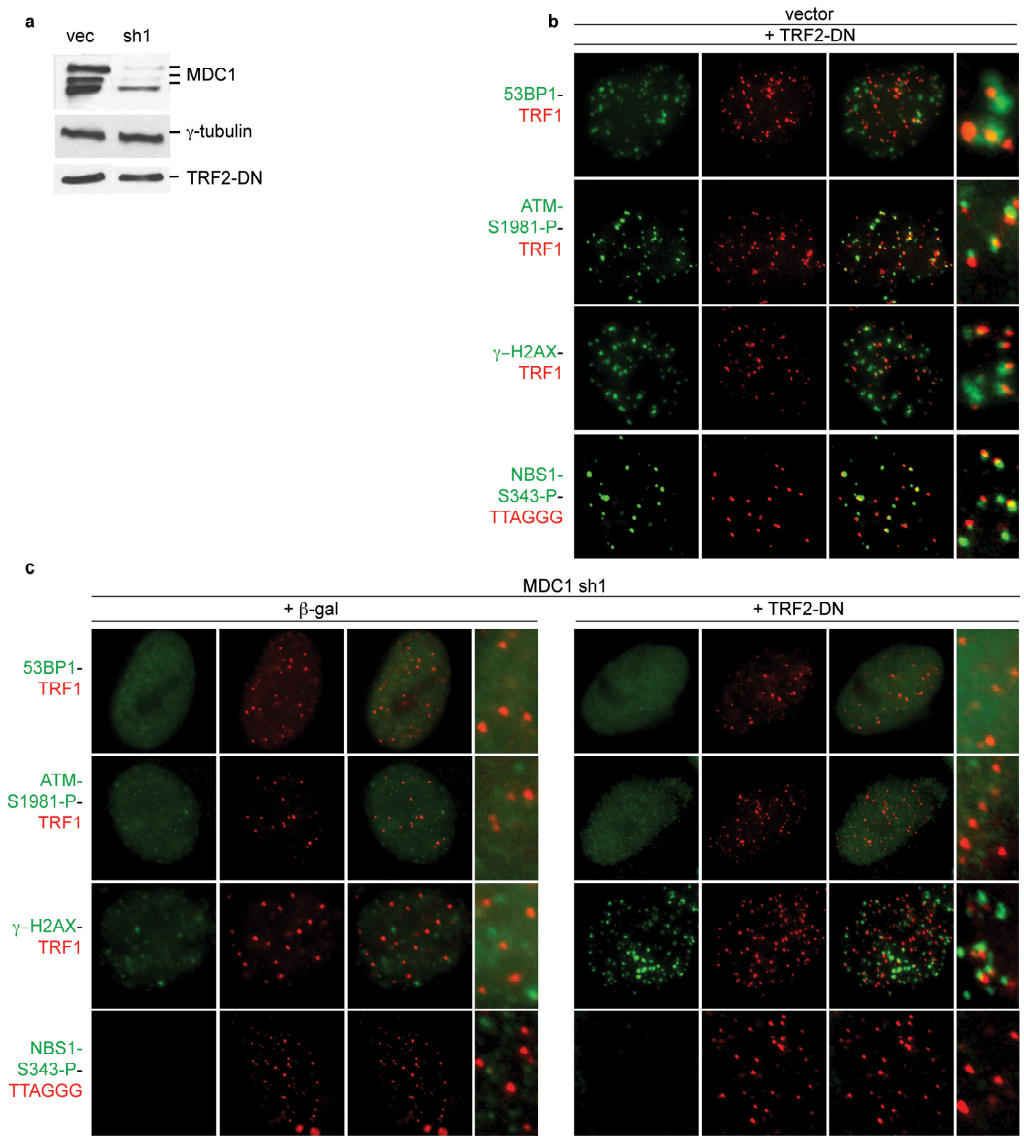

Figure 3.5. Effect of MDC1 RNAi on TIF formation in human cells

a, Immunoblot of whole cell lysates from HeLa1.2.11 cells, expressing empty vector or MDC1-specific shRNA, sh1, from pSuperior retroviral expression vector, harvested 48 hours after adenoviral infection with control β-gal or TRF2-DN to induce telomere dysfunction. Blots were probed with Abs specific to human MDC1, myc (9E10, which reports on the expression levels of myc-tagged TRF2-DN allele), and γ-tubulin (clone GTU, loading control).

b-c, Representative images of cells processed for IF with rabbit Ab raised against human TRF1 (371)(red) co-stained with mouse Abs raised against 53BP1, ATM-S1981-P, γ-H2AX (green), or for IF with rabbit Ab raised against NBS1-S343-P (green) performed in combination with telomere-specific FISH (red). HeLa1.2.11 cells with **(c)** or without **(b)** MDC1 sh1 were infected for 48 hours with control β-gal or TRF2-DN adenovirus. Images were merged and enlarged.

These results were further confirmed through inhibition of MDC1 with a dominant negative allele, MDC1-FHA (MDC1, aa 1-394; see Figure 3.6a for schematic. While MDC1-FHA does not directly associate with sites of DNA damage, previous experiments have shown that its overexpression inhibits MDC1, 53BP1 and MRN complex IRIF formation [107,251]. The N-terminal FHA domain of MDC1 was initially implicated in promoting multiple protein-protein interactions, including an association with itself as well as with the MRN complex. Subsequently, it has been determined that MDC1 interacts with NBS1 in the MRN complex through its S-T-D-rich domain [69-71]. Thus, the FHA domain does not play a role in this association. It is possible that in earlier experiments endogenous MDC1 bridged the recovery of MRN complex from MDC1-FHA-specific immunoprecipitates. The most likely explanation for the dominant negative effect of MDC1-FHA, therefore, seems to be its ability to interact with endogenous protein and to sequester it away from sites of damage.

We asked whether MDC1-FHA acted as a dominant negative allele with respect to TIF formation induced by treatment with the TRF2-DN allele. We overexpressed MDC1-FHA in immortalized human fibroblasts (BJ-hTERT) treated with TRF2-DN and analyzed TIF formation by IF (Figure 3.6b). We observed complete absence of 53BP1 TIFs in more than 100 cells examined, confirming the dominant negative effect of MDC1-FHA.

Next we addressed whether MDC1 functioned downstream of ATM or ATR kinases by testing whether the dominant negative effect of MDC1-FHA at TRF2-depleted telomeres could be observed in cells lacking ATM or functional ATR. We examined primary human ATM-deficient cells (A-T, derived from patient #504405) or

immortalized cells, which are hypomorphic for the ATR kinase (Seckel-hTERT, derived from Seckel syndrome patient, F02-98 [252]). In both cell types, introduction of TRF2-DN allele leads to 53BP1 TIF formation (Figure 3.6b, c and [83]), which was completely prevented by the overexpression of MDC1-FHA (Figure 3.6c, d). In each instance, more that 100 cells were examined by IF. These results demonstrated that TRF2-DN-induced, MDC1-mediated TIF formation was likely promoted by redundant kinase activities. The contribution of MDC1 to ATM, ATR, and, potentially, DNA-PKcs pathways can be explained by the ability of these kinases to phosphorylate H2AX, the recruiter of MDC1 to sites of DNA damage.

The presence of TIFs in A-T cells treated with TRF2-DN suggests that ATR and/or DNA-PKcs are also involved in the response to telomere dysfunction in human fibroblasts. This contrasts the TIF response induced by TRF2 deletion in mouse cells, which is entirely dependent on the ATM kinase. This discrepancy could be explained if the TRF2-DN allele, in addition to removing endogenous TRF2 from telomeres, also sequesters POT1 from chromosome ends. The interacting partner of TRF2, TIN2, binds to TPP1, which in turn binds to and recruits POT1 to telomeres (see Introduction for more detail and references). Therefore, it is possible that overexpressed TRF2-DN, which retains the TIN2 interaction domain, could remove TPP1 and POT1 from telomeres. Depletion of POT1 from telomeres has previously been shown to activate the ATR-dependent DNA damage response pathway [228], providing an explanation for the involvement of ATR in TRF2-DN-induced TIF formation.

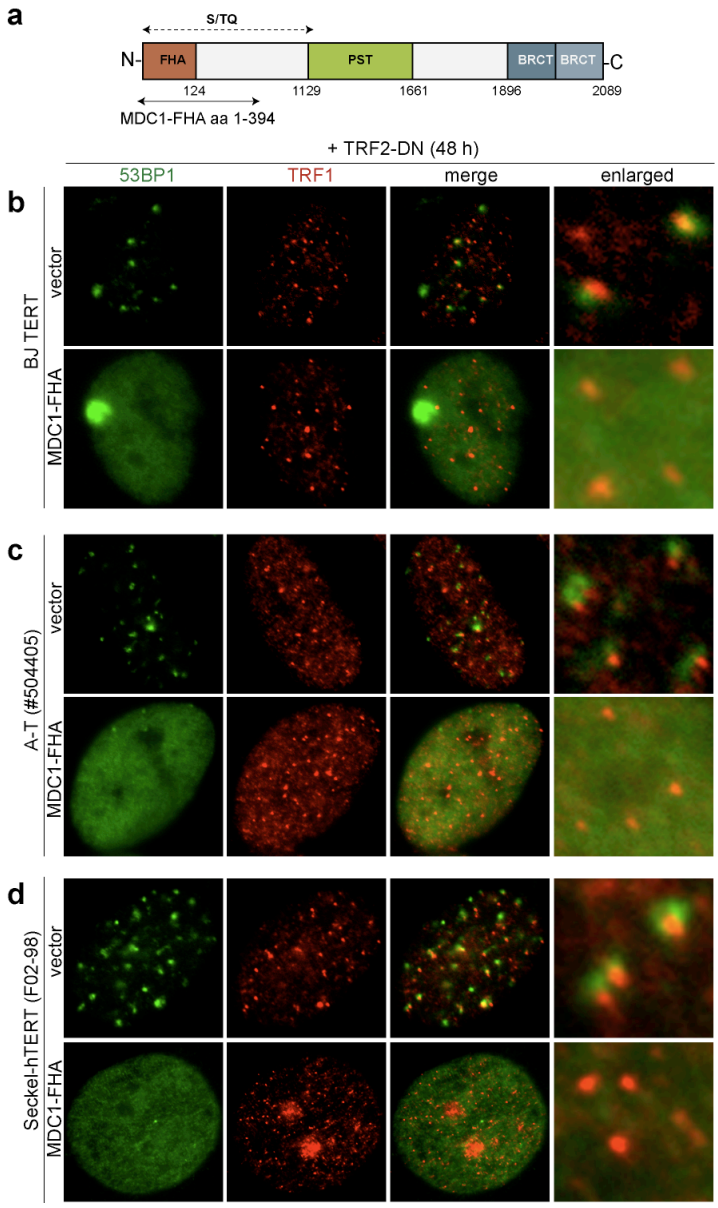

Figure 3.6. Effect of MDC1-FHA on 53BP1 TIF formation in BJ-hTERT, A-T and Seckel-hTERT cells.

a, Schematic representation of the domain structure of MDC1, indicating the location of the MDC1-FHA dominant negative allele.

b-d, Panels present typical images of **(b)** BJ-hTERT, **(c)** A-T (ATM-deficient; #504405), and **(d)** Seckel-hTERT (ATR-hypomorphic; F02-98) cells, with or without MDC1-FHA expressed from pLPC-puro retroviral delivery vector, fixed 48 hours after treatment with TRF2-DN adenovirus to induce telomere dysfunction and processed for IF. IF was performed with mouse Ab raised against human 53BP1 (green) co-stained with rabbit Ab raised against human TRF1 (371). Images were merged and enlarged.

Collectively, these data indicate that MDC1 promotes the formation of foci containing ATM-S1981-P, 53BP1, and Nbs1-S343-P at dysfunctional telomeres as it does at DSBs. In addition, the close parallels between the DNA damage responses at dysfunctional telomeres and at DSBs validate our model system. The similarities further underscore that insights gained from analysis of deprotected telomeres may lead to more detailed understanding of the response to DSBs.

MDC1 and γ-H2AX play an essential role in promoting the physiological pace of NHEJ at dysfunctional telomeres

Since knockdown of MDC1 inhibited the localization of MRN complex at dysfunctional telomeres, we asked whether similarly to NBS1, MDC1 also plays a role in NHEJ. We scored fusions in metaphases of control or MDC1 shRNA-treated $TRF2^{F/-}$ $p53^{-/-}$ MEFs collected at 72 hours after TRF2 deletion (Figure 3.7a). As expected, in control cells we observed 10-15% fusions per deprotected chromosome end, while in cells with lowered MDC1 levels we noted that only a small fraction of the metaphases showed fusions. Quantitative analysis revealed a 4-5 fold decrease in telomere fusions in cells with reduced MDC1 protein levels (Figure 3.7b). The effect of MDC1 inhibition was most prominent at the early timepoints of telomere deprotection (60-72 hours post Cre infection). At later timepoints, most chromosomes fused into long trains both in control and in MDC1 shRNA-treated cells.

Similar results were observed in human HeLa1.3 cells, where MDC1 was downregulated with two MDC1-specific shRNAs. We analyzed metaphase spreads of control or MDC1 shRNA-treated cells at 48 hours after TRF2-DN-induced telomere

dysfunction (Figure 3.7c) and recorded a 3-4 fold decrease in telomere fusion events in cells with reduced levels of MDC1 (Figure 3.7d).

The complimentary results in mouse and human cells established that MDC1 contributes to the NHEJ pathway. However, the appearance of delayed fusions argued against an essential role for MDC1 in NHEJ of dysfunctional telomeres. Instead, MDC1 seemed most likely involved in promoting the efficiency of the repair reaction or in regulating a step in NHEJ.

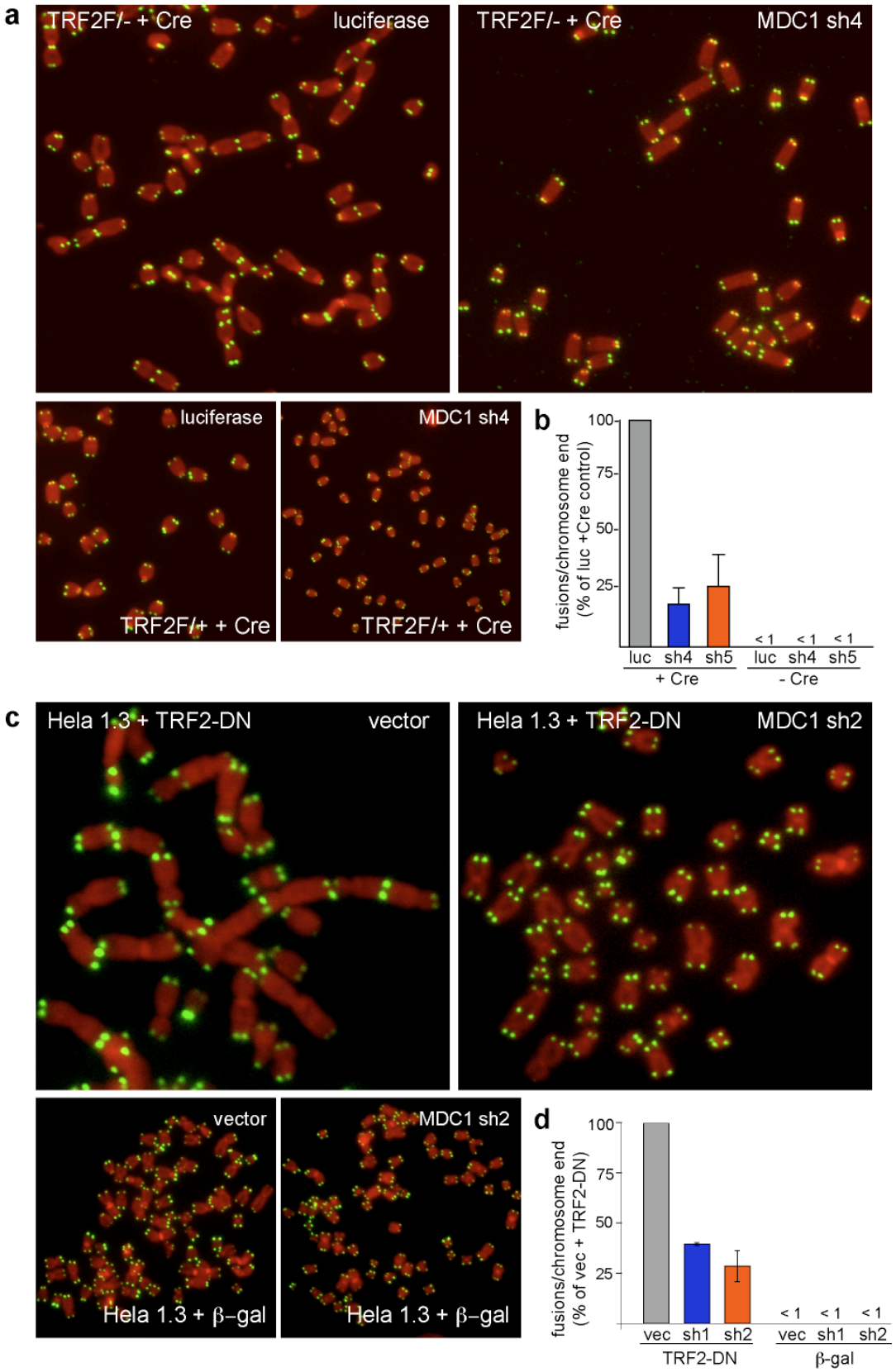

Figure 3.7. MDC1 stimulates NHEJ of dysfunctional telomeres.

Figure 3.7. MDC1 stimulates NHEJ of dysfunctional telomeres.

a, Metaphase spreads of $TRF2^{F/-}p53^{-/-}$ and $TRF2^{F/+}p53^{-/-}$ MEFs expressing luciferase- or mouse MDC1-specific shRNA, sh4, collected 60 hours after Hit&Run Cre infections and processed for telomere-specific FISH with FITC-OO-$(AATCCC)_3$ probe (green). DNA was stained with DAPI (red).

b, Bar graph summarizing the effect of MDC1 knockdown on the relative frequency of fused chromosome ends detected on metaphase spreads of $TRF2^{F/-}p53^{-/-}$ MEFs untreated or 60 hours after Hit&Run Cre infections and processed as in **(a)**.

c, Metaphase spreads of HeLa1.3 cells treated with control or human MDC1-specific shRNA, sh2, delivered from pSuperior retroviral expression vector, harvested 48 hours post-infection with control β-gal or TRF2-DN adenovirus. Telomere-specific FISH was performed as in (**a**)

d, Bar graph presenting the relative frequency of chromosome end fusions in human HeLa1.3 cells, expressing control or 2 human MDC1-specific shRNAs, sh1 and sh2, treated with control β-gal or TRF2-DN adenovirus and processed as in (**c).**

NHEJ-mediated repair of dysfunctional telomeres was also affected when the recruitment of MDC1 to chromatin was blocked by lowering the amount of its binding partner, γ-H2AX, with shRNA to H2AX. This shRNA [109] causes efficient knockdown of H2AX, which we confirmed in human HeLa1.3 cells by Western blotting and IF (Figure 3.8a, b). As expected from γ-H2AX recruiting MDC1, cells with lowered H2AX protein levels did not contain MDC1 foci upon TRF2-DN treatment (Figure 3.8b) and the overall fraction of cells that contained MDC1 foci at dysfunctional telomeres was reduced 4 times (Figure 3.8c). Reduction of H2AX and MDC1 localization at dysfunctional telomeres impacted the rate of NHEJ. At 48 hours post infection with Ad-TRF2-DN, these cells showed a 3-fold reduction in telomere fusion frequencies on metaphase spreads, which is similar to the effect of MDC1 knockdown. These results indicated that γ-H2AX mediated-recruitment of MDC1 to chromatin accelerates the rate by which dysfunctional telomeres are repaired by NHEJ.

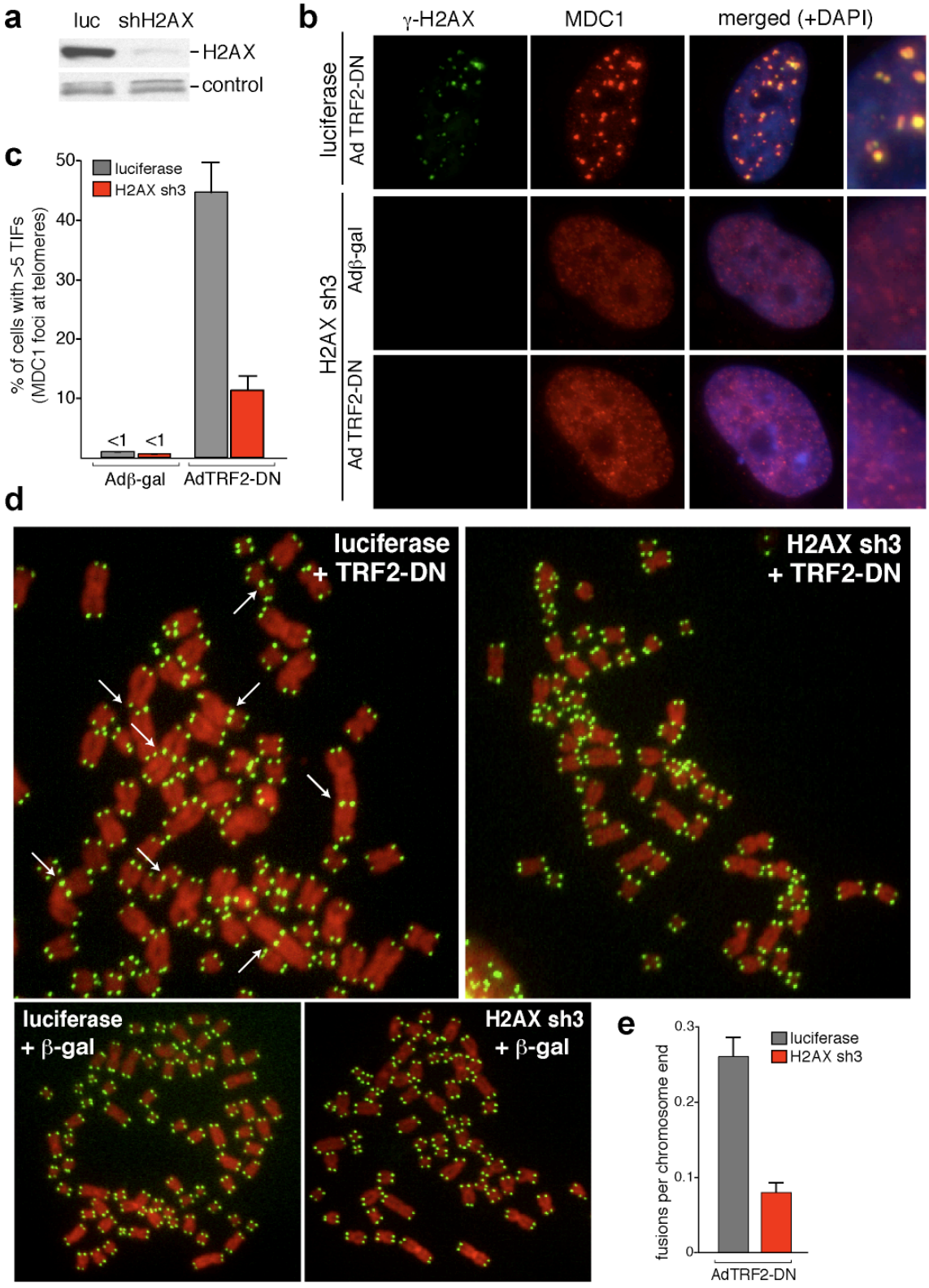

Figure 3.8. Effect of H2AX knockdown on the recruitment of MDC1 to dysfunctional telomeres and on the efficiency of NHEJ of dysfunctional telomeres.

Figure 3.8. Effect of H2AX knockdown on the recruitment of MDC1 to dysfunctional telomeres and on the efficiency of NHEJ of dysfunctional telomeres.

a, Immunoblot of whole cell lysates from HeLa1.3 cells expressing luciferase- or H2AX-specific shRNA, sh3, from pSuperior retroviral delivery vector. Blot was probed with H2AX-specific Ab (ab11175); non-specific bands from the same immunoblot were used as loading control.

b, Representative IF images of HeLa1.3 cells expressing luciferase- or H2AX-specific shRNA, sh3, fixed 48 hours post infection with control β-gal or TRF2-DN adenovirus and processed for IF with a rabbit Ab raised against γ-H2AX (green) co-stained with a mouse Ab raised against mouse MDC1 (red). DNA counterstained with DAPI (blue). Images were merged and enlarged.

c, Bar graph summarizing data from IF-FISH analysis of cell described in **(b)**. IF was performed with a mouse Ab raised against mouse MDC1 in combination with FISH performed with a OO-FITC-$(TTAGGG)_3$ telomere repeat-specific probe. Bars show the fraction of cells (n>100), which contained 5 or more IF signals for MDC1 co-localizing with TTAGGG-specific FISH. Error bars show s.d. derived from triplicate experiments

d, Metaphase spreads of HeLa1.3 cells, stably expressing luciferase- or H2AX-specific sh, sh3,harvested 48 hours post infection with control β-gal or TRF2-DN adenovirus. Telomere-specific FISH was performed with FITC-OO-$(AATCCC)_3$ probe (green). DNA was stained with DAPI (red).

e, Bar graph quantifying the effect of H2AX downregulation on the frequency of telomere fusions on metaphase spreads prepared as in **(d)**. Error bars indicated s.d. derived from 3 independent experiments.

In-gel overhang analysis of control and shRNA-treated cells provided independent support for the role of MDC1 in NHEJ of dysfunctional telomere. Prior data has shown that the 3' overhang of dysfunctional telomers is retained when the NHEJ pathway is blocked by Ku70 or DNA ligase IV deficiency [190,236]. In fact, when TRF2 is deleted from Ku70- or DNA ligase IV-deficient MEFs, the overhang signals increase slightly, presumably due to degradation of the deprotected C-rich telomeric DNA strand. A similar increase in the overhang signal occurred when TRF2 was deleted from $TRF2^{F/-}$ $p53^{-/-}$ MEFs with reduced MDC1 levels (Figure 3.9a, b). This effect was most pronounced at 72 hours after Cre-mediated TRF2 deletion and coincided with the inhibition of NHEJ by MDC1 knockdown. At later time points, 96 and 120 hour post Cre, the overhang signal decreased as expected from the occurrence of fusions at these stages (Figure 3.9a, b). Thus, MDC1 knockdown affected the initial rate of both overhang loss and fusions in mouse cells, as would be expected from the previously reported, tight coupling between NHEJ and overhang processing. We could not address in this experimental system whether MDC1 promoted the overhang processing step or regulated the end-to-end joining reaction.

Further insight on that issue was obtained in human cells. Previous work had shown that in human cells, overhang processing can occur before the actual joining of the telomeres, leading to the detection of telomeres with diminished overhangs that had not (yet) been joined [230]. Thus, in human cells, overhang processing is not strictly coupled to NHEJ as it is in mouse cells. This slight difference in the telomere fusion pathway in human and mouse cells allowed us to ask whether MDC1 affected the overhang processing step itself. Although MDC1 loss clearly delayed telomere fusion in

transformed human cells (Figure 3.7c, d), there was no effect on overhang processing (Figure 3.9c, d). We noted the same reduction in overhang signal (~40%) both in MDC1 knockdown and control cells analyzed 48 hours after introduction of TRF2-DN into HeLa1.3 cells. This result argues against a role for MDC1 in overhang processing per se and suggests that MDC1 promotes NHEJ of dysfunctional telomeres through another step.

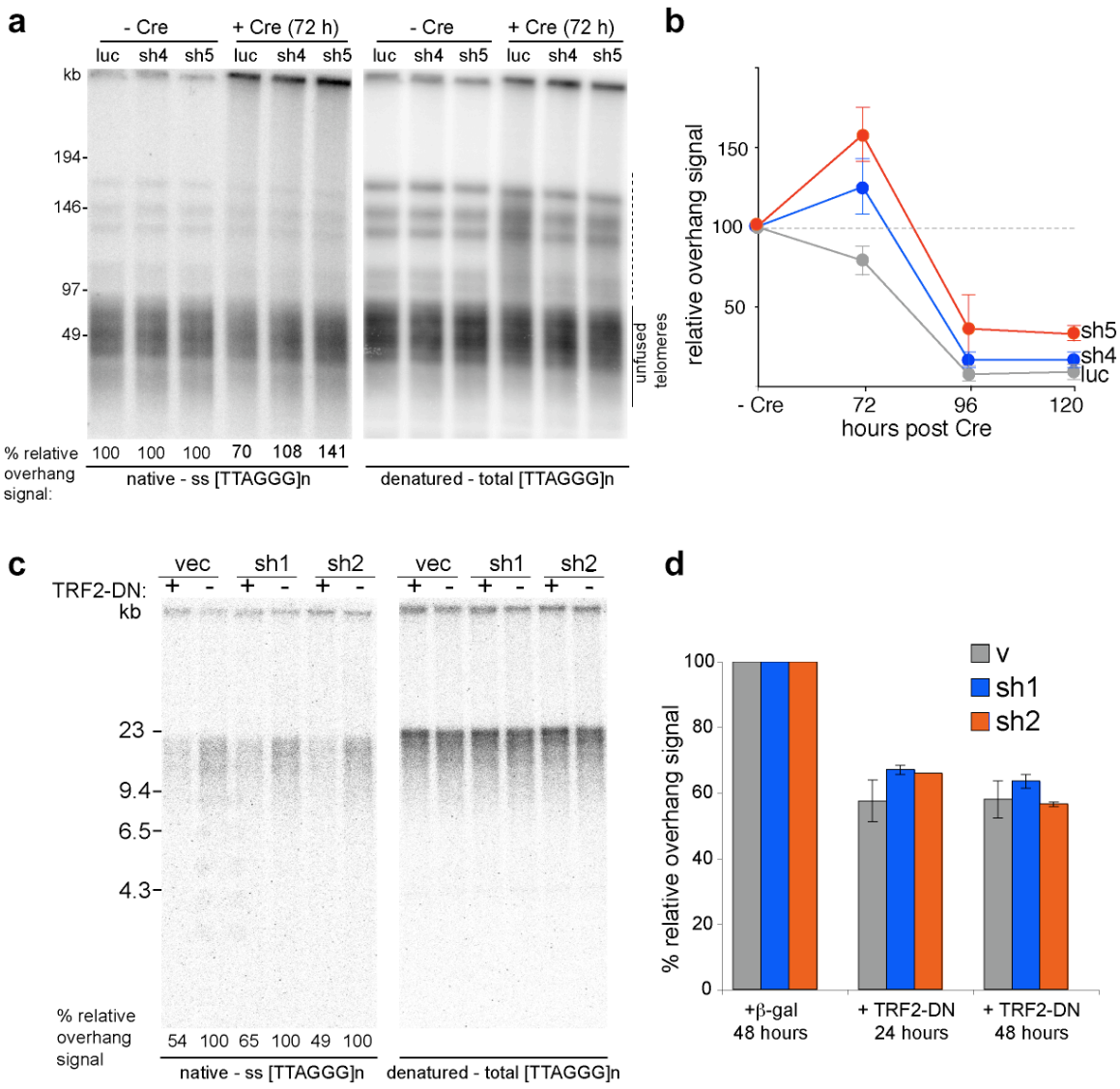

Figure 3.9. Effect of MDC1 knockdown on overhang processing of dysfunctional telomeres in mouse and human cells.

Figure 3.9. Effect of MDC1 knockdown on overhang processing of dysfunctional telomeres in mouse and human cells.

a, In-gel detection of telomeric DNA from $TRF2^{F/-}p53^{-/-}$ MEFs expressing luciferase- or mouse MDC1-specific shRNAs, sh4 or sh5, harvested at 72 hours post mock or Hit&Run Cre retroviral infections. DNA in agarose plugs was separated on agarose gel by pulse-field gel electophoresis and hybridized in-gel to a radioactively labeled $(CCCTAA)_4$ probe (*native*). The DNA was denatured *in situ* and rehybridized to the same probe (*denatured*). In each lane, the ssTTAGGG signal quantified under native condition was normalized to the total TTAGGG signal, detected after denaturation. The relative overhang signal represents the normalized ssTTAGGG signal in Cre-treated cells, compared to mock-treated cells (set at 100%) at each time point for each cell line.

b, Graph showing the effect of MDC1 knock down on overhang processing in cells described in **(a)**, untreated or treated with Hit&Run Cre retrovirus for 72, 96 and 120 hours and processed by in-gel overhang assay as in **(a)**. The relative overhang signal at different time points after Cre infection is calculated as a percentage of the overhang signal in the absence of Cre for each cell line. Error bars indicate the s.d. derived from three independent experiments.

c, In-gel detection of telomeric DNA isolated from HeLa1.3 cells expressing control or human MDC1-specific shRNAs, sh1 or sh2, harvested 48 hours post infection control β-gal or TRF2-DN adenovirus. Telomeric DNA was separated by agarose gel-electophoresis and hybridized in-gel to a radioactively labeled $(CCCTAA)_4$ probe (*native*). The DNA was denatured *in situ* and rehybridized to the same probe (*denatured*). In each lane, the ssTTAGGG signal quantified under native condition was normalized to the total TTAGGG signal, detected after denaturation. The relative overhang signal represents the normalized ssTTAGGG signal in TRF2-DN-treated cells, compared to control β-gal cells (set at 100%) for each cell line.

d, Bar graph quantifying the effect of MDC1 knock down on overhang processing in cells described in **(c)**, treated with control β-gal adenovirus for 48 hours or with TRF2-DN adenovirus for 24 or 48 hours, and processed by in-gel overhang assay as in **(c)**. For each cell line, the relative overhang signal at different time points after TRF2-DN infection is normalized to the overhang signal after control β-gal treatment. Error bars indicate the s.d. derived from triplicate experiments.

MDC1 is not required for checkpoint signaling in response to telomere dysfunction

Several reports have presented conflicting evidence as to whether or not MDC1 is required for checkpoint activation in response to DSBs induced by γ-irradiation. The current model, which reconciles these contradictory data, suggests that MDC1 is preferentially required to amplify the signal in response to low doses of γ-irradiation (1-2 Gy), whereas at higher levels of DNA damage (>5 Gy), activation of checkpoint effectors is MDC1-independent [118]. We asked whether signaling at dysfunctional telomeres could be placed in the first or second category with regard to requirement for MDC1 function. This question was also relevant to the potential role of MDC1 in facilitating NHEJ of dysfunctional telomeres. It was possible that in the absence of MDC1 impaired NHEJ was a consequence of a checkpoint-signaling defect. For instance, since TRF2-depleted mouse telomeres join preferentially in G1 [237], changes in the progression from G1 into S phase could affect the rate of NHEJ. Therefore, we examined the effect of MDC1 knockdown on relevant cell cycle effectors that mediate the G1/S arrest after telomere dysfunction. In contrast to NBS1-deficiency, immunoblotting indicated that MDC1 status affected neither the autophosphorylation of ATM nor the phosphorylation of Chk2 after TRF2 deletion from mouse cells (Figure 3.10a). Furthermore, in primary human fibroblasts (IMR90) the increase in p53 and p21 protein in response to TRF2-DN was unaltered by MDC1 knockdown (Figure 3.10b) and the cells senesced within a week after TRF2 inhibition regardless of the level of MDC1. Moreover, the TRF2-DN-induced senescence was associated with dramatic alterations in morphology regardless of MDC1 status. Both control and MDC1 shRNA-treated senescent cells appeared flatter compared to dividing fibroblasts, increased in size, often contained two or more nuclei, and stained

positive for senescence associated β-galactosidase activity (Figure 3.10c). These data indicate that reduced levels of MDC1 did not affect checkpoint signaling.

The results obtained with MDC1 knockdown in $TRF2^{F/-}p53^{-/-}$ mouse cells also argued against the possibility that MDC1 affects NHEJ in a manner that involves cell cycle progression. As these cells lack a functional p53 pathway, they fail to trigger the G1/S checkpoint in response to TRF2-deletion, although their growth was impaired significantly in the presence of telomere dysfunction. Downregulation of MDC1 in Cre-treated $TRF2^{F/-}p53^{-/-}$ did not additionally alter their proliferation rates, as shown by growth curves, which compare the total number of cells up to 120 hours after deletion of TRF2. In addition, we evaluated the fraction of cells that incorporated the thymidine analogue, BrdU, in 1 hour, as an indication for the portion of cells in S-phase during the labeling period. Again, there was no detectable difference between luciferase- and MDC1- shRNA treated cells, both in the presence and in the absence of Cre-induced telomere dysfunction.

Collectively, these data indicate that the activation of the G1/S checkpoint does not require the accumulation of MDC1, 53BP1, ATM-S1981-P, or Nbs1-S343-P at the sites of telomere damage. Most likely, the ATM kinase is activated and retains the ability to phosphorylate its targets in the nucleoplasm despite the lack of detectable association of ATM with the dysfunctional telomeres. Importantly, these results also argue against a model claiming that the contribution of MDC1 to NHEJ might be mediated through alteration of checkpoint signaling or cell cycle progression. Instead, we concluded that MDC1 regulates an aspect of the NHEJ pathway directly.

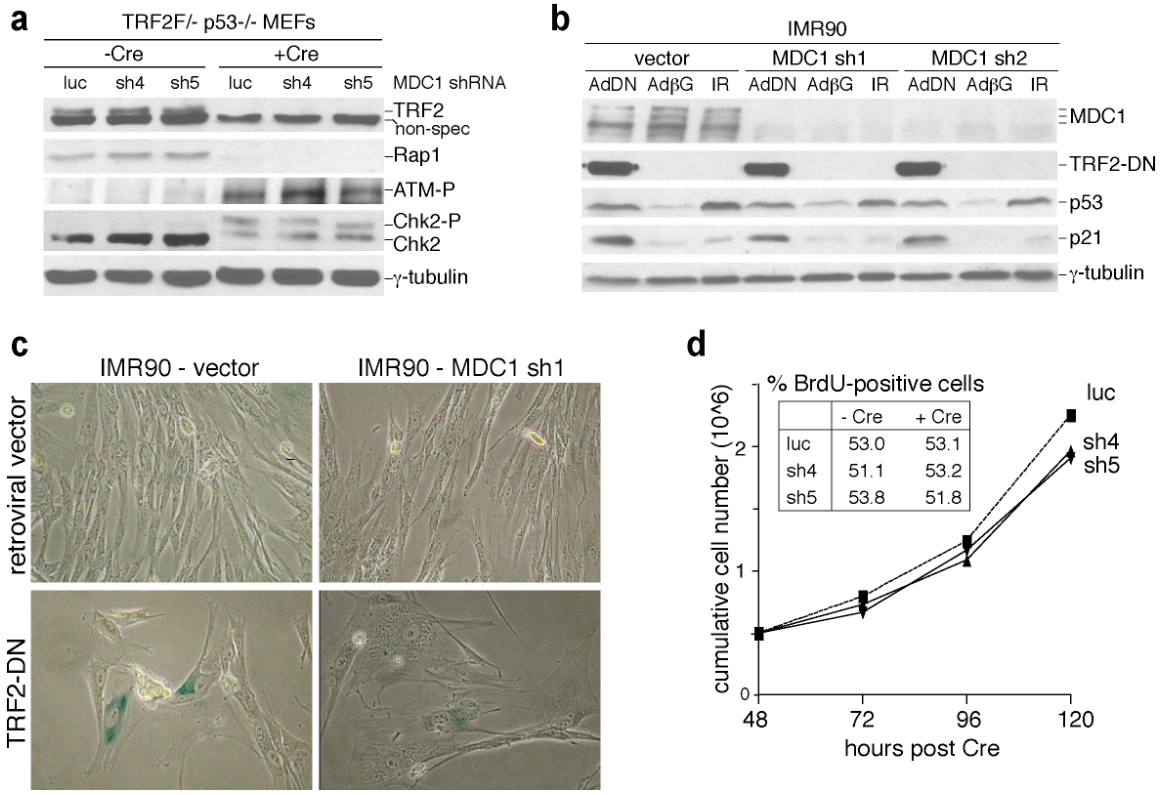

Figure 3.10. MDC1 knockdown does not affect checkpoint signaling in response to telomere dysfunction.

a, Immunoblots of whole cell lysates prepared from TRF2$^{F/-}$p53$^{-/-}$ MEFs, expressing luciferase- or mouse MDC1-specific shRNAs, sh4 or sh5, harvested 72 hours post mock or Hit&Run Cre retroviral infections. Blots were probed with Abs specific to TRF2 (647), mouse Rap1 (1252), ATM-S1981-P, Chk2, and γ- tubulin (clone GTU; as loading control).

b, Immunoblots of whole cell lysates prepared from primary human fibroblasts, IMR90, expressing vector- or human MDC1-specific shRNAs, sh1 or sh2, harvested 48 hours post control β-gal or TRF2-DN retroviral infections. Blots were probed for the induction of p53 (DO-1) and p21 (F-5) after inhibition of TRF2. Control blots were probed with Abs raised against human MDC1 (ab11169), myc (9E10, to detect myc-tagged TRF2-DN), and γ- tubulin (clone GTU; as loading control).

c, Light microscopyx photographs of IMR90 cells, expressing vector or MDC1 shRNA, sh1, infected with empty vector control or TRF2-DN retrovirus, delivered from pWzl-hygro expression vector, stained for SA-β-galactosidase activity at 12 days after infection.

d, Graph indicating the effect of MDC1 knockdown on cell growth. $TRF2^{F/-}p53^{-/-}$ MEFs, expressing luciferase- or mouse MDC1-specific shRNAs, sh4 or sh5, were plated 48 hours after Hit&Run Cre retroviral infections, and counted at 72, 96, and 120 hours post Cre.
Inset table presenting the percentage of cells with BrdU-specific IF signals. $TRF2^{F/-}p53^{-/-}$ MEFs, expressing luciferase- or mouse MDC1-specific shRNAs, sh4 or sh5, were grown for 1 hour in medium containing BrdU at 72 hours post mock or Hit&Run Cre retroviral infections. Cells were fixed and processed for IF with a fluorophore-conjugated anti-BrdU Ab. The fraction of cells exhibiting BrdU incorporation was determined by microscope analysis.

An MDC1-"specific" shRNA with a critical off-target effect

We noted that upon more prolonged culturing (>2 weeks), primary human fibroblasts expressing MDC1 shRNAs sh1 or sh2 started proliferating more slowly than the controls cells and attained a senescence phenotype (Figure 3.11a), even in absence of TRF2-DN. A senescence response to MDC1 knockdown, likely due to accumulation of unrepaired DSBs, is consistent with the diminished proliferation and senescent phenotype of MDC1 knockout MEFs [114]. However, a third human MDC1 shRNA, sh3, which downregulated MDC1 efficiently (Figure 3.11b), and has been used in previous studies [109,110,113,116], did not have this senescence phenotype (Figure 3.11a). Unexpectedly, we found that this shRNA (sh3) has extensive sequence identity to the mRNA for the ATM kinase (Figure 3.11c) and induced a significant reduction in ATM protein levels (Figure 3.11d). Thus, MDC1 sh3 has a remarkably pathway-specific off-target effect whereby it affects both MDC1 itself and ATM, the main kinase responsible for the generation of MDC1 binding sites in damaged chromatin.

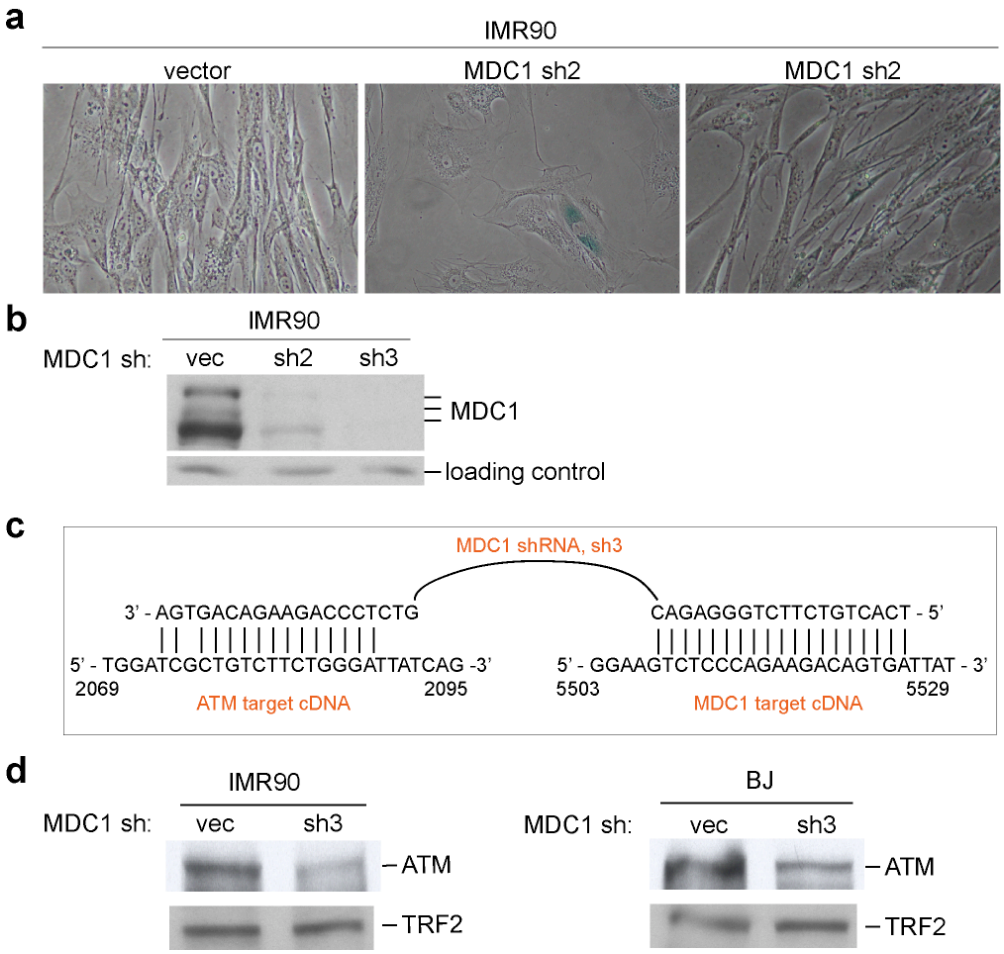

Figure 3.11. ATM-specific off-target effect of MDC1 shRNA, sh3.

a, Light microscopic photographs of IMR90 cells, stained for SA-β-galactosidase activity at 14 days after infection with vector or human MDC1-specific shRNA, sh2 or sh3, delivered by retroviral infections from pSuperior retroviral expression vector.

b, Immunoblot of whole cell lysates prepared from cells described in **(a)**. Blot was probed with Ab raised against human MDC1 (ab11169). Non-specific band from the same blot was used as loading control.

c, Schematic diagram of MDC1 sh3 sequence and its target sites in MDC1 and ATM.

d, Immunoblots detecting ATM protein levels in whole cell lysates prepared from IMR90 and BJ cells treated with vector or sh3. Blots were probed with Abs raised against human ATM (MAT3) and human TRF2 (647, as loading control).

Genetic deletion of MDC1 in the context of the TRF2 conditional knockout confirms shRNA studies

These RNAi studies suggested that whereas MDC1 promoted the repair of dysfunctional telomeres, it was not required for this process to occur. It was possible, however, that the partial inhibition of NHEJ was due to incomplete knockdown of MDC1. In order to address this caveat genetically, we obtained MDC1 knockout mice [114] and bred $MDC1^{+/-}$ mice to $TRF2^{F/F}$ mice to generate $TRF2^{F/F}MDC1^{+/-}$ progeny. Crosses of $TRF2^{F/F}MDC1^{+/-}$ generated E13.5 embryos of $TRF2^{F/F}MDC1^{-/-}$ and $TRF2^{F/F}MDC1^{+/+}$ genotypes. MEFs isolated from these embryos were immortalized at passage 2 with SV40-LT. Western blotting confirmed the absence of MDC1 and successful deletion of TRF2 in $TRF2^{F/F}MDC1^{-/-}$ MEFs, analyzed 72 hours after introduction of Hit&Run Cre recombinase. Absence of MDC1 abolished TIF formation by MRN complex and 53BP1 in all cells (n>200) that lacked TRF2 but did not affect the extent of γ-H2AX phosphorylation at dysfunctional telomeres (Figure 3.12b).

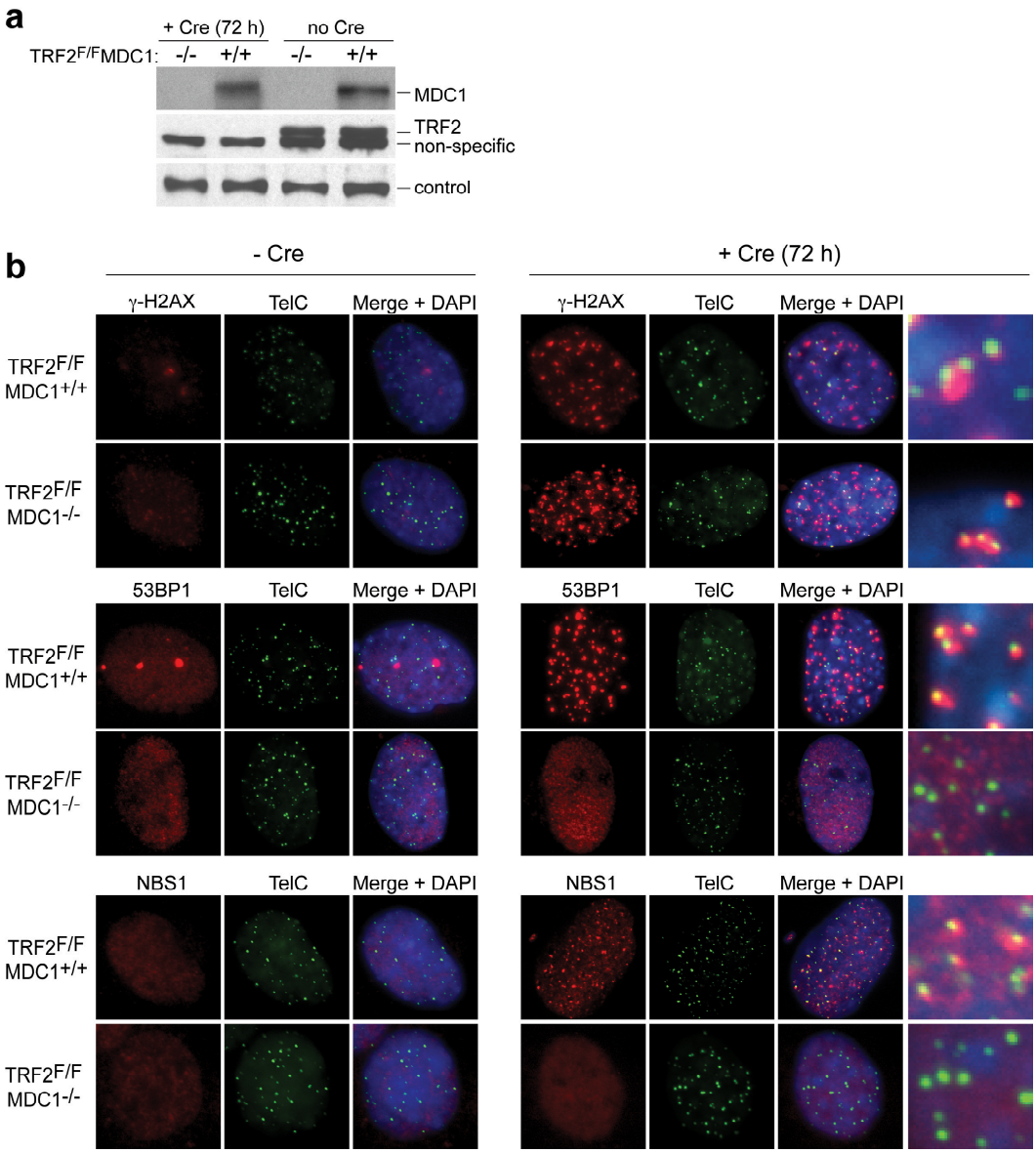

Figure 3.12. Effect of MDC1 deletion on TIF formation

a, Immunoblots of whole cell extracts prepared from TRF2$^{F/F}$MDC1$^{+/+}$ and TRF2$^{F/F}$MDC1$^{-/-}$ cells, untreated or treated with Hit&Run Cre retrovirus for 72 hours and probed with Abs raised against mouse MDC1 (300-757A) and human TRF2 (647). A non-specific band from the TRF2 blot was used as loading control.

b, Representative examples of TRF2$^{F/F}$MDC1$^{+/+}$ and TRF2$^{F/F}$MDC1$^{-/-}$ cells, fixed 72 h post mock or Hit&Run Cre retroviral infections, and processed for IF-FISH. IF (in red) was performed with Abs specific to γ–H2AX, 53BP1 (100-304), and NSB1 (93'6). Telomeric DNA was detected by FISH (in green) with a telomere repeat-specific FISH probe. DNA (in blue) was counterstained with DAPI. Images were merged and enlarged.

Next we compared the frequency of end-to-end fusions and the rate of overhang loss in $TRF2^{F/F}MDC1^{-/-}$ and $TRF2^{F/F}MDC1^{+/+}$ MEFs, treated with Cre to remove TRF2. The results confirmed the shRNA studies. Fusions occurred at a slower pace in MDC1-deficient MEFs compared to control cells. Metaphase spreads from MDC1-proficient cells contained 24±4% fusions per chromosome end at 96 hours post Cre. This frequency further increased to 33±2% at 120 hours post Cre. In contast, in absence of MDC1, we observed only 0.6±0.4% fusions per chromosome end at 96 hours post Cre and the percentage of fused chromosome ends increased only slightly to 14±5% at the latest timepoint. The overhang signal also diminished more slowly in $TRF2^{F/F}$ $MDC1^{-/-}$ MEFs compared to MEFs generated from a $TRF2^{F/F}$ $MDC1^{+/+}$ littermate, indicating a delay in the NHEJ reaction. We conclude that MDC1 is not essential for the NHEJ pathway but significantly promotes the efficiency of this process at dysfunctional telomeres.

The phenotype of MDC1 loss with regard to NHEJ of dysfunctional telomeres thus recapitulates the delayed fusion phenotype observed for ATM- or NBS1-deficient MEFs (Chapter 2 and [228]). In all cases, repair events occurred with delayed kinetics so that there was absence of NHEJ at early time points and a 2-4 fold decrease in fusion frequencies at later time points. The similarity between ATM, NBS1, and MDC1-deficient cells is consistent with the well-established model, which places MDC1 in the same pathway as the MRN complex and the ATM kinase. On the other hand, the residual fusions in MDC1-deficient cells were predominantly chromosome-type, establishing that, unlike ATM and NBS1 whose absence increased the frequency of chromatid-type fusions, MDC1 does not affect the occurrence of G2 telomere fusion events.

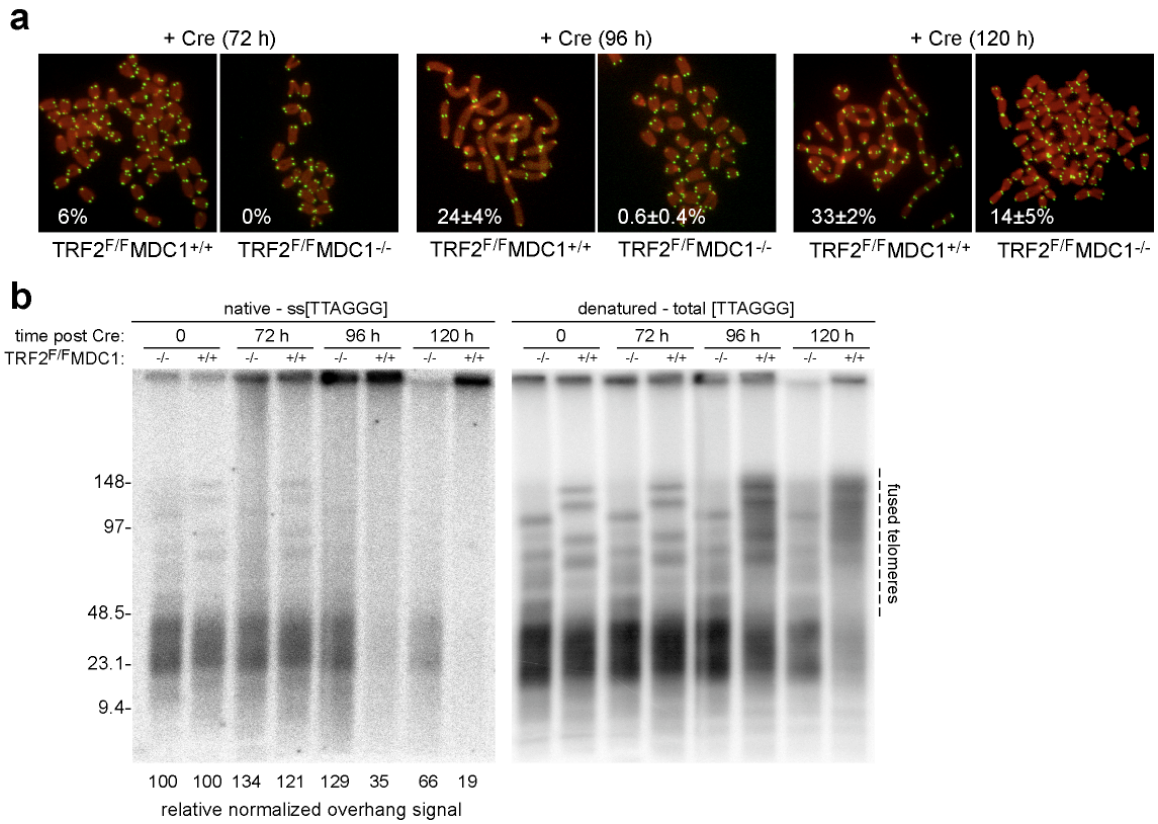

Figure 3.13. Effect of MDC1 deficiency on end-joining and overhang processing of dysfunctional telomeres

a, Detection of telomere fusions in metaphase spreads of TRF2$^{F/F}$MDC1$^{+/+}$ and TRF2$^{F/F}$MDC1$^{-/-}$ MEFs collected at 72, 96, or 120 hours after Hit&Run Cre retroviral infections. Telomeric signals (in green) were detected by TTAGGG-repeat specific probe. DNA was stained with DAPI and false colored in red. Numbers in each panel indicate the fraction of chromosome ends fused at that time point based on analysis of ≥ 350 metaphase chromosomes. s.d. from 3 independent experiments is given.

b, In-gel detection of telomeric DNA from TRF2$^{F/F}$MDC1$^{+/+}$ and TRF2$^{F/F}$MDC1$^{-/-}$ MEFs, harvested post 72 hours mock infection or 72, 96 or 120 hours post Hit&Run Cre retroviral infections. DNA in agarose plugs was separated on agarose gel by pulse-field gel electophoresis and hybridized in-gel to a radioactively labeled $(CCCTAA)_4$ probe (*native*). The DNA was denatured *in situ* and rehybridized to the same probe (*denatured*). In each lane, the ssTTAGGG signal quantified under native condition was normalized to the total TTAGGG signal, detected after denaturation. The relative overhang signal at each time point represents the normalized ssTTAGGG signal in Cre-treated cells, compared to mock-treated cells (set at 100%) for each cell line. Fused telomeres are indicated by dashed line.

Testing the role of MDC1 in the repair of non-telomeric DSBs

The evidence presented in this chapter argues that MDC1 is required to support the physiological pace of NHEJ of dysfunctional telomeres. These data raise the question whether MDC1 also contributes to other instances of NHEJ reactions or whether its role is limited to dysfunctional telomeres. We tested whether MDC1 was required for efficient repair of IR-induced chromosome-internal DSBs in FAR (Fraction of activity released) assay. In this assay, genomic DNA from cells, irradiated with a high dose of γ-irradiation (20-80 Gy), is separated on agarose gel by pulse-field gel electrophoresis. Genomic DNA from non-irradiated or from repair-proficient cells remains in the wells due to its size, whereas genomic DNA, fragmented by γ-irradiation in cells, harvested immediately after irratiation or in cells that are deficient for repair factors, is resolved in the lane. Therefore, one can monitor the ratio of unrepaired genomic DNA resolved in each lane to total genomic DNA (lane + well) (referred to as FAR ratio) as a measure for the progress of gross chromosomal repair at consecutive time points after IR. The FAR assay has previously been used to show that repair is impaired by wortmannin and caffeine, which inhibit the major kinase in the NHEJ pathway, DNA-PKcs. Although we were able to replicate these experiments (Figure 3.14a), we did not observe any difference in the FAR ratios of irradiated human and mouse cells containing wild-type or reduced MDC1 protein levels (Figure 3.14b, c). These data suggest that either MDC1 is not required for the repair of chromosome-internal DSBs, or the FAR assay, which generates ~10 times more sites of DNA damage than are created through inhibition of TRF2, probes for DSBs repair in a range of DNA damage that is less dependent on MDC1.

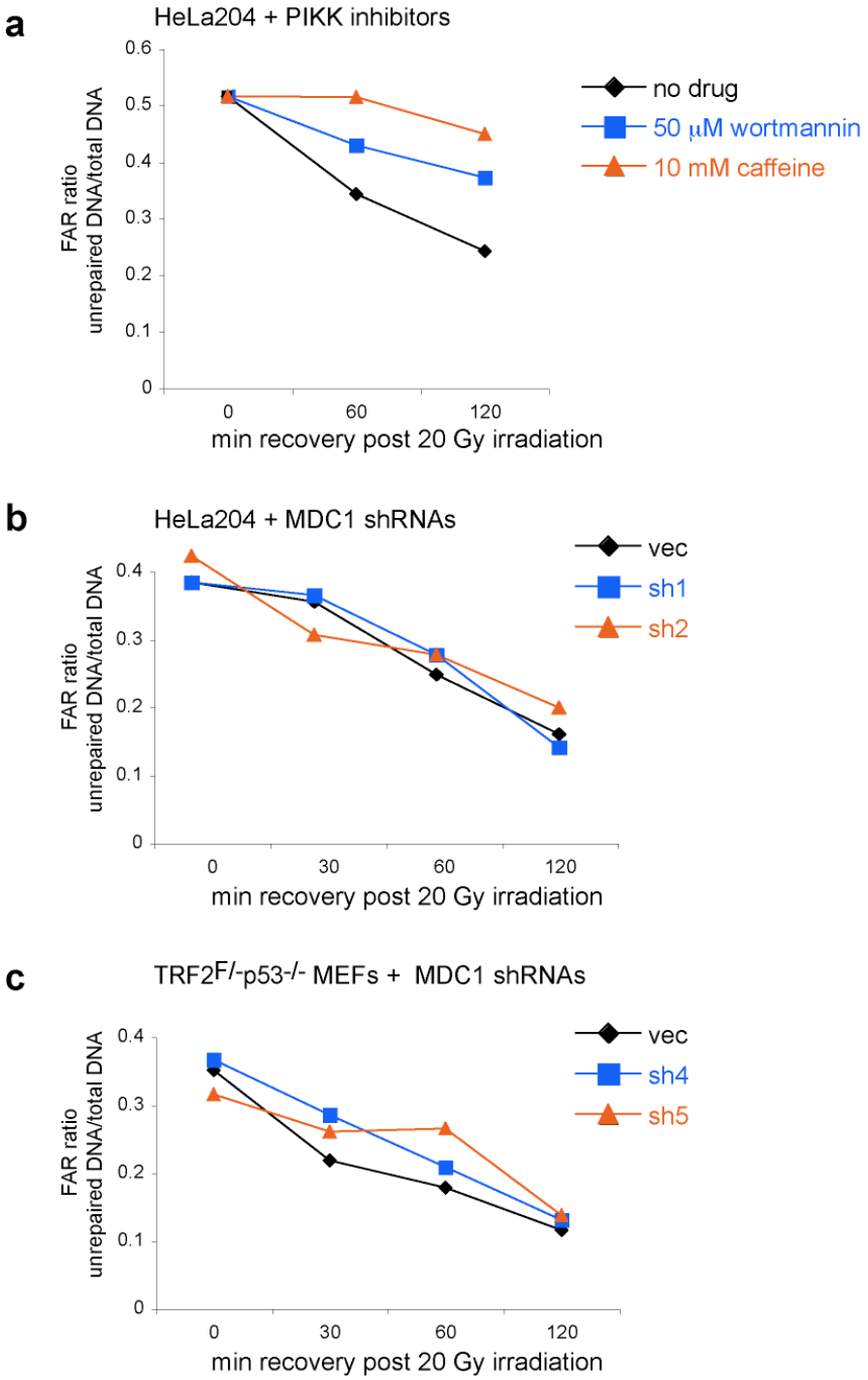

Figure 3.14. Effect of MDC1 downregulation on FAR ratio as a measure for the efficiency of gross chromosomal repair.

a, FAR assay on HeLa204 cells, irradiated with 20 Gy and harvested immediately after IR or after recovery for 60 or 120 minutes, in the presence of no drug, 50 μM wortmannin, or 10 mM caffeine. Genomic DNA in agarose plugs was resolved by pulse-field gel electrophoresis and

Southern blotting was performed using Alu-repeat specific radioactively-labeled probe. Graph presenting the ratio of the signal detected in each lane to the signal quantified in lane+well in cells treated as indicated and collected at the indicated time points after IR.

b, Graph presenting the results from FAR assay performed as in **(a)** on HeLa204 cells expressing control or human MDC1-specific shRNAs, sh1 or sh2, harvested 0, 30, 60, or 120 minutes after irradiation with 20 Gy.

c, Graph presenting the results of FAR assay performed as in **(a)** on $TRF2^{F/+}p53^{-/-}$ MEFs expressing control or mouse MDC1-specific shRNAs, sh4 or sh5, harvested 0, 30, 60, or 120 minutes after irradiation with 20 Gy.

Summary of findings in Chapter 3

In this chapter we established that MDC1 accumulates at chromosome ends only in the presence of telomere dysfunction. We showed that MDC1 requires γ-H2AX in order to localize to dysfunctional telomeres, and that, in turn, MDC1 promotes the accumulation of a number of DNA damage response factors, including 53BP1, ATM-S1981-P, and NBS1, at dysfunctional telomeres. These results draw a model for TIF formation that is identical to the currently established model for IRIF formation, and therefore, suggest a parallel between dysfunctional telomeres and chromosome-internal DSBs in terms of their association with DNA damage response factors.

Next, we used dysfunctional telomeres as a model system to dissect the relative contribution of MDC1 to the signaling and repair pathways activated by inhibition of TRF2 function. We found that MDC1 and the modified histone it binds to, γ-H2AX, are required for the physiological pace of NHEJ of dysfunctional telomeres. The delay in NHEJ that we observed in cells that lacked or contained diminished levels of MDC1 was not a consequence of either altered checkpoint signaling or reduced proliferation rates.

We also tested whether MDC1 promoted the repair of chromosome-internal DSBs. Despite the negative result in FAR assay, we have no reason to assume that the role of MDC1 in NHEJ is specific for telomere dysfunction. In fact, as described in the next, the differences between end-joining of dysfunctional telomeres and NHEJ-mediated repair of IR-induced DSBs might inform us on the function that MDC1 and its associated factors play in NHEJ.

Our conclusions on the involvement of MDC1 in the regulation of NHEJ are consistent with the lower rate of plasmid transfection in cells overexpressing a dominant

negative allele of MDC1 [112], the modest class switch defect of MDC1$^{-/-}$ mice, and their hypersensitivity to DSBs [114]. In contrast, MDC1$^{-/-}$ mice have no overt defect in V(D)J recombination [114], an established measure of NHEJ. Therefore, it was unclear whether MDC1 promotes DSB repair through an effect on NHEJ or through its effect on cell cycle progression. This issue is clarified by our study since MDC1 affected NHEJ without affecting the cell cycle effectors of the ATM signaling pathway or cell cycle progression.

Therefore, we conclude that MDC1 affects NHEJ of dysfunctional telomeres directly. It has been reported that MDC1 interacts with DNA-PKcs/Ku [163] and this might be related to its ability to accelerate NHEJ. MDC1 also interacts with the HR protein Rad51 [164], but the functional relevance these interactions remains to be established. However, we favor an alternative explanation. We propose that the ability of MDC1 to stabilize the association of other DNA damage response factors at dysfunctional telomeres and its capacity to enhance the extended domains of altered chromatin is pertinent to its role in NHEJ. We have confirmed this model in the next chapter, where we present direct evidence that 53BP1, a factor that requires MDC1 for its prolonged association in TIFs, is an essential component of the NHEJ pathway.

CHAPTER 4: THE CONTRIBUTION OF 53BP1 TO NHEJ OF DYSFUNCTIONAL TELOMERES

Introduction

In this chapter, we focus on 53BP1, a DNA damage response factor, which similarly to MDC1, accumulates at DSBs and at deprotected telomeres. As described in the introduction, the interaction of 53BP1 with chromatin near DSBs is mediated in part through the binding of its Tudor domain to H4-K20diMe and through a poorly understood γ-H2AX/MDC1-dependent interaction of 53BP1 with ubiquitilated chromatin. Unlike MDC1, however, 53BP1 does not play a role in the amplification of the DNA damage signal at DSBs [132], a result we confirmed here in the context of telomere dysfunction. On the other hand, experimental evidence has linked 53BP1 to certain aspects of NHEJ. While 53BP1 is not strictly required for NHEJ during V(D)J recombination, the repair of AID-induced DSBs in CSR is severely affected by 53BP1 deficiency[134,136]. Hence, we tested the role of 53BP1 in NHEJ of dysfunctional telomeres and investigated the mechanism by which 53BP1 promotes DNA repair.

Generation of 53BP1-deficient, TRF2-conditional knockout MEFs

In order to address the genetic contribution of 53BP1 to the response to telomere dysfunction, we bred $53BP1^{-/-}$ mice [132] with $TRF2^{F/-}$ mice [190] to generate $TRF2^{F/-}53BP1^{+/-}$ and $TRF2^{F/+}53BP1^{+/-}$ progeny. These were crossed and MEFs from E13.5 embryos with $TRF2^{F/-}53BP1^{-/-}$, $TRF2^{F/-}53BP1^{+/-}$, and $TRF2^{F/+}53BP1^{-/-}$ genotypes were isolated. MEFs were transformed at passage 2 with SV40-LT, abrogating the G1/S checkpoint, which is

activated in response to telomere dysfunction [232]. The presence or absence of 53BP1 protein in these cells was confirmed by immunoblotting (Figure 4.1a) and by IF (Figure 4.1b) using 53BP1-specific antibodies. To induce telomere dysfunction, the conditional allele of TRF2 was removed by Hit&Run Cre retroviral infection. Immunoblotting for TRF2 confirmed efficient deletion of TRF2 at 72 hours post Cre expression in $TRF2^{F/-}$ but not in $TRF2^{F/+}$ MEFs (Figure 4.1a).

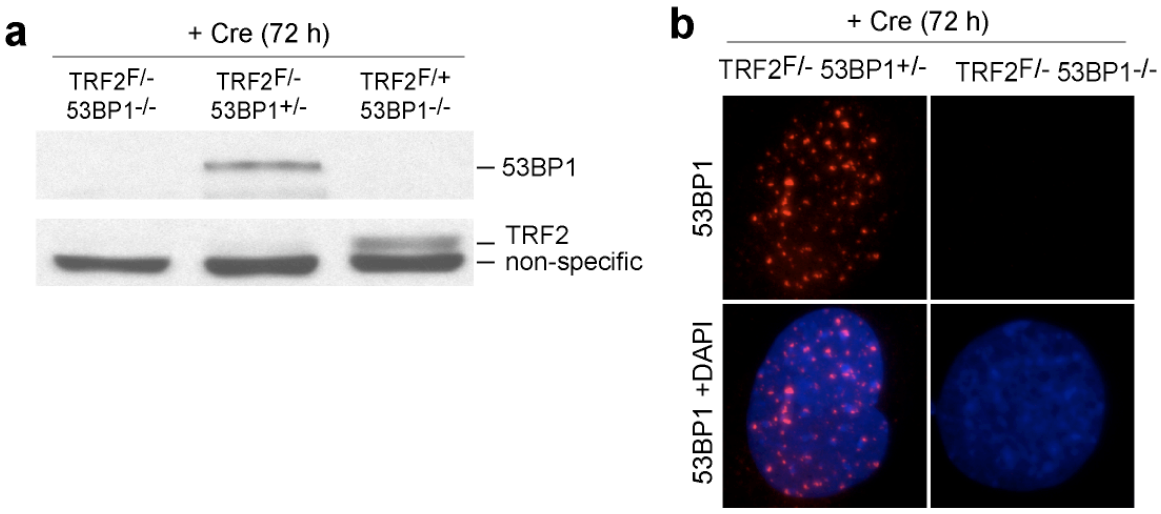

Figure 4.1. Characterization of $TRF2^{F/-}53BP1^{+/-}$, $TRF2^{F/-}53BP1^{-/-}$, and $TRF2^{F/+}53BP1^{-/-}$ MEFs.

a, Immunoblots of whole cell lysates from $TRF2^{F/-}53BP1^{-/-}$, $TRF2^{F/-}53BP1^{+/-}$, and $TRF2^{F/+}53BP1^{-/-}$ MEFs harvested 72 hours post Hit&Run Cre retroviral infections. Blots were probed with Abs specific to 53BP1 (100-305) and TRF2 (647). A non-specific band from the TRF2 blot was used as loading control.

b, IF for 53BP1 (red), performed with anti-53BP1 Ab (100-304) in $TRF2^{F/-}$ $53BP1^{+/-}$ and $TRF2^{F/-}$ $53BP1^{-/-}$ MEFs, fixed 72 hours post Hit&Run Cre infections. Images were merged with DNA counterstained with DAPI (blue).

53BP1 is required for NHEJ of dysfunctional telomeres

Using these MEFs, we determined the contribution of 53BP1 to NHEJ by scoring the frequency of telomere fusions on metaphase spreads. Deletion of TRF2 from $TRF2^{F/-}53BP1^{+/-}$ MEFs caused the expected level of telomere fusions: on average 33% of chromosome ends fused at 120 hours post Cre infections (equivalent to 4 population doublings) (Figure 4.2a, b). The frequency of chromosome end fusions was scored in parallel on metaphase spreads from $TRF2^{F/-}53BP1^{-/-}$ MEFs, collected at the same time point after Cre-mediated TRF2 deletion. Surprisingly, in the absence of 53BP1, we observed at least a 50-fold reduction in the frequency of NHEJ events (Figure 4.2a, b). This phenotype was significantly more severe than the 3-5 fold reduction in fusion frequency in NBS1- and MDC1-deficient MEFs (Chapters 2 and 3). In fact, the consequence of 53BP1 deficiency was comparable to observations previously reported in cells lacking DNA ligase IV [190]. Similarly to DNA ligase IV, 53BP1 thus appeared to be an essential component of the NHEJ pathway at dysfunctional telomeres.

a

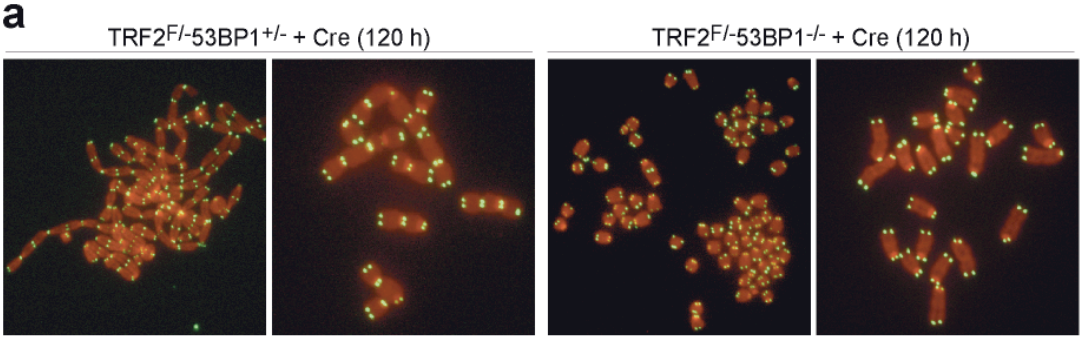

b

	% chromosome ends fused (number of chromosomes scored)				
	Expt 1	Expt 2	Expt 3	Expt 4	Median±SD
TRF2F/+53BP1-/-	0% (1030)				
TRF2F/-53BP1+/-	23% (760)	33% (370)	32% (293)	43% (523)	32.5±8.2%
TRF2F/-53BP1-/-	0.2% (1223)	0.8% (693)	0.4% (1560)	2% (784)	0.6±0.8%

Figure 4.2. NHEJ repair of dysfunctional telomeres in 53BP1-proficient and 53BP1-deficient cells

a, Representative metaphase chromosomes from TRF2$^{F/-}$53BP1$^{+/-}$ and TRF2$^{F/-}$53BP1$^{-/-}$ cells, harvested 120 hours after Hit&Run Cre infections. Images of telomeric DNA, detected with a telomere-specific FITC-OO-$(AATCCC)_3$ probe (in green) merged with total DNA, stained with DAPI (in red).

b, Table summarizing the frequency of fusion events, scored per chromosome end, in metaphase spreads prepared from cells described in **(a)**. The total number of chromosomes scored in each instance is indicated in parenthesis. The median±s.d. derived from 3 independent experiments is given.

Previous experiments using RNAi to stably downregulate 53BP1 in human HeLa1.3 cells did not result in impaired NHEJ of dysfunctional telomeres (Figure 4.3a, b), although by immunoblotting, 53BP1 protein appeared significantly reduced (Figure 4.3a). The conflicting results could be explained if fusions induced by the overexpression of TRF2-DN are not dependent on 53BP1. The alternative possibility that we favor is that a trace amount of 53BP1 protein is sufficient to promote NHEJ, emphasizing the advantage of using a genetic knockout over shRNA knockdown.

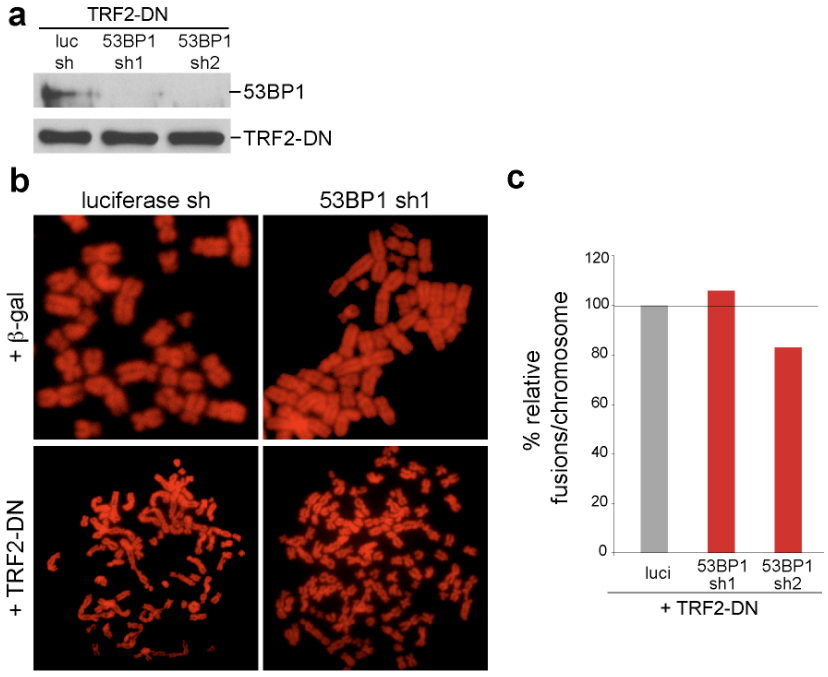

Figure 4.3. Effect of 53BP1 RNAi on telomere NHEJ in the presence of TRF2-DN

a, HeLa1.3 cells expressing luciferase- or 53BP1-specific shRNAs, sh1 or sh2, delivered from pSuperior retroviral vector, were harvested 48 hours post infection with control β-gal or myc-tagged TRF2-DN adenovirus. Immunoblots of whole cell lysates from these cells were probed with anti-53BP1 (100-305) and anti-myc (9E10) Abs.

(b) Bar graph indicating the average relative frequency of chromosome fusions scored in 2 independent experiments on metaphase spreads from cells in **(a)** stained with DAPI.

To confirm that 53BP1 is required for the repair of dysfunctional telomeres upon TRF2 deletion with an independent method, we monitored the fusion reaction by an in-gel hybridization assay. We harvested $TRF2^{F/-}53BP1^{+/-}$ and $TRF2^{F/-}53BP1^{-/-}$ cells at 72, 96, and 120 hours post Cre-mediated TRF2 deletion, and analyzed the progressive disappearance of the telomeric G-rich overhang as well as the concurrent appearance of high molecular weight fusion products on the denatured gel (Figure 4.4a). Both reactions, which are well-established measures for the process of NHEJ at TRF2-depleted telomeres, were impaired in 53BP1-deficient cells (Figure 4.4a, b). In fact, instead of overhang loss, we observed a 2-3 fold increase in the overhang signal upon TRF2 deletion from 53BP1-deficient cells (Figure 4.4b). A similar increase in overhang signal has been reported in Ku70- and DNA Ligase IV-deficient cells [190,236], where the fusion step is blocked, and we observed the same phenomenon in MDC1-deficient cells (Figure 3.9a), where NHEJ is delayed. Most likely, it represents progressive resection at deprotected chromosome termini in the absence of a functional NHEJ pathway.

The presence of long single-stranded DNA at DSBs is potentially inhibitory to the NHEJ pathway. Therefore, it is possible that the contribution of 53BP1 to NHEJ may be to prevent resection at DNA ends. That would explain why in absence of 53BP1 we observed inhibition of NHEJ, concomitant with the presence of elongated 3' G-rich tails. Such model, however, is unlikely because 53BP1 also localizes to chromosome ends in POT1a/POT1b double knockout cells but fails to prevent extensive 5' end resection in that setting [197].

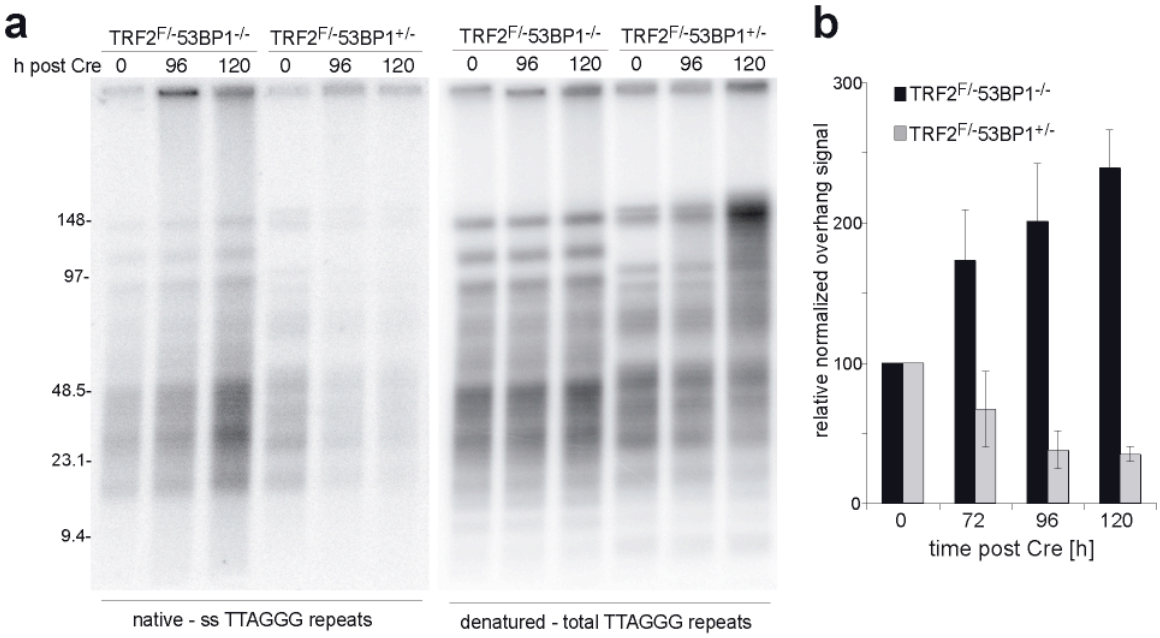

Figure 4.4. Analysis of overhang processing of dysfunctional telomeres in 53BP1-proficient and 53BP1-deficient cells.

a, In-gel detection of telomeric DNA from TRF2$^{F/-}$53BP1$^{-/-}$ and TRF2$^{F/-}$53BP1$^{+/-}$ MEFs, harvested 96 hours post mock infection or 96 and120 hours post Hit&Run Cre retroviral infections. DNA in agarose plugs was separated on agarose gel by pulse-field gel electophoresis and hybridized in-gel to a radioactively labeled $(CCCTAA)_4$ probe (*native*). The DNA was denatured *in situ* and rehybridized to the same probe (*denatured*).

b, Bar graph quantifying the effect of 53BP1 deficiency on overhang processing in cells described in **(a)**, mock treated or treated with Hit&Run Cre retrovirus for 72, 96, or 120 hours, and processed by in-gel overhang assay as in **(a)**. In each lane, the ssTTAGGG signal quantified under native condition was normalized to the total TTAGGG signal, detected after denaturation. The relative overhang signal at each time point represents the normalized ssTTAGGG signal in Cre-treated cells, compared to mock-treated cells (set at 100%) for each cell line. Error bars indicate s.d. from the mean in three independent experiments.

53BP1 deficiency does not affect checkpoint signaling or TIF formation

Whereas the NHEJ of dysfunctional telomeres was severely impaired in TRF2$^{F/-}$53BP1$^{-/-}$ cells, the DNA damage signaling pathway was not affected by the absence of 53BP1. Analysis of Western blots indicated that ATM and its downstream target Chk2 were phosphorylated to an equal extent in 53BP1-proficient and 53BP1-deficient MEFs following telomere deprotection (Figure 4.5a). Additionally, the number of cumulative population doublings of TRF2$^{F/-}$53BP1$^{+/-}$ and TRF2$^{F/-}$53BP1$^{-/-}$ MEFs at 72 and 120 hours after Hit&Run Cre infections indicated that these cells underwent a comparable number of cell divisions regardless of their 53BP1 status (Figure 4.5b). Moreover, the S-phase index of Cre-treated TRF2$^{F/-}$53BP1$^{+/-}$ and TRF2$^{F/-}$53BP1$^{-/-}$ MEFs, calculated as the percentage of cells that incorporated the thymidine analogue BrdU in 1 hour, was also not affected by 53BP1 deficiency (Figure 4.5c). Collectively, these important controls confirmed that, as previously established, 53BP1 does not play a significant role in checkpoint signaling. Moreover, these data ensured that the inhibitory effects of 53BP1-deficiency on NHEJ were not due to changes in cell cycle progression.

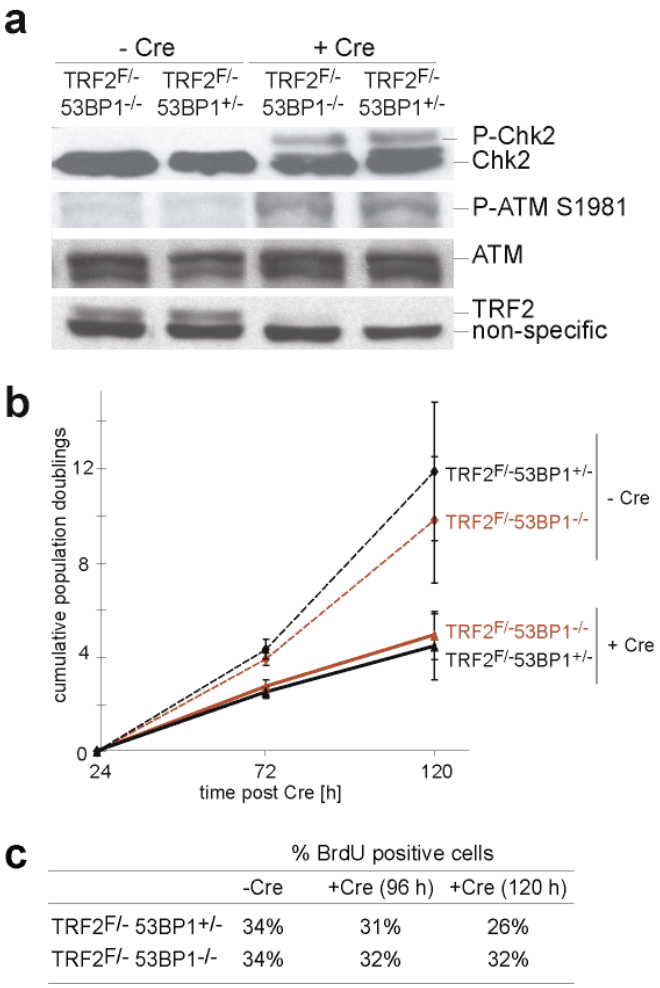

c

	% BrdU positive cells		
	-Cre	+Cre (96 h)	+Cre (120 h)
TRF2F/- 53BP1+/-	34%	31%	26%
TRF2F/- 53BP1-/-	34%	32%	32%

Figure 4.5. Effects of 53BP1 status on checkpoint signaling and proliferation rates

a, Immunoblots of whole cell lysates from TRF2$^{F/-}$53BP1$^{+/-}$ and TRF2$^{F/-}$53BP1$^{-/-}$ MEFs harvested 72 hours post mock or Hit&Run Cre retroviral infections. Blots were probed with Abs raised against Chk2, ATM-S1981-P, total ATM (MAT3), and TRF2 (1254). A non-specific band from the TRF2 Western was used as a loading control.

b, Growth curve of cumulative population doublings of TRF2$^{F/-}$53BP1$^{+/-}$ and TRF2$^{F/-}$53BP1$^{-/-}$ MEFs plated at 24 hours after Hit&Run Cre retroviral infections and counted at 72 and 120 hours post Cre. Error bars indicate s.d. in triplicate experiments.

c, Table presenting the percentage of cells with BrdU-specific IF signal. TRF2$^{F/-}$53BP1$^{+/-}$ and TRF2$^{F/-}$53BP1$^{-/-}$ MEFs were grown for 1 hour in medium containing BrdU at 96 and 120 hours post mock or Hit&Run Cre retroviral infections. Cells were fixed and processed for IF with a fluorophore-conjugated anti-BrdU Ab. The fraction of cells exhibiting BrdU incorporation was determined by fluorescent microscope analysis.

We also examined how absence of 53BP1 affected the accumulation of the DNA damage site markers γ-H2AX, MDC1, and NBS1 in TIFs. We found that at least 68% of both 53BP1-deficient and 53BP1-proficient cells contained γ-H2AX, MDC1, and NBS1 foci at telomeres (Figure 4.6a, b). This result is entirely consistent with previous experiments [132], which have not attributed any role to 53BP1 in the accumulation of these factors in IRIFs. In sum, 53BP1 was not involved in either checkpoint response or amplification of the DNA damage signal. We hypothesized that the main role of 53BP1 may be in promoting DNA repair.

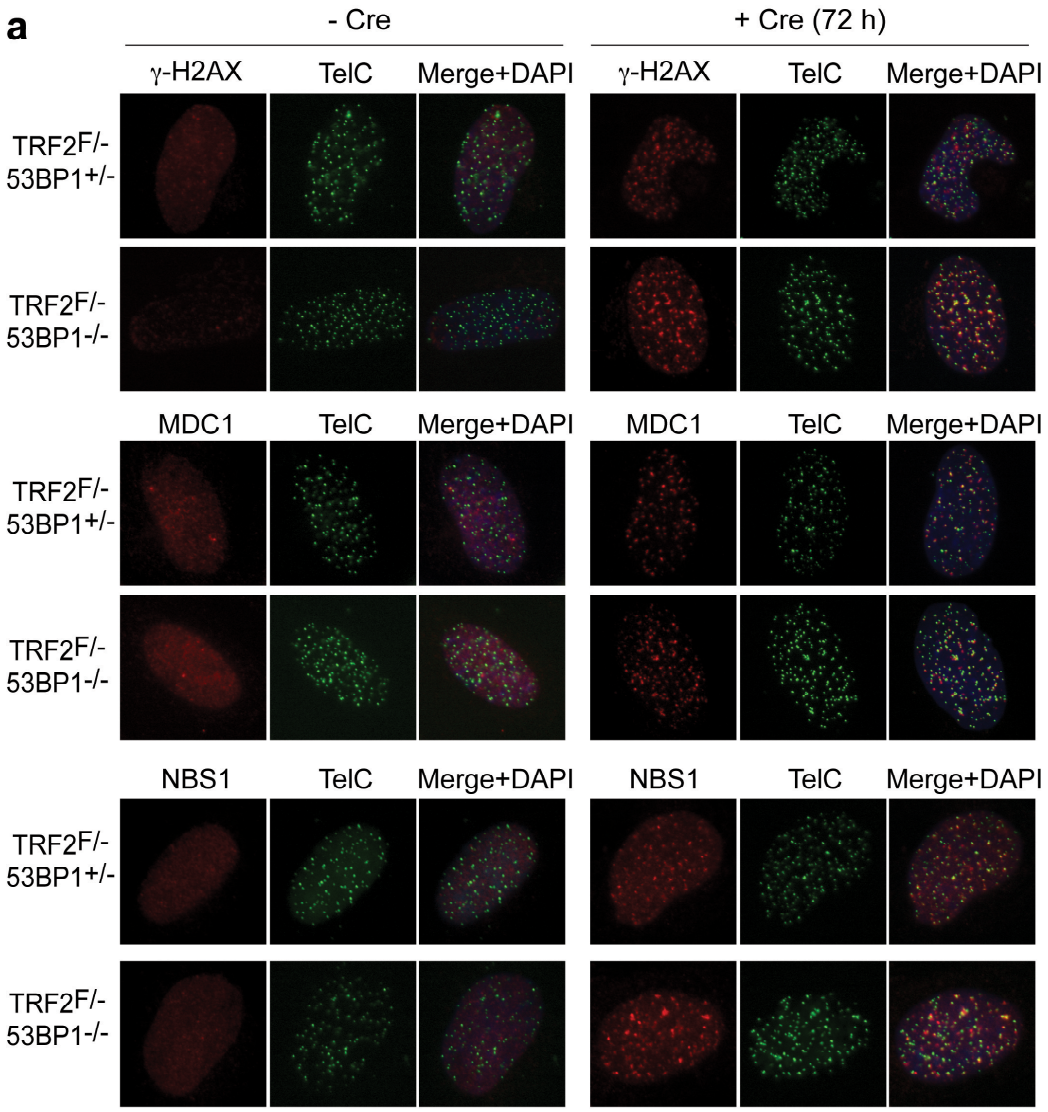

b

% TIF-positive cells (> 10 TIFs)

	TRF2F/-53BP1+/-		TRF2F/-53BP1-/-	
	- Cre	+ Cre	- Cre	+ Cre
γ-H2AX	2%	88%	2%	88%
MDC1	0%	92%	3%	87%
NBS1	2%	68%	0%	68%

Figure 4.6. Effect of 53BP1 status on TIF formation

Figure 4.6. Effect of 53BP1 status on TIF formation

a, Representative examples of fluorescent microscopic images of $TRF2^{F/-}$ $53BP1^{-/-}$ and $TRF2^{F/-}$ $53BP1^{+/-}$ MEFs, fixed 72 hours after mock or Hit&Run Cre retroviral infections and processed for IF-FISH. IF (in red) was performed with Abs raised against γ-H2AX, mouse MDC1, and mouse NSB1 (93'6). Telomeric DNA was detected by FISH (in green) performed with a TTAGGG repeat-specific FISH probe. DNA (in blue) was counterstained with DAPI. Images were merged. **b**, Table summarizing the effects of 53BP1 status on TIF formation. The frequency of cells (n>100) containing more than 10 IF signals for the indicated DNA damage response factors co-localizing with the telomere-specific FISH probe were scored in IF-FISH analysis performed in **(a)**.

The interactions of 53BP1 with modified chromatin contribute to its role in NHEJ

MDC1 is required for the stable accumulation of 53BP1 at chromatin surrounding sites of DNA damage, including dysfunctional telomeres (Figures 3.4, 3.5 and 3.12) and DSBs [120,121]. Therefore, the delayed repair phenotype we reported in Chapter 3 in MDC1-deficient cells was likely due to inefficient recruitment of 53BP1 to TIFs. Surprisingly, 53BP1 deletion caused a more severe repair defect than MDC1 absence (comparison between Figures 3.13 and 4.2). This can only be explained if 53BP1 is involved in a parallel, MDC1-independent pathway that contributes to its repair function. An obvious candidate is the association of 53BP1 with dimethylated H4-K20 (H4-K20diMe), which is required for the initial recruitment of 53BP1 to sites of DNA damage [138]. X-ray analysis has implicated D1521 located in the Tudor domain of 53BP1 to be required for binding to H4-K20diMe. Accordingly, 53BP1-D1521A mutant fails to bind H4-K20diMe and is characterized by impaired recruitment to IRIFs [138].

To test whether the Tudor domain-mediated recognition of H4-K20diMe contributed to the role of 53BP1 in NHEJ, we complemented $TRF2^{F/-}53BP1^{-/-}$ cells with

wild-type human 53BP1 or mutant 53BP1-D1521A allele (see schematic in Figure 4.7a). Previous work has established that expression of human 53BP1 can reconstitute 53BP1 function in 53BP1$^{-/-}$ MEFs [253]**.** The two forms of 53BP1 were expressed equally at levels comparable to endogenous 53BP1 as indicated by immunoblotting (Figure 4.7b). Immunofluorescence analysis showed that, as expected, the recruitment of 53BP1-D1521A to deprotected chromosome ends was diminished compared to exogenously expressed wild type 53BP1, which formed large TIFs upon deletion of TRF2 (Figure 4.7c).

Next, we analyzed how the D1521A mutation in 53BP1 affected NHEJ. In this experiment, as shown above, metaphase spreads of the control (vector) TRF2$^{F/-}$53BP1$^{-/-}$ cells showed no telomere fusions even at 120 hours after deletion of TRF2 (Figure 4.7d, e). As an additional control, cells complemented with wild type 53BP1 exhibited increasing frequency of telomere fusions at 96 and 120 hours post Cre expression. In contrast, TRF2$^{F/-}$53BP1$^{-/-}$ cells complemented with the 53BP1-D1521A mutant showed no telomere fusions at the 96 hour time point, and at 120 hours post-Cre, the frequency of fusions was 2-3 fold reduced compared to cells complemented with wild type 53BP1 (Figure 4.7d, e). Therefore, the Tudor domain-mediated interaction of 53BP1 with H4-K20diMe contributed to the timely execution of NHEJ at dysfunctional telomeres.

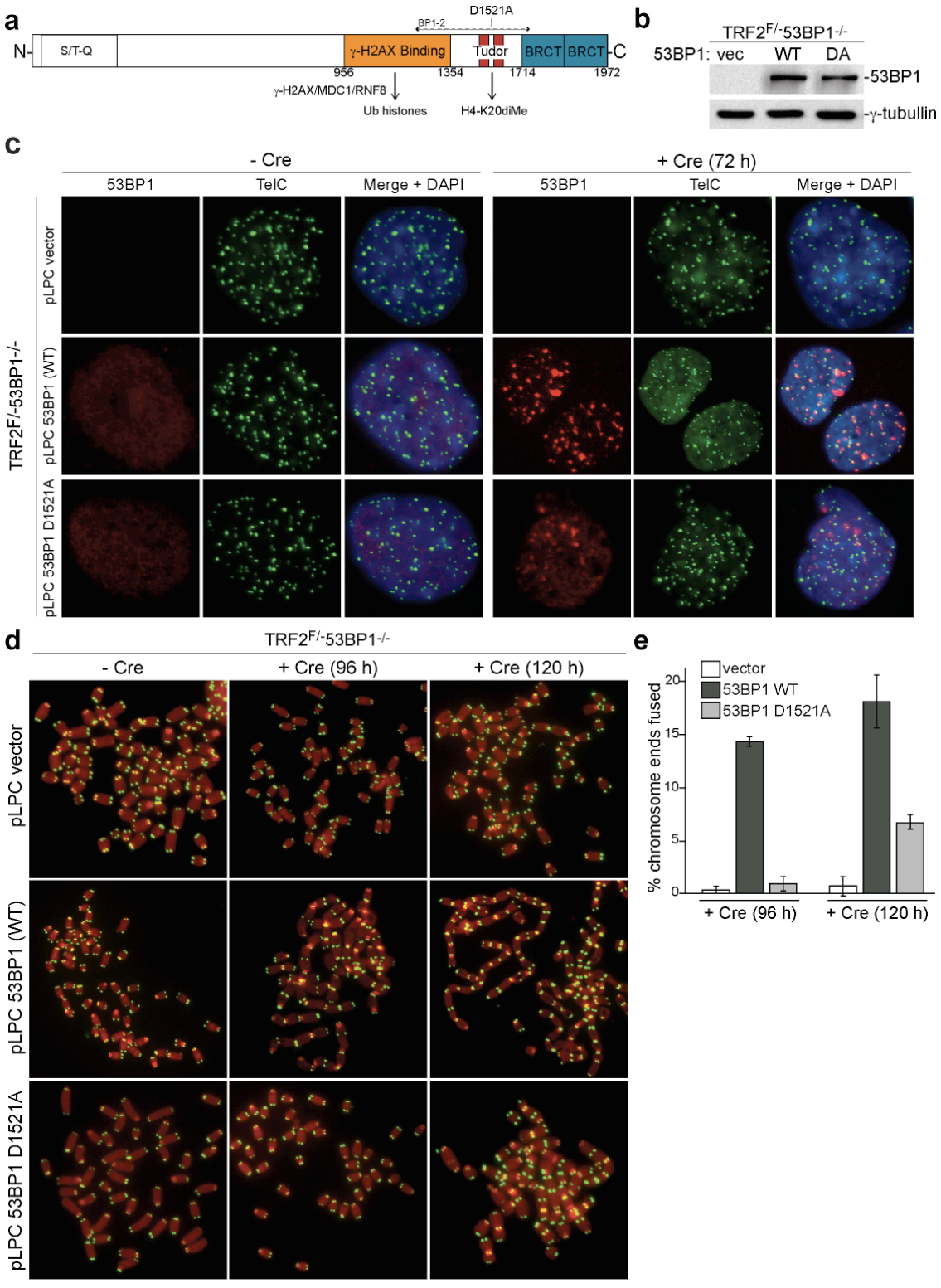

Figure 4.7. Analysis of 53BP1-D1521A mutant and its proficiency for NHEJ

Figure 4.7. Analysis of 53BP1-D1521A mutant and its proficiency for NHEJ

a, Schematic of the domain structure of 53BP1 highlights the N-terminal cluster of S/TQ ATM/ATR phosphorylation target sites, γ-H2AX interaction domain, Tudor domains, and C-terminal BRCT repeats. The critical Tudor domain D1521 residue is also indicated, as well as the location of the BP1-2 allele.

b, Immunoblots of whole cell lysates from $TRF2^{F/-}$ $53BP1^{-/-}$ cells, complemented with N-terminally myc-tagged vector, wild type 53BP1 (53BP1-WT), or 53BP1 D1521A mutant, expressed from pLPC-puro retroviral delivery vector. Blots were probed with Abs specific to myc (9E10) and γ-tubulin (clone GTU) as loading control.

c, Fluorescent microscopic images of cells described in **(b),** fixed 72 hours after mock or Hit&Run Cre retroviral infections, and processed for IF (in red), performed with Ab raised against 53BP1 (100-304), co-stained with TTAGGG-repeat specific FISH probe (in green). DNA (in blue) was counterstained with DAPI. Images were merged

d, Metaphase spreads of cells described in **(b),** fixed untreated or 96 and 120 hours after Hit&Run Cre retroviral infections. Telomeric DNA (in green) was detected with TTAGGG-repeat specific FISH probe. DNA (in red) was stained with DAPI.

c, Bar graph summarizing the effect of Tudor domain mutation on NHEJ of dysfunctional telomeres. The frequency of chromosome end fusions was scored on metaphase spreads prepared as described in **(d)**. More than 500 chromosomes were examined in each instance. Error bars indicated s.d. from median in triplicate experiments.

The finding that the Tudor domain mutation in 53BP1 did not abrogate NHEJ argued that γ-H2AX/MDC1-mediated interaction of 53BP1 with chromatin also contributed to NHEJ. This was already expected based on our analysis of $TRF2^{F/F}MDC1^{-/-}$ MEFs, where the rate of fusion of dysfunctional telomeres was reduced. However, to test this model, we downregulated MDC1 by two independent shRNAs in $TRF2^{F/-}53BP1^{-/-}$ cells expressing the 53BP1-D1521A mutant allele. Efficient knockdown of MDC1 in these cells was confirmed by immunoblotting (Figure 4.8a). Although cells rescued with 53BP1-D1521A already showed impaired ability to carry out NHEJ, MDC1 downregulation led to further decrease in the frequency of fusion events detected upon telomere deprotection (Figure 4.8b, c). The combination of Tudor domain 53BP1 mutant and MDC1 downregulation phenotypically resembled complete absence of 53BP1. These results demonstrated that efficient NHEJ of dysfunctional telomeres requires stable association of 53BP1 at TIFs, which in turn can be promoted by the additive functions of H4-K20diMe and γ-H2AX/MDC1.

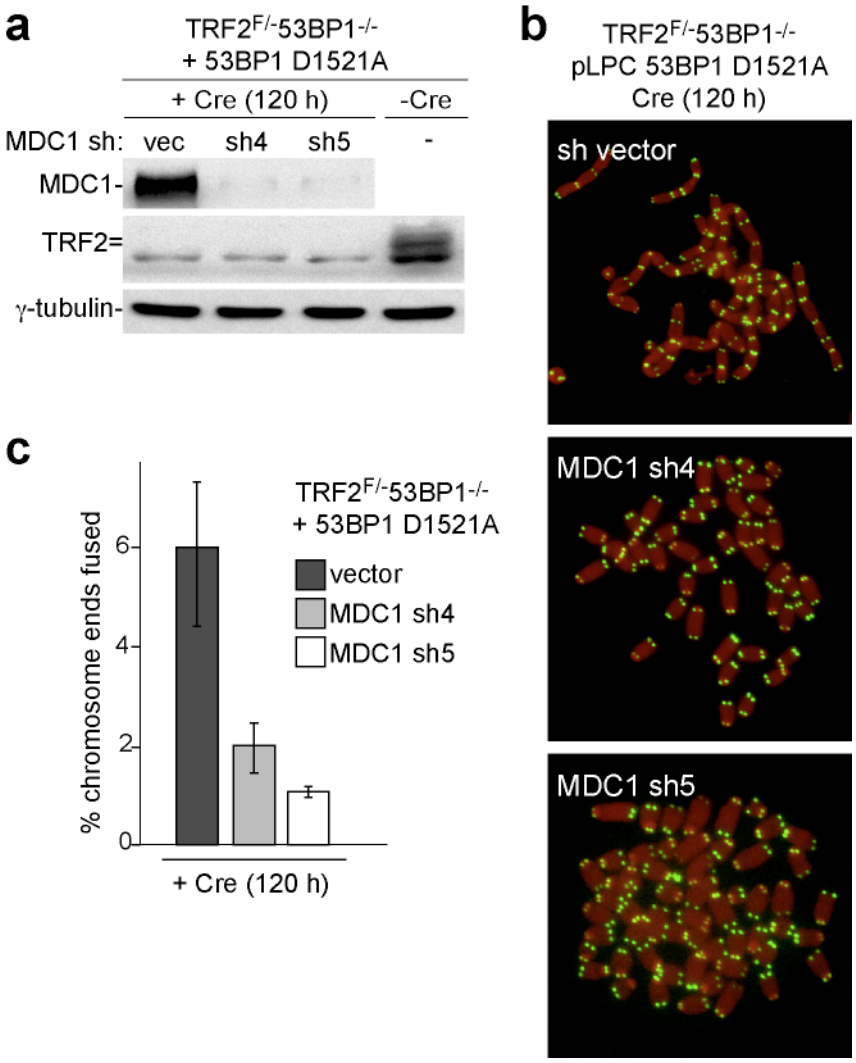

Figure 4.8. Role of MDC1-mediated recruitment of 53BP1 to chromatin in promoting NHEJ

a, Immunoblots of whole cell lysates from TRF2$^{F/-}$ 53BP1$^{-/-}$ MEFs, complemented with 53BP1-D1521A, and treated with vector or MDC1-specific shRNAs, sh4 or sh5, delivered by pSuperior retroviral vector. Cells were harvested 120 hours after mock or Hit&Run Cre retroviral infections. Blots were probed with Abs specific to mouse MDC1 (300-757A), mouse TRF2 (1254), and γ-tubulin (clone GTU) as a loading control.

b, Representative examples of metaphase spreads of cells described in **(a)** fixed 120 hours after Hit&Run Cre infections. Telomeric DNA (in green) was detected with TTAGGG-repeat specific FISH probe. DNA (in red) was stained with DAPI.

c, Bar graph indicating the median frequency of chromosome end fusions scored in metaphases prepared as described in **(b)**. More than 500 chromosomes were examined in each instance. Error bars represent s.d. in triplicate experiments.

Hypothesis: 53BP1 preferentially affects NHEJ of distant DNA ends

Our analysis established an indispensable role for 53BP1 in promoting NHEJ of dysfunctional telomeres. On one hand, the extensive requirement for 53BP1 in repair appeared puzzling since 53BP1 does not have any domains that would suggest DNA processing activities and 53BP1 is not required for NHEJ in the context of V(D)J recombination. On the other hand, 53BP1 protein contains several protein-protein interaction domains, at least one of which (the tandem Tudor domain) is known to associate with a specific chromatin modification and to contribute to the repair function of 53BP1. Hence, we tested whether 53BP1 might be involved in promoting NHEJ directly by influencing the behavior of damaged DNA ends.

Previous data have indicated that 53BP1 contributes to NHEJ in CSR. In contrast, 53BP1 is not required for NHEJ in the context of most V(D)J recombination or random chromosome-internal DSBs**.** It has been argued that the crucial difference between these processes might be the distance between the DNA ends involved in the end-joining reaction [135]. Whereas the two ends generated by RAG1/2 or chromosome-internal DNA damage are close together, the DNA ends generated by AID in CSR are often far apart as are dysfunctional telomeres, which are processed by NHEJ in G1 when chromosome ends are dispersed throughout the nucleus.

We considered two models for the mechanism by which 53BP1 might promote NHEJ at distant sites. In one model, originally proposed by Nussenzweig and colleagues, 53BP1 would promote synapsis, providing a molecular 'glue' that holds the ends together [135]. In another, non-exclusive, model, we proposed that 53BP1 would endow damaged

ends with higher mobility within the nucleus, thereby increasing the chance of their juxtaposition.

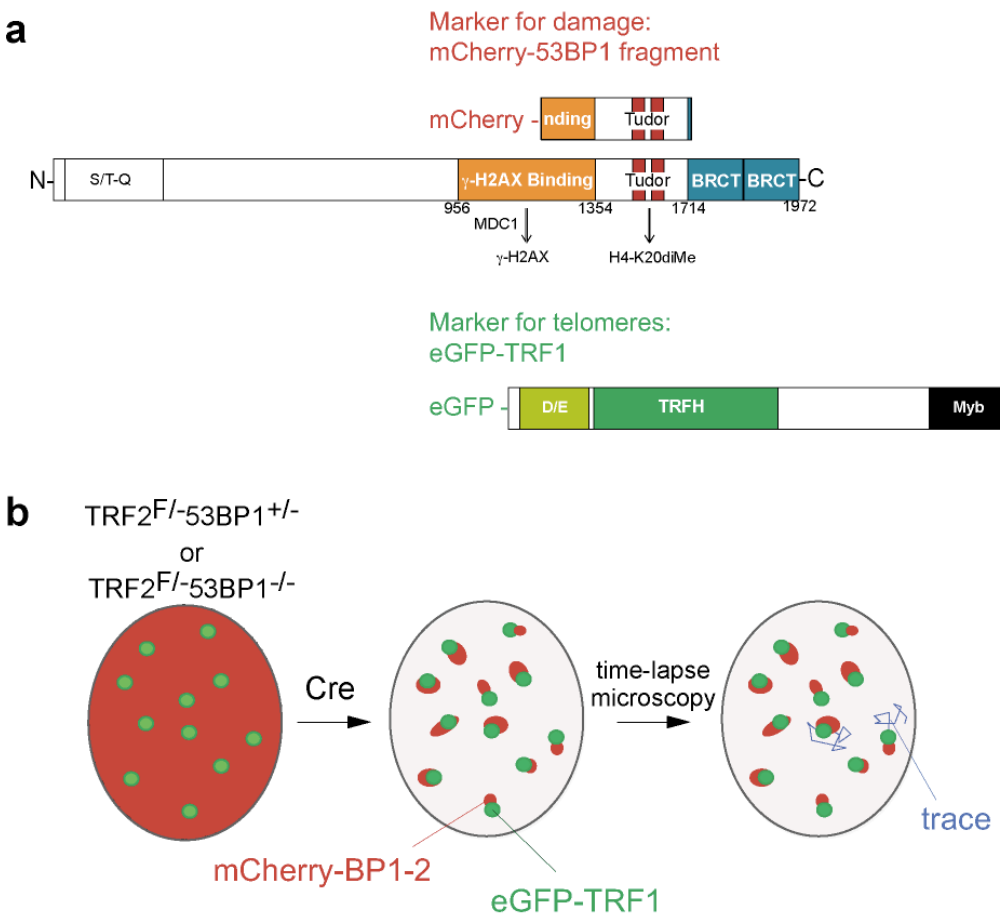

Figure 4.9. Schematic of the live-cell imaging experiments

a, Schematic diagram of the fluorescently-labeled markers used in live-cell imaging studies. **b,** eGFP-TRF1 to mark telomeres and mCherry-BP1-2 to mark dysfunctional telomeres were introduced into $TRF2^{F/-}$ $53BP1^{-/-}$ and $TRF2^{F/-}53BP1^{+/-}$ MEFs. Time-lapse microscopy was performed 72-84 hours after Hit&Run Cre-mediated deletion of TRF2. Individual dysfunctional telomeres were tracked and the dynamic properties of their traces were analyzed.

Time-lapse microscopy setup

We turned to time-lapse microscopy to address whether 53BP1 altered the synapsis and/or dynamics of deprotected telomeres (Figure 4.9a, b). To detect telomeres, we introduced an eGFP-tagged version of the shelterin component TRF1 into $TRF2^{F/-}$ $53BP1^{-/-}$ and $TRF2^{F/-}53BP1^{+/-}$ cells (Figure 4.9a). TRF1 is known to remain associated with telomeres when TRF2 is removed thereby providing a reliable marker for both functional and dysfunctional telomeres. Overexpression of this and other forms of TRF1 does not affect the protective function of telomeres [254]. As expected, eGFP-TRF1 fluorescent signals exhibited a nuclear pattern of discrete localization sites, which coincided with TRF2 signals (Figure 4.10a). The pattern of eGFP-TRF1 remained unchanged upon TRF2 deletion (Figure 4.10b).

In order to mark dysfunctional telomeres, we introduced an mCherry labeled, functionally impaired, allele of 53BP1 (mCherry-BP1-2, comprising aa 1220-1711**;** see Figure 4.7a for schematic, Figure 4.9a) that localizes to chromatin near DSBs and deprotected telomeres but lacks the N-terminal S/T-Q ATM/ATR target sites, most of the γ-H2AX binding region, and the C-terminal BRCT domains. Fluorescence microscopic analysis confirmed that in the absence of telomere dysfunction, mCherry-BP1-2 was homogeneously distributed throughout the nucleus, whereas upon deletion of TRF2, mCherry-BP1-2 localized to telomeric sites containing eGFP-TRF1 both in 53BP1-proficient and 53BP1-deficient cells (Figure 4.10b). Therefore, mCherry-BP1-2 was a good marker for telomere dysfunction.

Immunoblots verified that both fluorescently-labeled markers were expressed at equal levels in $TRF2^{F/-}53BP1^{-/-}$ and $TRF2^{F/-}53BP1^{+/-}$ cells (Figure 4.10c). Additionally,

for each imaging experiment, we confirmed by immunoblotting that Hit&Run Cre expression in these cells resulted in efficient deletion of TRF2, thereby inducing telomere dysfunction (Figure 4.10c).

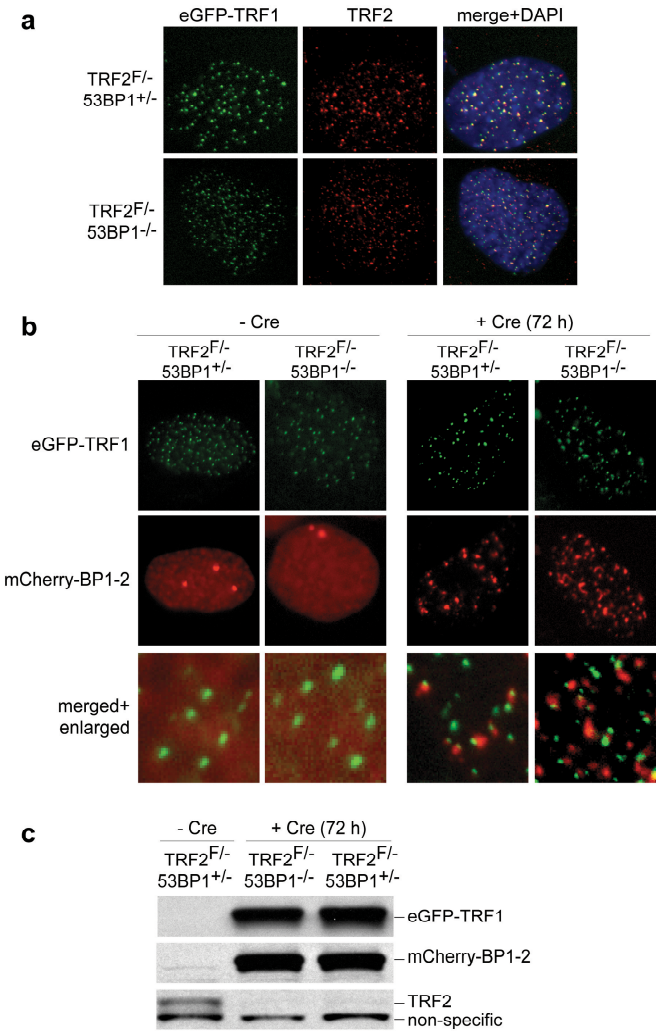

Figure 4.10. Expression and localization of fluorescent markers

a, Representative images of TRF2$^{F/-}$ 53BP1$^{-/-}$ and TRF2$^{F/-}$53BP1$^{+/-}$ cells expressing eGFP-TRF1 from pWzl-hygro retroviral expression vector, processed for IF with Ab specific to mouse TRF2 (1254) (in red). eGFP signal (in green) was detected by fluorescence microscope. DNA (in blue) was stained with DAPI.

b, Microscopic images of eGFP (in green) and mCherry (in red) fluorescence signals in TRF2$^{F/-}$ 53BP1$^{-/-}$ and TRF2$^{F/-}$53BP1$^{+/-}$ MEFs, expressing eGFP-TRF1 from pWzl-hygro and mCherry-

BP1-2 from pLPC-puro retroviral expression vectors. Cells were fixed untreated or 72 hours after Hit&Run Cre retroviral infections. Images were merged and enlarged.
c, Immunoblots of whole cell lysates prepared from cells in **(b)**. Blots were probed with the following Abs: anti-mouse TRF1, anti-53BP1 (100-305), and anti-TRF2 (647). $TRF2^{F/-}53BP1^{+/-}$ cells not expressing fluorescent markers and untreated with Cre were used as control. Non-specific band from the TRF2 blot was used as a loading control.

We also verified that the DNA damage marker mCherry-BP1-2 did not restore 53BP1 function in 53BP1-deficient cells and did not act as a strong dominant negative allele in 53BP1 wild type setting. Metaphase spreads from $TRF2^{F/-}53BP1^{-/-}$ cells expressing eGFP-TRF1/mCherry-BP1-2 did not contain fusions at 120 hours after deletion of TRF2, while metaphase spreads from $TRF2^{F/-}53BP1^{+/-}$ cells expressing eGFP-TRF1/mCherry-BP1-2 showed that ~15% of the chromosome ends had become fused at the same time point (Figure 4.11). These results established that the mCherry-BP1-2 marker might weakly, but not significantly, inhibit the NHEJ pathway. We also repeated key imaging experiments in cells lacking the 53BP1 fragment with the same outcome (see below) further establishing mCherry-BP1-2 as a neutral marker for DNA damage in this context.

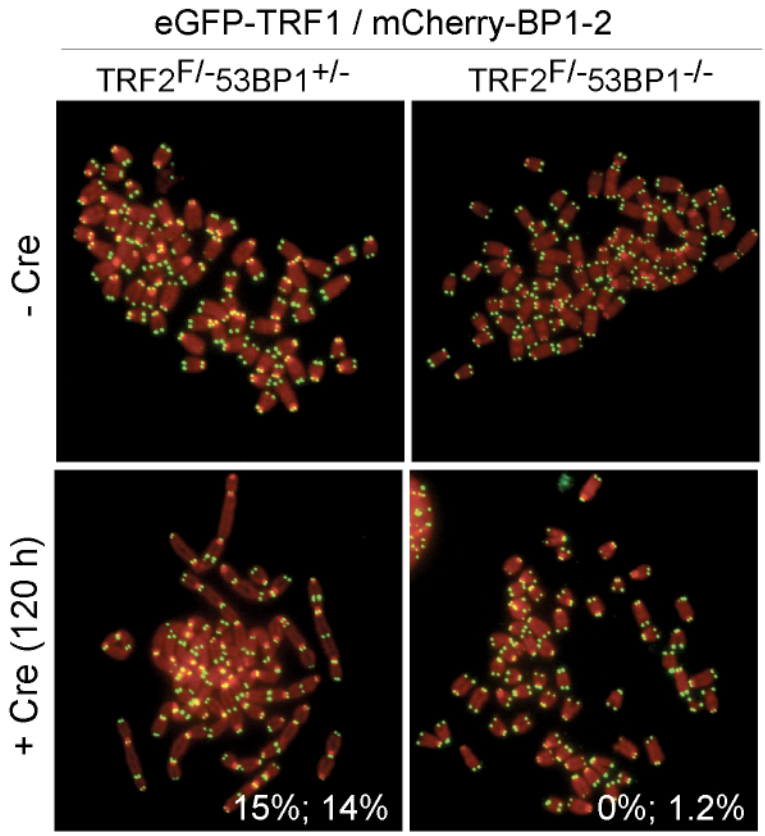

Figure 4.11. Validation of mCherry-BP1-2 as a neutral DNA damage marker

Detection of telomere fusions in metaphase spreads of $TRF2^{F/-}$ $53BP1^{+/-}$ and $TRF2^{F/-}53BP1^{-/-}$ MEFs, expressing eGFP-TRF1 and mCherry-BP1-2, fixed untreated or at 120 hours after Hit&Run Cre retroviral infections. Telomeric DNA (in green) was detected with a TTAGGG-repeat specific FISH probe. Total DNA (in red) was stained with DAPI. Numbers in the bottom two panels indicate the frequency of chromosome end fusions scored in 2 independent experiments. At least 330 chromosomes were scored in each instance.

Live-cell imaging of dysfunctional telomeres in the presence and absence of 53BP1

To analyze the movement of dysfunctional telomeres in the presence and in the absence of 53BP1, time-lapse microscopy was performed on $TRF2^{F/-}53BP1^{+/-}$ and $TRF2^{F/-}53BP1^{-/-}$ cells, expressing eGFP-TRF1 and mCherry-BP1-2 markers, at 72-84 hours after introduction of Cre. At this early stage after deletion of TRF2, DNA damage foci had formed at telomeres but telomere fusions were not yet prominent so that most TRF1-marked sites represented free chromosome ends. Cells were monitored using a DeltaVision RT microscope installed with an environmental chamber that maintained the temperature at 37°C. Three-dimensional stacks of eGFP and mCherry signals encompassing a 5 μm Z-distance were acquired every 30 seconds. Images were subsequently digitally deconvolved and projected in two dimensions.

Originally, we had intended to analyze the relative behavior of telomeres over long periods of time (~6 hours). We wanted to address the frequency of synapsis between dysfunctional telomeres in the absence of 53BP1 and ask whether such associations persisted over time, giving rise to productive repair events, or dissociated prematurely. Such analysis was geared towards testing the 'glue' model for 53BP1 function. However, it was not possible to image MEFs under high magnification for prolonged periods of time due to their mobility. Instead, we settled for 20-minute imaging sessions, when cell motility was not a significant factor but fusion events were rarely observed. Nevertheless, at this stage, we could still obtain information on the dynamic behavior of individual dysfunctional telomeres.

Initial analysis of 20-minute movies indicated that in $TRF2^{F/-}53BP1^{+/-}$ cells, the telomeres exhibited a greater mobility after TRF2 deletion whereas the dysfunctional

telomeres in TRF2$^{F/-}$53BP1$^{-/-}$ cells appeared more static (Video 3-8). We observed occasional apparent fusion events (two telomeres joining and staying together during the imaging session) in 53BP1-proficient cells lacking TRF2 (Video 1). In contrast, no potential fusions were observed in 53BP1 deficient cells even for telomeres that were closely apposed at the beginning of the imaging session (Video 2). These crude observations suggested that there might be quantitative difference in the mobility of dysfunctional telomeres in 53BP1-proficient and 53BP1-deficient cells.

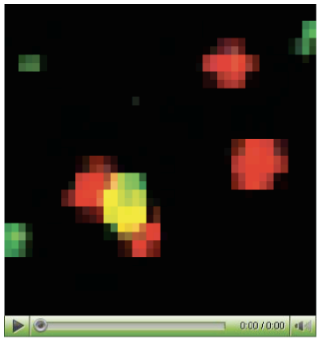
Video 1

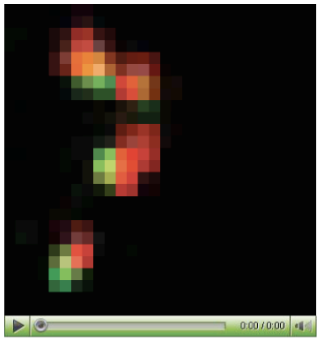
Video 2

Videos 1-2. Potential fusion events in TRF2$^{F/-}$53BP1$^{+/-}$ but not in TRF2$^{F/-}$53BP1$^{-/-}$ cells
The movies highlight telomeres undergoing a potential fusion reaction in a TRF2$^{F/-}$53BP1$^{+/-}$ cell (Video 1) or a group of closely apposed, but static telomeres in a TRF2$^{F/-}$53BP1$^{-/-}$ cell (Video 2). TRF2$^{F/-}$53BP1$^{+/-}$ and TRF2$^{F/-}$53BP1$^{-/-}$ cells were imaged 72 h after Hit&Run Cre infection. Z-stacks of eGFP-TRF1 [green] and mCherry-BP1-2 [red] signals were acquired every 30 sec over 20 min. Videos constructed from deconvolved and projected frames are supplemented in a DVD.

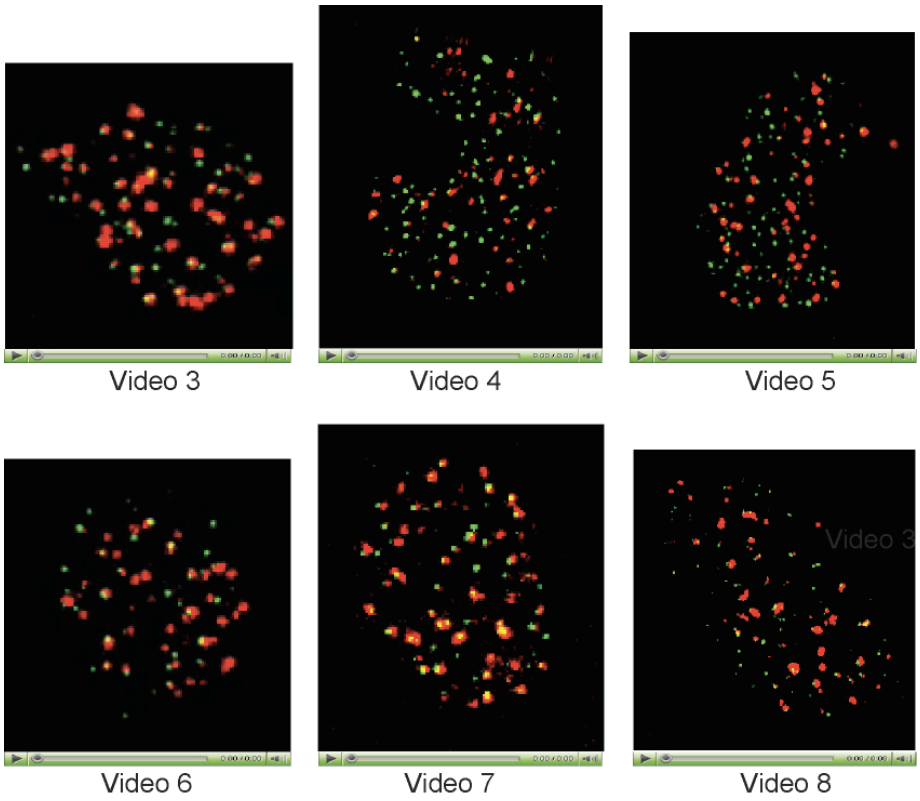

Videos 3-8. Dynamic movement of dysfunctional telomeres in 53BP1-proficient and 53BP1-deficient cells

Representative TRF2$^{F/-}$53BP1$^{+/-}$ (Videos 3-5) and TRF2$^{F/-}$53BP1$^{-/-}$ (Videos 6-8) cells imaged 72 h after Hit&Run Cre infection. Z-stacks of eGFP-TRF1 [green] and mCherry-BP1-2 [red] signals were acquired every 30 sec over 20 min. Videos constructed from deconvolved and projected frames are supplemented in a DVD.

Quantitative analysis of the movement of dysfunctional telomeres

To obtain a quantitative measure of telomere mobility, we tracked individual eGFP-TRF1-labeled dysfunctional telomeres that contained mCherry-BP1-2 within projected images using ImageJ software. Figure 4.12 shows telomeres tracked in representative nuclei of $TRF2^{F/-}53BP1^{+/-}$ and $TRF2^{F/-}53BP1^{-/-}$ cells, imaged 72 hours after Cre-mediated TRF2 deletion. As a control, eGFP-TRF1-marked functional telomeres in cells not treated with Cre were also examined. From each genotype and treatment, we chose at least 10 cells for analysis, and per cell, we focused on 5 representative telomeres. Only telomeres, which were continuously tracked for at least 18 out of 20 minutes were considered. The x and y coordinates were extracted for each telomere, at each time frame, and used to calculate two parameters – the cumulative distance traveled in 20 minutes and the maximal displacement from starting point recorded during the 20-minute imaging session. In order to correct for cell mobility, cells were registered using software that offset translational and rotational movements. To further manually correct for finer cell movements, the average x and y positions of all analyzed telomeres in a given cell were used as a reference point in the calculations (in literature also referred to as weight center). Telomeres that showed obvious aberrant synchronous movement due to local repositioning of part of the nucleus (see Figure 4.12b for example) were excluded from analysis.

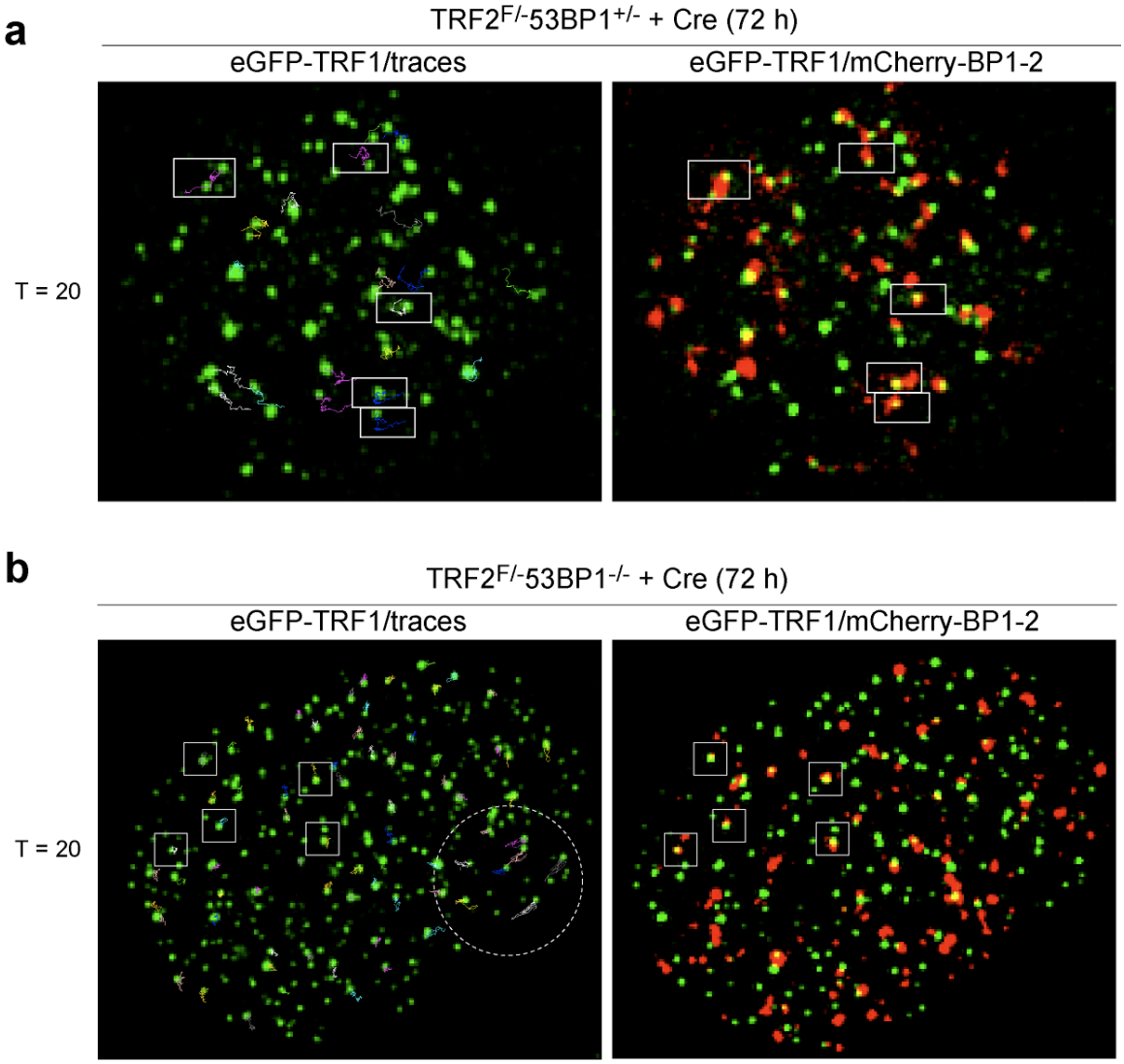

Figure 4.12 Tracking of individual dysfunctional telomeres in whole nuclei of 53BP1-proficient and 53BP1-deficient cells

a, (*Left*) Traces (multicolored) of individual eGFP signals (in green) tracked in a representative TRF2$^{F/-}$53BP1$^{+/-}$ cell, expressing eGFP-TRF1 and mCherry-BP1-2, imaged 72 hours after Hit&Run Cre retroviral infections. Snapshot is at t=20 minutes. (*Right*) Overlay of the eGFP (in green) and mCherry (in red) signals. Boxes indicate 5 eGFP-marked telomeres, which were chosen for further analysis based on two criteria. They co-localized with mCherry signals and were tracked for at least 18 minutes.

b, A representative TRF2$^{F/-}$ 53BP1$^{-/-}$ cell, presented as in **(a)**. Circle highlights telomeres that would be excluded from analysis due to aberrant movement of part of the nucleus.

53BP1 is required for increased mobility of deprotected telomeres

Detailed examination of tracks of individual functional and dysfunctional telomeres from TRF2$^{F/-}$53BP1$^{+/-}$ and TRF2$^{F/-}$53BP1$^{-/-}$ MEFs, imaged for 20 minutes (Figure 4.12) revealed two striking phenotypes. In the first place, we noted that in the 53BP1-proficient setting, dysfunctional telomeres were more dynamic than functional telomeres. This conclusion was made based on comparative visual analysis of telomere tracks (Figure 4.13a, *top*), which appeared to cover a greater territory in Cre-treated compared to untreated cells. In addition, there was a marked difference in the slopes of curves, which portrayed the cumulative distance travelled by individual telomeres as a function of time (Figure 4.13b, *top*). The slopes of curves derived from analysis of dysfunctional telomeres were steeper in comparison to the ones corresponding to functional telomeres, indicating faster movement. Second, we noticed that in 53BP1-deficient cells, the mobility of functional and dysfunctional telomeres differed less. Telomere tracks appeared similar in the absence and in the presence of telomere dysfunction in TRF2$^{F/-}$ 53BP1$^{-/-}$ MEFs (Figure 4.13a, *bottom*). Moreover, the slopes of curves, plotting cumulative distance traveled as a function of time, for representative functional and dysfunctional telomeres, were also indistinguishable in 53BP1-deficient cells (Figure 4.13b, *bottom*). These observations suggested that, in response to telomere dysfunction, chromosome ends become more mobile, and that this increase in dynamic behavior is dependent on 53BP1.

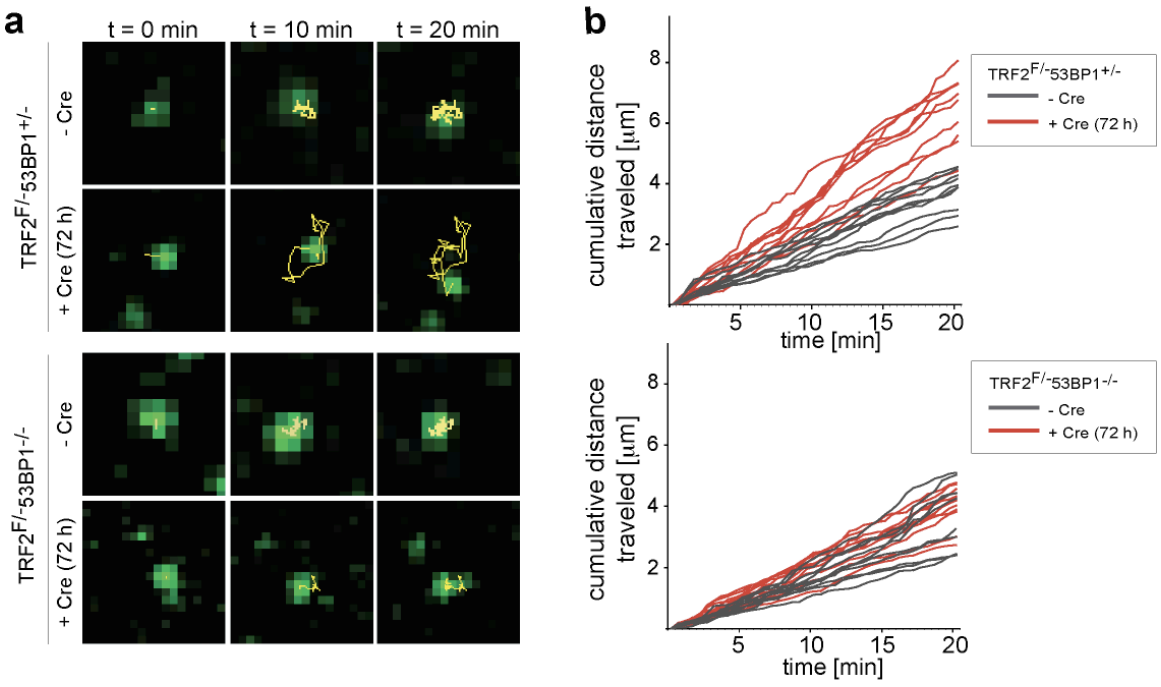

Figure 4.13. Tracking of individual telomeres

a, Representative traces (in yellow) of eGFP signals (in green) that also co-localized with mCherry in TRF2$^{F/-}$53BP1$^{+/-}$ and TRF2$^{F/-}$53BP1$^{-/-}$ MEFs, expressing eGFP-TRF1 and mCherry-BP1-2, imaged untreated or 72 hours post Hit&Run Cre retroviral infections. Snapshots were taken at indicated time points during a 20-minute imaging session.

b, Graphs of cumulative distance traveled by individual eGFP-marked telomeres, described in **(a)** plotted as a function of time.

These initial observations, made on individual telomeres, were confirmed when we analyzed statistically significant populations of functional and dysfunctional telomeres in cells of each genotype. The p-values were calculated using a two-tailed Mann-Whitney test (also referred to as rank sum test), which compares two unpaired groups without assuming Gaussian distribution.

We found that the behavior of functional telomeres in 53BP1-proficient and 53BP1-deficient cells was similar. Both traveled in a random walk over a total path of approximately 3.7-3.9 μm in a 20-minute imaging session (Figures 4.14a-c). The

calculated median speed, 180-190 nm/min^{-1}, is comparable to movement of human telomeres previously reported in [255]. In contrast, dysfunctional telomeres in Cre-treated TRF2$^{F/-}$53BP1$^{+/-}$ were significantly more mobile, traveling at a speed of 270-360 nm/min^{-1}, over a median cumulative distance ranging from 5.4 to 7.2 μm (Figures 4.14a, c). As expected from the visual observations above, the increased mobility associated with telomere dysfunction was attenuated in cells lacking 53BP1, resulting in a median cumulative distance traveled of 4.4±0.2 μm with a speed of 220 nm/min^{-1} (Figures 4.14b, c). These data established that telomeres become more mobile when they are deprived of their normal protection and that this change in their dynamic behavior is promoted by 53BP1.

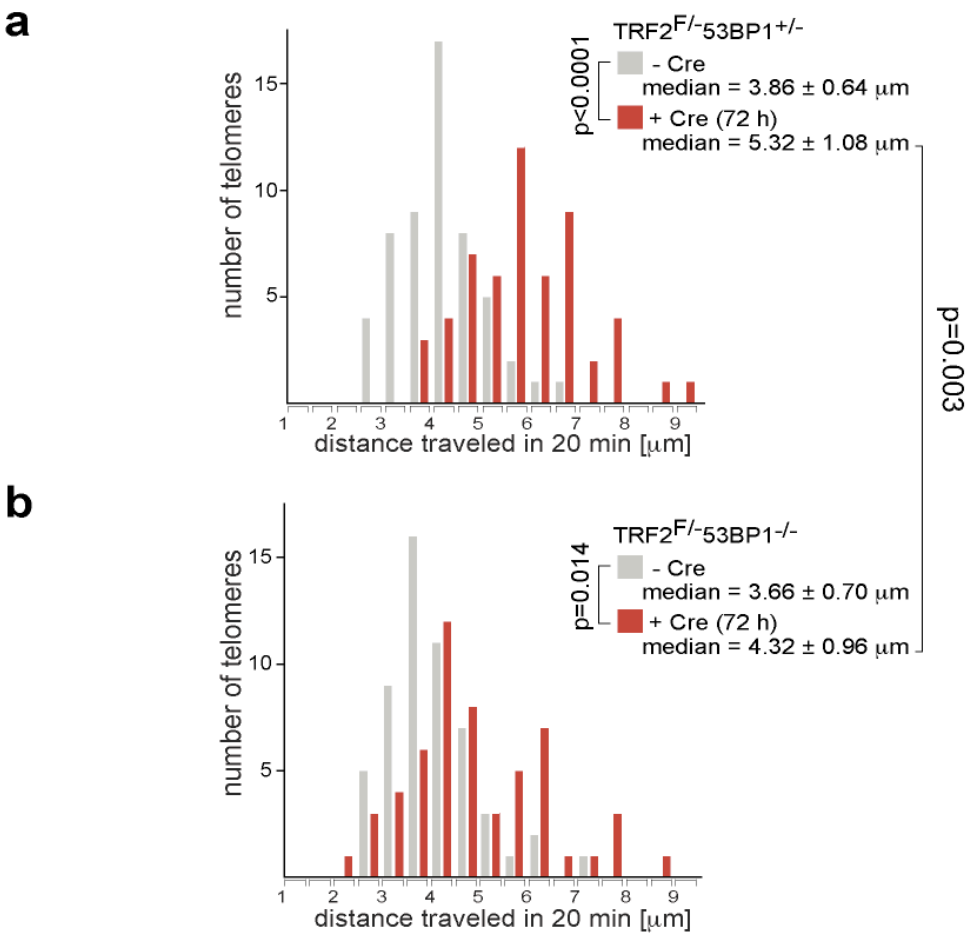

c

Summary: median speed [nm min^{-1}] and distance traveled in 20 min [μm]

	Experiment 1 (A/B)		Expt 2 (C/D)	Expt 3 (A/B)	Median ± SD
	- Cre (n=55)	+ Cre (72 h) (n=55)	+ Cre (72 h) (n=55)	+ Cre (72 h) (n=65)	+ Cre (72 h)
$TRF2^{F/-}$ $53BP1^{+/-}$	193 nm min^{-1}	271 nm min^{-1}	360 nm min^{-1}	268 nm min^{-1}	272 ± 40 nm min^{-1}
	3.86 ± 0.64 μm	5.43 ± 0.97 μm	7.19 ± 2.82 μm	5.36 ± 0.94 μm	5.43 ± 0.80 μm
$TRF2^{F/-}$ $53BP1^{-/-}$	182 nm min^{-1}	216 nm min^{-1}	244 nm min^{-1}	218 nm min^{-1}	218 ± 12 nm min^{-1}
	3.66 ± 0.70 μm	4.32 ± 1.13 μm	4.88 ± 1.28 μm	4.36 ± 0.70 μm	4.36 ± 0.24 μm

Figure 4.14. Effect of 53BP1 absence on the mobility of dysfunctional telomeres

a-b, Graph of the frequency distribution of the number of eGFP/mCherry-traced telomeres plotted against the cumulative distance they traveled in 20 minutes. **(a)** $TRF2^{F/-}53BP1^{+/-}$ and **(b)** $TRF2^{F/-}53BP1^{-/-}$ MEFs, expressing eGFP-TRF1 and mCherry-BP1-2 markers were imaged untreated (grey bars) or 72 hours post Hit&Run Cre retroviral infections (red bars). 55 telomeres

in 11 cells were analyzed for each genotype and treatment. The median values and s.d. are indicated. P-values were calculated using a two-tailed Mann-Whitney test.
c, Summary of the median speed and median cumulative distance traveled in 20 minutes, recorded in three independent imaging sessions. Cells with the indicated genotypes, expressing eGFP-TRF1 and mCherry-BP1-2 markers were imaged at 72 hours after mock or Hit&Run Cre infections. The difference between experiments 1/3 and experiment 2 might be due to the different cell lines used ((A/B) vs (C/D) as indicated).

53BP1 functions to expand the two dimensional territory that dysfunctional telomeres sample

We also examined the maximum displacement from their starting point for individual telomeres during a 20-minute imaging session, which is a measure for the territory that these telomeres sampled. Previous data have indicated that chromosomal sites have a limited range of motion, showing constrained diffusion within a territory with a diameter ≤0.5 μm [255,256]. We asked whether functional telomeres were similarly constrained. Indeed, we found that functional telomeres in $TRF2^{F/-}53BP1^{+/-}$ and $TRF2^{F/-}53BP1^{-/-}$ MEFs sampled territories with comparable median diameters of 0.51-0.53 μm (Figure 4.15a-c). Next, we determined whether dysfunctional telomeres had the dynamic potential to explore larger nuclear compartments compared to functional telomeres. Noticeably, induction of telomere dysfunction in $TRF2^{F/-}53BP1^{+/-}$ cells caused a 2-fold increase in the median maximum displacement. Whereas functional telomeres in 53BP1-proficient cells were constrained within a territory with a median diameter of 0.51±0.29 μm, dysfunctional telomeres moved within a significantly larger region with a median diameter of 1.2±0.3 μm (Figures 4.15a, c). Again, 53BP1 deficiency affected the extent of territory expansion upon induction of telomere dysfunction. For dysfunctional

telomeres in TRF2$^{F/-}$53BP1$^{-/-}$ cells, we calculated that the median maximum displacement from their starting point only slightly increased to 0.8±0.15 μm (Figures 4.15b, c). These data established that 53BP1 also functions to expand the territories explored by dysfunctional telomeres.

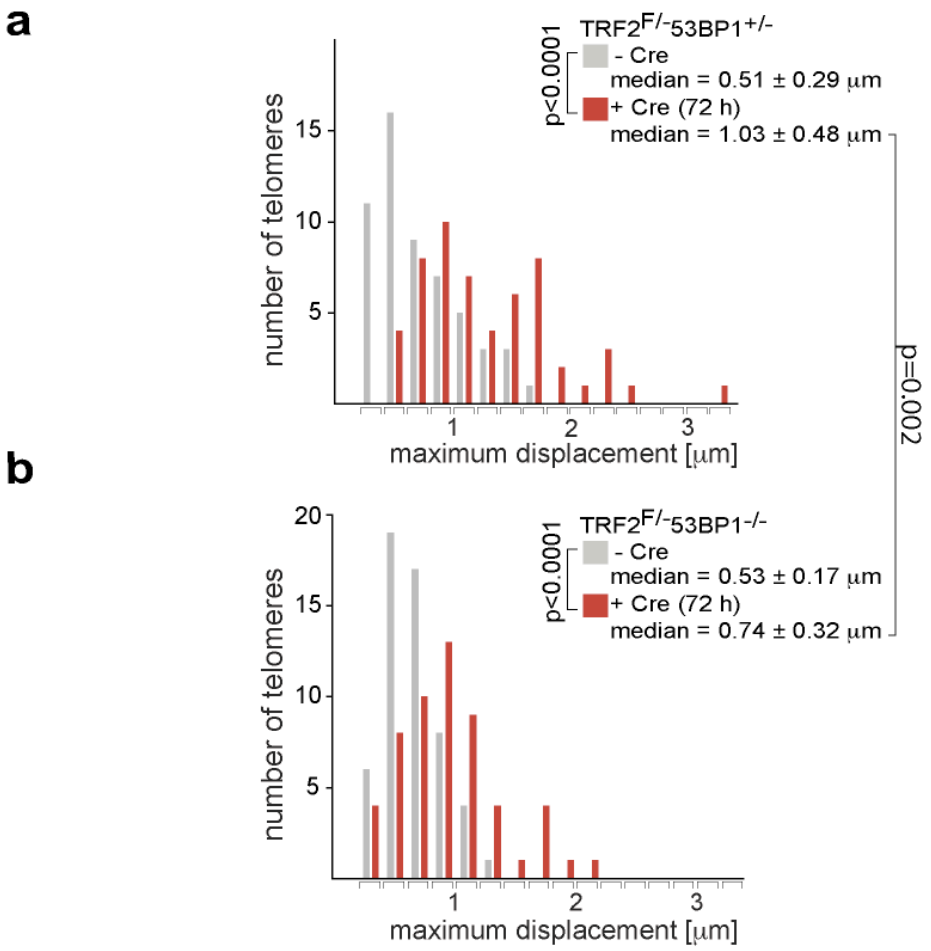

c Summary: median maximum displacement from starting point in 20 min [μm]

	Experiment 1 (A/B)		Expt 2 (C/D)	Expt 3 (A/B)	Median ± SD
	- Cre (n=55)	+ Cre (72 h) (n=55)	+ Cre (72 h) (n=55)	+ Cre (72 h) (n=65)	+ Cre (72 h)
TRF2F/- 53BP1+/-	0.51 ± 0.29 μm	1.03 ± 0.48 μm	1.7 ± 0.98 μm	0.99 ± 0.39 μm	1.24 ± 0.31 μm
TRF2F/- 53BP1-/-	0.53 ± 0.17 μm	0.74 ± 0.32 μm	1.02 ± 0.81 μm	0.64 ± 0.22 μm	0.8 ± 0.15μm

Figure 4.15. Effect of 53BP1 absence on the size of the territory sampled by dysfunctional telomeres

a-b, Graph of the frequency distribution of the number of eGFP/mCherry-traced telomeres plotted against maximum displacement from starting point registered in 20 minutes. **(a)** TRF2$^{F/-}$53BP1$^{+/-}$ and **(b)** TRF2$^{F/-}$53BP1$^{-/-}$ MEFs, expressing eGFP-TRF1 and mCherry-BP1-2 markers

were imaged untreated (grey bars) or 72 hours post Hit&Run Cre retroviral infections (red bars). 55 telomeres in 11 cells were examined for each genotype and treatment. The median values and s.d. are indicated. P-values were calculated based on a two-tailed Mann-Whitney test.
c, Summary of maximum displacement from starting point registered in 20 minutes, from three independent imaging sessions, recorded 72 hours after mock or Hit&Run Cre infections. Cells with the indicated genotypes expressed the eGFP-TRF1 and mCherry-BP1-2 markers. The difference between experiments 1/3 and experiment 2 might be due to the different cell lines used ((A/B) vs (C/D) as indicated).

mCherry-BP1-2 is a neutral marker

The presence of the mCherry-BP1-2 DNA damage marker did not affect the outcome. Comparable cumulative distance and maximum displacement results were obtained after deletion of TRF2 from 53BP1$^{+/-}$ or 53BP1$^{-/-}$ cells that expressed the eGFP-TRF1 marker but lacked the 53BP1 fragment (Figure 4.16a, b; Videos 9-16).

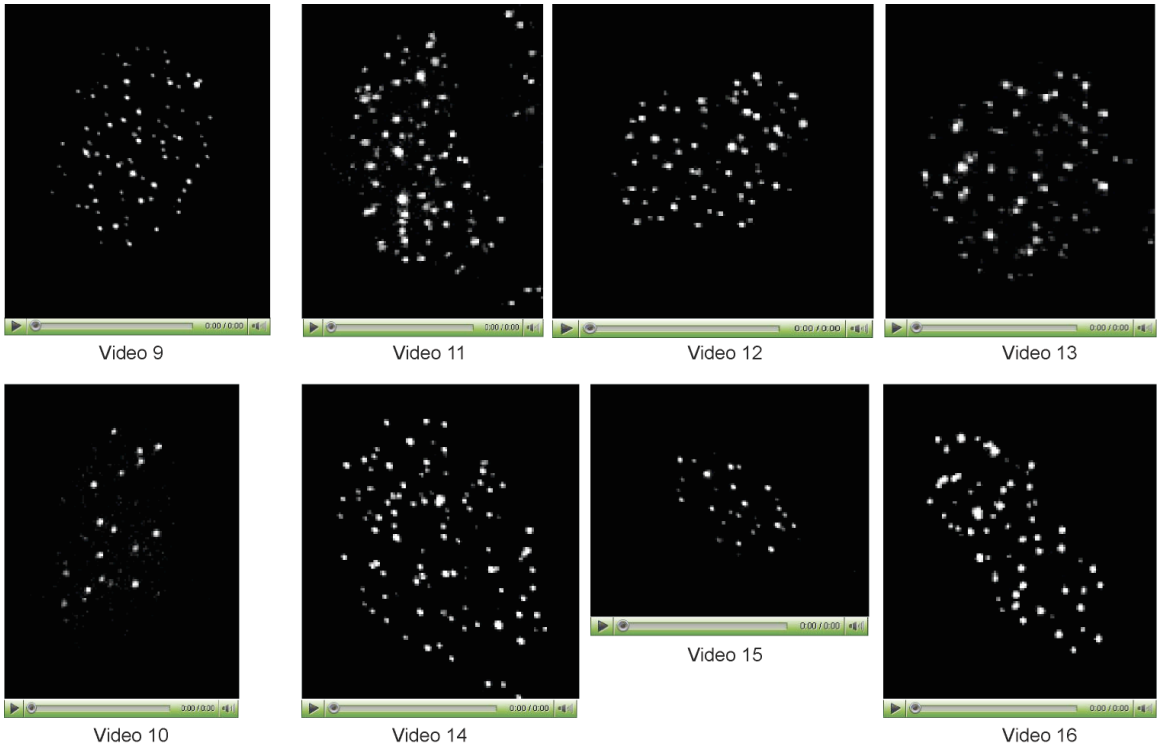

Videos 9-16. Dynamic movement of functional and dysfunctional telomeres in 53BP1-proficient and 53BP1-deficient cells in the absence of mCherry-BP1-2

Representative TRF2$^{F/-}$53BP1$^{+/-}$ (Videos 9, 11-13) and TRF2$^{F/-}$53BP1$^{-/-}$ (Videos 10, 14-16) cells were imaged untreated (Videos 9-10) or 72 h after Hit&Run Cre infection (Videos 11-16). Z-stacks of eGFP-TRF1 signal were acquired every 30 sec over 20 min. Videos constructed from deconvolved and projected frames are supplemented in a DVD.

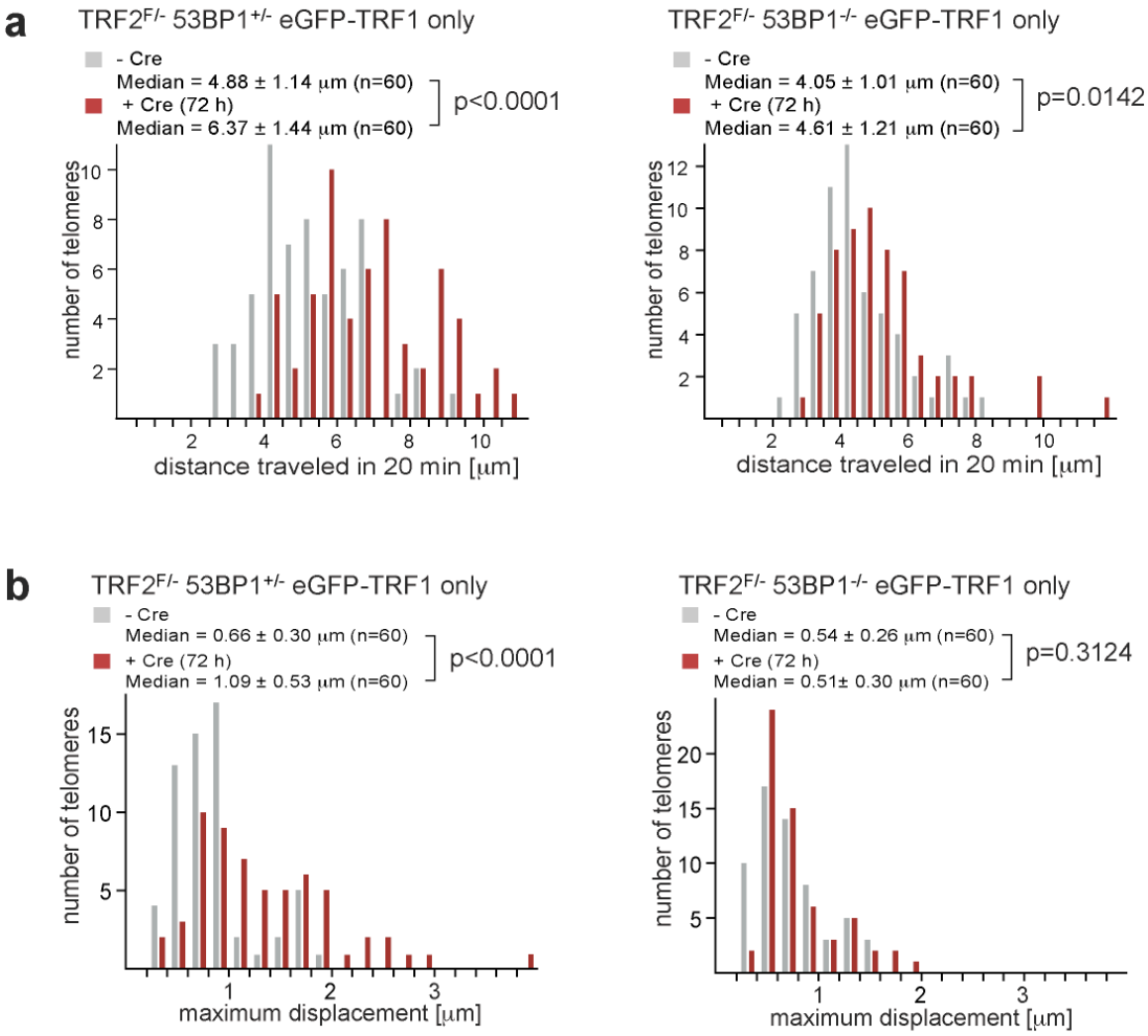

Figure 4.16. Confirmation of results in cells expressing mCherry-BP1-2 marker

a, Graph of the frequency distribution of the number of eGFP-traced telomeres plotted against the cumulative distance they traveled in 20 minutes. (*left*) TRF2$^{F/-}$53BP1$^{+/-}$ and (*right*) TRF2$^{F/-}$53BP1$^{-/-}$ MEFs, expressing eGFP-TRF1 only, were imaged untreated (grey bars) or 72 hours post Hit&Run Cre retroviral infections (red bars). 60 telomeres in 12 cells were analyzed for each genotype and treatment. The median values and s.d. are indicated. P-values were calculated based on a two-tailed Mann-Whitney test.

b, Graph of the frequency distribution of the number of eGFP-traced telomeres plotted against maximum displacement from starting point registered in 20 minutes in cells from **(a)**.

Outliers may determine the rate of NHEJ of dysfunctional telomeres

The median results described above were derived from analysis of populations of telomeres. When we looked at the maximum displacement of individual telomeres, we noticed that a substantial fraction (>10%) of the dysfunctional telomeres in 53BP1-proficient cells roamed well beyond 2 μm whereas none of the 115 functional telomeres analyzed moved beyond that distance (Figure 4.15 and 4.16). When 53BP1 was not present, not only the median maximum displacement diminished, but also only one out of 115 dysfunctional telomeres in 53BP1 null cells sampled an area beyond 2 μm. Given that the diameter of an average MEF nucleus is 20 μm, dysfunctional telomeres, for which we recorded a maximum displacement from their starting point greater than 2 μm in 20 minutes, would have the capacity to probe a significant fraction of the nuclear volume over the course of G1 (6 hours), when NHEJ of dysfunctional telomeres takes place [237]. Assuming that the rate of NHEJ correlates with the probability of an encounter between two telomeres, the ability of 53BP1 to expand the territory visited by dysfunctional telomeres could be an explanation for its effect on telomere fusion.

Preliminary MSD analysis further corroborated this conclusion. The area covered by the most mobile dysfunctional telomeres in 53BP1-proficient cells was found to increase proportionally to time, whereas dysfunctional telomeres in 53BP1-deficient cells remained corralled within limited territories that did not expand as a function of time (Figure 4.17). We propose that the telomeres sampling the largest territories have the greatest chance of meeting a fusion partner, and thereby undergo NHEJ repair.

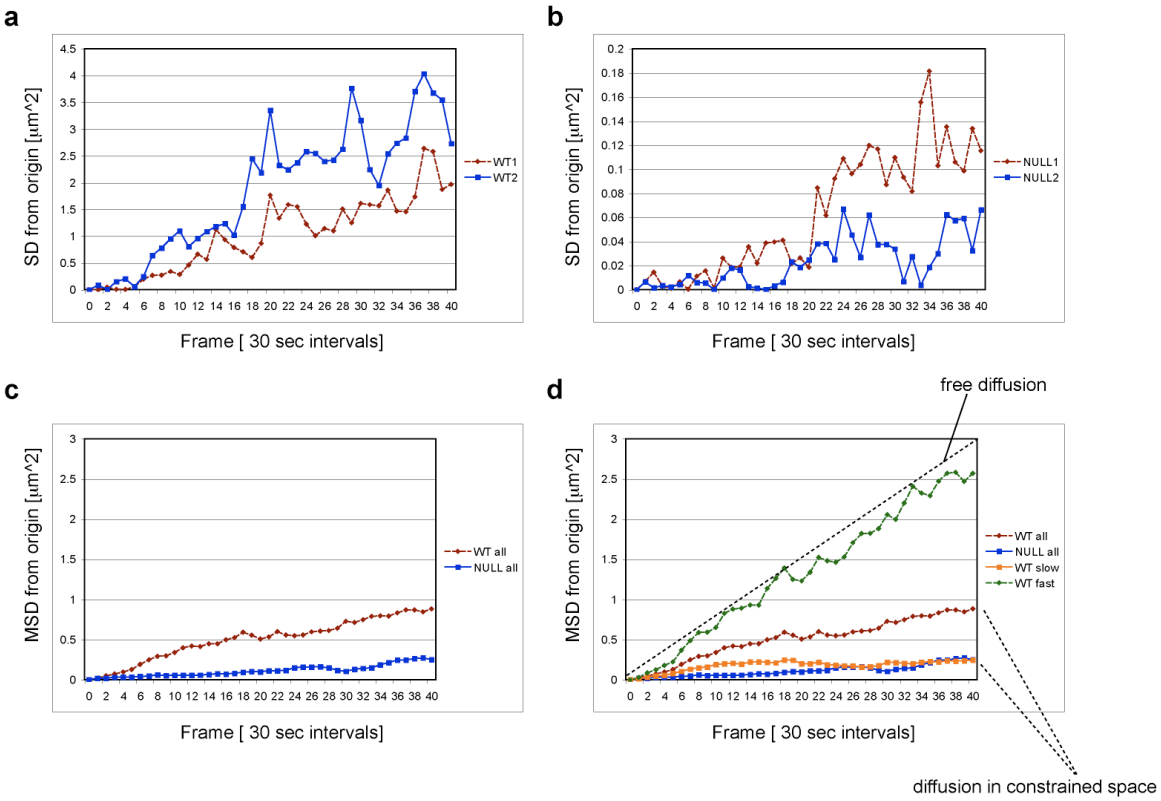

Figure 4. 17. MSD analysis

a-b, Graph of the square displacement (SD) of two representative eGFP-traced telomeres, imaged in TRF2$^{F/-}$53BP1$^{+/-}$ **(a)** or TRF2$^{F/-}$53BP1$^{-/-}$ **(b)** MEFs at 72 hours after Hit&Run Cre retroviral infection, plotted against time. The displacement from starting position (t=0) was calculated at each time-point (frame), squared, and plotted against time. The plots depict the random back and forth movement of individual telomeres

c, Graph of the mean square displacement (MSD) of 60 eGFP-traced telomeres, imaged in TRF2$^{F/-}$53BP1$^{+/-}$ (red line) or TRF2$^{F/-}$53BP1$^{-/-}$ (blue line) MEFs at 72 hours after Hit&Run Cre retroviral infection, plotted against time. For each telomere, the displacement from starting position (t=0) was calculated at each time-point (frame) and squared. The mean value for 60 telomeres in each cell line was plotted against time. Plots indicate that although individual telomeres can have eratic motion **(a, b)**, on average, telomeres tend to move away from starting point as time progresses.

d, Same as in **(c)** but telomeres from TRF2$^{F/-}$53BP1$^{+/-}$ MEFs were separated in two populations, fast (24 telomeres, green line) and slow (36 telomeres, orange line). The movement of the fast telomeres has the characteristics of free diffusion (dashed line). On the other hand, the plot of the

slow telomeres overlaps with the plot of the telomeres imaged in TRF2$^{F/-}$53BP1$^{-/-}$ MEFs (blue line. The plateau these plots reach is characteristics for diffusion in constrained space.

ATM, but not DNA ligase IV, is required for increased mobility of deprotected telomeres

Since cells lacking 53BP1 failed to execute NHEJ of dysfunctional telomeres, we tested whether the absence of the NHEJ reaction itself might explain the slower movement of the telomeres. To test this hypothesis, we introduced the eGFP-TRF1 telomere marker into TRF2$^{F/-}$lig4$^{-/-}$p53$^{-/-}$ MEFs, which are impaired for NHEJ. As before, we performed live-cell imaging with these cells at 72 hours after mock or Hit&Run Cre retroviral infections. Similarly to what we observed above in TRF2$^{F/-}$53BP1$^{+/-}$ cells, eGFP-TRF1-marked telomeres in TRF2$^{F/-}$lig4$^{-/-}$p53$^{-/-}$ cells exhibited a considerable increase in their mobility upon TRF2 deletion. Whereas functional telomeres in these cells traveled over a median distance of 3.94±0.81 μm in 20 minutes and covered territory with a diameter of 0.34±0.15 μm, dysfunctional telomeres traveled over a median distance of 5.16±1.36 μm in 20 minutes and doubled the median diameter of their territory to 0.68±0.32 μm (Figure 4.18a, c, d). Therefore, with respect to the dynamic behavior exhibited by dysfunctional telomeres, DNA ligase IV deficiency did not appear to make a difference, despite its essential role in NHEJ. We concluded that the attenuation in the movement of the dysfunctional telomeres in 53BP1-deficient cells was not due to lack of their processing by NHEJ.

On the other hand, we hypothesized that ATM kinase, the upstream regulator of 53BP1, which is required for efficient telomere fusions, may also be involved in promoting the mobility of dysfunctional telomeres. To test this model, we performed

time-lapse microscopy with TRF2$^{F/-}$ATM$^{-/-}$ cells, expressing the eGFP-TRF1 telomere marker. As before, we imaged live cells untreated or 72 hours after Cre-mediated TRF2 deletion. Indeed, in absence of ATM, dysfunctional telomeres failed to gain their maximal mobility. In Cre-treated TRF2$^{F/-}$ATM$^{-/-}$ cells, the median cumulative distance traveled by dysfunctional telomeres in 20 minutes was 3.93±1.11 μm (Figure 4.18b, c), similar to the range of motion we recorded for functional telomeres in ATM-deficient cell, 3.44±0.68 μm. The difference between the territories covered by functional and dysfunctional telomeres in ATM-deficient cells was also not significant (Figure 4.18d). Thus, one mechanism by which ATM signaling may promote NHEJ is through 53BP1.

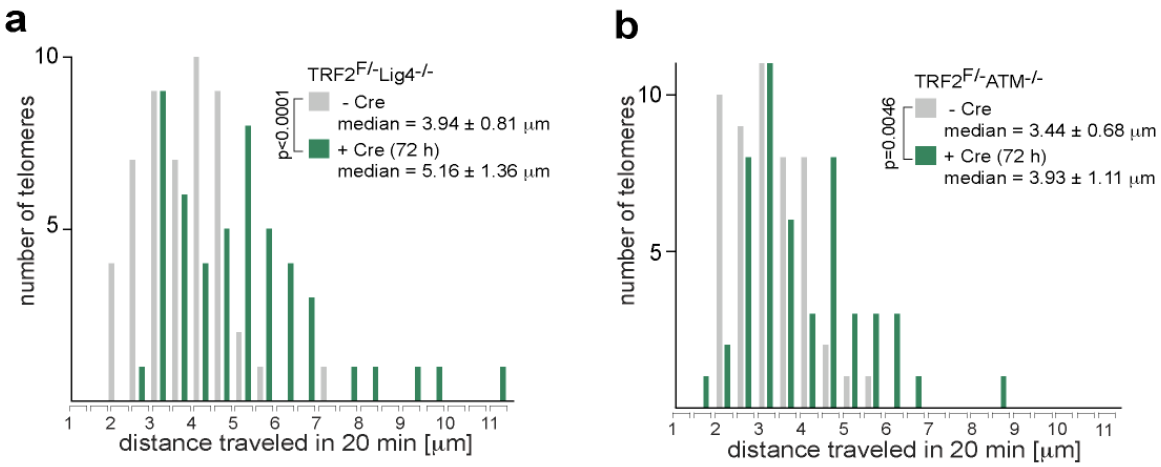

c Summary: median speed [nm min^{-1}] and distance traveled in 20 min [μm]

	Experiment 1		Experiment 2	
	- Cre (n=50)	+ Cre (72 h) (n=50)	- Cre (n=50)	+ Cre (72 h) (n=50)
TRF2$^{F/-}$ Lig4$^{-/-}$ p53$^{-/-}$	197 nm min^{-1} 3.94 ± 0.81 μm	258 nm min^{-1} 5.16 ± 1.36 μm	192 nm min^{-1} 3.83 ± 0.66 μm	266 nm min^{-1} 5.32 ± 1.43 μm
TRF2$^{F/-}$ ATM$^{-/-}$	172 nm min^{-1} 3.44 ± 0.68 μm	197 nm min^{-1} 3.93 ± 1.11 μm	210 nm min^{-1} 4.19 ± 0.99 μm	186 nm min^{-1} 3.71 ± 0.76 μm
TRF2$^{F/-}$ ATM$^{+/-}$				267 nm min^{-1} 5.34 ± 1.31 μm

d Summary: median maximum displacement from starting point in 20 min [μm]

	Experiment 1		Experiment 2	
	- Cre (n=50)	+ Cre (72 h) (n=50)	- Cre (n=50)	+ Cre (72 h) (n=50)
TRF2$^{F/-}$ Lig4$^{-/-}$ p53$^{-/-}$	0.34 ± 0.15 μm	0.68 ± 0.32 μm	0.43 ± 0.20 μm	0.69 ± 0.34 μm
TRF2$^{F/-}$ ATM$^{-/-}$	0.38 ± 0.15 μm	0.49 ± 0.22 μm	0.47 ± 0.21 μm	0.55 ± 0.26 μm
TRF2$^{F/-}$ ATM$^{+/-}$				0.63 ± 0.34 μm

Figure 4. 18. Effect of ATM or DNA ligase IV deficiency on the dynamics of dysfunctional telomeres

a-b, Graphs of the frequency distribution of the number of eGFP-traced telomeres plotted against the cumulative distance they traveled in 20 minutes. **(a)** TRF2$^{F/-}$Lig4$^{-/-}$p53$^{-/-}$ and **(b)** TRF2$^{F/-}$ATM$^{-/-}$ MEFs, expressing eGFP-TRF1, were imaged untreated (grey bars) or 72 hours post Hit&Run Cre retroviral infections (green bars). 50 telomeres in 10 cells were examined for each genotype

and treatment. The median values and s.d. are indicated. P-values were calculated using a two-tailed Mann-Whitney test.
c-d, Summary of **(c)** median speed and median cumulative distance traveled in 20 minutes and **(d)** median maximum displacement from starting point registered in 20 minutes, from two independent experiments, performed 72 hours after mock or Hit&Run Cre infections of cells with the indicated genotypes, expressing eGFP-TRF1.

Increased mobility is a local event, limited to the chromatin surrounding a DSB

Next, we tested whether the increase in mobility was limited to the damaged chromatin as would be expected if 53BP1 acts locally. We reasoned that if chromatin mobility was a global response to DNA damage, functional telomeres should become more mobile upon the induction of damage elsewhere in the genome. We used a modest amount of IR (1 Gy) to induce ~100 chromosome-internal DSBs and examined the mobility of chromosome ends, tagged with the telomeric marker eGFP-TRF1. We tracked telomeres immediately after the induction of DNA damage, or after 2 hours recovery. In both cases, we found that the mobility of the telomeres was unaffected by IR arguing that increased mobility is a local event taking place at the site of damage where 53BP1 accumulates (Figure 4.19).

It could be argued that since dysfunctional telomeres have been eliciting a DNA damage signal continuously for two days prior to imaging, the chromatin might be in an altered state. This model is contradicted by evidence suggesting that TIF factors are constantly exchanged between the chromatin and the nucleoplasmic pool, and therefore TIFs are always "freshly" assembled [83]. The ideal experiment to test whether telomere dysfunction affects global chromatin behavior would be to examine a random genomic locus in the presence or absence of telomere dysfunction. However, we could not perform

this experiment because we did not have an appropriate fluorescently-labeled marker. Instead we analyzed the dynamics of protected telomeres after the induction of genome wide damage by IR in the absence of a functional NHEJ repair pathway by tracing the mobility of eGFP-TRF1-containing telomeres in irradiated lig4$^{-/-}$p53$^{-/-}$ cells (Figure 4.19, green bars). Our results clearly indicate that the presence of unrepaired DSBs for extended periods of time did not affect the mobility of telomeres (as an example of undamaged chromatin).

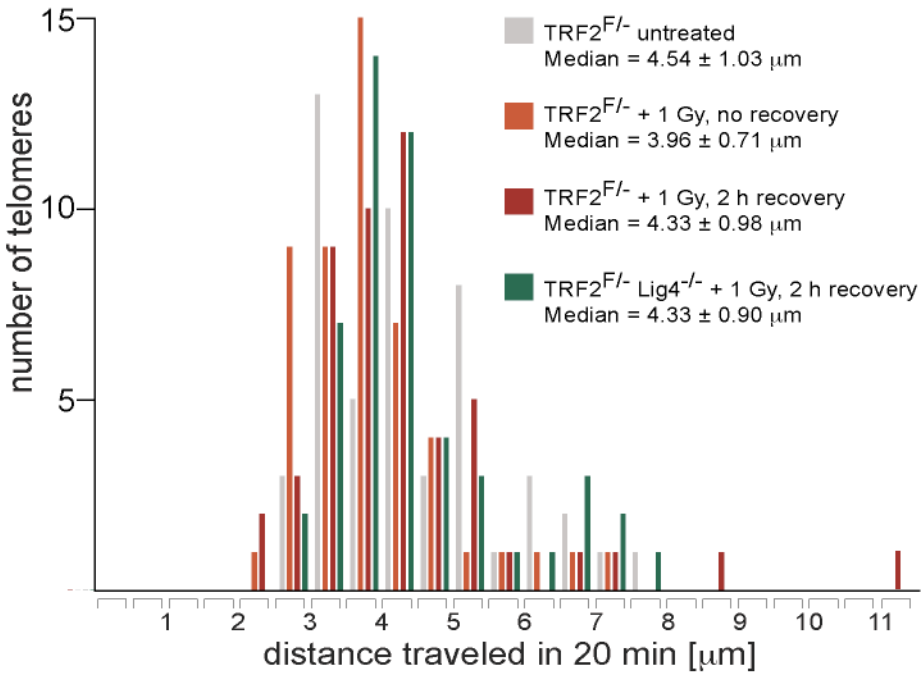

Figure 4.19. Increased mobility is a local event

Graph of the frequency distribution of the number of eGFP-traced telomeres plotted against the cumulative distance they traveled in 20 minutes. TRF2$^{F/-}$ or TRF2$^{F/-}$lig4$^{-/-}$p53$^{-/-}$ cells, expressing eGFP-TRF1 telomere marker, untreated (grey) or treated with 1 Gy of γ-irradiation, were imaged for 20 minutes immediately after irradiation (orange) or after 2 hours of recovery (red and green). 50 in 10 cells telomeres were examined for each treatment. The median values and s.d. are indicated.

Summary of findings in Chapter 4

In this chapter, we uncovered a novel aspect of the NHEJ repair of dysfunctional telomeres. We found that telomere NHEJ is dependent on the DNA damage response factor, 53BP1, which localized to H4-K20diMe and γ-H2AX/MDC1-containing chromatin at TIFs. We established that the interactions of 53BP1 with chromatin modifications were required not only for its stable association with dysfunctional telomeres, but also for its role in promoting NHEJ of deprotected chromosome ends.

In the second part of the chapter, we described a live-cell imaging assay, in which we could quantitatively analyze the dynamic features of sites of DSBs (dysfunctional telomeres) before and after the induction DNA damage (TRF2-deletion induced telomere dysfunction). The hypothesis we tested was based on the argument that the homogeneous distribution of dysfunctional telomeres throughout the nucleus in G1 impedes NHEJ, which requires close proximity of its substrates. Therefore, we reasoned that a mechanism must exist to translocate telomeres within the nucleus in order to establish fusion partners. In confirmation, we found that induction of telomere dysfunction activated a 53BP1-dependent mechanism, which promoted the dynamic behavior of telomeric sites, increasing both their speed and the diameter of their territory by a factor of two. In addition, we found that ATM but not DNA ligase IV contributed to this pathway. In the following chapter we have probed the mechanism by which 53BP1 promotes the dynamic behavior of dysfunctional telomeres.

CHAPTER 5: DISSECTING THE MECHANISM THAT PROMOTES MOBILITY OF DYSFUNCTIONAL TELOMERES

Introduction

In the previous chapter, we presented data suggesting that upon deprotection, the dynamic behavior of telomeres alters. We showed that while functional telomeres explore limited territories within the nucleus, chromosome ends perceived as DSBs acquire increased mobility and sample larger territories. We suggested that this active behavior, promoted by 53BP1, directly augments the probability that two dysfunctional telomeres encounter each other. In this chapter we examine in more detail the nature of the increased mobility of dysfunctional telomeres and address the pathways that might be responsible for promoting the dynamic behavior of unrepaired sites of DNA damage.

Increased mobility of dysfunctional telomeres is not specific to TRF2 deletion

In the first place, we tested whether increased mobility of dysfunctional telomeres is specific to TRF2 deletion and the resulting activation of the ATM-dependent DNA damage-signaling pathway. We examined another instance of telomere dysfunction, induced by POT1a/b deletion, which activates ATR signaling and leads to the accumulation of 53BP1 at dysfunctional telomeres [197,228].

We introduced eGFP-TRF1 and mCherry-BP1-2 markers into $POT1a^{F/-}POT1b^{F/S}$ MEFs and performed live-cell imaging 72 hours after Cre-mediated deletion of POT1a/b. As before, in cells treated with Hit&Run Cre, we tracked eGFP-TRF1-containing

dysfunctional telomeres that co-localized with mCherry-BP1-2 signals, and compared their mobility to eGFP-TRF1-marked functional telomeres in cells that were not treated with Cre (Figure 5.1a). The median cumulative distance traveled by POT1a/b-depleted telomeres in 20 minutes was 4.8±0.9 μm, while POT1a/b-containing telomeres covered only 3.2±0.7 μm during the same time period (Figure 5.1b). The analysis, however, was complicated by the fact that cells lacking POT1a/b had undergone massive endoreduplication, a known consequence of POT1a/b loss [197]. The unresolved association of sister chromatids may have limited the mobility of chromosome ends and therefore, the results were difficult to interpret. Nevertheless, the increase in mobility was statistically significant (Mann-Whitney test; $p<0.0001$) (Figure 5.1b; Videos 26-27).

Based on these data, we concluded that increased mobility of dysfunctional telomeres is most likely not limited to TRF2-deletion but can occur as a consequence of POT1a/b loss as well. These experiments also suggest that both ATM and ATR signaling can activate this pathway, most likely through γ-H2AX phosphorylation, which in turn plays a crucial role in the recruitment of 53BP1.

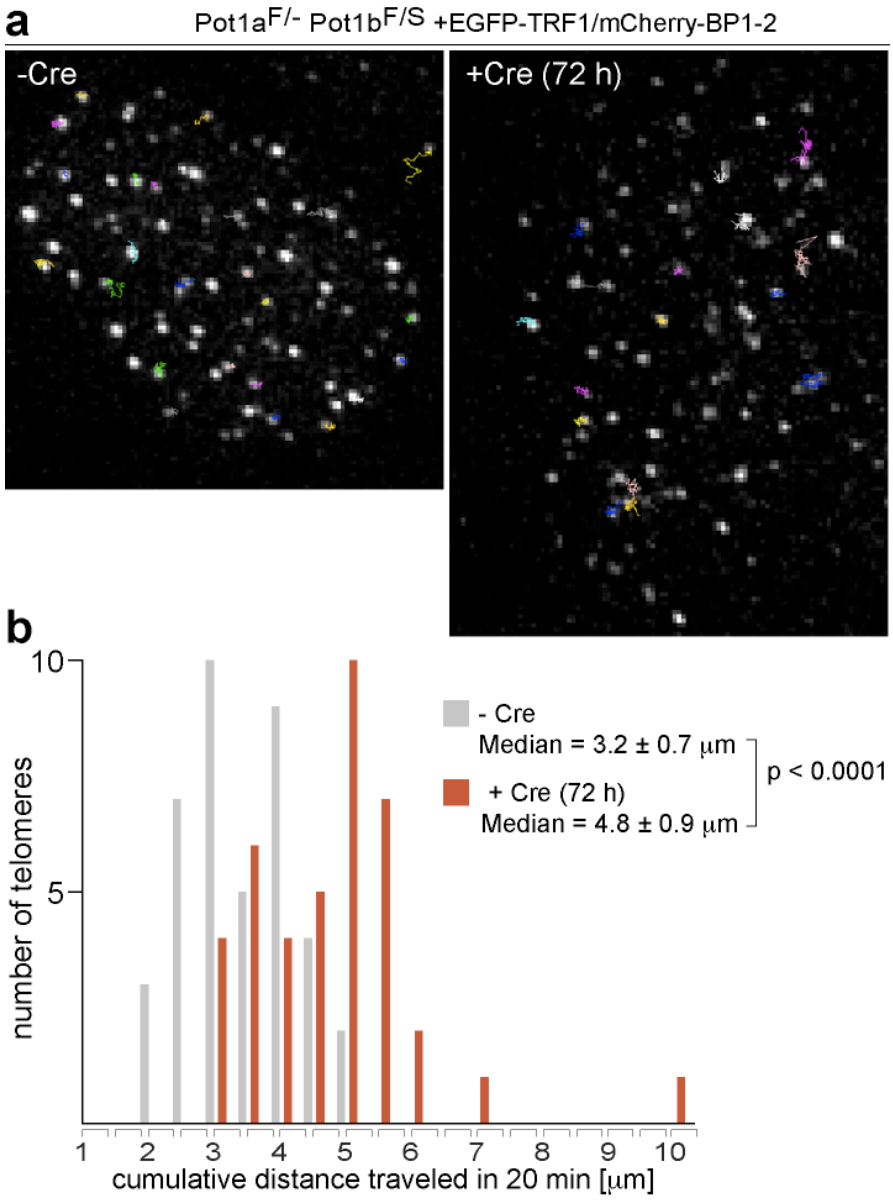

Figure 5.1. Effect of POT1a/b deletion on the mobility of dysfunctional telomeres

a, Traces (multicolored) of individual eGFP-marked telomeres (in white) tracked for 20 minutes in a representative POT1a$^{F/-}$POT1b$^{F/S}$ cell, expressing eGFP-TRF1 and mCherry-BP1-2 markers, imaged (*Left*) untreated (Video 26) or (*Right*) 72 hours after Hit&Run Cre retroviral infections (Video 27). Videos are supplemented in a DVD.

b, Graph of the frequency distribution of the number of eGFP/mCherry-traced telomeres plotted against the cumulative distance they traveled in 20 minutes. 40 telomeres from 8 cells were analyzed in MEFs treated as described in **(a)**. The median values and s.d. are indicated. P-value was calculated using a two-tailed Mann-Whitney test.

53BP1 does not affect the thermal persistence length of the chromatin fiber

As described in Chapter 4, 53BP1 requires extensive contacts with chromatin modifications in order to efficiently execute its role in promoting NHEJ. When the binding between 53BP1 and H4-K20diMe is disrupted or when the interaction mediated through γ-H2AX/MDC1 is impaired, NHEJ of dysfunctional telomeres occurs inefficiently and with delayed kinetics. Furthermore, when both contacts are removed simultaneously, NHEJ is drastically inhibited; strongly arguing that 53BP1 needs to be chromatin-bound in order to promote the repair of dysfunctional telomeres.

We asked whether 53BP1 might be involved in altering chromatin compaction when bound at sites of DNA damage. We imagined that the increased dynamics of dysfunctional telomeres might be due to a change in the rigidity of the chromatin fiber. In this scenario, the mobility we observe is not due to a dynamic, active process, but a consequence of the intrinsic characteristics (thermal persistence length) of the chromatin fiber at the site of damage. Of particular interest in this regard are residues located in the vicinity of H4-K20. Acetylation at H4-K16 has been implicated in altering the higher order chromatin structure by preventing compaction *in vitro* [257]. It is possible that when 53BP1 is bound to chromatin, it might promote or prevent this histone modification, thus regulating the higher order status of the nucleosome array. Alternatively, 53BP1 could function similarly to the transcriptional repressor L3MBTL1, which has been shown to compact chromatin through its association with histone methylation marks, including H4-K20diMe among others [258].

Following a protocol that has previously been used to demonstrate that gene-rich domains are enriched for open chromatin fibers[259,260], we performed sucrose gradient

fractionation of chromatin isolated from TRF2$^{F/-}$53BP1$^{+/-}$ and TRF2$^{F/-}$53BP1$^{-/-}$ MEFs, untreated or 96 hours after Cre-mediated deletion of TRF2. In this protocol, chromatin fragments are separated based on their shape as well as their size. Open/unstructured chromatin sediments slower compared to compact/rigid chromatin fibers despite having the same length of DNA. Following micrococcal nuclease (MNase) digestion and gradient sedimentation, we resolved the DNA fractions on agarose gel and hybridized to a telomere-specific probe to analyze the telomeric chromatin (Figure 5.2). As a control, we hybridized to a general (Bam) repeat-specific probe to detect bulk genomic DNA (Figure 5.2). As previously reported, we noted that the nucleosome ladder in telomeric chromatin was more diffuse in the top (small molecular weight) fractions compared to bulk chromatin [261]. However, we did not observe any difference in the structure of the chromatin fiber between functional and dysfunctional telomeres, consistent with [262]. In addition, no detectable distinction was noted between 53BP1-proficient and 53BP1-deficient cells. These findings suggested that 53BP1 does not alter the persistence length of the chromatin fiber.

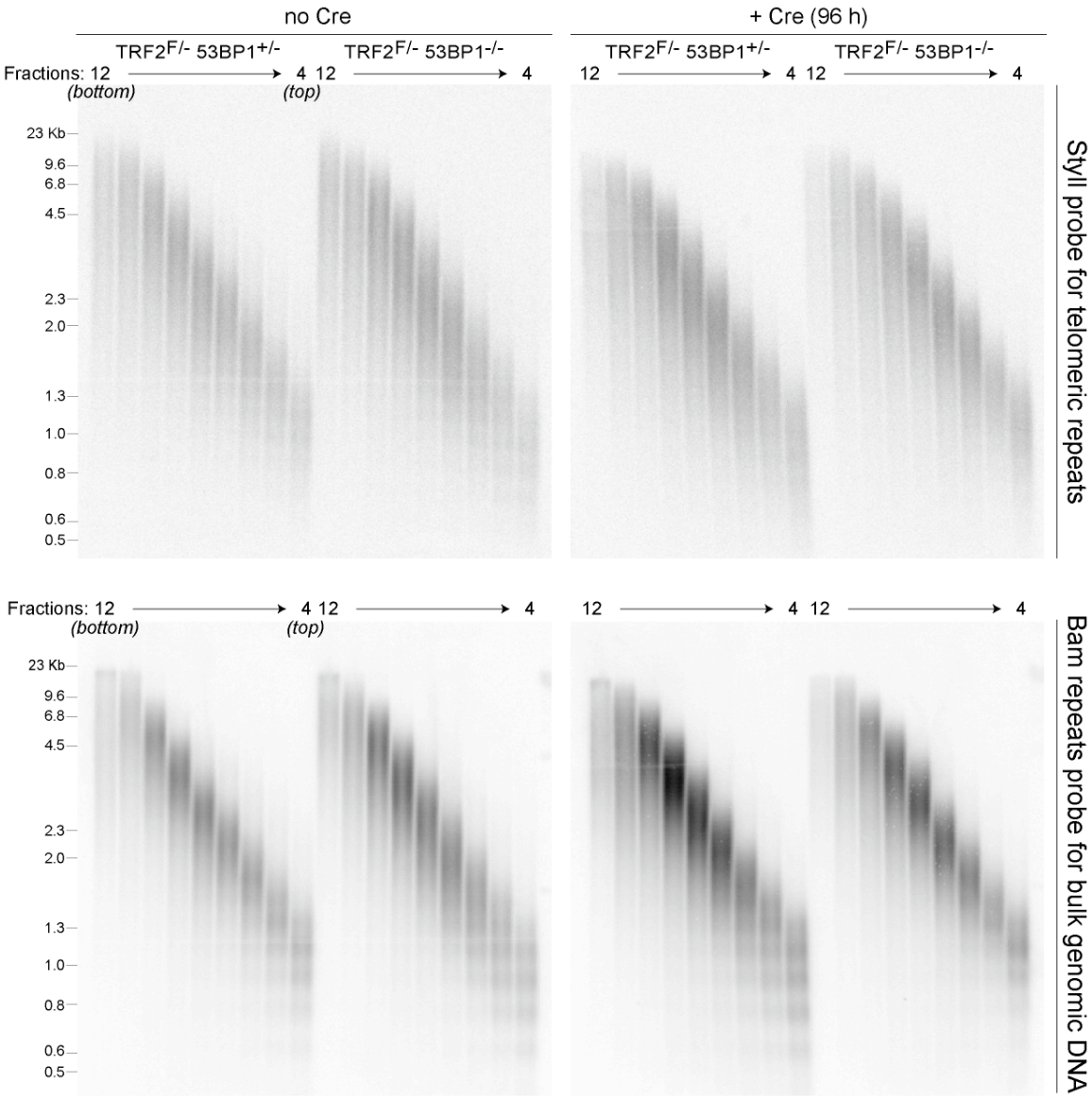

Figure 5.2. Analysis of the effects of 53BP1 absence and telomere dysfunction on the structure of telomeric chromatin

Chromatin isolated from TRF2$^{F/-}$53BP1$^{+/-}$ and TRF2$^{F/-}$53BP1$^{-/-}$ nuclei, harvested untreated or 96 hours after Hit&Run Cre infections were digested by MNase, and the fragments were separated on a 6-40% sucrose gradient. The gradient was fractionated from top (fraction 4) to bottom (fraction 12). The DNA purified from each fraction was resolved by agarose gel electophoresis and examined by Southern blotting. Blots were probed with telomere-repeat-specific (Sty11) probe to examine telomeric DNA. Blots were stripped and reprobed with a Bam repeat-specific (Bam) probe to detect total DNA.

The mobility of dysfunctional telomeres is an active process

Since we did not obtain evidence for a structural change in the chromatin at telomeres, we tested whether chromatin mobility is mediated through a dynamic mechanism.

Actin

Actin is the main component of multiple dynamic processes in the cell, such as cell motility, cell division, vesicle and organelle movement. In addition, actin has been implicated in many nuclear processes, including chromatin dynamics and gene expression [263]. Finally, rapid telomere movement during meiotic prophase I in yeast has recently been linked to dynamic actin cables [264,265].

In order to test whether actin plays a role in promoting the mobility of dysfunctional telomeres, we used a well-characterized actin inhibitor, Latrunculin A, which inhibits actin polymerization and disrupts microfilament organization by sequestering actin monomers.

This and other experiments in this chapter were performed in $TRF2^{F/-}53BP1^{+/-}$ or $TRF2^{F/-}53BP1^{-/-}$ MEFs, expressing eGFP-TRF1 telomere marker, in which we have confirmed that induction of telomere dysfunction led to increased telomere mobility in 53BP1-proficient, but not 53BP1-deficient cells (Figure 5.3a). In addition, we verified that each experiment showed efficient TRF2 deletion and expression of eGFP-TRF1 marker (Figure 5.3b).

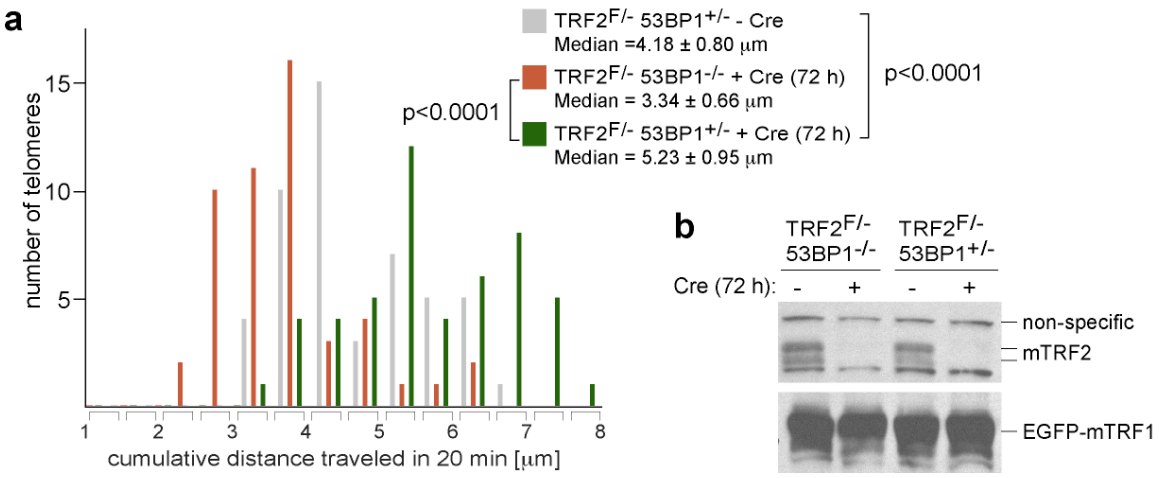

Figure 5.3. Representative example of controls performed in all imaging experiments in Chapter 5

a, Graph of the frequency distribution of the number of eGFP-labeled telomeres plotted against the cumulative distance they traveled in 20 minutes. $TRF2^{F/-}53BP1^{+/-}$ and $TRF2^{F/-}53BP1^{-/-}$ MEFs, expressing eGFP-TRF1 marker, were imaged untreated (grey bars) or 72 hours post Hit&Run Cre retroviral infections (red and green bars). 50 telomeres in 10 cells were analyzed for each genotype and treatment. The median values and s.d. are indicated. P-values were calculated using a two-tailed Mann-Whitney test.

b, Immunoblots of whole cell lysates from cells in **(a)** probed with Abs raised against mouse TRF2 and TRF1. A non-specific band from the TRF2 blot was used as a loading control.

Treatment of $TRF2^{F/-}53BP1^{+/-}$ cells with 0.1 μg/ml (~0.25 μM) Latrunculin A did not have an effect on the mobility of dysfunctional telomeres (Figure 5.4a). Since the recommended final concentration ranges from 0.1 to 10 μg/ml, it is possible that we were not inhibiting actin efficiently. Increasing the drug concentration to 1 μg/ml, however, led to dramatic changes in cell shape; the fibroblasts rounded up and detached from the imaging plate within minutes, making time-lapse imaging impossible. We also tried to use alternative actin inhibitors, such as Cytochalasin B and D, which shorten actin filaments by blocking monomer addition, at the recommended 10 μM concentration, but

the consequences for cell shape were similar. If 0.1 μg/ml Latrunculin A is enough to inhibit the dynamic properties of actin in the nucleus, we can conclude that the movement of dysfunctional telomeres is not an actin-driven process. On the other hand, the data cannot exclude that higher drug concentrations might be required to inhibit such activity.

Dynein, Light Chain 8

A recent study reports on a potential interaction between 53BP1 and light chain 8 (LC8) of dynein, a motor protein that walks along cytoskeletal microtubules [266]. This interaction appears to be of functional significance since in its absence p53 fails to accumulate in the nucleus following DNA damage. We tested whether this interaction contributed to the dynamics of dysfunctional telomeres. The binding between 53BP1 and LC8 can be disrupted by the introduction of a Tat-tagged KSTQT peptide (Tat-LC8), which mimics the LC8-interaction motifs in 53BP1 and competes for the binding cleft of LC8. Although we introduced the recommended concentration of Tat-LC8 or control Tat-KSAAA (Tat-Con) peptides into the imaging medium of Cre-treated $TRF2^{F/-}53BP1^{+/-}$ cells for 24 hours prior to the imaging session, we did not observe an effect on the movement of dysfunctional telomeres (Figure 5.4b). This negative result, however, was not interpretable. Since our analysis was performed in SV40-immortalized cells, we could not replicate the previously published effect on p53 localization. Therefore, we could not exclude that the peptide might not have been functional in our experimental setting.

Microtubules

Since disrupting the interaction between 53BP1 and LC8 led to inconclusive results, we sought a more general way of suppressing microtubule dynamics. The microtubule network has several important roles in the cell, including vesicular transport and mitotic spindle formation, but it is excluded from the nucleoplasm in interphase mammalian cells.

A potential role for microtubules in nuclear processes has been studied extensively in *S. pombe*, where the oscillatory nuclear movement (also referred to as horse-tail movement) characteristic of meiotic prophase is dependent on cytoplasmic dynein. The horse-tail movement, driven by cytoplasmic dynein–dynactin complexes in combination with telomere clustering, is thought to facilitate the pairing of homologous chromosomes as a prerequisite for accurate chromosome segregation [267,268].

In addition, a network that provides a physical link between the nucleus and cytoplasmic microtubules has recently been identified in fission yeast. This connection is established by SUN and KASH domain-containing proteins as well as by an inner nuclear membrane protein called, Ima1 [269]. Ima1 simultaneously interacts with heterochromatin regions within the nucleus and is enriched at sites of microtubule-organizing centers. In this manner, cytoplasmic microtubules are mechanically coupled to nuclear chromatin, suggesting the existence of a robust framework for communication between the cytoplasmic cytoskeleton and the nuclear interior [269].

We asked whether microtubules contributed to telomere movement. Microtubules can be efficiently and specifically inhibited by treatment with nocodazole, a well-known anti-neoplastic agent that results in the depolymerization of microtubules. Nocodazole is

often used as a tool for cell cycle synchronization, arresting cells in G2- or M-stages of the cell cycle.

72 hours post Cre-mediated deletion of TRF2 from $TRF2^{F/-}53BP1^{+/-}$ MEFs, we introduced into the imaging medium a low, non-toxic dose of nocodazole (1 μg/ml) for a short period (2 hours) before performing time-lapse microscopy. Treatment with nocodazole had a profound effect on the movement of dysfunctional telomeres (Video 17-19). Whereas dysfunctional telomeres in DMSO (dimethyl sulfoxide)-treated cells, traveled 5.17±1.15 μm in 20 minutes, in cells treated with nocodazole, dysfunctional telomeres covered only 3.40±0.99 μm (Figure 5.4c). The decrease in mobility was also evident by eye as shown in the whole-nuclei tracking of dysfunctional telomeres in control and nocodazole-treated cells (Figure 5.5).

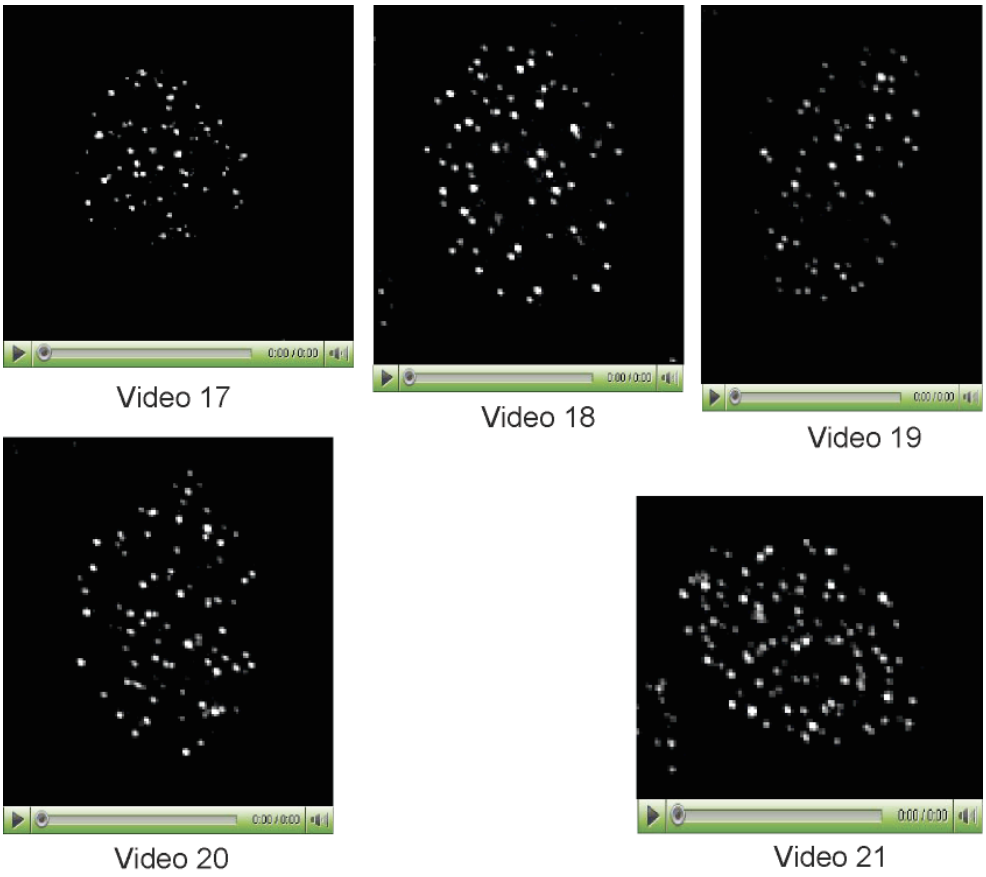

Videos 17-21. Role of microtubule inhibition on the mobility of dysfunctional telomeres
Representative TRF2$^{F/-}$53BP1$^{+/-}$ cells imaged 72 h after Hit&Run Cre infection in the presence of DMSO (Video 17), 1 μg/ml Nocodazole (Video 18-19) for 1 hour, 1 hour recovery after the treatment with 1 μg/ml Nocodazole (Video 20), or 20 μM taxol (Video 21) for 1 hour. Z-stacks of eGFP-TRF1 signal were acquired every 30 sec over 20 min. Videos constructed from deconvolved and projected frames are supplemented in a DVD.

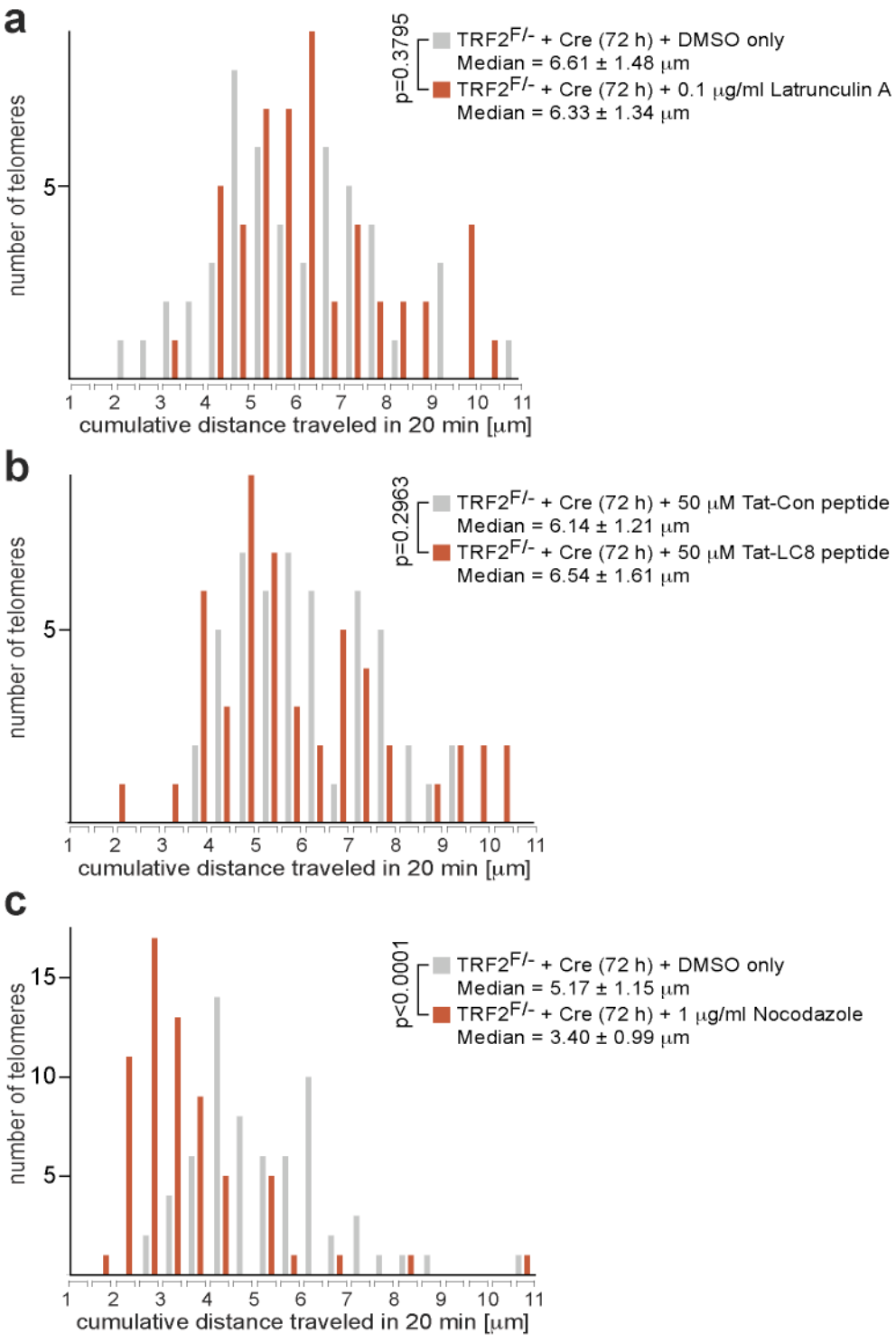

Figure 5.4. Role of cytoskeleton dynamics on the mobility of dysfunctional telomeres

a-c, Graphs of the frequency distribution of the number of eGFP-labeled telomeres plotted against the cumulative distance they traveled in 20 minutes. $TRF2^{F/-}53BP1^{+/-}$ MEFs, expressing eGFP-TRF1 marker, were imaged 72 hours after Hit&Run Cre retroviral infections. Prior to imaging

cells were incubated with DMSO only (grey bars) or with **(a)** 0.1 μg/ml Latrunculin A for 30 minutes, **(b)** 50 μM Tat-tagged LC8-specific peptide overnight, or **(c)** 1μg/ml Nocodazole for 2 hours (red bars). 50 telomeres in 10 cells were analyzed for each treatment. The median values and s.d. are indicated. P-values were calculated using a two-tailed Mann-Whitney test.

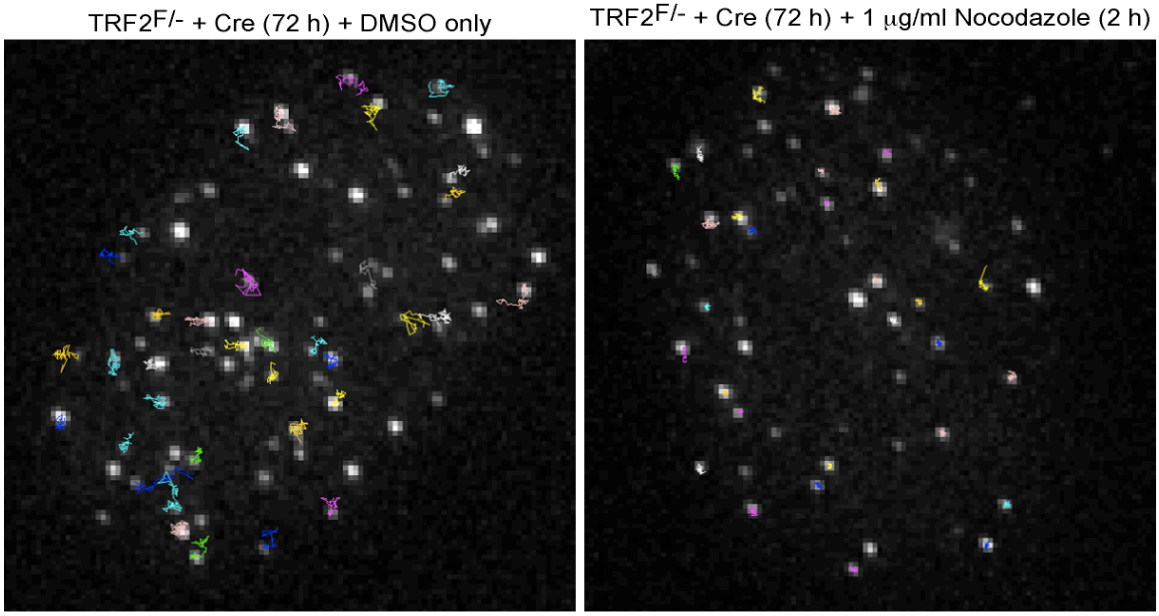

Figure 5.5. Effect of nocodazole treatment on the mobility of dysfunctional telomeres
Traces (multicolored) of individual eGFP-labeled telomeres (in white) tracked for 20 minutes in a representative TRF2$^{F/-}$53BP1$^{+/-}$ cell, expressing eGFP-TRF1 marker, imaged 72 hours after Hit&Run Cre retroviral infections. Prior to imaging cells were incubated for 2 hours with (*Left*) DMSO only or (*Right*) 1μg/ml Nocodazole.

Disruption of microtubules did not affect chromatin mobility in general since there was no effect of nocodazole on the movement of functional telomeres in $TRF2^{F/-}$ $53BP1^{+/-}$ MEFs not treated with Cre (Mann-Whitney test; p=0.0168) (Figure 5.6).

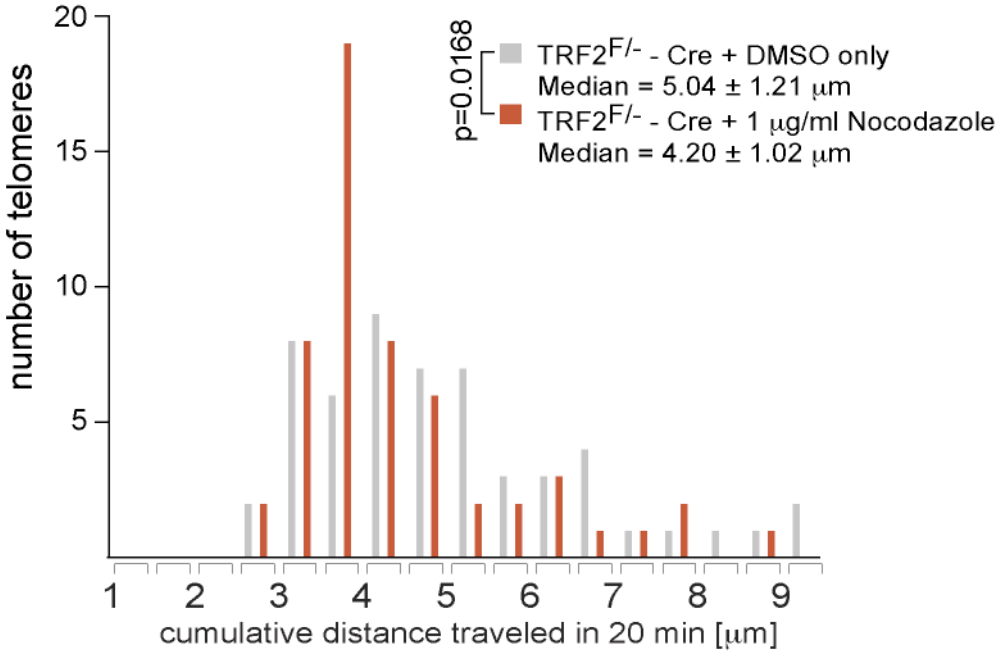

Figure 5.6. Effect of nocodazole treatment on the mobility of functional telomeres

Graph of the frequency distribution of the number of eGFP-labeled telomeres plotted against the cumulative distance they traveled in 20 minutes. $TRF2^{F/-}53BP1^{+/-}$ MEFs, expressing eGFP-TRF1 marker were treated for 2 hours prior to imaging with DMSO only (grey bars) or with 1μg/ml Nocodazole (red bars). 50 telomeres in 10 cells were analyzed for each treatment. The median values and s.d. are indicated. P-value was calculated using a two-tailed Mann-Whitney test.

In contrast to actin inhibitors, nocodazole did not affect cell adhesion and there were not any obvious changes in nuclear shape. Moreover, 53BP1 TIF formation in nocodazole treated cells was unaffected (Figure 5.7).

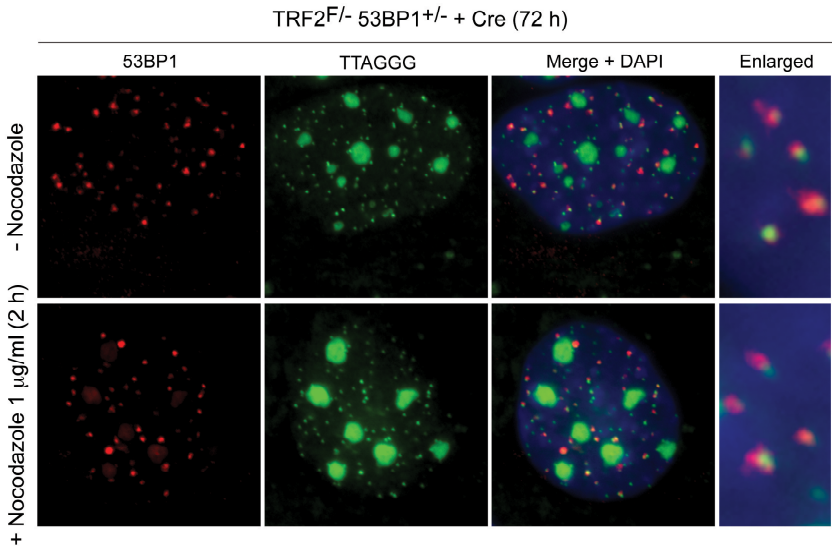

Figure 5.7. Effect of nocodazole treatment on 53BP1 TIF formation

Fluorescence images of representative TRF2$^{F/-}$53BP1$^{+/-}$ MEFs, infected with Hit&Run Cre retrovirus for 72 hours, fixed after treatment with DMSO only or 1 μg/ml Nocodazole for 2 hours, and process for IF-FISH. IF was performed with an Ab specific to 53BP1 (red). Telomeric DNA was detected with a CCCTAA-repeat specific FISH probe (green) (gives a strong nucleolar non-specific background). DNA was stained with DAPI. Images were merged and enlarged.

Moreover, the effect of nocodazole was fully reversible. After imaging in the presence of nocodazole, cells were washed and incubated for one hour in medium that did not contain nocodazole. Dysfunctional telomeres imaged after the recovery period had fully regained their mobility (Figure 5.8a, b; Video 20). In fact, there was no difference in the distribution of the mobility of telomeres from DMSO-treated cells and from cells that were allowed to recover after nocodazole treatment (Mann-Whitney test; $p=0.9698$) (Figure 5.8a).

This important control ensured that nocodazole treatment did not lead to permanent changes in the nucleoplasm, such as ATP depletion, which would affect nuclear dynamics irreversibly. Finally, the effect of nocodazole was highly reproducible between independent experiments, establishing the robust contribution of microtubule dynamics to the mobility of dysfunctional telomeres.

a

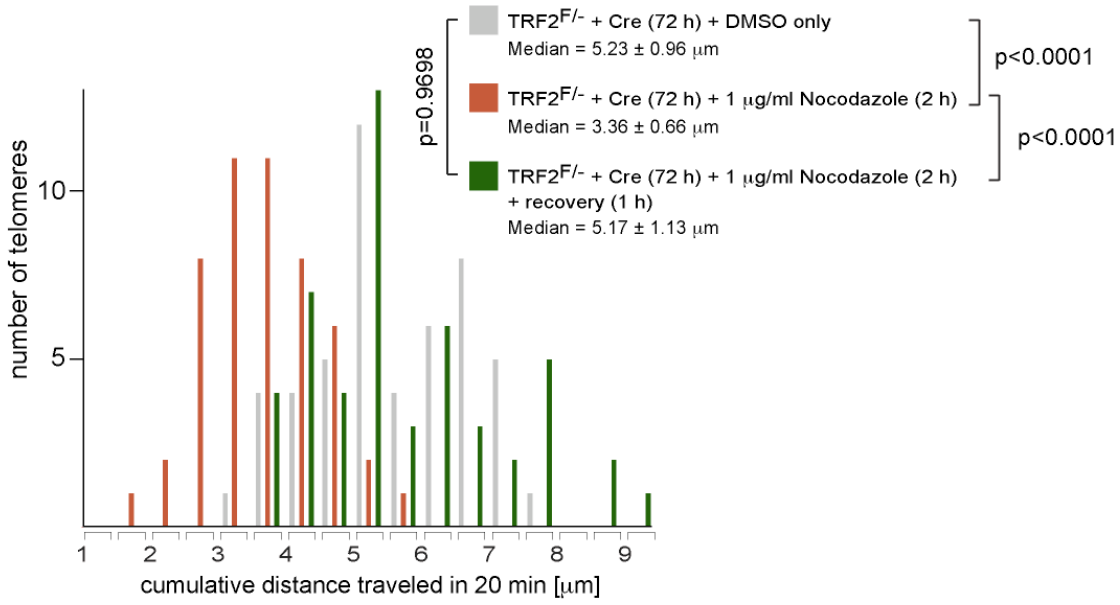

b

Summary of cumulative distance traveled in 20 min [μm] from 3 independent experiments

TRF2F/- + Cre (72 h)	+ mock treatment	+ 1 μg/ml Nocodazole (2 h)	+ 1 μg/ml Nocodazole (2 h) + Recovery (1 h)
Experiment 1 (n=50)	5.17 ± 1.15 μm	3.40 ± 0.99 μm	
Experiment 2 (n=50)	5.23 ± 0.96 μm	3.36 ± 0.66 μm	5.17 ± 1.13 μm
Experiment 3 (n=50)	5.79 ± 1.39 μm	4.40 ± 0.99 μm	6.48 ± 1.45 μm

Figure 5.8. Test for the reversibility of the effect of nocodazole treatment on the mobility of dysfunctional telomeres

a, Graph of the frequency distribution of the number of eGFP-labeled telomeres plotted against the cumulative distance they traveled in 20 minutes. TRF2$^{F/-}$53BP1$^{+/-}$ MEFs, expressing eGFP-TRF1 marker, were imaged 72 hours after Hit&Run Cre infections. Prior to imaging, cells were treated with DMSO only (grey bars) or with 1μg/ml Nocodazole (red bars) for 2 hours. Cells imaged in the presence of Nocodazole were washed and imaged 1 hour later in the absence of Nocodazole (green bars). 50 telomeres in 10 cells were analyzed for each treatment. The median values and s.d. are indicated. P-values were calculated using a two-tailed Mann-Whitney test.

b, Table demonstrating the reversibility of the effects of Nocodazole treatment on the mobility of eGFP-TRF1-marked dysfunctional telomeres in Cre-treated TRF2$^{F/-}$53BP1$^{+/-}$ MEFs in 2 independent experiments, performed as in **(a)**.

Microtubule polymerization is required to promote the dynamic movement of dysfunctional telomeres

In addition to nocodazole, two other drugs are commonly used to inhibit microtubule dynamics: taxol and vincristine. Similarly to nocodazole, taxol leads to mitotic arrest but in contrast to nocodazole, it stabilizes microtubules, thus preventing the microtubule dynamics required in mitosis. Vincristine, on the other hand, affects microtubules differently, depending on its concentration. At low doses (<10 nM), vincristine suppresses microtubule dynamics and therefore acts similarly to taxol, while at high concentrations (100 nM ~ 1 μM), it acts like nocodazole to promote depolymerization.

Taxol treatment did not change the mobility of dysfunctional telomeres in $TRF2^{F/-}$ $53BP1^{+/-}$ MEFs 72 hours post Cre infection (Figure 5.9a; Video 21), suggesting that unless depolymerization is induced, the microtubule network can support telomere dynamics. Consistent with this model, in two separate imaging sessions, high but not low dose of vincristine reduced the dynamics of dysfunctional telomeres (Figure 5.9b, c).

The effects of nocodazole and high dose vincristine provided independent evidence that microtubules play an essential role in promoting the increased movement of dysfunctional telomeres. This finding establishes a potential model for the dynamic behavior of deprotected chromosome ends (see Discussion). However, how 53BP1, which accumulates at chromatin in the vicinity of DSBs, mediates the movement along cytoplasmic microtubules remains to be established.

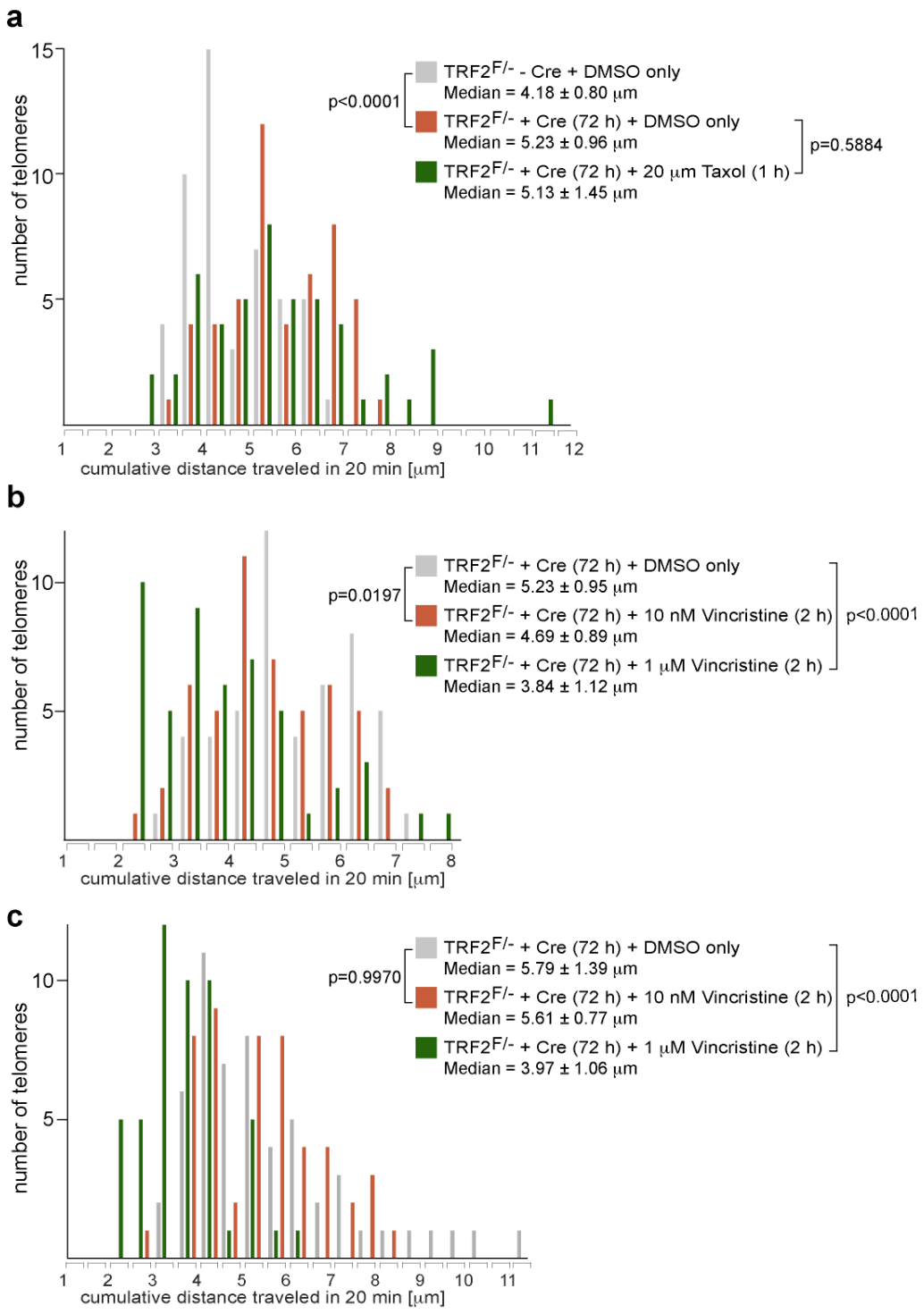

Figure 5.9. Effects of the microtubule inhibitors, taxol and vincristine, on the mobility of dysfunctional telomeres

a, Graph of the frequency distribution of the number of eGFP-labeled telomeres plotted against the cumulative distance they traveled in 20 minutes. TRF2$^{F/-}$53BP1$^{+/-}$ MEFs expressing eGFP-

TRF1 marker were imaged untreated (grey bars) or 72 hours after Hit&Run Cre retroviral infections (red bars). Prior to imaging, Cre-treated cells were incubated with 20 μM Taxol for 1 hour (green bars). 50 telomeres in 10 cells were analyzed for each treatment. The median values and s.d. are indicated. P-values were calculated using a two-tailed Mann-Whitney test.
b-c, Graphs of the frequency distribution of the number of eGFP-labeled telomeres plotted against the cumulative distance they traveled in 20 minutes. In two independent experiments, presented in **(b)** and **(c)**, TRF2$^{F/-}$53BP1$^{+/-}$ MEFs expressing eGFP-TRF1 marker were imaged 72 hours after Hit&Run Cre retroviral infections. Prior to imaging, cells were incubated for 2 hours with DMSO only (grey bars), or with 10 nM (red bars) or 1 μM Vincristine (green bars). 50 telomeres in 10 cells were analyzed for each treatment. The median values and s.d. are indicated. P-values were calculated using a two-tailed Mann-Whitney test.

53BP1 promotes chromatin mobility by inhibiting HDAC activity

We also explored a potential functional interaction between 53BP1 and HDAC4 (Histone deacetylase 4). In a recent study, Kao et al. report on the recruitment of HDAC4 to 53BP1-containing IRIFs [270]. Furthermore, they establish that similarly to γ-H2AX, the persistence of HDAC4 at sites of DNA damage correlates with the presence of unrepaired DSBs, suggesting that the resolution of HDAC4 IRIFs is linked to repair. Interestingly, silencing of HDAC4 by RNAi also decreases the levels of 53BP1 protein and vice versa, establishing a potential co-regulation link between these two factors.

We asked whether HDACs play a role in promoting the movement of dysfunctional telomeres by treating cells with the general HDAC inhibitor, Trichostatin A (TSA). TSA is a potent and selective inhibitor of class I and II mammalian HDACs, and successfully interferes with the removal of acetyl groups from histones. Consequently, TSA has the potential to alter nuclear processes that are regulated by chromatin acetylation.

We treated TRF2$^{F/-}$53BP1$^{+/-}$ and TRF2$^{F/-}$53BP1$^{-/-}$ cells, from which TRF2 has been efficiently depleted, with varying doses of TSA for 24 hours prior to imaging. Cells tolerated 10 and 50 ng/ml TSA for 24 hours without detrimental effects, but appeared to die upon treatment with higher doses (100 ng/ml).

First, we examined the effects of TSA on the movement of dysfunctional telomeres in Cre-treated 53BP1-proficient cells and observed that TSA did not affect the mobility in this setting (Figure 5.10a). Our analysis demonstrated that telomeres acquired increased dynamic behavior upon TRF2 deletion both in the presence and in the absence of the drug. Therefore, HDAC activity was not required to promote increased dynamics of deprotected chromosome ends.

Next, we analyzed how TSA treatment affected the movement of dysfunctional telomeres in Cre-treated 53BP1-deficient cells, where mobility is suppressed due to the absence of 53BP1. In these cells, TSA had a notable effect in promoting the movement of dysfunctional telomeres (Videos 22-23). Whereas, in control, DMSO-treated cells, we recorded a median cumulative displacement of 4.63±0.76 μm, in TSA-treated cells this number significantly increased to 6.08±1.10 μm (Mann-Whitney test; $p<0.0001$) (Figure 5.10b). In fact, as a consequence of TSA treatment, dysfunctional telomeres in 53BP1-null cells moved with comparable kinetics to dysfunctional telomeres in 53BP1-wild type cells. Therefore, inhibition of HDAC activity could rescue 53BP1 deficiency. The effect of TSA on augmenting the mobility of dysfunctional telomeres in Cre-treated TRF2$^{F/-}$ 53BP1$^{-/-}$ cells was highly reproducible in three independent experiments (Figure 5.10c).

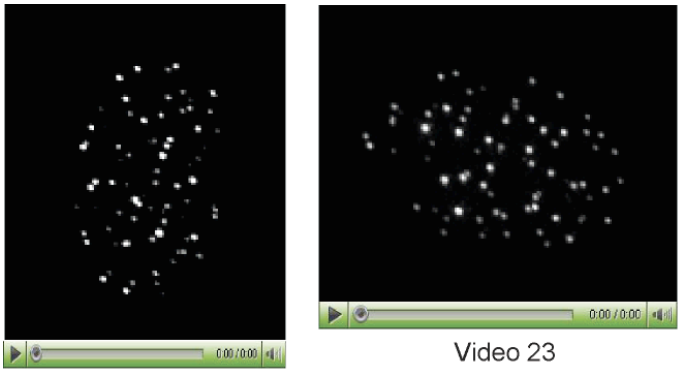

Video 22

Video 23

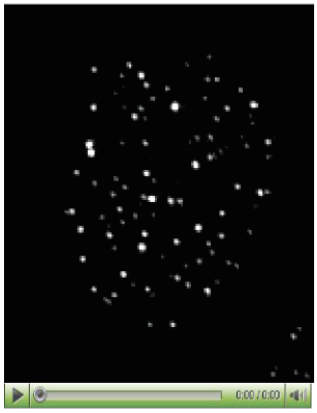

Video 24

Video 25

Videos 22-25. Role of HDAC inhibitors on the mobility of dysfunctional telomeres in the absence of 53BP1

Representative TRF2$^{F/-}$53BP1$^{-/-}$ cells imaged 72 h after Hit&Run Cre infection and treated for 24 hours with DMSO (Video 22), 50 ng/ml Trichostatin A (Video 23), 50 nM SAHA (Video 24), or 1 mM Valproic acid (Video 25). Z-stacks of eGFP-TRF1 signal were acquired every 30 sec over 20 min. Videos constructed from deconvolved and projected frames are supplemented in a DVD.

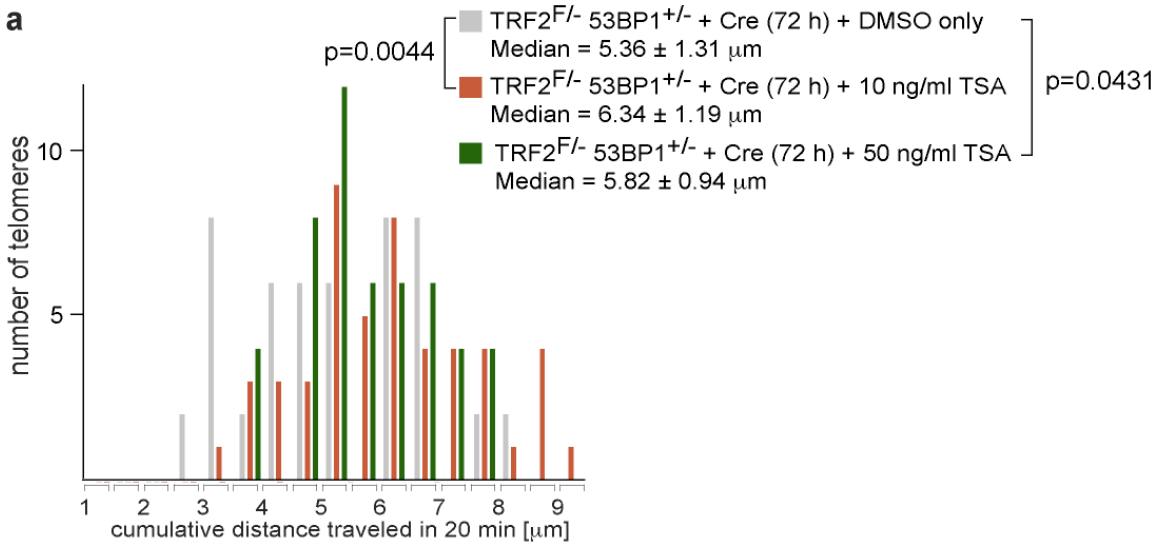

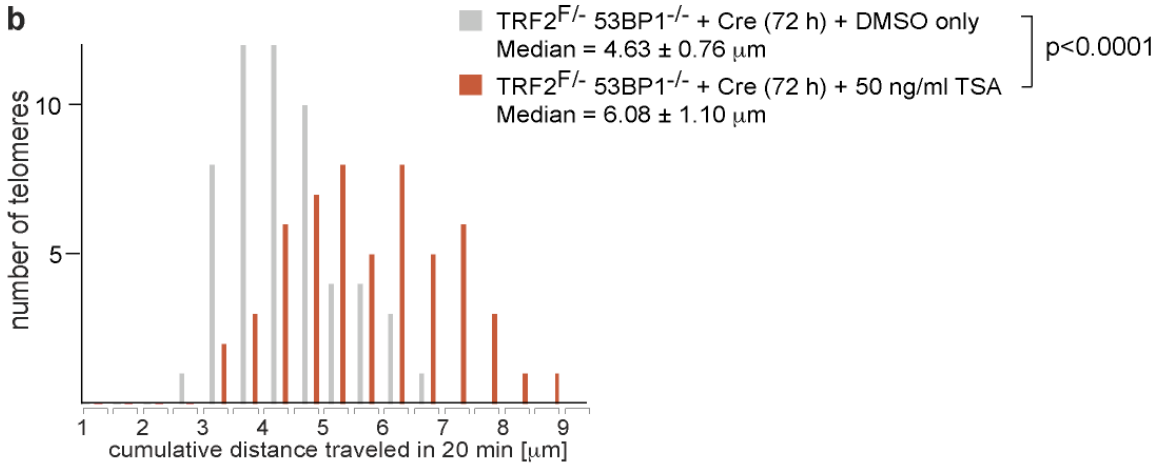

c

TRF2F/- 53BP1-/- + Cre (72 h)	no TSA	+ 50 ng/ml TSA (24 h)	Statistics
Experiment 1 (n=50)	3.34 ± 0.66 μm	4.78 ± 1.05 μm	p<0.0001
Experiment 2 (n=50)	4.63 ± 0.76 μm	6.08 ± 1.10 μm	p<0.0001
Experiment 3 (n=50)	3.96 ± 0.70 μm	5.03 ± 1.22 μm	p=0.0004

Figure 5.10. Effect of the HDAC inhibitor, TSA, on the mobility of dysfunctional telomeres in 53BP1-proficient and 53BP1-deficient cells

a, Graph of the frequency distribution of the number of eGFP-labeled telomeres plotted against the cumulative distance they traveled in 20 minutes. TRF2$^{F/-}$53BP1$^{+/-}$ MEFs, expressing eGFP-TRF1 marker, were imaged 72 hours after Hit&Run Cre retroviral infections. Prior to imaging cells were incubated for 24 hours with DMSO only (grey bars), 10 ng/ml TSA (red bars), or 50

ng/ml TSA (green bars). 50 telomeres in 10 cells were analyzed for each treatment. The median values and s.d. are indicated. P-values were calculated using a two-tailed Mann-Whitney test.
b, Graph of the frequency distribution of the number of eGFP-labeled telomeres plotted against the cumulative distance they traveled in 20 minutes. $TRF2^{F/-}53BP1^{-/-}$ MEFs, expressing eGFP-TRF1 marker, were imaged 72 hours after Hit&Run Cre retroviral infections. Prior to imaging cells were incubated for 24 hours with DMSO only (grey bars) or 50 ng/ml TSA (red bars). 50 telomeres in 10 cells were analyzed for each treatment. The median values and s.d. are indicated. P-value was calculated using a two-tailed Mann-Whitney test.
c, Table summarizing three independent experiments, performed as in **(b)**. The median cumulative distance ± s.d. traveled in the absence and in the presence of 50 ng/ml TSA and P-value in each experiment are indicated.

This result was further confirmed using two independent HDAC inhibitors: the 'second generation' inhibitor SAHA (suberoylanilide hydroxamic acid, also called Vorinostat in clinical trials for cancer treatment) (Video 24) and valproic acid, a less potent, but nevertheless highly selective HDAC inhibitor (Video 25). In both cases, introduction for 24 hours prior to imaging into the medium of Cre-treated $TRF2^{F/-}53BP1^{-/-}$ cells led to significant increase in the dynamics of dysfunctional telomeres (Figure 5.11a). Furthermore, the data reproduced closely the effect of TSA treatment.

On the other hand, we confirmed that enhanced mobility was not recorded in $TRF2^{F/-}53BP1^{-/-}$ cells, not treated with Cre (Figure 5.11b). This negative control verified that telomere dysfunction is required in order to promote mobility.

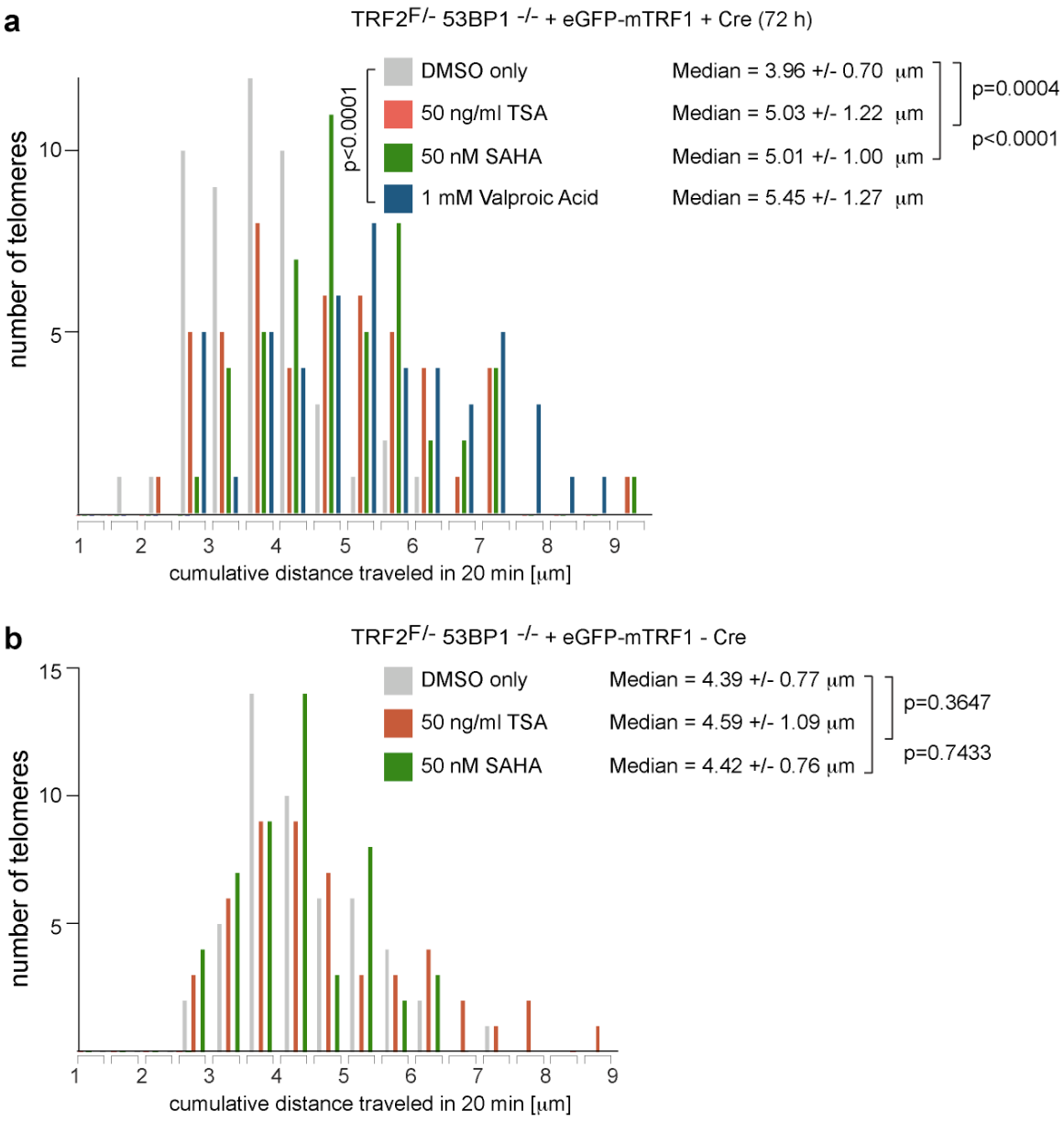

Figure 5.11. Effect of the HDAC inhibitors, TSA, SAHA and VPA, on the mobility of dysfunctional and functional telomeres in 53BP1-deficient cells

a, Graph of the frequency distribution of the number of eGFP-labeled telomeres plotted against the cumulative distance they traveled in 20 minutes. $TRF2^{F/-}53BP1^{-/-}$ MEFs, expressing eGFP-TRF1 marker, were imaged 72 hours after Hit&Run Cre retroviral infections. Prior to imaging, cells were incubated for 24 hours with DMSO only (grey bars), 50 ng/ml TSA (red bars), 50 nM SAHA (green bars), or 1 mM Valproic acid. 50 telomeres in 10 cells were analyzed for each treatment. The median values and s.d. are indicated. P-values were calculated using a two-tailed Mann-Whitney test.

b, Graph of the frequency distribution of the number of eGFP-labeled telomeres plotted against the cumulative distance they traveled in 20 minutes. $TRF2^{F/-}53BP1^{-/-}$ MEFs, expressing eGFP-TRF1 marker, were imaged in the absence of Cre. Prior to imaging, cells were incubated for 24 hours with DMSO only (grey bars), 50 ng/ml TSA (red bars), 50 nM SAHA (green bars). 50 telomeres in 10 cells were analyzed for each treatment. The median values and s.d. are indicated. P-value was calculated using a two-tailed Mann-Whitney test.

Altogether, these data suggest that HDAC activity is inhibitory to chromatin mobility. Our findings also argue that 53BP1 represses HDAC activity at dysfunctional telomeres. By combining these two arguments, we propose that chromatin mobility is regulated by a double negative pathway, in which 53BP1 inhibits HDAC activity, which in turn suppresses chromatin mobility. This model explains why treatment with an HDAC inhibitor boosts chromatin dynamics only in the absence of 53BP1. Presumably in the presence of 53BP1, HDAC activity is already suppressed by 53BP1 and therefore, treatment with HDAC-specific drugs does not have any additional consequences for mobility.

It is not known whether in our experiments HDAC inhibition altered the acetylation status of chromatin or of other factors. Interestingly, it has been shown that the microtubule component tubulin is acetylated by HDAC6. Acetylated tubulin associates mostly with stable microtubules and appears to be absent from dynamic structures such as growth cones and leading edge of fibroblasts [271]. Therefore, it is possible that the enhanced mobility of dysfunctional telomeres that we observed in 53BP1-deficient cells upon treatment with HDAC inhibitors may be due to enhanced tubulin acetylation, which leads to microtubule stabilization and prevents its depolymerization. This model could be tested with the HDAC inhibitor, trapoxin (TPX),

which does not affect the tubulin-specific HDAC6 but inhibits the histone-specific HDACs.

In sum, we have found that acetylation may play a role in chromatin dynamics. In order to understand the pathway that promotes the mobility of dysfunctional telomeres, it would be important to determine the acetylation target and to dissect the role of HDACs in chromatin dynamics.

Evidence for microtubule-dependent proofreading during HDR

So far, we have presented evidence for a 53BP1- and microtubule-dependent mechanism that promotes the mobility of distant DNA ends. However, we consider it unlikely that a special mechanism has evolved to promote long-distance joining. Although in our model system we detect how chromatin mobility facilitates the synapsis of distant ends, we believe that the primary function of this pathway may be to promote the reverse behavior -- to separate inappropriate associations during DNA repair. We imagine that this proofreading mechanism would be most critical during HDR, where repair occurring between non-sister chromatids can lead to genome instability. In agreement with this model, faulty HDR events that involve non-sister chromatids have been reported to occur with higher frequency in the absence of 53BP1 [272] and can be detected on metaphase spreads of cells treated with IR as quadri-radial chromosomes.

Since we have implicated microtubules in chromatin mobility, we tested whether treatment with the microtubule inhibitor nocodazole caused a similar spectrum of irradiation-induced chromosome aberrations as 53BP1 deficiency. Cells were irradiated with 5 Gy and allowed to recover for 12 hours in the presence or in the absence of

nocodazole before harvesting metaphase spreads. In support of our model, the presence of nocodazole led to a 6-fold increase in the number of radial events per chromosome (Figure 5.12), providing compelling evidence that microtubule dynamics might be involved in promoting the fidelity of HDR. In the future, we plan to exclude any non-specific effects of the nocodazole treatment by repeating this experiment in the presence of taxol. Taxol and nocodazole similarly stall cell cycle progression in M phase but based on our earlier findings we expect taxol not to affect chromatin mobility (Figure 5.9). In addition, we plan to address whether 53BP1 and microtubules function in the same pathway.

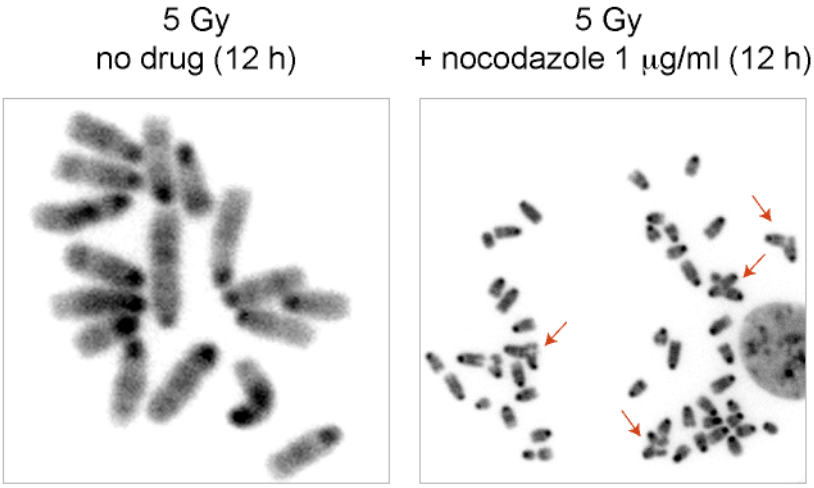

	% radial events/chromosome	total # of chromosomes scored
no drug	1.4 %	996
nocodazole 1 μg/ml	7.9 %	884

Figure 5.12. Effect of nocodazole on IR-induced DSB repair

Metaphase spreads of MEFs treated with 5 Gy and allowed to recover for 12 hours in the absence or in the presence of 1 μg/ml nocodazole. Metaphases were stained with DAPI and shown in inverse grey. Table summarizing the number of radial events scored per chromosome. The total number of chromosome scored in each instance is also indicated.

Summary of findings in Chapter 5

In this chapter we have defined the mechanism that promotes the mobility of deprotected chromosome ends.

First of all, we established that POT1a/b-deficient telomeres behave similarly to TRF2-deficient telomeres, suggesting that there is nothing unique about losing TRF2-mediated protection of chromosome ends. In addition, the increase in mobility occurred regardless of the kinase (ATM or ATR) that activated the response to telomere dysfunction. Therefore, by extrapolation, we argue that all sites of DNA damage (suffices they contain 53BP1) could be subject to this dynamic mechanism.

Next, by using inhibitors to target specific cellular processes, we found that the movement of dysfunctional telomeres relies on the microtubule network and is inhibited by microtubule depolymerization. The potential existence of mechanical coupling between 53BP1-containing chromatin and cytoplasmic microtubules has exciting implications for the process of DNA repair (see Discussion). We imagine that it might be mediated by a nuclear envelope-associated factor, similar to the earlier introduced Ima1, which bridges nuclear heterochromatin and cytoplasmic microtubule organizing centers.

In addition, we have found an interesting connection between the acetylation status of cells containing dysfunctional telomeres and the dynamic behavior of their chromosome ends. We argue that 53BP1 functions to inhibit deacetylation, which in turn is inhibitory to mobility. We imagine that 53BP1 might promote acetylation or prevent deacetylation of a specific residue(s) (e.g. H4-K16Ac, which is adjacent to the docking site of 53BP1, H4-K20diMe). Similarly to Ima1, which recognizes heterochromatin, a nuclear envelope factor may exist that couples acetylated chromatin to cytoplasmic

microtubules. Alternatively, as discussed earlier, the acetylation status may be affecting tubulin dynamics.

Finally, we have exciting preliminary evidence suggesting that the mobility mechanism that we have described as an integral part of NHEJ of distant ends may function to disassemble inappropriate repair interactions, such as between non-sister chromatids during HDR. We discuss the implications of this finding in the Discussion chapter.

CHAPTER 6: DISCUSSION

In this thesis, we have applied TRF2-deficient dysfunctional telomeres as a model system to study the regulation of signaling and repair pathways activated in response to DSBs. Using this system, we have provided conclusive evidence that the MRN complex is the only sensor in the ATM pathway. In addition, we have established a previously unknown role for 53BP1 in NHEJ of dysfunctional telomeres, and we have uncovered a novel mechanism through which 53BP1 promotes repair of distant sites. We have shown that 53BP1 acts by increasing chromatin mobility through a mechanism reliant on microtubules and the acetylation status of chromatin. Finally, we have found preliminary evidence for a microtubule-dependent mechanism that promotes chromosome integrity by preventing inappropriate repair of DSBs. Altogether, these data indicate that 53BP1 is an essential component of the DSB response and reveal its indispensable role for maintaining genome integrity.

TIF factors contribute to NHEJ by promoting the stable association of 53BP1 at dysfunctional telomeres

In an effort to understand the regulation of the NHEJ pathway at dysfunctional telomeres, we have characterized its genetic requirements. Our findings indicate that 53BP1, localized at the chromatin of dysfunctional telomeres, is essential for this process. This conclusion implies that all DNA damage response factors that are required for the recruitment of 53BP1 to deprotected chromosome ends would also have a role in repair. We have established that prolonged stabilization of 53BP1 at dysfunctional telomeres is

mediated by the same pathway that promotes its association with IRIFs at chromosome-internal DSBs (Figure 1.2). In agreement, we have found that factors that participate in this well-characterized pathway also promote the rate of NHEJ of dysfunctional telomeres. Specifically, we have examined the role of the NBS1 component of MRN, which signals the presence of dysfunctional telomeres as well as the roles of H2AX and MDC1, which promote 53BP1 binding to deprotected chromosome ends. Our studies indicate that all of these factors function in a common pathway to promote NHEJ since the absence of ATM [228], NBS1, H2AX, or MDC1 causes an identical phenotype with respect to NHEJ of dysfunctional telomeres: a 2-3 fold reduction in the rate of the repair process. These data are consistent with the modest decrease in CSR detected in B-cells deficient for ATM, NBS1, H2AX, or MDC1 (see Introduction for more details and references). The data are also comparable to previously published results from *in vitro* assays, which attribute a minor role to these factors in the repair of chromosome-internal DSBs (see Introduction for more details and references). In contrast, studies examining the contribution of these factors to V(D)J recombination showed ATM-, NBS1-, H2AX-, or MDC1-deficient mice can acquire a mature immune system (see Introduction for more details and references). One caveat of V(D)J recombination is that it only monitors the presence or absence of final repair products but does not measure the rate of the process. As a consequence, even if V(D)J recombination occurs more slowly, it may still give rise to a mature immune system. In contrast, in our analysis of telomere NHEJ we can examine the kinetics of repair at consecutive time points after TRF2 deletion. Therefore, we believe that our assay provides a more precise indicator for the role of these genes in NHEJ.

Additionally, it was not clear whether IRIF factors contribute directly to NHEJ during CSR, or whether the reduced rate of class switching is an indirect consequence of altered cell cycle progression. In this regard, ATM, NBS1, and to a more modest extent MDC1, are known contributors to the G1/S, intra-S-phase and G2/M transition checkpoints (see Figure 1.1 and introduction for more details). This question was addressed in our studies. In the absence of MDC1, we observed defective NHEJ of dysfunctional telomeres without any perturbations either in the proliferation rates or in the activation of the two main checkpoint effectors in the ATM pathway, p53 and Chk2. Our observations strongly argue that the effect of MDC1 deficiency on fusion rates is not mediated through changes in cell cycle progression.

We propose that the main contribution of TIF factors to NHEJ is their ability to associate with extended domains of chromatin at deprotected chromosome ends and to form a scaffold for the recruitment of DNA repair factors. This process requires both the initial recognition of dysfunctional telomeres by the MRN complex and the γ-H2AX-MDC1-NBS1-mediated signal amplification. We argue that, amongst these TIF factors, the ultimate transducer to the NHEJ pathway is 53BP1, whereas the other factors play secondary roles by mediating its prolonged association with chromatin.

Evidence for an MRN and ATM-independent DNA damage response pathway

Interestingly, 53BP1 deficiency leads to a more severe phenotype compared to depletion of the other TIF factors, causing a 50-fold decrease in the rate of NHEJ. This observation argues that 53BP1 can promote the NHEJ pathway in a TIF-independent manner, possibly through its highly specific but transient interaction with H4-K20diMe. In

support of this model, we have presented evidence that 53BP1 promotes NHEJ of dysfunctional telomeres via two independent pathways – one that is dependent on the ability of 53BP1 to bind to H4-K20diMe and one that is mediated by H2AX/MDC1 and their ability to promote extensive 53BP1-containing TIFs. Simultaneous disruption of both of these pathways causes an additive phenotype that is functionally equivalent to 53BP1 deficiency. Accordingly, we argue that these two independent mechanisms are necessary and sufficient to stimulate 53BP1-mediated NHEJ.

It follows from this argument that 53BP1, bound to H4-K20diMe, is the driver for the delayed fusion events observed in NBS1- or ATM-deficient MEFs. This finding is puzzling because H4-K20diMe is a constitutive chromatin mark and not a DNA damage-specific modification. It has been speculated that changes in the chromatin structure might be required to expose the dimethylated mark on H4-K20, and it has been proposed that phosphorylation of H2AX might be the trigger [138]. However, our data argue against a role for H2AX. We have established that a functional MRN complex is absolutely required for the ATM-dependent phosphorylation of H2AX but, as mentioned above, residual NHEJ products are still observed in absence of ATM or NBS1. In these cases, it is not clear how 53BP1 specifically recognizes H4-K20diMe at dysfunctional telomeres. To answer this question, we hypothesize the existence of an ATM-, MRN-, H2AX-, and MDC1-independent pathway that would allow 53BP1 to engage H4-K20diMe at sites of DNA damage in the absence of these factors. It is possible that this may be an entirely novel DNA damage response pathway that is activated in response to TRF2 loss. However, we favor an alternative model. Previously, Kastan and colleagues have proposed that an ATM-independent pathway alters chromatin structure upon loss of DNA

integrity [11]. However, in view of our data indicating that increased chromatin mobility in response to DNA damage is a local, and not a global event, we believe this structural change to be limited to the chromatin adjacent to DNA lesions. To date, players in a pathway of this kind have not been identified. Arguing against this model are experiments that have examined the effects of telomere deprotection on nucleosome structure without detecting any changes [262]. However, it is possible that these studies did not address subtle changes in nucleosome organization.

53BP1 supports NHEJ of dysfunctional telomeres by promoting mobility of distant DNA ends

The 50-fold reduction in the rate of end-joining that we observe in absence of 53BP1 is unexpected for several reasons. First, this phenotype is comparable to the phenotype previously noted in DNA ligase IV-deficient cells, establishing 53BP1 as an essential component of the NHEJ pathway at dysfunctional telomeres. Secondly, previous characterization of the role of 53BP1 in NHEJ-mediated repair of DSBs has yielded conflicting results. Whereas a recent study has reported a role for 53BP1 in the NHEJ-mediated repair of an I-SceI cut, previous investigations have found that 53BP1 does not contribute significantly to the repair of chromosome-internal DSBs (see Introduction for more detail and references). In addition, 53BP1-deficient mice do not have an overt defect in V(D)J recombination [136], although a previously unappreciated role of 53BP1 in a subset of joining events was recently reported [273]. In accordance with a possible role for 53BP1 in NHEJ, CSR is significantly impaired in 53BP1-null B-cells (at least 15-fold) [134,136].

We have proposed that the phenotypic variability can be explained by the ability of 53BP1 to promote the dynamic mobility of DNA ends. Quantitative analysis of time-lapse movies recording the movement of dysfunctional telomeres have revealed that deprotected telomeres exhibit a 53BP1-dependent two-fold increase both in their rate of movement and in the diameter of the territory that they sample. This change in chromatin mobility is a novel aspect of the response to DNA damage. We speculate that a mechanism promoting the mobility of damaged sites is of key importance for long-distance repair, such as the joining of dysfunctional telomeres and CSR.

Dysfunctional telomeres are homogeneously distributed throughout the nucleus in G1, when NHEJ takes place [237]. Similarly, the distance between two constant regions in the immunoglobulin locus of a B-cell can be a hundred kilobases apart. So far, no mechanism has been identified in CSR to promote the synapsis of these two regions prior to their ligation. In contrast, a dynamic mechanism would play less significant role in NHEJ during V(D)J recombination and in the repair of chromosome-internal DSBs, where the ends are presumably synapsed by the RAG complex and Ku, respectively [162,274]. In accordance with thid model, the joining of distal but not proximal gene segments in the process of V(D)J recombination was found to be preferentially impaired in absence of 53BP1 [273].

The rate of NHEJ and the probability of encounter

One outstanding question raised by our model is how the two-fold difference in mobility that we observe between 53BP1-proficient and -deficient dysfunctional telomeres

accounts for the 50-fold difference in fusion rates. We believe that this inconsistency can be explained by the following two arguments.

First, our analysis was performed on projected, two-dimensional images and therefore, a two-fold increase in diameter would correspond to an eight-fold expansion of the three-dimensional space. In addition, we monitored telomere behavior for relatively short periods of time (20 minutes). Given that it takes approximately five days for the majority of telomeres in a cell lacking TRF2 to fuse, we expect the difference to be larger.

Second, we suggest that the fastest moving telomeres, not their median rate, determine the rate of NHEJ. In this respect, we noted that in 53BP1-proficient cells, more than 10% of dysfunctional telomeres explored territories with diameter greater than two μm, whereas in 53BP1-deficient cells, less than 1% exhibited comparable dynamic features. In an average nucleus with diameter of 20 μm, the most mobile dysfunctional telomeres, observed in 53BP1-wild type cells, are poised to explore a significant fraction of the nuclear volume in relatively short periods of time, thereby increasing their chances of encountering a fusion partner. The absence of these outliers in the 53BP1-null setting might directly cause the absence of NHEJ events.

Increased mobility of dysfunctional telomeres requires microtubules

We have found that the dynamic movement of dysfunctional telomeres is inhibited by drugs that cause microtubule depolymerization, whereas it is not prevented by microtubule stabilizing drugs or by actin inhibitors. These data strongly argue that the enhancement in mobility is driven by an actin-independent, microtubule-mediated

mechanism, thus implicating a role for microtubules in an essential nuclear process in mammalian interphase cells, the process of DNA repair. A few previous studies have linked microtubules to interphase nuclear events. A well-known example is the 'horse-tail' movement in meiotic prophase in fission yeast during which the nucleus oscillates on astral microtubules between the two poles of the cell [267,268]. The oscillatory nuclear movement is led by the spindle pole body, to which telomeres are attached, causing the chromosomes to drag along. Another example is the recent description of a set of proteins in fission yeast that physically couple centromeric heterochromatin to microtubule organizing centers at the nuclear envelope, presumably in order to buttress the nuclear envelope against cytoskeletal forces [269]. Finally, 53BP1 has been found to interact directly with dynein, one of the major motor proteins that move along microtubules [266]. It is very likely that a motor protein is involved in promoting the movement of dysfunctional telomeres. Abrogation of microtubule dynamics, which can generate movement by itself, does not affect the mobility of dysfunctional telomeres, whereas microtubule depolymerization, which disrupts the tracks along which motors translocate, has a dramatic impact.

In sum, our results have suggested that dynamic mobility of 53BP1-containing chromatin is promoted by microtubules, with the movement most likely being generated by a motor protein. In the future, it will be important to determine the link between nuclear sites of DNA damage and cytoplasmic microtubules. Based on the findings of King et al. [269], we speculate that dysfunctional telomeres may be recruited to the nuclear envelope prior to their repair by the NHEJ pathway. Recently, two reports have described the occurrence of telomere-led rapid prophase movement of chromosomes in *S.*

cerevisiae that is preceded by the clustering of telomeres in bouquet structures at the nuclear envelope, although, in this case, the basis for motility was found to be dependent on actin [264,265]. The potential latching of dysfunctional telomeres onto the nuclear envelope would reduce the complexity in the search for a fusion partner from a three-dimensional problem to a two-dimensional problem. We are in the process of testing this hypothesis. An additional implication of the findings of King et al. is that there might be a specialized factor that couples modified chromatin in TIFs to the nuclear envelope. In their experiments, they identified the trans-nuclear envelope factor Ima1 as a heterochromatin-specific binder. It is not known whether Ima1 or a factor with an analogous function plays a role in repair.

Increased mobility of dysfunctional telomeres is promoted by chromatin acetylation

We envision that chromatin marked by a specific modification might be linked to a mobile structure at the nuclear envelope. In support of that model, we have found that dynamic behavior of dysfunctional telomeres depends on histone acetylation. We observed that treatment with HDAC inhibitors selectively augmented the mobility of dysfunctional telomeres in 53BP1-deficient cells, indicating that HDAC activity is inhibitory to mobility in these cells. Importantly, we did not observe similar effects in cells with functional telomeres or in 53BP1-proficient cells with uncapped telomeres. Based on these data, we conclude that the effects of HDAC inhibition are specific to the response to telomere dysfunction. In addition, since the effects of HDAC inhibition only become apparent in the absence of 53BP1, it follows that the role of 53BP1 may be to promote histone acetylation or to prevent histone deacetylation. One possibility is that

tubulin acetylation regulates chromatin dynamics. Another possibility is that 53BP1 directly promotes histone acetylation, prevents deacetylation, or influences the interaction of acetylated histones with acetyl-specific binding partners.

In this regard, several publications have reported on the hyperacetylated state of the activated immunoglobulin region during the process of CSR [275-277]. These observations are not unexpected because transcription is known to be important for CSR since AID-mediated induction of DSBs occurs through a transciption-dependent mechanism. Recently, it has been shown that telomeres are also transciptionally active [278]. Therefore, the effects of HDAC inhibitors on mobility might be specific to transcribed regions. However, in constrast to the immunoglobulin locus, telomeric chromatin is of heterochromatic nature, as evidenced by the hypoacetylated [279] and hypermethylated states of telomeric H3/H4 [280]. In addition, telomeres can silence the transcription of adjacent genes by a mechanism known as the telomere position effect (TPE) [281,282]. TPE in human cells can be alleviated by treatment with an HDAC inhibitor, indicating that it is a consequence of chromatin hypoacetylation. Finally, at the immunoglobulin locus, acetylation occurs exclusively in an AID-dependent manner, which directly links the deposition of acetylation marks to the induction of DSBs and possibly to its role in promoting NHEJ repair [275,277]. It remains to be determined whether acetylation of histones occurs at all sites of DNA damage, including at dysfunctional telomeres, and whether such chromatin marks function to promote chromatin mobility and repair.

Future directions for studying how dynamic behavior influences the rates of NHEJ

We have shown by live-cell imaging that mobility of dysfunctional telomeres is mediated by microtubules and that it is dependent on the acetylation status of chromatin. In order to solidify the connection between these processes and the repair of dysfunctional telomeres, we are currently testing whether treatments with drugs that affect mobility also impact the formation of end-to-end fusions. The role of microtubules has been difficult to address because microtubule inhibitors cause an acute cell cycle arrest at the G2/M transition or in M phase. This precludes the analysis of NHEJ of dysfunctional telomeres, which requires the cumulative effect of G1 events over at least three days to yield a robust signal. On the other hand, it is known that fusions also occur in non-cycling cells that are TRF2-deficient. Therefore, we plan to treat TRF2-deficient G0-arrested cells with nocodazole or taxol and assay directly whether microtubules are required for end-to-end fusions by telomere blot. Because the two drugs impact microtubule stability differently, we expect to see absence of fusion events in nocodazole-treated cells but no effect in cells treated with taxol. We plan to test in a similar manner the role of acetylation by treating TRF2-deficient cells with HDAC inhibitors and examining their effect on telomere fusions.

Telomeres as a model for DSB repair

Our analysis has been performed in the context of dysfunctional telomeres, which are a unique substrate for the NHEJ pathway, since their deprotection generates a single DNA end rather than two ends as in the case of all other types of DSBs. In addition, telomeres are composed of repetitive DNA sequences that are bound by the telomere-specific

shelterin complex. Nevertheless, we believe that the molecular events that take place during telomere deprotection upon TRF2 loss recapitulate the sequence of events that occur in response to DSBs. This parallel is substantiated by previous reports indicating that the DNA damage response to TRF2 loss is ATM-dependent; it involves the recruitment of all known IRIF factors to chromosome ends to form TIFs; it causes the activation of checkpoint signaling; and it results in NHEJ-mediated repair of deprotected chromosome ends (see Introduction for more details and references). Therefore, we believe that our findings may apply to chromosome-internal DSBs as well.

One direct piece of evidence arguing that mobility is not a specific consequence of the removal of TRF2 from chromosome ends is that we observed a similar change in the dynamic behavior of telomeres whose protection was impaired by POT1a/b deletion. Telomere dysfunction in absence of POT1a/b is mechanistically different from the DNA damage events activated by TRF2 deletion, as it involves signaling through the ATR pathway and does not lead to NHEJ-mediated joining of telomeres [197,228]. A common feature of both TRF2 and POT1a/b loss, however, is TIF formation, including accumulation of 53BP1, arguing that dynamic mobility may be a consequence of all 53BP1-containing chromatin.

Hence we have no reason to suspect that TRF2-depleted dysfunctional telomeres, as a substrate to the NHEJ pathway, are treated differently from DSBs except that a repair partner is not immediately available. Therefore, we propose that our findings may apply to the repair of all DNA ends that are located at a distance. In addition, we speculate that dynamic behavior of chromatin may also be advantageous at IRIF-marked chromosome-internal DSBs under certain circumstances (discussed below).

A dynamic view of DNA repair involving distant DNA ends

Based on the findings in this thesis, we propose a novel model for how cells deal with the problem of repairing sites of damage that are located at a distance. Although our results are based on an experimental system that is rather unique and does not have immediate biological relevance, a similar set of events is thought to occur in the immune system where efficient repair of programmed DSBs during V(D)J recombination and CSR is essential for the diversification of the immune system.

We propose that activation of the DNA damage signaling pathways, whose purpose is to prevent cell cycle progression, also lays down the groundwork for a series of histone modifications. The first of these events, the PIKK-dependent phosphorylation of H2AX, functions to recruit a number of DNA damage response factors, including the MRN complex, H2AX, MDC1, RNF8, 53BP1, and others, to sites of damage. A feed-forward amplification loop, which is interwoven into multiple protein-protein interactions, promotes the accumulation of these DNA damage response factors in large structures that can extend for several megabases. We propose that among these factors, 53BP1, which also associates with dimethylated H4-K20, functions to promote H3 and/or H4 acetylation or alternatively, prevents their deacetylation. We hypothesize that the acetylation status of the chromatin at a site of DNA damage determines its ability to acquire increased mobility, possibly by coupling the chromatin at the site of damage to microtubules in the cytoplasm. We argue that DNA ends that have acquired microtubule-mediated dynamic behavior are in turn more likely to encounter a partner to repair with. In our model, the process of NHEJ is enhanced by a mechanism that promotes the temporary association of DNA lesions with the nuclear envelope. We envision that such

mechanism would allow sites of damage to establish a connection with the cytoplasmic microtubule network in order to acquire dynamic potential. In addition, we imagine that local concentration of distant ends in a two-dimensional space will increase their chance for repair.

Whereas most chromosome-internal DSBs are held together so that mobility will not affect their repair, the increased mobility of dysfunctional telomeres would be expected to significantly improve the chance of fusion of two spatially separated chromosome ends. Similarly, during the process of CSR, mobility of DNA ends may be essential to promote the efficiency of NHEJ. Inability to switch regions impairs the development of B-cells and limits the scope of the immune response. In addition, delayed repair of AID-induced DSBs may increase the chance for translocation events. In support of this model, translocations between the immunoglobulin region and the region where the proto-oncogene c-myc is located have been found to occur with increased frequency in 53BP1-deficient B-cells [106]. Translocations between these two loci are well-documented as one of the direct causes of B-cell lymphoma.

Mobility may be a novel mechanism to promote accuracy of DNA repair

The ability of 53BP1 to promote the mobility of DNA ends contradicts its role in preventing translocations. We argue that at chromosome-internal DSBs, the bridging between the two ends established by Ku is enough to counteract chromatin mobility stimulated by 53BP1. On the other hand, if an occasional separation between the two ends at a DSB occurs, mobility would be instrumental in bringing the two ends back together.

This argument suggests that increased mobility cannot harm NHEJ-mediated repair of a chromosome-internal DSB but does not explain how 53BP1 protects from translocations. Since we consider it unlikely that 53BP1 evolved to promote long-distance NHEJ, we would like to extend our hypothesis and claim that 53BP1-mediated mobility can actually function as a quality-control mechanism during the repair of DSBs. We argue that in S-phase, 53BP1-containing mobile DNA ends would be prevented from repairing on a non-sister chromatid. In our model, microtubules provide the dynamic force required to counteract incorrect repair events that lack sister cohesion. This safety mechanism would ensure that only pairing between sister chromatids, which are tightly held together through cohesion, will lead to productive progression of the repair pathway (predominantly HDR). Our hypothesis is, in this respect, analogous to the 'horse-tail' movement described earlier, where microtubule-mediated chromatin oscillations in prophase have been proposed to contribute to the correct pairing of homologous chromosome by applying a dynamic force to counteract incorrect associations [267]. In support of this model, it has been found that, following treatment with modest doses of IR, 53BP1 is instrumental in preventing the formation of radial chromosomes, which are indicative of incorrect HDR events between non-sister chromatids [272]. We have found preliminary evidence for similar genomic instability occurring as a consequence of microtubule inhibition. Therefore, we argue that a 53BP1- and microtubule-dependent mechanism exists to proofread repair events in S-phase and to disrupt inappropriate non-sister interactions. If this model were correct, it would implicate 53BP1 as a critical component of the HDR pathway, in addition to its role in the NHEJ pathway, which we have studied in this thesis.

Concluding remarks

In conclusion, we have proposed a unifying mechanism to explain the contribution of DNA damage response factors to the NHEJ pathway. Our analysis explains why 53BP1 stands out among these factors, by virtue of promoting the dynamic behavior of DNA ends. In addition, we have uncovered the nature of this dynamic mechanism. We have found evidence for a novel microtubule-driven process that acts on interphase cells to promote chromatin mobility during NHEJ and HDR. We propose that the primary role of this dynamic mechanism may be to correct inaccurate repair in S-phase, and that, as a by-product, it also functions to accelerate the repair of distant DNA ends. Finally, we have found that histone modifications, including phosphorylation, methylation, and acetylation marks work synchronously to stimulate these processes.

This work exemplifies how telomeres can be used as an experimental tool to study various aspects of the DNA damage response. Using dysfunctional telomeres as a model system, we have resolved a previously controversial question and unequivocally established that the MRN complex is the only sensor in the ATM pathway. We have also characterized a previously unknown mechanism of how 53BP1 contributes to the NHEJ pathway. In the process, we have uncovered a novel aspect of the repair of dysfunctional telomeres that is mediated through a dynamic mechanism. Based on our findings, we have put forward a model speculating that this mechanism may be required to promote the fidelity and efficiency of DNA repair at all lesions. In the future, telomeres can be used as a tool to further dissect this pathway as well as to characterize novel aspects of the DNA damage response.

MATERIALS AND METHODS

Constructs

Full-length human MDC1 was cloned from pcDNA3[251] into a N-3xFLAG-pLPC-puro retroviral expression vector by restriction enzyme digestion cloning. The construct was used for transient overexpression of MDC1 in 293T cells.

Full-length human 53BP1 was cloned by PCR into a N-myc-pLPC-puro retroviral expression vector. The D1521A mutation was introduced by a PCR-based mutagenesis strategy using the following mutagenesis primers: 5'-AAATTGCTCTTTGATGCTGGGTACGAATGTGAT-3' and 5'-ATCACATTCGTACCCAGCATCAAAGAGCAATTT-3'. The mutation was confirmed by sequencing. Wild-type and D1521A rescue alleles were introduced into $TRF2^{F/-}$ $53BP1^{-/-}$ cells by five consecutive retroviral infections with virus-containing supernatants from Phoenix cells, delivered at 12-h intervals. Puromycin selection was applied. Infection with the empty vector was used as a negative control.

Fluorescently amino-terminally tagged mCherry-BP1-2 and eGFP-TRF1 were cloned by PCR into pLPC-puro and pWzl-hygro, respectively. In-frame fusions were confirmed by sequencing. mCherry-BP1-2 and eGFP-TRF1 constructs were consecutively introduced into $TRF2^{F/-}$ $53BP1^{+/-}$ and $TRF2^{F/-}$ $53BP1^{-/-}$ cells by retroviral infections, followed by puromycin (4 days) and hygromycin (7 days) selection, respectively.

Mammalian cell culture

Refer to list of cell lines in Appendix 1.

Mouse embryonic fibroblasts (MEFs) were obtained from E13.5 embryos of timed pregnancies using standard techniques and were grown in DMEM containing 15% Fetal Bovine Serum (Gibco), supplemented with 100 U/ml penicillin (Sigma), 0.1 μg/ml of streptomycin (Sigma), 2 mM L-glutamine (Invitrogen), 0.1 mM non-essential amino acids (Invitrogen), 1 mM sodium pyruvate (Sigma), and 50 μM β-mercaptoethanol (Chemicon). Primary MEFs were immortalized at passage 2 with pBabe SV40-LT (a gift from G. Hannon) using retroviral protocol given below.

SV40-LT transformed and $p53^{-/-}$ MEFs, Pheonix ecotropic packaging cell line (ATCC), IMR90 primary lung fibroblasts (ATCC), BJ fibroblasts (Clontech), BJ-hTERT, A-T fibroblasts (ATCC), and F02-98 fibroblasts (refer to table below for details and references) were grown in DMEM supplemented with 100 U/ml penicillin (Sigma), 0.1 μg/ml of streptomycin (Sigma), 2 mM L-glutamine (Invitrogen), 0.1 mM non-essential amino acids (Invitrogen), and 15% Fetal Bovine Serum (Gibco). HeLa 1.2.11, HeLa 204, HeLa 1.3, 293T, and Phoenix amphotropic packaging cell line (ATCC) were grown in DMEM supplemented as above except for the serum which was replaced with 10% Bovine Calf Serum (HyClone). All cells were grown at 37°C in the presence of 5% CO_2 and 95% relative humidity. Cells were passaged by pre-rinsing with room temperature trypsin-EDTA (Gibco, 0.25%) followed by incubation in trypsin-EDTA for 2-5 min. Tripsin was inactivated by adding serum-containing medium. Cells were counted with a Counter Z1 Particle counter and seeded onto a new plate as desired.

Retroviral gene delivery

24 h prior to transfection, $5x10^6$ Phoenix packaging cells were plated in 10 cm dishes. For infection of mouse cells, Phoenix ecotropic cells were used, whereas for infection of human cells, Phoenix amphotropic cells were used. Prior to infection the medium was changed. Phoenix cells were transfected with 20 μg of the appropriate plasmid DNA by $CaPO_4$ coprecipitation (described below). The media was refreshed 5-8 h later. 36 h after transfection, media was collected and was filtered through a 0.4 μm filter. Polybrene was added to a final concentration of 4 μg/mL and the virus containing medium was used to infect desired cells plated 24 h earlier at a density of $5x10^5$ cells per 10 cm dish. Fresh media was added to the virus producing cells and same cells were used for a total of 3-4 consecutive infections delivered at 12-h intervals. 12 h after the last selection, if appropriate, cells were split into fresh media containing antibiotics for selection (puromycin 2 μg/ml, hygromycin 90 μg/ml). Selection was maintained for 3 days in the presence of puromycin and 7 days in the presence of hygromycin, until uninfected control cells had died.

Knockdown of protein levels

Protein levels of desired targets were stably reduced in human and mouse cells using shRNAs expressed from the pSUPERIOR retroviral vector (OligoEngine). Retrovirus was produced in ampho- or eco-tropic Phoenix cells and used to infect human or mouse cells, respectively, 4 times at 12-hr intervals, followed by puromycin selection.

The following target sequences were cloned into pSUPERIOR and confirmed by DNA sequencing:

luciferase control: 5'-CGTACGCGGAATACTTCGA-3' (Dharmacon);

hMDC1 sh1: 5'-GCAGAAGCCAATCAGCAAA-3';

hMDC1 sh2: 5'-AGAGGGACAATGATACAAA-3';

hMDC1 sh3: 5'-GTCTCCCAGAAGACAGTGA-3'; [110]

mMDC1 sh4: 5'-ACAGCATGCAGTAATTGAA-3';

mMDC1 sh5: 5'-ACACAGCCGTTCTGTCTAA-3';

hH2AX sh3: 5' –CAACAAGAAGACGCGGAATC-3'; [109]

hMre11.4: 5'-CCTGCCTCGAGTTATTAAG-3'; [283]

hMre11.5: 5'-CTGCGAGTGGACTATAGTG-3'; [283]

hMre11.6: 5'-GATGCCATTGAGGAATTAG-3'; [283]

h53BP1.1: 5'-GCCAGGTTCTAGAGGATGA-3'; [127]

h53BP1.2: 5'-GATACTCCTTGCCTGATAA-3'; [127]

CtIP sh1: 5' -GCAGACCTTTCTCAGTATA-3'; [58]

CtIP sh2: 5' -GCATTAACCGGCTACGAAA-3'; [58]

Efficient knockdown of human MDC1, Mre11, 53BP1, H2AX, and mouse CtIP were verified by immunoblotting. Mouse MDC1 protein was detected by immunofluorescence and reduction of RNA levels after shRNA treatment was confirmed by reverse transcriptase PCR. RT-PCR was performed using oligo-dT ThermoScript RT-PCR system (Invitrogen). RNA was isolated from approximately 10^6 cells using Qiagen RNAeasy kit. 3 μg RNA was reverse transcribed using ThermoScript RT-PCR system (Invitrogen) using oligo dT priming and the protocol provided by the manufacturer. The

primers used for PCR after cDNA synthesis are: mMDC1 (forward CTGTCCCTGAACTGGCTGTACCAG and reverse GGTAGATGACATTTCCAAATTGGA) and GAPDH (forward TGAAGGTCGGTGTGAACGGATTTGGC and reverse CATGTAGGCCATGAGGTCCACCAC) served as a control.

Protein levels of human MDC1 were transiently downregulated by siRNA using a previously published target (5'-ACAGTTGTCCCCACAGCCC-3' [110]) using Oligofectamine (Invitrogen) transfection protocol supplied by the manufacturer and performed in OPTI-MEM medium (Invitrogen) in the absence of serum and antibiotics.

Introduction of Cre recombinase

Cre recombinase was introduced using the retroviral infection technique described above. MEFs were infected 3 times at 12 h intervals with pMMP Hit&Run Cre [284] retrovirus. Mock infection was used as negative control. No selection was applied. The experimental time-points were counted as h or days after the second retroviral infection, presumably at the point of protein expression and were referred to as h or days post infection.

For live cell imaging, 4 Hit&Run Cre infections were performed, the first and the second spaced by 12 h and the last 3 infections spaced by 6 h. Cells were plated on imaging plates 12 hours after the last infection or at least 48 hours prior to imaging. No selection was applied.

For long term analyses that required selectable Cre expression, infection with retrovirus expressing pWzl-hygro-Cre or empty vector, as a negative control, was performed, followed by hygromycin selection. The experimental time-points were

counted as h or days after the second retroviral infection, presumably at the point of protein expression and were referred to as h or days post infection.

Alternatively, Cre recombinase was delivered via adenoviral infection. Cells were infected in suspension with virus at concentration of 1000 pfu/cell. Infection was repeated on attached cells 8-12 h later. The experimental time-points were similarly counted after the second infection and were referred to as h or days post infection.

Cells were harvested by trypsiniziation at indicated timepoints post infection, counted, and processed according to each experiment.

Inhibition of TRF2 function in human cells

TRF2-DN and control β-gal adenovirus were used at 100 pfu/cell for HeLa 204, HeLa 1.3, and IMR90 cells. Cells were infected in suspension and the medium was changed 24 h later. Cells were harvested for analysis 48 h post infection. For immunofluorescence analysis, cells/virus suspension was plated on coverslips.

Growth analysis

For growth curves following Cre infections, $5x10^5$, $2.5x10^5$, and $1.25x10^5$ cells were plated on 10 cm dishes 24 h post retroviral infection and counted, respectively 72, 96, and 120 h post infection. Alternatively, $5x10^5$ cells were plated on a 10 cm dish 24 h after the retroviral infections and harvested, counted, and replated at the same density at 72 h. These cells were harvested and counted at 120 h post infection. Growth curve was presented as cumulative cell numbers plotted against time or as PDs plotted against time.

PDs were determined by the following formula: PD = original PD + [ln(# cells at passage/#cells seeded)/ln(2)] using Excel and.

Calcium phosphate transfection of 293T and Phoenix cells

16-24 h prior to transfection, 3-4 x 10^6 293T cells were plated in 10 cm dishes. Cells were transfected with 10 μg total DNA of the appropriate plasmids using $CaPO_4$ coprecipitation. For each plate, 428 μl H_20, 62 μl 2M $CaCl_2$, and 10 μg total plasmid DNA were mixed with an equal amount of 2 x HBS (50 mM HEPES pH 7.05, 10 mM KCl, 12 mM dextrose, 280 mM NaCl, 1.5 mM Na_2PO_4). During the process of mixing the solution was aerated by blowing air through a 2 ml pipette with a Pipet-aid (Drummond). Media was refreshed 5-8 h after transfection.

Co-IP of overexpressed proteins in 293T cells

For immunoprecipitation of proteins transiently expressed in 293T cells, transfection was performed as above. 48 h after transfection, cells were harvested, washed with PBS, and resuspended in 200-500 μl of lysis buffer (50 mM Tris-HCl pH 7.4, 1% Triton X-100, 0.1% SDS, 150 mM NaCl, 1 mM EDTA, 1 mM DTT, 100 μM PMSF, with a complete mini-protease inhibitor tablet [Roche] per 10 ml). The NaCl concentration was raised to 400 mM, and the lysate was incubated on ice for 5 min. The NaCl concentration was reduced to 200 mM with an equal volume of cold water and cell debris were removed by centrifugation at 13K for 10 min at 4°C. 50 μl of 2 x Laemmli buffer was added to 50 μl of lysate and set aside as the "Input." 5 μl of anti-myc Ab (9E10, Oncogene) were added

to 800 µl of lysate. Samples were nutated at 4°C for 5 h. 60 µl of a Protein G sepharose slurry (50% [v/v] Protein-G sepharose [Amersham] in PBS in 1 mg/ml BSA) were added and samples were nutated at 4°C for an additional 60 min. Beads were washed 4 times at 4°C with lysis buffer, and immunoprecipitated protein was eluted with 60 µl 2 x Laemmli buffer. Samples were boiled for 5 min before loading onto SDS-PAGE gels.

IPs of endogenous proteins

IPs of endogenous proteins were performed in BJ-hTERT, HeLa 1.2.11, and MEFs. Cells were harvested by trypsinization and the cell pellet was resuspended on ice for 30 min in Buffer C (20 mM HEPES-KOH, pH 7.9, 420 mM KCl, 25% glycerol, 0.1 mM EDTA, 5 mM MgCl2, and 0.2% NP-40, with freshly added 1 mM DTT, 100 µM PMSF, and 1 mini-protease inhibitors tablet (Roche) per 10 ml). Cells were centrifuged at 15K for 10 min at 4^0C and the supernatant as dialyzed for at least 6 h against Buffer D (20 mM HEPES-KOH, pH 7.9, 100 mM KCl, 25% glycerol, 0.1 mM EDTA, containing freshly added 1 mM DTT and 100 µM PMSF). After dialysis, the lysate was centrifuged again and the cleared supernatant was used for IPs. 10% of IP volume was set aside as input. 5 µl of desired antibodies (Appendix II) were added to the lysate and samples were nutated overnight at 4^0C. 60 µl of a Protein G sepharose slurry (50% [v/v] Protein-G sepharose [Amersham] in PBS in 1 mg/ml BSA) were added and samples were nutated at 4°C for an additional 60 min. Beads were washed 4 times at 4°C with Buffer C, and immunoprecipitated protein was eluted with 60 µl 2 x Laemmli buffer. Samples were boiled for 5 min before loading onto SDS-PAGE gels. The phosphatase inhibitors, 10 mM NaF and 50 mM β-glycerophosphate were added to Buffers C and D.

Whole cell lysates and Western blots

Cells were lysed in 2 × Laemmli buffer (100 mM Tris-HCl, pH 6.8, 200 mM DTT, 3% SDS, 20% glycerol, 0.05% bromophenol blue) at 10^4 cells per microlitre, denatured for 7 min at 100 °C, and sheared with a 28 gauge insulin needle before loading the equivalent of 1×10^5 cells per lane. Protein samples were separated by SDS-PAGE and blotted onto nitrocellulose membranes. Membranes were blocked in 5% milk in PBST (0.5% Tween-20 in PBS) for 30 min at RT and nutated with primary antibodies (Appendix II) in 5% or 0.1% milk in PBST overnight at 4°C. Membranes were washed 3 times in PBST, nutated in secondary antibody in 5% milk in PBST for 1 hr at RT, and washed 3 times with PBST at RT. Blots were developed with enhanced chemiluminescence (Amersham).

Chromatin Immunoprecipitation (ChIP)

Cells were trypsinized and washed with PBS, fixed in 1% formaldehyde in PBS for 60 min at RT, washed in PBS, and lysed in 1% SDS, 50 mM Tris-HCl pH 8.0, 10 mM EDTA at a density of $1x10^7$ cells/ml. Lysates were sonicated on ice for 10 cycles of 20 seconds each (0.5 seconds on/0.5 seconds off) on power setting 5 on a Misonix Sonicator 3000. Two 50 µl aliquots of lysates were set aside at 4°C to represent "Total" DNA. 200 µl of lysate was diluted with 1.2 ml 0.01% SDS, 1.1% Triton X-100, 1.2 mM EDTA, 16.7 mM Tris-HCl pH 8.0, and 150 mM NaCl. Antibody (20 µl crude serum or 4 µl affinity purified antibody; Appendix II) was added and cells were nutated overnight at 4°C. 30 µl protein G sepharose beads (Amersham; blocked with 30 µg BSA and 5 µg sheared E. coli DNA) was added and samples were nutated for an additional 30 min at

4°C. Beads were pelleted by centrifugation and pellets were washed with 0.1% SDS, 1% Triton X-100, 2 mM EDTA pH 8.0, 20 mM Tris-HCl pH 8.0, 150 mM NaCl. The second wash was the same except with 500 mM NaCl. Subsequent washes were with 0.25 M LiCl, 1% NP-40, 1% Na-deoxycholate, 1 mM EDTA pH 8.0, 10 mM Tris-HCl pH 8.0, 1 mM EDTA. Chromatin was eluted from beads with 500 µl 1% SDS, 0.1M Na_2CO_3. 450 µl 1% SDS, 0.1M Na_2CO_3 was added to the "Total" fractions, and these were subsequently processed along with the rest of the samples. 20 µl 5M NaCl was added and samples were incubated for 4 hr at 65°C to reverse cross-links. At this point, 20 µl 1M Tris-HCl pH 6.5, 10 µl 0.5 M EDTA, and 20 µg DNase free RNase A was added and samples were incubated at 37°C for 30 min 40 µg proteinase K was added and samples were digested for 60 min at 37°C and extracted with phenol. 20 µg of glycogen was added and samples were mixed. 1 ml ethanol was added and DNA was precipitated overnight at -20°C. Precipitated DNA was dissolved in 100 µl H_20, denatured at 95°C for 5 min, and blotted onto Hybond membranes in 2 x SSC (0.3M NaCl, 0.03M Sodium citrate). "Total" fractions were diluted 1/4, 1/8, and 1/16 and blotted as well. Membranes were treated with 1.5M NaCl, 0.5 N NaOH for 10 min and then with 1 M NaCl, 0.5 M Tris-HCl pH 7.0 for 10 min Hybridization was performed with a γ^{32-}P endlabeled $[CCCTAA]_4$ probe as described for in gel hybridization of genomic DNA. Membranes were washed 4 times in 2 x SSC and exposed overnight to a PhosphorImager screen. Screens were developed using a STORM 820 Phosphorimager (Molecular Dynamics). ImageQuant software was used to quantify the percent of total telomeric DNA that was precipitated by each antibody.

In-gel analysis of telomeric DNA from mouse cells

For the analysis of mouse genomic DNA, $1x10^6$ or $0.5x10^6$ MEFs were resuspended in PBS and mixed 1:1 (v/v) with 2% agarose (SeaKem agarose) to obtain 5×10^5 cells per agarose plug. Plugs were digested overnight with 1 mg/ml Proteinase K (in buffer containing 10 mM Tris-HCl pH 7.9, 250 mM EDTA, 0.2% sodium deoxycolate, 1% sodium lauryl sarcosine), washed extensively with TE buffer (10 mM Tris-HCl, pH 8.0, 1 mM EDTA) and incubated overnight at 37 °C with 60 U MboI. The following day, the plugs were washed once in TE and once in water, and were equilibrated in 0.5 × TBE. Plugs were loaded on a 1% agarose/0.5 × TBE gel and run for 24 h using CHEF-DRII PFGE apparatus (BioRad) in 0.5 × TBE running buffer. The settings were as follows: initial pulse, 5 min; final pulse, 5 min; 6 V/cm;14°C. Gels were dried and then prehybridized in Church Mix (0.5M Na_2HPO_4 pH 7.2, 1 mM EDTA, 7% SDS, 1% BSA) for 1 hr at 50°C. Hybridization was performed overnight at 50°C in Church Mix with 4 ng of a γ-^{32}P-ATP end-labeled probe, $[CCCTAA]_4$ (See below for labeling protocol). The gel was washed at 55°C: 3 times for 30 min each in 4X SSC and one time for 30 min in 4X SSC, 0.1% SDS and exposed to a PhosphorImager screen overnight. Subsequently, the gel was denatured in 0.5 M NaOH, 1.5 M NaCl for 30 min, neutralized with two 15 min washes in 0.5 M Tris-HCl pH 7.5, 3 M NaCl, prehybridized in Church mix for 1 hr at 55°C, and hybridized with the same probe as above overnight at 55°C. The gel was washed and exposed as above. The single-stranded G-overhang signal was quantified with ImageQuant software and normalized to the total telomeric DNA quantified after denaturation.

In-gel analysis of telomeric DNA from human cells

DNA was isolated from human cells, resuspended in TNE (10 mM Tris-HCl, pH 7.4, 100 mM NaCl, 10 mM EDTA) and digested overnight in 1 mg/ml Proteinase K in TENS buffer (TNE containing 0.1% SDS) at 37^0C, followed by phenol-chloroform extraction and isopropanol precipitation in the presence of sodium acetate. The isolated DNA was resuspended in TNE, containing 100 μg/ml RNase A and incubated for 30 min at 37^0C, followed by a second round of Proteinase K digestion and phenol-chroroform extraction/isopropanol precipitation. The purified DNA, dissolved in TE, was digested overnight with AluI and MboI in the presence of RNase A. The final concentration of the digested DNA was measured by Hoechst fluorimetry. Equal amounts of DNA from each sample were loaded on a 0.7% agarose gel in 1 x TAE with ethidium bromide and separated by electophoresis for 1 h at 30 V and then at 45V until the 1.3 Kb marker was at the bottom of the gel. The gel was photographed with a ruler next to the markers and processed as described above for in-gel analysis of telomeric DNA in mouse cells.

γ-^{32}P end labeling of oligonucleotides with T4 polynucleotide kinase (PNK)

2 μl H_20, 1 μl 10X T4 DNA PNK buffer (NEB), 1 μl 10 U/μl T4 DNA PNK (NEB), 1 μl 50 ng/μl $[CCCTAA]_4$ oligonucleotide and 5 μl 10.0 mCi/ml γ-^{32}P (NEN) were mixed and incubated for 45 min at 37°C. 80 μl TES (10 mM Tris-HCl pH 8.0, 10 mM EDTA pH 8.0, 0.01% SDS) were added to stop the reaction. The probe was loaded onto a 3 ml G25 Sephadex column equilibrated with TNES (10 mM Tris-HCl pH 7.4, 10 mM EDTA, 100 mM NaCl, 1% SDS). The column was washed with 700 μl TNES and the probe was

eluted with 600 µl TNES and diluted into 25 ml of Church mix (0.5M Na_2HPO_4 pH 7.2, 1 mM EDTA, 7% SDS, 1% BSA).

Telomere fluorescence in situ hybridization (FISH)

Cells were grown to approximately 80% confluence on 10 cm dishes and incubated for 1 h 15 min in 0.1 µg/ml colcemide (Sigma) for human cells and 0.2 µg/ml colcemide (Sigma) for mouse cells. Cells were harvested by trypsinization, centrifuged at 1K for 5 min, and resuspended in 0.075M KCl prewarmed to 37°C. Cells were incubated at 37°C for 15 min with occasional inversion. Cells were centrifuged at 1K for 5 min and the supernatant was decanted. Cells were loosened by tapping in the remaining (~200 µl) supernatant. 500 µl of cold 3:1 methanol:glacial acetic acid fixative was added dropwise while cells were mixed gently on a vortexer (<1000 rpm). Another 500 µl fixative was added slowly while cells were being mixed. Tubes were then filled to 10 ml with the fixative and fixed at 4°C for at least 24 h. To prepare metaphase spreads, cells were centrifuged at 1K rpm for 5 min and the supernatant was decanted. Cells were resuspended in the remaining fixative (~300 µl) and 100 µl were dropped from approximately 6 inches onto glass slides, which had been soaked in cold water. Slides were washed with fresh fixative and placed on a humidified heating block set to 70°C for 1 min. Spreading efficiency was checked under a light microscope. Slides were dried overnight. Alternatively, 100 µl of cells resuspended in fixative were dropped on dry slides in a temperature-controlled chamber (settings at 20^0C and 50% humidity) (Thermotron). Slides were washed with fresh fixative and allowed to dry overnight in the chamber.

If only DAPI staining was desired, slides were rehydrated in PBS for 5 min, stained with DAPI in PBS for 5 min, washed in PBS for 5 min, and allowed to dry before mounting.

For peptide nucleic acid (PNA) FISH, slides, prepared as above, were washed in PBS once and fixed in 4% formaldehyde for 2 min at room temperature. After extensive PBS washes, spreads were digested for 10 min at 37 °C with 1 mg/ml pepsin dissolved in 10 mM glycine, pH 2.2. Slides were then washed in PBS, fixed again in 4% formaldehyde for 2 min at room temperature, and washed in PBS before dehydration by consecutive 5-min incubations in 70%, 95% and 100% ethanol. After air-drying, Hybridizing Solution (70% formamide, 1 mg/ml blocking reagent (Roche), 10 mM Tris-HCl, pH 7.2) containing FIu-OO-$(AATCCC)_3$ PNA probe (Applied Biosystems) was added and spreads were denatured by heating for 3 min at 80 °C on a heat block. Spreads were then allowed to hybridize in the dark for 2 h at room temperature. Two 15-min washes were performed in a mixture containing 70% formamide, 10 mM Tris-HCl, pH 7.0, and 0.1% BSA, followed by three washes in a mixture containing 0.1 M Tris-HCl, pH 7.0, 0.15 M NaCl and 0.08% Tween-20, with DAPI added to the second wash to counter-stain the chromosomal DNA. Slides were mounted in antifade reagent (ProLong Gold, Invitrogen), and digital images were captured with a Zeiss Axioplan II microscope with a Hamamatsu C4742-95 camera using Improvision OpenLab software.

Immunofluorescence

Cells were grown on coverslips. Cells were rinsed with PBS, fixed with 2% paraformaldehyde in PBS for 10 min at RT and washed twice with PBS for 5 min. Cells were either stored in PBS with the addition of 0.02% azide or processed immediately. If extraction was desired, prior to fixation, cells were treated with Triton X-100 extraction buffer (0.5% Triton X-100, 20 nM HEPES-KOH pH 7.9, 50 mM NaCl, 3 mM $MgCl_2$, 300 mM sucrose). Extracted cells were fixed with 3% paraformaldehyde, 2% sucrose for 10 min at RT, and washed twice with PBS. Cells were permeabilized with Triton X-100 buffer after fixation. After permeabilization, cells were washed three times with PBS and blocked with PBG (0.2% (w/v) cold water fish gelatin (Sigma), 0.5% (w/v) BSA (Sigma) in PBS) for 1 h at RT. Cells were incubated with primary antibody (Appendix II) diluted in PBG for 2 h at RT or overnight at 4°C, washed 3 times with PBG at RT, incubated with secondary antibody diluted 1:250 in PBG for 1 h at RT, and washed 3 times with PBS. To the second PBS wash 0.1 μg/ml 4,6-diamidino-2-phenylindole (DAPI) was added. Coverslips were sealed onto glass sides with embedding media (ProLong Gold Antifade Reagent, Invitrogen). Digital images were captured with a Zeiss Axioplan II microscope with a Hamamatsu C4742-95 camera using Improvision OpenLab software.

Immunofluorescence-FISH

Cells were grown on coverslips and fixed for 10 min in 2% paraformaldehyde at room temperature followed by PBS washes (γ-H2AX, MDC1 and 53BP1) or fixed for 10 min in methanol:acetone (1:1) at -20°C followed by dehydration and rehydration in PBS for 5 min (NBS1). Coverslips were blocked for 30 min in blocking solution (1 mg/ml BSA,

3% goat serum, 0.1% Triton X-100, 1 mM EDTA in PBS). Next, the cells were incubated with primary antibodies (Appendix II) diluted in blocking solution for 1 h at room temperature. After PBS washes, coverslips were incubated with Alexa 488- or Rhodamine-Red-X-labelled secondary antibody raised against mouse or rabbit (Jackson) for 30 min and washed in PBS. At this point, coverslips were fixed with 2% paraformaldehyde for 10 min at room temperature, washed extensively in PBS, dehydrated consecutively in 70%, 95% and 100% ethanol for 5 min each, and allowed to dry completely. Hybridizing solution (70% formamide, 1 mg/ml blocking reagent (Roche), 10 mM Tris-HCl, pH 7.2, containing PNA probe FITC-OO-$(AATCCC)_3$ (Applied Biosystems) was added to each coverslip and the cells were denatured by heating for 10 min at 80 °C on a heat block. After 2 h incubation at room temperature in the dark, cells were washed twice with washing solution (70% formamide, 10 mM Tris-HCl, pH 7.2) and twice in PBS. DNA was counterstained with DAPI and slides were mounted in antifade reagent (ProLong Gold, Invitrogen). Digital images were captured with a Zeiss Axioplan II microscope with a Hamamatsu C4742-95 camera using Improvision OpenLab software.

To detect expression and localization of fluorescently marked proteins, cells were fixed for 10 min in 2% paraformadehyde at room temperature. Digital images of fluorescent eGFP and mCherry signals were captured as described above.

BrdU analysis

Cells on coverslips were incubated for 1 h in 10 μm BrdU at 37^0C; fixed in 75% ethanol, 25% 0.05 M glycine (pH 2.2) for 45 min at -20^0C, washed twice in PBS, and processed for IF using α-BrdU-FITC-conjugated antibody. DNA was counterstained with DAPI. Digital images were captured with a Zeiss Axioplan II microscope with a Hamamatsu C4742-95 camera using Improvision OpenLab software. The fraction of BrdU positive cells was scored.

Senescence-associated β-gal staining

TRF2-DN or empty vector control were expressed in amphotrophic Phoenix cells from pWzl-hygro. Virus containing supernatant was used to infect IMR90 cells 3 times at 12 h intervals, followed by hygromycin selection for 10 days. At this point, equal number of TRF2-DN and control cells was plated and 48 h later senescence-associated β-galactosidase staining was performed. After PBS wash, cells were fixed for 5 min in Fixing solution (2% formaldehyde and 0.2% glutaraldehyde in PBS). Cells were washed once more in PBS before staining with Staining solution (1 mg/ml X-gal, 150 mM NaCl, 2 mM $MgCl_2$, 5 mM $K_3F(CN)_6$, 5 mM $K_4F(CN)_6$, 40 mM NaPi pH 6.0) at 37^oC for 6 to 16 h. The plates were then washed twice with PBS and photographed.

Live-cell imaging

TRF2$^{F/-}$53BP1$^{+/-}$ and TRF2$^{F/-}$53BP1$^{-/-}$ cells, expressing eGFP-TRF1 (to visualize telomeres) and mCherry-BP1-2 (h53BP1 aa 1220-1711, to mark sites of DNA damage), or TRF2$^{F/-}$53BP1$^{+/-}$, TRF2$^{F/-}$53BP1$^{-/-}$, TRF2$^{F/-}$Lig4$^{-/-}$p53$^{-/-}$, and TRF2$^{F/-}$ATM$^{-/-}$ cells expressing eGFP-TRF1 only, untreated or treated with Cre, were seeded onto MatTek glass bottom plates and grown for 2 days before imaging. Imaging was performed 72-84 h after Cre-mediated deletion of TRF2. Right before imaging, cells were changed into Leibovitz's L-15 medium (Gibco) supplemented with 30% Fetal Bovine Serum, 100 U/ml penicillin (Sigma), and 0.1 μg/ml of streptomycin (Sigma) and were allowed to equilibrate for 30 minutes. During the imaging session, the temperature was maintained at 37°C with an environmental chamber. Cells were monitored using a DeltaVision RT microscope system (Applied Precision) with a PlanApo 60x 1.40 n.a. objective lens (Olympus America, Inc.). 5 mm Z-stacks at 0.5 mm steps in both eGFP and mCherry channels were acquired using SoftWoRx software with 50 msec and 30 msec exposure time, respectively, every 30 seconds over 20 minutes (t=40 frames) at 2 x 2 binning with 512 x 512 pixels in final size. Images were deconvolved and projected in two dimensions using SoftWoRx software.

The tracking analysis of eGFP-TRF1-marked telomeres was performed with ImageJ software for at least 10 cells for each genotype [285]. Cells were registered by StackReg plugin using both Translation and Scaled Rotation options. Next, particles were tracked using Particle Detector and Tracker plugin with the following parameters for particle detection and tracking (radius=2 pixels; cutoff=2 pixels; percentile=1; link

range=1; displacement=5 pixels). The x and y coordinates of each trajectory were output for further calculation.

Per cell, 5 telomeres were chosen for analysis based on two criteria: first, they were continuously tracked for at least 35 out of 40 frames and second, they co-localized with the mCherry-BP1-2 dysfunctional telomere marker for at least 18 min. In order to correct for cell mobility, the average x and y values of the 5 telomeres were calculated in each frame and this was used as a reference point. All data output in pixels (standard ImageJ output) were converted to meters by the formula, 1 pixel = 0.2156 mm, based on the characteristics of the objective.

The following formulas were used to calculate the distance traveled between two timepoints, cumulative distance traveled and average speed of an individual telomere, T ($x_T^{t=n}$, $y_T^{t=n}$) relative to the reference point R ($x_R^{t=n}$, $y_R^{t=n}$):

Displacement, D_n, between two timepoints t=n-1 and t=n:

$D_n = \text{sqrt}(((x_T^{t=n} - x_R^{t=n}) - (x_T^{t=n-1} - x_R^{t=n-1}))^2 + ((y_T^{t=n} - y_R^{t=n}) - (y_T^{t=n-1} - y_R^{t=n-1})^2))$ [mm];

Cumulative Distance traveled in 20 min (t=40), D_{cum}:

$D_{cum} = \text{sum}\ (D_1, D_2, \ldots, D_{40})$ [mm];

Average Speed, S:

$S = D_{cum}/20$ [nm min^{-1}].

To calculate the displacement from the starting point (t=0) for a given telomere T ($x_T^{t=n}$, $y_T^{t=n}$) at t=n, the following calculation was performed based on a reference point, R, defined as above:

Displacement from origin, $D_{ori,t}$:

$$D_{ori,\,t} = \mathrm{sqrt}(((x_T^{t=n} - x_R^{t=n}) - (x_T^{t=0} - x_R^{t=0}))\text{^}2 + ((y_T^{t=n} - y_R^{t=n}) - (y_T^{t=0} - y_R^{t=0}))\text{^}2).$$

Maximum displacement from starting point, $D_{ori\ MAX}$, for a given telomere recorded during an imaging session was used as a measure of the territory that the telomere has sampled during the imaging session and calculated as shown below:

$$D_{ori\ MAX} = \max (D_{ori,\,1}, D_{ori,\,2}, \ldots D_{ori,\,40}).$$

Statistical analysis was performed using Prism Software. Mann-Whitney test (also referred to as rank sum test), which compares two unpaired groups without assuming Gaussian distribution, was applied to calculate the statistical significance values.

Treatment with drugs and IR

Cells were treated with the following drugs diluted in imaging medium:

Actin inhibitors:

Latrunculin A, 0.1 μg/ml, 1 h prior to imaging

Cytochalasin B, 10 μM, 15 min prior to imaging

Cytochalasin D, 10 μM, 15 min prior to imaging

Microtubule inhibitors:

Nocodazole, 1 μg/ml, 1 h prior to imaging

Taxol (paclitaxel), 20 μM, 1 h prior to imaging

Vincristine, 10 nM, 1 h prior to imaging

1 μM,1 h prior to imaging

HDAC inhibitors:

Trichostatin A: 10 ng/ml, 24 h prior to imaging

50 ng/ml, 24 h prior to imaging

100 ng/ml, 24 h prior to imaging (lethal)

SAHA: 50 nM, 24 h prior to imaging

Valproic acid: 1 mM, 24 h prior to imaging

IR treatment:

For live-cell imaging experiments, wild-type or $Lig4^{-/-}p53^{-/-}$ cells, expressing eGFP-TRF1, plated on imaging plates, were irradiated with 1 Gy γ-irradiation from Ce source and imaged immediately (with 10 min delay to setup the imaging) or allowed to recover for 2 h.

For metaphase analysis, wild-type cells were irradiated in suspension with 5 Gy, and plated in the presence or absence of 1 μg/ml nocodazole. Cells were harvested 12 h post-IR and processed for metaphase analysis by DAPI staining as described above.

FAR assay

Subconfluent HeLa 204 human cells or $TRF2^{F/+}p53^{-/-}$ MEFs were pre-cooled on ice before irradiation with a range from 10 to 60 Gy. DNA was embedded in 0.8% agarose plug, approximately $1x10^6$ cells/plug. Plugs were digested overnight with Proteinase K (as in In-gel detection of telomeric DNA) and washed extensively in TE before loading in 0.8% agarose/0.5 x TBE gel and ran for 65 hours using CHEF-DRII PFGE apparatus (BioRad, Hercules, CA) in 0.5 x TBE running buffer (initial pulse, 50 s; final pulse, 5000 s; 1.5 V/cm; at 14°C). The gels were processed further by Southern blotting for telomeric and Bam repeats (see below).

FAR (fraction of activity released) ratio represents the ratio of the signal in the lane (released from the well) to the total signal (lane + well). 20 Gy was chosen as the least amount of DNA damage that allowed reproducible analysis of the repair slope. For the PIKK inhibitor experiment, HeLa 204 cells were irradiated with 20 Gy and harvested immediately (0 time point) or allowed to recover for the indicated time at 37°C in medium that contained 50 μM wortmannin or 10 mM caffeine as indicated.

Southern blotting for telomeric, human-specific Alu and mouse-specific Bam repeats

For Southern blotting, the gel was depurinated for 30 min in 0.25 M HCl, denatured 2x30 min in 1.5 M NaCl; 0.5 M NaOH and neutralized 2x30 min in 1 M Tris HCl pH 7.4; 1.5 M NaCl before blotting onto Hybond membrane for 24 hours in 20xSSC (3 M NaCl; 0.3 M Sodium Citrate). DNA was crosslinked in Stratalinker and pre-hybridized for 1 hour in Church mix at 65°C before incubating with radioactively labeled probes specific to the

human Alu repeats (for human cells) or mouse Bam repeats (for mouse embryo fibroblasts). Briefly, 50 ng probe was mixed with random hexamer primers and boiled for 5 min. After cooling down on ice, ^{32}P-dCTP, unlabeled dATP, dGTP and TTP and Klenow polymerase were added and the reaction was allowed to proceed for at least 90 min at RT. The labeled probe was subsequently isolated over G-50 column and the eluate was denatured for 5 min at 100^{o}C before diluting immediately in Church mix. An excess (500 ng) of unlabeled denatured probe DNA was added at this point. Telomere-specific probe was prepared as described above using a Sty11 probe, which containts 700 bp of telomeric repeats, and for the labeling reaction, a telomeric sequence-specific $(CCCTAA)_3$ oligo was used. After overnight hybridization with radioactively labeled probe at 65^{o}C, the blot was washed at 65^{o}C in Church wash (40 mM NaPi pH 7.2; 1 mM EDTA pH 8.0; 1% w/v SDS) and exposed onto a PhosphorImager screen. Signals were quantified with ImageQuant software.

Sucrose-gradient sedimentation

To prepare columns, 5.5 ml of 6% sucrose/$TEEP_{80}$ (10 mM Tris-HCl, pH 8.0, 1 mM EDTA,1 mM EGTA, 80 mM NaCl and freshly added 250 μM PMSF) were carefully added dropwise on top of a layer of 5.5 ml of 40% sucrose/$TEEP_{80}$ (containing blue dye) in 12 ml polyallomer centrifuge tubes (Beckman). Tubes were consecutively frozen at -20^{0}C and thawed at 4^{0}C 3 times. The blending of the dye was used as a visual indicator for gradient formation. After the third freeze, gradients can be stored at -20^{0}C for several months.

To prepare nuclei, cells were trypsinized, suspended in growth medium, and harvested by centrifugation in an RT6000 centrifuge at 1.5 K for 5 min. Cells were suspended in buffer A (100 mM KCl, 10 mM Tris [pH 7.5], 3 mM $MgCl_2$, 1 mM $CaCl_2$, 0.5 mM phenylmethylsulfonyl fluoride), washed twice with buffer A, and then resuspended in buffer A with 0.6% Nonidet P-40 to lyse cells. After gently mixing and incubating on ice for 5 min, nuclei were harvested at 2K for 5 min and resuspended in buffer A without NP-40 at 4 x 10^6 cells/ml. Nuclei were homogenized in a dounce with 10 strokes with a tight B-type pestle. Aliquots of 150 µl were digested for 5 min at 30°C with MNase (Roche Diagnostics) at 7.5 U/ml. Reactions were stopped by adding EDTA to a final concentration of 10mM. Tubes were centrifuged at 5K for 5 min and the pellet was carefully washed with buffer A, without pipetting. Tube were re-centrifuged and 300 µL of $TEEP_{20}$ (10 mM Tris-HCl, pH 8.0, 1 mM EDTA,1 mM EGTA, 20 mM NaCl and freshly added 250 µM PMSF) was added on top of the pellet. To allow chromatin to dissolve tubes were incubated overnight at 4^0C. The following day the tubes were centrifuged to remove nuclear debris and the supernatant was layered on top of the 6-40% sucrose gradient. 10% of supernatant was saved as input.

Sucrose gradient sedimentation was performed in Optima 100XL Ultracentrifuge (Beckman Coulter) with SW41 rotor at 41,000 rpm for 2.5 h at 4^0C. Gradient was fractionated by carefully pipetting 1 ml fractions from top to bottom. Fractions were digested overnight with 1 mg/ml Proteinase K in the presence of 0.1% SDS. DNA was purified by phenol-chloroform extraction and ethanol precipitation. DNA pellet was air dried and resuspended in 60 µl TE by shaking for 1 h at 55^0C.

15 μl of DNA was loaded from each sample on a 0.8% agarose gel/ 0.5 x TBE and separated in 0.5 x TBE by gel elecrophoresis at 25 V for 2 h, 45 V overnight, and 90 V until the 300 bp molecular marker ran out. Southern blotting was performed and the blot was hybridized overnight to a radioactively labeled StyII probe (described above). The following day, blots were washed 3 x 15 min in Church wash and exposed onto a PhosphorImager screen overnight. Blots were stripped by treating the membrane with boiling 0.1% SDS in water and allowing it to cool to RT. The membrane was washed briefly in 2 x SSC before an overnight hybridization to a radioactively labeled Bam probe (described above).

APPENDIX I - LIST OF CELL LINES

Human cell lines

Name	Organism/organ	Notes
293T	Human/kidney	highly tranfectable; express SV40-LT antigen
A-T	Human, A-T patient	fibroblast; ATM-deficient
BJ	Human/foreskin	primary fibroblast
BJ-hTERT	Human/foreskin	BJ cells immortalized with hTERT
F02-98	Human, Seckel patient	fibroblast; hypomorphic ATR allele
HeLa 1.2.11	Human/epithelial	derived from HeLa2; long telomeres
HeLa 1.3	Human/epithelial	HeLa 1.2.11 derivative; long telomeres
HeLa 204	Human/epithelial	HeLa1.2.11 derivative; heterogeneous telomere length
IMR90	Human/lung	primary fibroblast

Retrovirus packaging cell lines

Phoenix, eco	Human/epithelial	293T derivative; retroviral packaging
Phoenic, ampho	Human/epithelial	293T derivative; retroviral packaging

Mouse embryonic fibroblasts

$TRF2^{F/-}$ $p53^{-/-}$	Mouse/ E13.5 MEF	Ref. [190]
$TRF2^{F/+}$ $p53^{-/-}$	Mouse/ E13.5 MEF	Ref. [190]
$TRF2^{F/-}$ $lig4^{-/-}$ $p53^{-/-}$	Mouse/ E13.5 MEF	Ref. [190]
$TRF2^{F/-}$ $53BP1^{-/-}$	Mouse/ E13.5 MEF	SV40-LT transformed, this work
$TRF2^{F/-}$ $53BP1^{+/-}$	Mouse/ E13.5 MEF	SV40-LT transformed, this work
$TRF2^{F/+}$ $53BP1^{-/-}$	Mouse/ E13.5 MEF	SV40-LT transformed, this work
$TRF2^{F/-}$ $ATM^{-/-}$	Mouse/ E13.5 MEF	SV40-LT transformed, Ref. [228]
$TRF2^{F/-}$ $ATM^{+/-}$	Mouse/ E13.5 MEF	SV40-LT transformed, Ref. [228]
$TRF2^{F/F}$ $MDC1^{-/-}$	Mouse/ E13.5 MEF	SV40-LT transformed, this work
$TRF2^{F/F}$ $MDC1^{+/+}$	Mouse/ E13.5 MEF	SV40-LT transformed, this work
$TRF2^{F/F}$ $NBS1^{F/-}$	Mouse/ E13.5 MEF	SV40-LT transformed, this work
$TRF2^{F/F}$ $NBS1^{F/+}$	Mouse/ E13.5 MEF	SV40-LT transformed, this work
$NBS1^{F/-}$	Mouse/ E13.5 MEF	SV40-LT transformed, this work

APPENDIX II - LIST OF ANTIBODIES

ID	antigen	Type	Applications	Origin
371	hTRF1	Rb, poly	IF 1:1000 Western 1:1000 Crude serum; ChIP	de Lange lab
647	hTRF2 (baculoviral-FL)	Rb poly	Western 1:2000 Crude serum; ChIP	Zhu, de Lange lab
765	hRap1	Rb, poly	IF 1:2000 Western 1:2000 Crude serum; ChIP	Li, de Lange lab
864	hTin2	Rb, poly	Western 1:2000 Crude serum; ChIP	Ye, de Lange lab
874	hMre11	Rb, poly	Western 1:5000 Crude serum; ChIP	Zhu, de Lange lab
1048	hPOT1	Rb, poly	Crude serum; ChIP	Loayza, de Lange lab
1252	mRap1	Rb, poly	Western 1:5000	Celli, de Lange lab
1254	mTRF2	Rb poly	Western 1:5000	Celli, de Lange lab
mTRF1	mTRF1	Rb, poly	Western 1:1000	Overbeek/de Lange lab
9E10	c-myc peptide	Mo mono	Western 1:1000	Calbiochem
9E10	c-myc peptide	Mo mono	IF 1:5000	Sigma
M2	Flag peptide	Mo mono	Western 1:10,000 Crude serum; ChIP	Sigma
11	HA peptide	Mo mono	Western 1:1000 IF 1:1000 Crude serum; ChIP	Covance
GTU88	γTubulin	Mo mono	Western 1:5000	Sigma

ID	antigen	Type	Applications	Origin
DO-1	p53	Mo, mono	Western 1:300	Santa Cruz
F-5	p21	mo, mono	Western 1:500	Santa Cruz
α-γH2AX	γH2AX-P (S139)	Mo mono	IF 1:1000	Upstate
α-ATM-P	ATM-P (S1981)	Mo mono	Western 1:500 IF 1:500	Cell Signaling
α-NBS1-P	Human NBS1-P (S343)	Rb, poly	IF 1:500	Abcam
11175	mH2AX	Rb, poly	Western 1:1000	Abcam
MAT3	ATM	Mo, mono	Western 1:1000	Abcam
Chk2	Chk2	Mo, mono	Western 1:300	BD Transduction Lab
93'6	mNBS1	Rb poly	Western 1:5000 IF 1:5000 Purified Ab; ChIP	Petrini lab, MSKCC
11169	hMDC1	Rb, poly	Western 1:1000 IF 1:500	Abcam
300-757A	mMDC1	Rb, poly	Western 1:500	Bethyl Labs
αMDC1	mMDC1	Mo, mono	IF 1:20	Chen lab, Yale U
α53BP1	h53BP1	Mo mono	IF 1:50 Recognizes human only	Halazonetis, The Wistar Institute, PA
100-304	h53BP1	Rb poly	IF 1:1000 Recognizes mouse and human 53BP1	Novus
100-305	h53BP1	Rb, poly	Western 1:1000 Recognizes mouse and human	Novus

ID	antigen	Type	Applications	Origin
H-300	mCtIP	Rb, poly	Western 1:250	Santa Cruz Biotechnology

Rb: Rabbit; Mo: mouse; poly: polyclonal; mono: monoclonal

BIBLIOGRAPHY

1. Savitsky, K. et al. A single ataxia telangiectasia gene with a product similar to PI-3 kinase. *Science* **268**, 1749-1753 (1995).
2. Gotoff, S. P., Amirmokri, E. & Liebner, E. J. Ataxia telangiectasia. Neoplasia, untoward response to x-irradiation, and tuberous sclerosis. *Am J Dis Child* **114**, 617-625 (1967).
3. Morgan, J. L., Holcomb, T. M. & Morrissey, R. W. Radiation reaction in ataxia telangiectasia. *Am J Dis Child* **116**, 557-558 (1968).
4. Lavin, M. F. & Shiloh, Y. Ataxia-telangiectasia: a multifaceted genetic disorder associated with defective signal transduction. *Curr Opin Immunol* **8**, 459-464 (1996).
5. Chen, G. & Lee, E. The product of the ATM gene is a 370-kDa nuclear phosphoprotein. *J Biol Chem* **271**, 33693-33697 (1996).
6. Keith, C. T. & Schreiber, S. L. PIK-related kinases: DNA repair, recombination, and cell cycle checkpoints. *Science* **270**, 50-51 (1995).
7. Kim, S. T., Lim, D. S., Canman, C. E. & Kastan, M. B. Substrate specificities and identification of putative substrates of ATM kinase family members. *J Biol Chem* **274**, 37538-37543 (1999).
8. O'Neill, T. et al. Utilization of oriented peptide libraries to identify substrate motifs selected by ATM. *J Biol Chem* **275**, 22719-22727 (2000).
9. Siliciano, J. D. et al. DNA damage induces phosphorylation of the amino terminus of p53. *Genes Dev* **11**, 3471-3481 (1997).

10. Matsuoka, S. et al. Ataxia telangiectasia-mutated phosphorylates Chk2 in vivo and in vitro. *Proc Natl Acad Sci U S A* **97**, 10389-10394 (2000).
11. Bakkenist, C. J. & Kastan, M. B. DNA damage activates ATM through intermolecular autophosphorylation and dimer dissociation. *Nature* **421**, 499-506 (2003).
12. Ziv, Y. et al. Chromatin relaxation in response to DNA double-strand breaks is modulated by a novel ATM- and KAP-1 dependent pathway. *Nat Cell Biol* **8**, 870-876 (2006).
13. Berkovich, E., Monnat, R. J. J. & Kastan, M. B. Roles of ATM and NBS1 in chromatin structure modulation and DNA double-strand break repair. *Nat Cell Biol* **9**, 683-690 (2007).
14. Kozlov, S. V. et al. Involvement of novel autophosphorylation sites in ATM activation. *EMBO J* **25**, 3504-3514 (2006).
15. Pellegrini, M. et al. Autophosphorylation at serine 1987 is dispensable for murine Atm activation in vivo. *Nature* **443**, 222-225 (2006).
16. Carson, C. T. et al. The Mre11 complex is required for ATM activation and the G2/M checkpoint. *Embo J* **22**, 6610-6620 (2003).
17. Uziel, T. et al. Requirement of the MRN complex for ATM activation by DNA damage. *Embo J* **22**, 5612-5621 (2003).
18. Difilippantonio, S. et al. Role of Nbs1 in the activation of the Atm kinase revealed in humanized mouse models. *Nat Cell Biol* **7**, 675-685 (2005).
19. Dupre, A., Boyer-Chatenet, L. & Gautier, J. Two-step activation of ATM by DNA and the Mre11-Rad50-Nbs1 complex. *Nat Struct Mol Biol* **13**, 451-457 (2006).

20. Lee, J. H. & Paull, T. T. ATM activation by DNA double-strand breaks through the Mre11-Rad50-Nbs1 complex. *Science* **308**, 551-554 (2005).

21. You, Z., Chahwan, C., Bailis, J., Hunter, T. & Russell, P. ATM activation and its recruitment to damaged DNA require binding to the C terminus of Nbs1. *Mol Cell Biol* **25**, 5363-5379 (2005).

22. Chehab, N. H., Malikzay, A., Stavridi, E. S. & Halazonetis, T. D. Phosphorylation of Ser-20 mediates stabilization of human p53 in response to DNA damage. *Proc Natl Acad Sci USA* **96**, 13777-13782 (1999).

23. Maya, R. et al. ATM-dependent phosphorylation of Mdm2 on serine 395: role in p53 activation by DNA damage. *Genes Dev* **15**, 1067-1077 (2001).

24. Kastan, M. B. et al. A mammalian cell cycle checkpoint pathway utilizing p53 and GADD45 is defective in ataxia-telangiectasia. *Cell* **71**, 587-597 (1992).

25. Falck, J., Mailand, N., Syljuasen, R. G., Bartek, J. & Lukas, J. The ATM-Chk2-Cdc25A checkpoint pathway guards against radioresistant DNA synthesis. *Nature* **410**, 842-847 (2001).

26. Falck, J., Petrini, J. H., Williams, B. R., Lukas, J. & Bartek, J. The DNA damage-dependent intra-S phase checkpoint is regulated by parallel pathways. *Nat Genet* **30**, 290-294 (2002).

27. Lim, D. S. et al. ATM phosphorylates p95/nbs1 in an S-phase checkpoint pathway. *Nature* **404**, 613-617 (2000).

28. Kitagawa, R., Bakkenist, C. J., McKinnon, P. J. & Kastan, M. B. Phosphorylation of SMC1 is a critical downstream event in the ATM-NBS1-BRCA1 pathway. *Genes Dev* **18**, 1423-1438 (2004).

29. Matsuoka, S., Huang, M. & Elledge, S. J. Linkage of ATM to cell cycle regulation by the Chk2 protein kinase. *Science* **282**, 1893-1897 (1998).

30. Chaturvedi, P. et al. Mammalian Chk2 is a downstream effector of the ATM-dependent DNA damage checkpoint pathway. *Oncogene* **18**, 4047-4054 (1999).

31. Tominaga, K. et al. Role of human Cds1 (Chk2) kinase in DNA damage checkpoint and its regulation by p53. *J Biol Chem* **274**, 31463-31467 (1999).

32. Zhou, B. B. et al. Caffeine abolishes the mammalian G(2)/M DNA damage checkpoint by inhibiting ataxia-telangiectasia-mutated kinase activity. *J Biol Chem* **275**, 10342-10348 (2000).

33. Hopfner, K. P. et al. Structural biochemistry and interaction architecture of the DNA double-strand break repair Mre11 nuclease and Rad50-ATPase. *Cell* **105**, 473-485 (2001).

34. de Jager, M. et al. Human Rad50/Mre11 is a flexible complex that can tether DNA ends. *Mol Cell* **8**, 1129-1135 (2001).

35. Hopfner, K. P. et al. Structural biology of Rad50 ATPase: ATP-driven conformational control in DNA double-strand break repair and the ABC-ATPase superfamily. *Cell* **101**, 789-800 (2000).

36. Hopfner, K. P. et al. The Rad50 zinc-hook is a structure joining Mre11 complexes in DNA recombination and repair. *Nature* **418**, 562-566 (2002).

37. Williams, R. S. et al. Mre11 dimers coordinate DNA end bridging and nuclease processing in double-strand-break repair. *Cell* **135**, 97-109 (2008).

38. Moreno-Herrero, F. et al. Mesoscale conformational changes in the DNA-repair complex Rad50/Mre11/Nbs1 upon binding DNA. *Nature* **437**, 440-443 (2005).

39. Williams, R. S. & Tainer, J. A. A nanomachine for making ends meet: MRN is a flexing scaffold for the repair of DNA double-strand breaks. *Mol Cell* **19**, 724-726 (2005).

40. Williams, R. S., Williams, J. S. & Tainer, J. A. Mre11-Rad50-Nbs1 is a keystone complex connecting DNA repair machinery, double-strand break signaling, and the chromatin template. *Biochem Cell Biol* **85**, 509-520 (2007).

41. Furuse, M. et al. Distinct roles of two separable in vitro activities of yeast Mre11 in mitotic and meiotic recombination. *EMBO J* **17**, 6412-6425 (1998).

42. Paull, T. T. & Gellert, M. The 3' to 5' exonuclease activity of Mre 11 facilitates repair of DNA double-strand breaks. *Mol Cell* **1**, 969-979 (1998).

43. Trujillo, K. M., Yuan, S. S., Lee, E. Y. & Sung, P. Nuclease activities in a complex of human recombination and DNA repair factors Rad50, Mre11, and p95. *J Biol Chem* **273**, 21447-21450 (1998).

44. Moreau, S., Ferguson, J. R. & Symington, L. S. The nuclease activity of Mre11 is required for meiosis but not for mating type switching, end joining, or telomere maintenance. *Mol Cell Biol* **19**, 556-566 (1999).

45. Paull, T. T. & Gellert, M. Nbs1 potentiates ATP-driven DNA unwinding and endonuclease cleavage by the Mre11/Rad50 complex. *Genes Dev* **13**, 1276-1288 (1999).

46. de Jager, M. et al. DNA-binding and strand-annealing activities of human Mre11: implications for its roles in DNA double-strand break repair pathways. *Nucleic Acids Res* **29**, 1317-1325 (2001).

47. D'Amours, D. & Jackson, S. P. The Mre11 complex: at the crossroads of dna repair and checkpoint signalling. *Nat Rev Mol Cell Biol* **3**, 317-327 (2002).

48. Tauchi, H. et al. Nbs1 is essential for DNA repair by homologous recombination in higher vertebrate cells. *Nature* **420**, 93-98 (2002).

49. Moore, J. K. & Haber, J. E. Cell cycle and genetic requirements of two pathways of nonhomologous end-joining repair of double-strand breaks in Saccharomyces cerevisiae. *Mol Cell Biol* **16**, 2164-2173 (1996).

50. Bressan, D. A., Baxter, B. K. & Petrini, J. H. The Mre11-Rad50-Xrs2 protein complex facilitates homologous recombination-based double-strand break repair in Saccharomyces cerevisiae. *Mol Cell Biol* **19**, 7681-7687 (1999).

51. Lewis, L. K. et al. Role of the nuclease activity of Saccharomyces cerevisiae Mre11 in repair of DNA double-strand breaks in mitotic cells. *Genetics* **166**, 1701-1713 (2004).

52. Llorente, B. & Symington, L. S. The Mre11 nuclease is not required for 5' to 3' resection at multiple HO-induced double-strand breaks. *Mol Cell Biol* **24**, 9682-9694 (2004).

53. Krogh, B. O., Llorente, B., Lam, A. & Symington, L. S. Mutations in Mre11 phosphoesterase motif I that impair Saccharomyces cerevisiae Mre11-Rad50-Xrs2 complex stability in addition to nuclease activity. *Genetics* **171**, 1561-1570 (2005).

54. Buis, J. et al. Mre11 nuclease activity has essential roles in DNA repair and genomic stability distinct from ATM activation. *Cell* **135**, 85-96 (2008).

55. Alani, E., Padmore, R. & Kleckner, N. Analysis of wild-type and rad50 mutants of yeast suggests an intimate relationship between meiotic chromosome synapsis and recombination. *Cell* **61**, 419-436 (1990).

56. Ivanov, E. L., Korolev, V. G. & Fabre, F. XRS2, a DNA repair gene of Saccharomyces cerevisiae, is needed for meiotic recombination. *Genetics* **132**, 651-664 (1992).

57. Ivanov, E. L., Sugawara, N., White, C. I., Fabre, F. & Haber, J. E. Mutations in XRS2 and RAD50 delay but do not prevent mating-type switching in Saccharomyces cerevisiae. *Mol Cell Biol* **14**, 3414-3425 (1994).

58. Sartori, A. A. et al. Human CtIP promotes DNA end resection. *Nature* **450**, 509-514 (2007).

59. Lengsfeld, B. M., Rattray, A. J., Bhaskara, V., Ghirlando, R. & Paull, T. T. Sae2 is an endonuclease that processes hairpin DNA cooperatively with the Mre11/Rad50/Xrs2 complex. *Mol Cell* **28**, 638-651 (2007).

60. Takeda, S., Nakamura, K., Taniguchi, Y. & Paull, T. T. Ctp1/CtIP and the MRN complex collaborate in the initial steps of homologous recombination. *Mol Cell* **28**, 351-352 (2007).

61. Kim, H. S. et al. Functional interactions between Sae2 and the Mre11 complex. *Genetics* **178**, 711-723 (2008).

62. Huertas, P., Cortes-Ledesma, F., Sartori, A. A., Aguilera, A. & Jackson, S. P. CDK targets Sae2 to control DNA-end resection and homologous recombination. *Nature* **455**, 689-692 (2008).

63. Mimitou, E. P. & Symington, L. S. Sae2, Exo1 and Sgs1 collaborate in DNA double-strand break processing. *Nature* **455**, 770-774 (2008).

64. Zhu, Z., Chung, W. H., Shim, E. Y., Lee, S. E. & Ira, G. Sgs1 helicase and two nucleases Dna2 and Exo1 resect DNA double-strand break ends. *Cell* **134**, 981-994 (2008).

65. Durocher, D., Henckel, J., Fersht, A. R. & Jackson, S. P. The FHA domain is a modular phosphopeptide recognition motif. *Mol Cell* **4**, 387-394 (1999).

66. D'Amours, D. & Jackson, S. P. The yeast Xrs2 complex functions in S phase checkpoint regulation. *Genes Dev* **15**, 2238-2249 (2001).

67. Lee, J. H. et al. Distinct functions of Nijmegen breakage syndrome in ataxia telangiectasia mutated-dependent responses to DNA damage. *Mol Cancer Res* **1**, 674-681 (2003).

68. Mirzoeva, O. K. & Petrini, J. H. DNA damage-dependent nuclear dynamics of the Mre11 complex. *Mol Cell Biol* **21**, 281-288 (2001).

69. Chapman, J. R. & Jackson, S. P. Phospho-dependent interactions between NBS1 and MDC1 mediate chromatin retention of the MRN complex at sites of DNA damage. *EMBO Rep* **9**, 795-801 (2008).

70. Melander, F. et al. Phosphorylation of SDT repeats in the MDC1 N terminus triggers retention of NBS1 at the DNA damage-modified chromatin. *J Cell Biol* **181**, 213-226 (2008).

71. Spycher, C. et al. Constitutive phosphorylation of MDC1 physically links the MRE11-RAD50-NBS1 complex to damaged chromatin. *J Cell Biol* **181**, 227-240 (2008).

72. Wu, L., Luo, K., Lou, Z. & Chen, J. MDC1 regulates intra-S-phase checkpoint by targeting NBS1 to DNA double-strand breaks. *Proc Natl Acad Sci U S A* **105**, 11200-11205 (2008).

73. Xu, C. et al. Structure of a second BRCT domain identified in the nijmegen breakage syndrome protein Nbs1 and its function in an MDC1-dependent localization of Nbs1 to DNA damage sites. *J Mol Biol* **381**, 361-372 (2008).

74. Lee, J. H. & Paull, T. T. Direct activation of the ATM protein kinase by the Mre11/Rad50/Nbs1 complex. *Science* **304**, 93-96 (2004).

75. Falck, J., Coates, J. & Jackson, S. P. Conserved modes of recruitment of ATM, ATR and DNA-PKcs to sites of DNA damage. *Nature* **434**, 605-611 (2005).

76. Carney, J. P. et al. The hMre11/hRad50 protein complex and Nijmegen breakage syndrome: linkage of double-strand break repair to the cellular DNA damage response. *Cell* **93**, 477-486 (1998).

77. Varon, R. et al. Nibrin, a novel DNA double-strand break repair protein, is mutated in Nijmegen breakage syndrome. *Cell* **93**, 467-76. (1998).

78. Stewart, G. S. et al. The DNA double-strand break repair gene hMRE11 is mutated in individuals with an ataxia-telangiectasia-like disorder. *Cell* **99**, 577-587 (1999).

79. Zhao, S. et al. Functional link between ataxia-telangiectasia and Nijmegen breakage syndrome gene products. *Nature* **405**, 473-477 (2000).

80. Wu, X. et al. ATM phosphorylation of Nijmegen breakage syndrome protein is required in a DNA damage response. *Nature* **405**, 477-82. (2000).

81. Xu, B., Kim, S. T., Lim, D. S. & Kastan, M. B. Two molecularly distinct G(2)/M checkpoints are induced by ionizing irradiation. *Mol Cell Biol* **22**, 1049-1059 (2002).

82. Kobayashi, J. et al. NBS1 localizes to gamma-H2AX foci through interaction with the FHA/BRCT domain. *Curr Biol* **12**, 1846-1851 (2002).

83. Takai, H., Smogorzewska, A. & de Lange, T. DNA damage foci at dysfunctional telomeres. *Curr Biol* **13**, 1549-1556 (2003).

84. Kim, S. T., Xu, B. & Kastan, M. B. Involvement of the cohesin protein, Smc1, in Atm-dependent and independent responses to DNA damage. *Genes Dev* **16**, 560-570 (2002).

85. Yazdi, P. T. et al. SMC1 is a downstream effector in the ATM/NBS1 branch of the human S-phase checkpoint. *Genes Dev* **16**, 571-582 (2002).

86. Nakanishi, K. et al. Interaction of FANCD2 and NBS1 in the DNA damage response. *Nat Cell Biol* **4**, 913-920 (2002).

87. Girard, P. M., Riballo, E., Begg, A. C., Waugh, A. & Jeggo, P. A. Nbs1 promotes ATM dependent phosphorylation events including those required for G1/S arrest. *Oncogene* **21**, 4191-4199 (2002).

88. Theunissen, J. W. et al. Checkpoint failure and chromosomal instability without lymphomagenesis in Mre11(ATLD1/ATLD1) mice. *Mol Cell* **12**, 1511-1523 (2003).

89. Stiff, T. et al. ATR-dependent phosphorylation and activation of ATM in response to UV treatment or replication fork stalling. *EMBO J* **25**, 5775-5782 (2006).

90. Morales, M. et al. The Rad50S allele promotes ATM-dependent DNA damage responses and suppresses ATM deficiency: implications for the Mre11 complex as a DNA damage sensor. *Genes Dev* **19**, 3043-3054 (2005).

91. Williams, B. R. et al. A murine model of Nijmegen breakage syndrome. *Curr Biol* **12**, 648-653 (2002).

92. Kastan, M. B. & Lim, D. S. The many substrates and functions of ATM. *Nat Rev Mol Cell Biol* **1**, 179-186 (2000).

93. Shiloh, Y. ATM and related protein kinases: safeguarding genome integrity. *Nat Rev Cancer* **3**, 155-168 (2003).

94. Lukas, C., Falck, J., Bartkova, J., Bartek, J. & Lukas, J. Distinct spatiotemporal dynamics of mammalian checkpoint regulators induced by DNA damage. *Nat Cell Biol* **5**, 255-260 (2003).

95. Ward, I. M. & Chen, J. Histone H2AX is phosphorylated in an ATR-dependent manner in response to replicational stress. *J Biol Chem* **276**, 47759-47762 (2001).

96. Burma, S., Chen, B. P., Murphy, M., Kurimasa, A. & Chen, D. J. ATM phosphorylates histone H2AX in response to DNA double-strand breaks. *J Biol Chem* **276**, 42462-42467 (2001).

97. Rogakou, E. P., Pilch, D. R., Orr, A. H., Ivanova, V. S. & Bonner, W. M. DNA double-stranded breaks induce histone H2AX phosphorylation on serine 139. *J Biol Chem* **273**, 5858-5868 (1998).

98. Rogakou, E. P., Boon, C., Redon, C. & Bonner, W. M. Megabase chromatin domains involved in DNA double-strand breaks in vivo. *J Cell Biol* **146**, 905-916 (1999).

99. Paull, T. T. et al. A critical role for histone H2AX in recruitment of repair factors to nuclear foci after DNA damage. *Curr Biol* **10**, 886-95. (2000).

100. Celeste, A. et al. Genomic instability in mice lacking histone H2AX. *Science* **296**, 922-927 (2002).

101. Celeste, A. et al. H2AX haploinsufficiency modifies genomic stability and tumor susceptibility. *Cell* **114**, 371-383 (2003).

102. Celeste, A. et al. Histone H2AX phosphorylation is dispensable for the initial recognition of DNA breaks. *Nat Cell Biol* **5**, 675-679 (2003).

103. Sedelnikova, O. A., Rogakou, E. P., Panyutin, I. G. & Bonner, W. M. Quantitative detection of (125)IdU-induced DNA double-strand breaks with gamma-H2AX antibody. *Radiat Res* **158**, 486-492 (2002).

104. Bassing, C. H. et al. Increased ionizing radiation sensitivity and genomic instability in the absence of histone H2AX. *Proc Natl Acad Sci U S A* **99**, 8173-8178 (2002).

105. Xie, A. et al. Control of sister chromatid recombination by histone H2AX. *Mol Cell* **16**, 1017-1025 (2004).

106. Franco, S. et al. H2AX prevents DNA breaks from progressing to chromosome breaks and translocations. *Mol Cell* **21**, 201-214 (2006).

107. Goldberg, M. et al. MDC1 is required for the intra-S-phase DNA damage checkpoint. *Nature* **421**, 952-956 (2003).

108. Lou, Z., Minter-Dykhouse, K., Wu, X. & Chen, J. MDC1 is coupled to activated CHK2 in mammalian DNA damage response pathways. *Nature* **421**, 957-961 (2003).

109. Lukas, C. et al. Mdc1 couples DNA double-strand break recognition by Nbs1 with its H2AX-dependent chromatin retention. *EMBO J* **23**, 2674-2683 (2004).

110. Stewart, G. S., Wang, B., Bignell, C. R., Taylor, A. M. & Elledge, S. J. MDC1 is a mediator of the mammalian DNA damage checkpoint. *Nature* **421**, 961-966 (2003).

111. Lee, M. S., Edwards, R. A., Thede, G. L. & Glover, J. N. Structure of the BRCT repeat domain of MDC1 and its specificity for the free COOH-terminal end of the gamma-H2AX histone tail. *J Biol Chem* **280**, 32053-32056 (2005).

112. Stucki, M. et al. MDC1 directly binds phosphorylated histone H2AX to regulate cellular responses to DNA double-strand breaks. *Cell* **123**, 1213-1226 (2005).

113. Bekker-Jensen, S. et al. Spatial organization of the mammalian genome surveillance machinery in response to DNA strand breaks. *J Cell Biol* (2006).

114. Lou, Z. et al. MDC1 maintains genomic stability by participating in the amplification of ATM-dependent DNA damage signals. *Mol Cell* **21**, 187-200 (2006).

115. Xie, A. et al. Distinct roles of chromatin-associated proteins MDC1 and 53BP1 in mammalian double-strand break repair. *Mol Cell* **28**, 1045-1057 (2007).

116. Bekker-Jensen, S., Lukas, C., Melander, F., Bartek, J. & Lukas, J. Dynamic assembly and sustained retention of 53BP1 at the sites of DNA damage are controlled by Mdc1/NFBD1. *J Cell Biol* **170**, 201-211 (2005).

117. Nakada, D., Matsumoto, K. & Sugimoto, K. ATM-related Tel1 associates with double-strand breaks through an Xrs2-dependent mechanism. *Genes Dev* **17**, 1957-1962 (2003).

118. Stucki, M. & Jackson, S. P. gammaH2AX and MDC1: Anchoring the DNA-damage-response machinery to broken chromosomes. *DNA Repair (Amst)* **10**, 534-543 (2006).

119. Huen, M. S. et al. RNF8 transduces the DNA-damage signal via histone ubiquitylation and checkpoint protein assembly. *Cell* **131**, 901-914 (2007).

120. Kolas, N. K. et al. Orchestration of the DNA-damage response by the RNF8 ubiquitin ligase. *Science* **318**, 1637-1640 (2007).

121. Mailand, N. et al. RNF8 ubiquitylates histones at DNA double-strand breaks and promotes assembly of repair proteins. *Cell* **131**, 887-900 (2007).

122. Wang, B. & Elledge, S. J. Ubc13/Rnf8 ubiquitin ligases control foci formation of the Rap80/Abraxas/Brca1/Brcc36 complex in response to DNA damage. *Proc Natl Acad Sci U S A* **104**, 20759-20763 (2007).

123. Iwabuchi, K., Bartel, P. L., Li, B., Marraccino, R. & Fields, S. Two cellular proteins that bind to wild-type but not mutant p53. *Proc Natl Acad Sci USA* **91**, 6098-6102 (1994).

124. Schultz, L. B., Chehab, N. H., Malikzay, A. & Halazonetis, T. D. p53 binding protein 1 (53BP1) is an early participant in the cellular response to DNA double-strand breaks. *J Cell Biol* **151**, 1381-1390 (2000).

125. Rappold, I., Iwabuchi, K., Date, T. & Chen, J. Tumor suppressor p53 binding protein 1 (53BP1) is involved in DNA damage-signaling pathways. *J Cell Biol* **153**, 613-620 (2001).

126. DiTullio, R. A., Jr et al. 53BP1 functions in an ATM-dependent checkpoint pathway that is constitutively activated in human cancer. *Nat Cell Biol* **4**, 998-1002 (2002).

127. Wang, B., Matsuoka, S., Carpenter, P. B. & Elledge, S. J. 53BP1, a mediator of the DNA damage checkpoint. *Science* **298**, 1435-1438 (2002).

128. Fernandez-Capetillo, O., Liebe, B., Scherthan, H. & Nussenzweig, A. H2AX regulates meiotic telomere clustering. *J Cell Biol* **163**, 15-20 (2003).

129. Ward, I. M. et al. 53BP1 cooperates with p53 and functions as a haploinsufficient tumor suppressor in mice. *Mol Cell Biol* **25**, 10079-10086 (2005).

130. Gorgoulis, V. G. et al. Activation of the DNA damage checkpoint and genomic instability in human precancerous lesions. *Nature* **434**, 907-913 (2005).

131. Saka, Y., Esashi, F., Matsusaka, T., Mochida, S. & Yanagida, M. Damage and replication checkpoint control in fission yeast is ensured by interactions of Crb2, a protein with BRCT motif, with Cut5 and Chk1. *Genes Dev* **11**, 3387-3400 (1997).

132. Ward, I. M., Minn, K., van Deursen, J. & Chen, J. p53 Binding protein 53BP1 is required for DNA damage responses and tumor suppression in mice. *Mol Cell Biol* **23**, 2556-2563 (2003).

133. Anderson, L., Henderson, C. & Adachi, Y. Phosphorylation and rapid relocalization of 53BP1 to nuclear foci upon DNA damage. *Mol Cell Biol* **21**, 1719-1729 (2001).

134. Manis, J. P. et al. 53BP1 links DNA damage-response pathways to immunoglobulin heavy chain class-switch recombination. *Nat Immunol* **5**, 481-487 (2004).

135. Reina-San-Martin, B., Chen, J., Nussenzweig, A. & Nussenzweig, M. C. Enhanced intra-switch region recombination during immunoglobulin class switch recombination in 53BP1-/- B cells. *Eur J Immunol* **37**, 235-239 (2007).

136. Ward, I. M. et al. 53BP1 is required for class switch recombination. *J Cell Biol* **165**, 459-464 (2004).

137. Reina-San-Martin, B., Nussenzweig, M. C., Nussenzweig, A. & Difilippantonio, S. Genomic instability, endoreduplication, and diminished Ig class-switch recombination in B cells lacking Nbs1. *Proc Natl Acad Sci U S A* **102**, 1590-1595 (2005).

138. Botuyan, M. V. et al. Structural basis for the methylation state-specific recognition of histone H4-K20 by 53BP1 and Crb2 in DNA repair. *Cell* **127**, 1361-1373 (2006).

139. Huyen, Y. et al. Methylated lysine 79 of histone H3 targets 53BP1 to DNA double-strand breaks. *Nature* **432**, 406-411 (2004).

140. Schotta, G. et al. A chromatin-wide transition to H4K20 monomethylation impairs genome integrity and programmed DNA rearrangements in the mouse. *Genes Dev* **22**, 2048-2061 (2008).

141. Aylon, Y., Liefshitz, B. & Kupiec, M. The CDK regulates repair of double-strand breaks by homologous recombination during the cell cycle. *EMBO J* **23**, 4868-4875 (2004).

142. Ira, G. et al. DNA end resection, homologous recombination and DNA damage checkpoint activation require CDK1. *Nature* **431**, 1011-1017 (2004).

143. Sonoda, E., Hochegger, H., Saberi, A., Taniguchi, Y. & Takeda, S. Differential usage of non-homologous end-joining and homologous recombination in double strand break repair. *DNA Repair (Amst)* **5**, 1021-1029 (2006).

144. Sartori, A. A. et al. Human CtIP promotes DNA end resection. *Nature* **450**, 509-514 (2007).

145. Moore, J. K. & Haber, J. E. Cell cycle and genetic requirements of two pathways of nonhomologous end-joining repair of double-strand breaks in Saccharomyces cerevisiae. *Mol Cell Biol* **16**, 2164-2173 (1996).

146. Baumann, P. & West, S. C. DNA end-joining catalyzed by human cell-free extracts. *Proc Natl Acad Sci U S A* **95**, 14066-14070 (1998).

147. Tuteja, N. et al. Human DNA helicase II: a novel DNA unwinding enzyme identified as the Ku autoantigen. *EMBO J* **13**, 4991-5001 (1994).

148. Walker, J. R., Corpina, R. A. & Goldberg, J. Structure of the Ku heterodimer bound to DNA and its implications for double-strand break repair. *Nature* **412**, 607-14. (2001).

149. Rooney, S. et al. Defective DNA repair and increased genomic instability in Artemis-deficient murine cells. *J Exp Med* **197**, 553-565 (2003).

150. Rooney, S. et al. Leaky Scid phenotype associated with defective V(D)J coding end processing in Artemis-deficient mice. *Mol Cell* **10**, 1379-1390 (2002).

151. Jeggo, P. A. DNA breakage and repair. *Adv Genet* **38**, 185-218 (1998).

152. Capp, J. P. et al. The DNA polymerase lambda is required for the repair of non-compatible DNA double strand breaks by NHEJ in mammalian cells. *Nucleic Acids Res* **34**, 2998-3007 (2006).

153. Davis, B. J., Havener, J. M. & Ramsden, D. A. End-bridging is required for pol mu to efficiently promote repair of noncomplementary ends by nonhomologous end joining. *Nucleic Acids Res* **36**, 3085-3094 (2008).

154. Ma, Y. et al. A biochemically defined system for mammalian nonhomologous DNA end joining. *Mol Cell* **16**, 701-713 (2004).

155. Ahnesorg, P., Smith, P. & Jackson, S. P. XLF interacts with the XRCC4-DNA ligase IV complex to promote DNA nonhomologous end-joining. *Cell* **124**, 301-313 (2006).

156. Buck, D. et al. Cernunnos, a novel nonhomologous end-joining factor, is mutated in human immunodeficiency with microcephaly. *Cell* **124**, 287-299 (2006).

157. Lieber, M. R., Ma, Y., Pannicke, U. & Schwarz, K. Mechanism and regulation of human non-homologous DNA end-joining. *Nat Rev Mol Cell Biol* **4**, 712-720 (2003).

158. Barnes, D. E., Stamp, G., Rosewell, I., Denzel, A. & Lindahl, T. Targeted disruption of the gene encoding DNA ligase IV leads to lethality in embryonic mice. *Curr Biol* **8**, 1395-138. (1998).

159. Gao, Y. et al. A critical role for DNA end-joining proteins in both lymphogenesis and neurogenesis. *Cell* **95**, 891-902. (1998).

160. Gu, Y. et al. Growth retardation and leaky SCID phenotype of Ku70-deficient mice. *Immunity* **7**, 653-665 (1997).

161. Gao, Y. et al. A targeted DNA-PKcs-null mutation reveals DNA-PK-independent functions for KU in V(D)J recombination. *Immunity* **9**, 367-376 (1998).

162. Soutoglou, E. et al. Positional stability of single double-strand breaks in mammalian cells. *Nat Cell Biol* **9**, 675-682 (2007).

163. Lou, Z. et al. MDC1 regulates DNA-PK autophosphorylation in response to DNA damage. *J Biol Chem* **279**, 46359-46362 (2004).

164. Zhang, J., Ma, Z., Treszezamsky, A. & Powell, S. N. MDC1 interacts with Rad51 and facilitates homologous recombination. *Nat Struct Mol Biol* **12**, 902-909 (2005).

165. Harfst, E., Cooper, S., Neubauer, S., Distel, L. & Grawunder, U. Normal V(D)J recombination in cells from patients with Nijmegen breakage syndrome. *Mol Immunol* **37**, 915-929 (2000).

166. Yeo, T. C. et al. V(D)J rearrangement in Nijmegen breakage syndrome. *Mol Immunol* **37**, 1131-1139 (2000).

167. Lou, Z., Chini, C. C., Minter-Dykhouse, K. & Chen, J. Mediator of DNA damage checkpoint protein 1 regulates BRCA1 localization and phosphorylation in DNA damage checkpoint control. *J Biol Chem* **278**, 13599-13602 (2003).

168. Soulas-Sprauel, P. et al. V(D)J and immunoglobulin class switch recombinations: a paradigm to study the regulation of DNA end-joining. *Oncogene* **26**, 7780-7791 (2007).

169. Casellas, R. et al. Ku80 is required for immunoglobulin isotype switching. *EMBO J* **17**, 2404-2411 (1998).

170. Manis, J. P. et al. Ku70 is required for late B cell development and immunoglobulin heavy chain class switching. *J Exp Med* **187**, 2081-2089 (1998).

171. Soulas-Sprauel, P. et al. Role for DNA repair factor XRCC4 in immunoglobulin class switch recombination. *J Exp Med* **204**, 1717-1727 (2007).

172. Corneo, B. et al. Rag mutations reveal robust alternative end joining. *Nature* **449**, 483-486 (2007).

173. Yan, C. T. et al. IgH class switching and translocations use a robust non-classical end-joining pathway. *Nature* **449**, 478-482 (2007).

174. Lee, J. & Desiderio, S. Cyclin A/CDK2 regulates V(D)J recombination by coordinating RAG-2 accumulation and DNA repair. *Immunity* **11**, 771-781 (1999).

175. Petersen, S. et al. AID is required to initiate Nbs1/gamma-H2AX focus formation and mutations at sites of class switching. *Nature* **414**, 660-665 (2001).

176. Muller, H. J. The remaking of chromosomes. *The Collecting Net, Woods Hole* **8**, 182-195 (1938).

177. McClintock, B. The stability of broken ends of chromosomes in Zea mays. *Genetics* **26**, 234-282 (1941).

178. Moyzis, R. K. et al. A highly conserved repetitive DNA sequence, (TTAGGG)n, present at the telomeres of human chromosomes. *Proc Natl Acad Sci USA* **85**, 6622-6626 (1988).

179. Makarov, V. L., Hirose, Y. & Langmore, J. P. Long G tails at both ends of human chromosomes suggest a C strand degradation mechanism for telomere shortening. *Cell* **88**, 657-666 (1997).

180. Zhong, Z., Shiue, L., Kaplan, S. & de Lange, T. A mammalian factor that binds telomeric TTAGGG repeats in vitro. *Mol Cell Biol* **12**, 4834-4843 (1992).

181. Bilaud, T. et al. Telomeric localization of TRF2, a novel human telobox protein. *Nat Genet* **17**, 236-239 (1997).

182. Broccoli, D., Smogorzewska, A., Chong, L. & de Lange, T. Human telomeres contain two distinct Myb-related proteins, TRF1 and TRF2. *Nat Genet* **17**, 231-235 (1997).

183. Bianchi, A. et al. TRF1 binds a bipartite telomeric site with extreme spatial flexibility. *Embo J* **18**, 5735-5744 (1999).

184. Court, R., Chapman, L., Fairall, L. & Rhodes, D. How the human telomeric proteins TRF1 and TRF2 recognize telomeric DNA: a view from high-resolution crystal structures. *EMBO Rep* **6**, 39-45 (2005).

185. Hanaoka, S., Nagadoi, A. & Nishimura, Y. Comparison between TRF2 and TRF1 of their telomeric DNA-bound structures and DNA-binding activities. *Protein Sci* **14**, 119-130 (2005).

186. Bianchi, A., Smith, S., Chong, L., Elias, P. & de Lange, T. TRF1 is a dimer and bends telomeric DNA. *Embo J* **16**, 1785-1794 (1997).

187. Griffith, J., Bianchi, A. & de Lange, T. TRF1 promotes parallel pairing of telomeric tracts in vitro. *J Mol Biol* **278**, 79-88 (1998).

188. Karlseder, J. et al. Targeted deletion reveals an essential function for the telomere length regulator Trf1. *Mol Cell Biol* **23**, 6533-6541 (2003).

189. Iwano, T., Tachibana, M., Reth, M. & Shinkai, Y. Importance of TRF1 for functional telomere structure. *J Biol Chem* **279**, 1442-1448 (2004).

190. Celli, G. & de Lange, T. DNA processing not required for ATM-mediated telomere damage response after TRF2 deletion. *Nat Cell Biol* **7**, 712-718 (2005).

191. Kim, S. H., Kaminker, P. & Campisi, J. TIN2, a new regulator of telomere length in human cells. *Nat Genet* **23**, 405-412 (1999).

192. Ye, J. Z. et al. TIN2 binds TRF1 and TRF2 simultaneously and stabilizes the TRF2 complex on telomeres. *J Biol Chem* **279**, 47264-47271 (2004).

193. Ye, J. Z. et al. POT1-interacting protein PIP1: a telomere length regulator that recruits POT1 to the TIN2/TRF1 complex. *Genes Dev* **18**, 1649-1654 (2004).

194. Kim, S. H. et al. TIN2 mediates functions of TRF2 at human telomeres. *J Biol Chem* **279**, 43799-43804 (2004).

195. Houghtaling, B. R., Cuttonaro, L., Chang, W. & Smith, S. A dynamic molecular link between the telomere length regulator TRF1 and the chromosome end protector TRF2. *Curr Biol* **14**, 1621-1631 (2004).

196. Liu, D. et al. PTOP interacts with POT1 and regulates its localization to telomeres. *Nat Cell Biol* **6**, 673-680 (2004).

197. Hockemeyer, D., Daniels, J. P., Takai, H. & de Lange, T. Recent expansion of the telomeric complex in rodents: Two distinct POT1 proteins protect mouse telomeres. *Cell* **126**, 63-77 (2006).

198. Wu, L. et al. Pot1 deficiency initiates DNA damage checkpoint activation and aberrant homologous recombination at telomeres. *Cell* **126**, 49-62 (2006).

199. Li, B., Oestreich, S. & de Lange, T. Identification of human Rap1: implications for telomere evolution. *Cell* **101**, 471-483 (2000).

200. Zhu, X. D., Kuster, B., Mann, M., Petrini, J. H. & de Lange, T. Cell-cycle-regulated association of RAD50/MRE11/NBS1 with TRF2 and human telomeres. *Nat Genet* **25**, 347-352 (2000).

201. Zhu, X. D. et al. ERCC1/XPF Removes the 3' Overhang from Uncapped Telomeres and Represses Formation of Telomeric DNA-Containing Double Minute Chromosomes. *Mol Cell* **12**, 1489-1498 (2003).

202. Lenain, C. et al. The Apollo 5' exonuclease functions together with TRF2 to protect telomeres from DNA repair. *Curr Biol* **16**, 1303-1310 (2006).

203. van Overbeek, M. & de Lange, T. Apollo, an Artemis-related nuclease, interacts with TRF2 and protects human telomeres in S phase. *Curr Biol* **16**, 1295-1302 (2006).

204. Hsu, H. L., Gilley, D., Blackburn, E. H. & Chen, D. J. Ku is associated with the telomere in mammals. *Proc Natl Acad Sci USA* **96**, 12454-12458 (1999).

205. d'Adda di Fagagna, F. et al. Effects of DNA nonhomologous end-joining factors on telomere length and chromosomal stability in mammalian cells. *Curr Biol* **11**, 1192-116. (2001).

206. O'Connor, M. S., Safari, A., Liu, D., Qin, J. & Songyang, Z. The human Rap1 protein complex and modulation of telomere length. *J Biol Chem* **279**, 28585-28591 (2004).

207. Song, K., Jung, D., Jung, Y., Lee, S. G. & Lee, I. Interaction of human Ku70 with TRF2. *FEBS Lett* **481**, 81-5. (2000).

208. Crabbe, L., Verdun, R. E., Haggblom, C. I. & Karlseder, J. Defective telomere lagging strand synthesis in cells lacking WRN helicase activity. *Science* **306**, 1951-1953 (2004).

209. Lillard-Wetherell, K. et al. Association and regulation of the BLM helicase by the telomere proteins TRF1 and TRF2. *Hum Mol Genet* **13**, 1919-1932 (2004).

210. Machwe, A., Xiao, L. & Orren, D. K. TRF2 recruits the Werner syndrome (WRN) exonuclease for processing of telomeric DNA. *Oncogene* **23**, 149-156 (2004).

211. Opresko, P. L. et al. Telomere binding protein TRF2 binds to and stimulates the Werner and Bloom syndrome helicases. *J Biol Chem* **277**, 41110-41119 (2002).

212. Tarsounas, M. et al. Telomere maintenance requires the RAD51D recombination/repair protein. *Cell* **117**, 337-347 (2004).

213. Hemann, M. T. & Greider, C. W. G-strand overhangs on telomeres in telomerase-deficient mouse cells. *Nucleic Acids Res* **27**, 3964-3969 (1999).

214. Huffman, K. E., Levene, S. D., Tesmer, V. M., Shay, J. W. & Wright, W. E. Telomere shortening is proportional to the size of the G-rich telomeric 3'-overhang. *J Biol Chem* **275**, 19719-19722 (2000).

215. Wright, W. E., Tesmer, V. M., Huffman, K. E., Levene, S. D. & Shay, J. W. Normal human chromosomes have long G-rich telomeric overhangs at one end. *Genes Dev* **11**, 2801-2809 (1997).

216. Hockemeyer, D., Palm, W., Wang, R. C., Couto, S. S. & de Lange, T. Engineered telomere degradation models dyskeratosis congenita. *Genes Dev* **22**, 1773-1785 (2008).

217. Sfeir, A. J., Chai, W., Shay, J. W. & Wright, W. E. Telomere-end processing the terminal nucleotides of human chromosomes. *Mol Cell* **18**, 131-138 (2005).

218. Hockemeyer, D., Sfeir, A. J., Shay, J. W., Wright, W. E. & de Lange, T. POT1 protects telomeres from a transient DNA damage response and determines how human chromosomes end. *EMBO J.* **24**, 2667-2678 (2005).

219. Griffith, J. D. et al. Mammalian telomeres end in a large duplex loop. *Cell* **97**, 503-14. (1999).

220. Nikitina, T. & Woodcock, C. L. Closed chromatin loops at the ends of chromosomes. *J Cell Biol* **166**, 161-165 (2004).

221. Stansel, R. M., de Lange, T. & Griffith, J. D. T-loop assembly in vitro involves binding of TRF2 near the 3' telomeric overhang. *EMBO J* **20**, 5532-5540 (2001).

222. Amiard, S. et al. A topological mechanism for TRF2-enhanced strand invasion. *Nat Struct Mol Biol* **14**, 147-154 (2007).

223. Bao, S. et al. ATR/ATM-mediated phosphorylation of human Rad17 is required for genotoxic stress responses. *Nature* **411**, 969-974 (2001).

224. Zou, L., Cortez, D. & Elledge, S. J. Regulation of ATR substrate selection by Rad17-dependent loading of Rad9 complexes onto chromatin. *Genes Dev* **16**, 198-208 (2002).

225. Bermudez, V. P. et al. Loading of the human 9-1-1 checkpoint complex onto DNA by the checkpoint clamp loader hRad17-replication factor C complex in vitro. *Proc Natl Acad Sci USA* **100**, 1633-1638 (2003).

226. Zou, L. & Elledge, S. J. Sensing DNA damage through ATRIP recognition of RPA-ssDNA complexes. *Science* **300**, 1542-1548 (2003).

227. Liu, Q. et al. Chk1 is an essential kinase that is regulated by Atr and required for the G(2)/M DNA damage checkpoint. *Genes Dev* **14**, 1448-1459 (2000).

228. Lazzerini Denchi, E. & de Lange, T. Protection of telomeres through independent control of ATM and ATR by TRF2 and POT1. *Nature* **448**, 1068-1071 (2007).

229. Hockemeyer, D. et al. Telomere protection by mammalian POT1 requires interaction with TPP1. *Nat Struct Mol Biol* **14**, 754-761 (2007).

230. van Steensel, B., Smogorzewska, A. & de Lange, T. TRF2 protects human telomeres from end-to-end fusions. *Cell* **92**, 401-413 (1998).

231. Karlseder, J., Broccoli, D., Dai, Y., Hardy, S. & de Lange, T. p53- and ATM-dependent apoptosis induced by telomeres lacking TRF2. *Science* **283**, 1321-1325 (1999).

232. Smogorzewska, A. & de Lange, T. Different telomere damage signaling pathways in human and mouse cells. *Embo J* **21**, 4338-4348 (2002).

233. Karlseder, J. et al. The telomeric protein TRF2 binds the ATM kinase and can inhibit the ATM-dependent DNA damage response. *PLoS Biol* **2**, E240 (2004).

234. McClintock, B. 1-48 (Garland Publishing, Inc, New York and London, 1938).

235. Smogorzewska, A., Karlseder, J., Holtgreve-Grez, H., Jauch, A. & de Lange, T. DNA Ligase IV-Dependent NHEJ of Deprotected Mammalian Telomeres in G1 and G2. *Curr Biol* **12**, 1635 (2002).

236. Celli, G. B., Lazzerini Denchi, E. & de Lange, T. Ku70 stimulates fusion of dysfunctional telomeres yet protects chromosome ends from homologous recombination. *Nat Cell Biol* **8**, 885-890 (2006).

237. Konishi, A. & de Lange, T. Cell cycle control of telomere protection and NHEJ revealed by a ts mutation in the DNA-binding domain of TRF2. *Genes Dev* **22**, 1221-1230 (2008).

238. Ranganathan, V. et al. Rescue of a telomere length defect of Nijmegen breakage syndrome cells requires NBS and telomerase catalytic subunit. *Curr Biol* **11**, 962-96. (2001).

239. Chai, W., Sfeir, A. J., Hoshiyama, H., Shay, J. W. & Wright, W. E. The involvement of the Mre11/Rad50/Nbs1 complex in the generation of G-overhangs at human telomeres. *EMBO Rep* **7**, 225-230 (2006).

240. de Lange, T. & Petrini, J. A new connection at human telomeres: association of the Mre11 complex with TRF2. *Cold Spring Harb Symp Quant Biol* **LXV**, 265-273 (2000).

241. Chen, Y. et al. A shared docking motif in TRF1 and TRF2 used for differential recruitment of telomeric proteins. *Science* **319**, 1092-1096 (2008).

242. Palm, W. & de Lange, T. How shelterin protects mammalian telomeres. *Ann Rev Genetics* **42**, 16.1-16.34 (2008).

243. Gatei, M. et al. ATM-dependent phosphorylation of nibrin in response to radiation exposure. *Nat Genet* **25**, 115-119 (2000).

244. Zhu, J., Petersen, S., Tessarollo, L. & Nussenzweig, A. Targeted disruption of the Nijmegen breakage syndrome gene NBS1 leads to early embryonic lethality in mice. *Curr Biol* **11**, 105-109 (2001).

245. Palm, W., Hockemeyer, D., Kibe, T. & de Lange, T. Functional dissection of human and mouse POT1 proteins. *Mol Cell Biol* **29**, 471-482 (2009).

246. Zhu, Z., Chung, W.-H., Shim, E. Y., Lee, S. E. & Ira, G. Sgs1 helicase and two nucleases Dna2 and Exo1 resect DNA double-strand break ends. *Cell* **134**, 981-994 (2008).

247. Dupre, A. et al. A forward chemical genetic screen reveals an inhibitor of the Mre11-Rad50-Nbs1 complex. *Nat Chem Biol* **4**, 119-125 (2008).

248. Petrini, J. & Stracker, T. H. The cellular response to DNA double strand breaks: defining the sensors and mediators. *Trends Cell Biol* **13**, 458-462 (2003).

249. Wang, R. C., Smogorzewska, A. & de Lange, T. Homologous recombination generates T-loop-sized deletions at human telomeres. *Cell* **119**, 355-368 (2004).

250. Smogorzewska, A. et al. Control of human telomere length by TRF1 and TRF2. *Mol Cell Biol* **20**, 1659-1668 (2000).

251. Xu, X. & Stern, D. F. NFBD1/MDC1 regulates ionizing radiation-induced focus formation by DNA checkpoint signaling and repair factors. *FASEB J* **17**, 1842-1848 (2003).

252. O'Driscoll, M., Ruiz-Perez, V. L., Woods, C. G., Jeggo, P. A. & Goodship, J. A. A splicing mutation affecting expression of ataxia-telangiectasia and Rad3-related protein (ATR) results in Seckel syndrome. *Nat Genet* **33**, 497-501 (2003).

253. Ward, I. et al. The tandem BRCT domain of 53BP1 is not required for its repair function. *J Biol Chem* **281**, 38472-38477 (2006).

254. van Steensel, B. & de Lange, T. Control of telomere length by the human telomeric protein TRF1. *Nature* **385**, 740-743 (1997).

255. Molenaar, C. et al. Visualizing telomere dynamics in living mammalian cells using PNA probes. *Embo J* **22**, 6631-6641 (2003).

256. Abney, J. R., Cutler, B., Fillbach, M. L., Axelrod, D. & Scalettar, B. A. Chromatin dynamics in interphase nuclei and its implications for nuclear structure. *J Cell Biol* **137**, 1459-1468 (1997).

257. Shogren-Knaak, M. et al. Histone H4-K16 acetylation controls chromatin structure and protein interactions. *Science* **311**, 844-847 (2006).

258. Trojer, P. et al. L3MBTL1, a histone-methylation-dependent chromatin lock. *Cell* **129**, 915-928 (2007).

259. Gilbert, N. et al. Chromatin architecture of the human genome: gene-rich domains are enriched in open chromatin fibers. *Cell* **118**, 555-566 (2004).

260. Noll, H. & Noll, M. Sucrose gradient techniques and applications to nucleosome structure. *Methods Enzymol* **170**, 55-116 (1989).

261. Tommerup, H., Dousmanis, A. & de Lange, T. Unusual chromatin in human telomeres. *Mol Cell Biol* **14**, 5777-5785 (1994).

262. Wu, P. & de Lange, T. No overt nucleosome eviction at deprotected telomeres. *Mol Cell Biol* **28**, 5724-5735 (2008).

263. Kumaran, R. I., Thakar, R. & Spector, D. L. Chromatin dynamics and gene positioning. *Cell* **132**, 929-934 (2008).

264. Koszul, R., Kim, K. P., Prentiss, M., Kleckner, N. & Kameoka, S. Meiotic chromosomes move by linkage to dynamic actin cables with transduction of force through the nuclear envelope. *Cell* **133**, 1188-1201 (2008).

265. Conrad, M. N. et al. Rapid telomere movement in meiotic prophase is promoted by NDJ1, MPS3, and CSM4 and is modulated by recombination. *Cell* **133**, 1175-1187 (2008).

266. Lo, K. W. et al. The 8-kDa dynein light chain binds to p53-binding protein 1 and mediates DNA damage-induced p53 nuclear accumulation. *J Biol Chem* **280**, 8172-8179 (2005).

267. Yamamoto, A., West, R. R., McIntosh, J. R. & Hiraoka, Y. A cytoplasmic dynein heavy chain is required for oscillatory nuclear movement of meiotic prophase and efficient meiotic recombination in fission yeast. *J Cell Biol* **145**, 1233-1249 (1999).

268. Yamashita, A. & Yamamoto, M. Fission yeast Num1p is a cortical factor anchoring dynein and is essential for the horse-tail nuclear movement during meiotic prophase. *Genetics* **173**, 1187-1196 (2006).

269. King, M. C., Drivas, T. G. & Blobel, G. A network of nuclear envelope membrane proteins linking centromeres to microtubules. *Cell* **134**, 427-438 (2008).

270. Kao, G. D. et al. Histone deacetylase 4 interacts with 53BP1 to mediate the DNA damage response. *J Cell Biol* **160**, 1017-1027 (2003).

271. Hubbert, C. et al. HDAC6 is a microtubule-associated deacetylase. *Nature* **417**, 455-458 (2002).

272. Morales, J. C. et al. Role for the BRCA1 C-terminal repeats (BRCT) protein 53BP1 in maintaining genomic stability. *J Biol Chem* **278**, 14971-14977 (2003).

273. Difilippantonio, S. et al. 53BP1 facilitates long-range DNA end-joining during V(D)J recombination. *Nature* (2008).

274. Mundy, C. L., Patenge, N., Matthews, A. G. & Oettinger, M. A. Assembly of the RAG1/RAG2 synaptic complex. *Mol Cell Biol* **22**, 69-77 (2002).

275. Wang, L., Whang, N., Wuerffel, R. & Kenter, A. L. AID-dependent histone acetylation is detected in immunoglobulin S regions. *J Exp Med* **203**, 215-226 (2006).

276. Nambu, Y. et al. Transcription-coupled events associating with immunoglobulin switch region chromatin. *Science* **302**, 2137-2140 (2003).

277. Li, Z., Luo, Z. & Scharff, M. D. Differential regulation of histone acetylation and generation of mutations in switch regions is associated with Ig class switching. *Proc Natl Acad Sci U S A* **101**, 15428-15433 (2004).

278. Azzalin, C. M., Reichenbach, P., Khoriauli, L., Giulotto, E. & Lingner, J. Telomeric repeat containing RNA and RNA surveillance factors at mammalian chromosome ends. *Science* **318**, 798-801 (2007).

279. O'Neill, L. P. & Turner, B. M. Histone H4 acetylation distinguishes coding regions of the human genome from heterochromatin in a differentiation-dependent but transcription-independent manner. *EMBO J* **14**, 3946-3957 (1995).

280. Gonzalo, S. et al. DNA methyltransferases control telomere length and telomere recombination in mammalian cells. *Nat Cell Biol* **8**, 416-424 (2006).

281. Baur, J. A., Zou, Y., Shay, J. W. & Wright, W. E. Telomere position effect in human cells. *Science* **292**, 2075-207. (2001).

282. Gottschling, D. E., Aparicio, O. M., Billington, B. L. & Zakian, V. A. Position effect at S. cerevisiae telomeres: reversible repression of Pol II transcription. *Cell* **63**, 751-762 (1990).

283. Pichierri, P. & Rosselli, F. The DNA crosslink-induced S-phase checkpoint depends on ATR-CHK1 and ATR-NBS1-FANCD2 pathways. *EMBO J* **23**, 1178-1187 (2004).

284. Silver, D. P. & Livingston, D. M. Self-excising retroviral vectors encoding the Cre recombinase overcome Cre-mediated cellular toxicity. *Mol Cell* **8**, 233-243 (2001).

285. Sbalzarini, I. F. & Koumoutsakos, P. Feature point tracking and trajectory analysis for video imaging in cell biology. *J Struct Biol* **151**, 182-195 (2005).